



Swansea University
Prifysgol Abertawe

Novel Porous Polymers as Flame Retardant and Gas Separation Materials

Yue Wu

Department of Chemistry

Swansea University

Submitted to Swansea University in fulfilment of the requirements for the Degree of
Doctor of Philosophy

August 2024

Supervisor: Dr Mariolino Carta

Abstract

Nowadays, polymer materials have permeated every aspect of our daily life, bringing not only convenience but also fire hazards. The limiting oxygen index of most polymer materials is lower than 21, that means they are flammable or combustible in air. A large amount of toxic and corrosive smoke and gas are released during combustion, that pose a big threat to people's safety and cause environmental pollution. Therefore, the development of flame retardant materials has attracted the attention of researchers around the world.

This project aims to develop novel PIM-based flame retardant additives. Specifically, we designed three series of PIM materials. The first discussion chapter includes the preparation of boroxine and boronic ester-based PIMs. We verified the feasibility of boroxine network polymerisation and its satisfactory thermal decomposition behaviour. Boronic ester-PIMs containing different contorted units were synthesized using two different heating devices and compared in terms of purity, thermal stability and porosity, especially to understand if porosity influences the flame retardation capability. It was shown that their thermal properties meet the requirements of standard flame retardant additives. The second series shows PIMs composed of hexaphenylbenzene core units and Tröger's Base linkages with different C/N ratios and porosities, as it is known that increasing the amount of N per repeat unit improves the thermal stability. It was confirmed that these polymers have excellent thermal properties, which can be enhanced by increasing their functionality, i.e., improving their content of nitrogen and porosity. In the third series, cyclophosphazene was polymerised respectively with catechols and amines using two heating methods. This is a very challenging and new method to make phosphorous-containing PIMs. Two catechol-based polymers were successfully obtained and exhibited desirable thermal decomposition behaviours. The preparation of the amine-based polymer was preliminarily explored as well. Furthermore, the performance of the novel PIMs from series 1 and 2 in gas separation was also investigated. (Polymers from series 3 were excluded due to their low specific surface areas.) The results also indicated that the high heteroatom content, specific surface area and narrow microporosity helped to improve both the CO₂ uptake and CO₂/N₂ selectivity of the materials.

Declarations

This work has not previously been accepted in substance for any degree and is not being concurrently submitted in candidature for any degree.

Signed.....



Date..... 15/08/2024

This thesis is the result of my own investigations, except where otherwise stated. Other sources are acknowledged by footnotes giving explicit references. A bibliography is appended.


Signed.....



Date..... 15/08/2024

I hereby give consent for my thesis, if accepted, to be available for electronic sharing

Signed.....



Date..... 15/08/2024

The University's ethical procedures have been followed and, where appropriate, that ethical approval has been granted.

Signed.....



Date..... 15/08/2024

Content

Abstract	i
Declarations.....	ii
Content.....	iii
Acknowledgements	v
Abbreviations.....	vi
Chapter 1 – Introduction	1
1.1 Porous Materials	1
1.1.1 Characterization of Porosity	1
1.1.2 Classification of Porous Frameworks	3
1.2 Organic Flame Retardants (FRs)	23
1.2.1 Flame Retardant Mechanism	23
1.2.2 Evaluation of Combustion Performance	25
1.2.3 Classification of Flame Retardants (FRs).....	26
Aims of the Project.....	35
Chapter 2 – Novel Boron-containing PIMs for Flame Retardation and Gas Separation	36
2.1 Introduction	36
2.1.1 Boroxine-based PIMs.....	36
2.1.2 Boronic Ester-based PIMs (BE-PIMs)	38
2.2 Results and Discussion	39
2.2.1 Boroxine-based PIMs.....	39
2.2.2 Boronic Ester-based PIMs (BE-PIMs)	48
2.3 Conclusion	61
Chapter 3 – Novel Nitrogen-containing PIMs for Flame Retardation and Gas Separation	62
3.1 Introduction	62

3.2	Results and Discussion	65
3.2.1	Diamino-HPB Monomers	65
3.2.2	Tetraamino-HPB Monomer	66
3.2.3	Hexaamino-HPB Monomer	69
3.2.4	TB-based Polymers	70
3.3	Conclusion	82
Chapter 4 – Novel Cyclophosphazene-based PIMs for Flame Retardation and Gas Separation		83
4.1	Introduction	83
4.2	Results and Discussion	86
4.2.1	Catechol-based CTP-PIMs	86
4.2.2	Amine-based CTP-PIMs	96
4.3	Conclusion	104
Chapter 5 – Conclusions and Future Work		106
Chapter 6 – Experimental Section		109
6.1	General Methods and Equipment	109
6.2	IAST Selectivity Calculation	110
6.3	Synthesis of Monomers	111
6.4	Synthesis of Model Compounds and Polymers	124
Chapter 7 – References		135
Appendix		151
8.1	SSNMR	151
8.2	FT-IR	155
8.3	TGA	168
8.4	Isotherms	180
8.5	PSD	190

Acknowledgements

First of all, I am very grateful to my supervisor Lino. Thank you for your guidance and support over the past four years, and particularly for always trusting and encouraging me to face challenges, even when I didn't trust myself. What I learned from you is not only knowledge and skills but also optimism, independence and patience.

Thank you to Grazia for guiding me in writing this thesis, which is only possible with your sincere advice and careful guidance. Thank you to Ariana for always helping me and answering my questions in the lab and for building a wonderful friendship with me. And Natasha, thank you for all your help and kindness both at work and after work. Thank you to Kevin and Rebecca for assisting me with my experiments at my very busy time. I am glad to join our group and meet these lovely people.

Thank you to everyone in the Swansea Chemistry research family, especially Kate, Chiara, Martina, Ben and Michael, who helped me out of difficulty in my experiments.

Thank you to Dr Daniel Dawson from the University of St Andrews for your excellent work on Solid State NMR.

Thank you to my best friend Luyao for being available online from the other side of the earth whenever I need you. I see you as a sister forever even without a blood relation.

Thank you to the lovely girls in the Gals Practicing Chemistry group chat. The coffee time I spent with you is a precious memory for me.

Thank you to my family: To my mum and dad, thank you for always unconditionally supporting and helping me turn all my dreams into reality. I hope to be your pride. To my cousin Dan, for our reciprocal companionship since childhood.

Thank myself for never giving up. You look beautiful when you keep running with tears.

Finally, to all the people I am about to say goodbye: The World Is Round. We will meet again somewhere sometime, as long as we keep moving forward,

Thank you to EPSRC for funding this research.



Abbreviations

BE-PIM – Boronic ester-based PIM

BET – Brunauer-Emmett-Teller theory

CANAL – Catalytic norbornene-arene annulation

CMP – Conjugated microporous polymer

COF – Covalent-organic framework

CPD – Cyclopentadienone

CTF – Covalent triazine framework

CTP – Cyclotriphosphazene

DCM – Dichloromethane

DMF – Dimethylformamide

DMSO – Dimethylsulfoxide

DSC – Differential scanning calorimetry

DTG – Differential thermogravimetric analysis

EA – Ethanoanthracene

Et₃N – Triethylamine

FR – Flame retardant

FT-IR – Fourier-transform infrared spectroscopy

GPC – Gel permeation chromatography

HCCP – Hexachlorocyclotriphosphazene

HCP – Hypercross-linked polymer

HPB – Hexaphenylbenzene

IAST – Ideal Adsorbed Solution Theory

LOI – Limiting oxygen index

LRMS – Low-resolution mass spectrometry

MeCN – Acetonitrile

MeOH – Methanol

MOF – Metal-Organic Framework

Mp – Melting point

***n*-BuLi** – *n*-butyllithium

NLDFT – Non-local density functional theory

NMR – Nuclear Magnetic Resonance

PAF – Porous aromatic framework

PI – Polyimide

PIM – Polymer of intrinsic microporosity

POF – Porous Organic Framework

PSD – Pore Size Distribution

Q_{st} – Isosteric heat of adsorption

SA_{BET} – BET specific surface area

SBC – Spirobichroman

SBF – Spirobifluorene

SBI – Spirobisindane

SEM – Scanning electron microscopy

SSNMR – Solid state (¹³C) NMR

T_d – Thermal decomposition temperature

T_g – Glass transition temperature

T_i – Initial decomposition temperature

T_{max} – Maximum weight loss rate temperature

TB – Tröger's Base

TBPB – 1,3,5-Tris(4-bromophenyl)benzene

TGA – Thermogravimetric analysis

THF – Tetrahydrofuran

TLC – Thin layer chromatography

TPB – 1,3,5-Triphenylbenzene

TPE – Tetraphenylethylene

Trip – Triptycene

Chapter 1 – Introduction

1.1 Porous Materials

Porous materials are rich in interconnected or closed pore structures and play an irreplaceable role in many fields of materials science such as membranes, adsorption, catalysis and energy storage.^{1, 2} They consist of two parts: pores and frameworks. The pore's structure can be evaluated based on their size, volume and type, which directly affects the properties and applications of the final materials. Depending on pore sizes, porous materials are classified into macroporous (pore width more than 50 nm), mesoporous (pore width between 2 nm and 50 nm) and microporous materials (pore width less than 2 nm).³

1.1.1 Characterization of Porosity

The porosity of these materials is generally characterized by gas adsorption-desorption techniques. Under controlled temperature and pressure, reversible adsorption-desorption occurs between the solid sample surface and the probe gas and then a certain equilibrium adsorption amount will be reached. The adsorption isotherms are obtained by measuring the gas uptake against the change of the partial pressure (P/P_0 , where P_0 is usually atmospheric pressure), and the values of specific surface area, pore volume and pore size distribution (PSD) are calculated according to appropriate theoretical models such as Brunauer-Emmett-Teller theory (BET), Langmuir theory, Non-local density functional theory (NLDFT), etc.⁴ Adsorption isotherms resulting from these measurements are classified into six types according to International Union of Pure and Applied Chemistry (**Fig 1.1**). Type-I isotherms correspond to monolayer adsorption.⁵ They usually occur in microporous materials with pore sizes not wider than 2 nm.⁶ Type-II to Type-VI isotherms correspond to multilayer adsorption.⁵ These adsorption behaviours can be described by the BET isotherm model,^{7, 8} which assumes homogeneous adsorption for the first layer and ideal evaporation-condensation for subsequent layers.⁵ It is generally believed that monolayer formation occurs in the relative pressure (P/P_0) range from 0.05 to 0.30, called the BET standard pressure range, which was specially modified to $P/P_0 < 0.05$ for microporous adsorbents. Most calculation and analysis are based on this linear region in isotherms.⁹

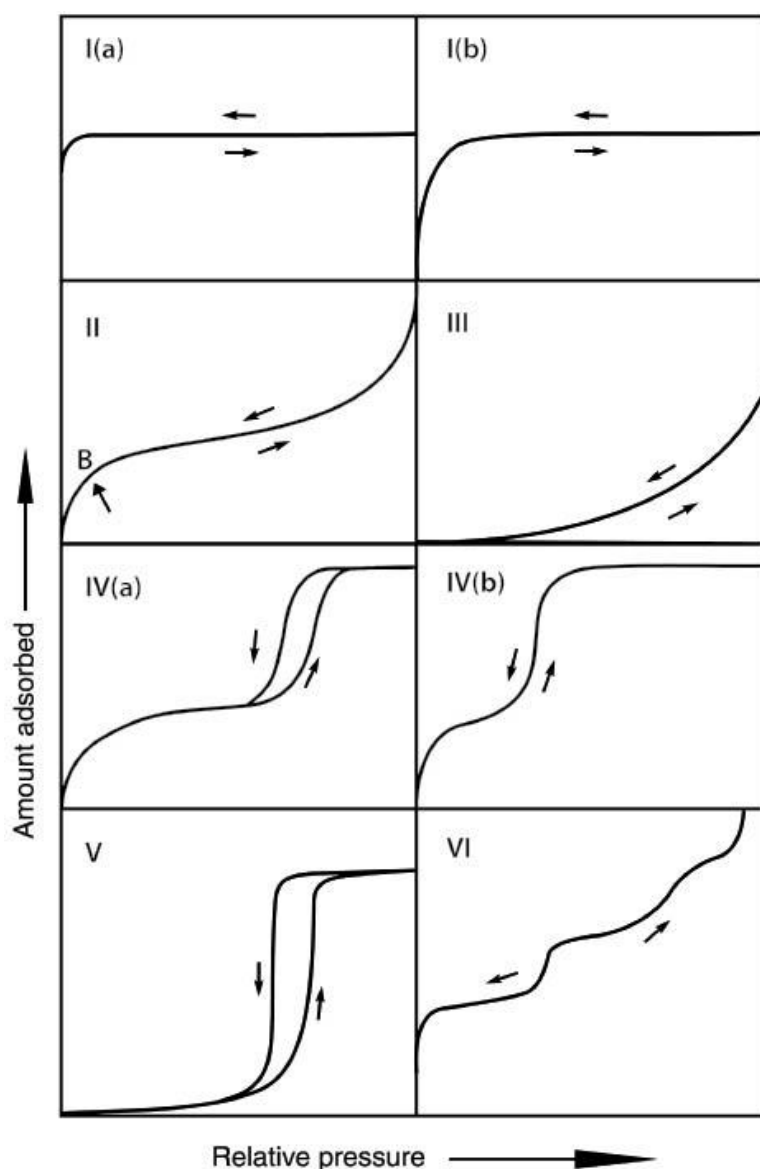


Figure 1.1 Classification of physisorption isotherms.³

Selection of probe gases depends on the characteristics of the tested porous materials. Nitrogen is inert, cheap, readily available, and offers good reversible adsorption. Nitrogen adsorption at 77 K is generally the preferred measurement for determining surface area and mesopore size distribution.⁶ However, when the sample has microporosity or a small surface area, argon and CO₂¹⁰ provide better accuracy than nitrogen. Argon adsorption is carried out at 87 K. A high temperature is conducive to shortening the equilibrium time and improving the test efficiency. Argon is a non-polar, monatomic molecule, and is not prone to specific adsorption with polar samples. The small molecular size enables it to approach narrow pores. Therefore, argon can generally only be used for measuring microporous materials. CO₂ can be adsorbed at 273 K, which is much higher than the adsorption temperature of argon and nitrogen,

greatly enhancing gas diffusion. One potential drawback is that CO₂ adsorption cannot typically reach exact values of P/P_0 , because of its high saturated vapor pressure (3485.3 kPa) at 273 K, unless the measurement is performed in high pressure conditions. For this reason, we approximate this measurement assuming it will reach saturated pressure and analysing the curve at 1 atm (which corresponds to 0.03 P/P_0). This assumption is well accepted, and measurements of porosity and PSD using CO₂ at 273 K are becoming very common.¹⁰

1.1.2 Classification of Porous Frameworks

The framework is the other component of porous materials. Generally, they are rigid skeletons that form the boundaries of the pores and support the entire structure. The earliest porous materials were mainly inorganic compounds obtained from nature. Many of them, like zeolite, activated carbon and porous silica, are still widely used in modern industry. Porous materials have been revolutionized with the development of organic synthesis and processing, ranging from the traditional inorganic framework to inorganic-organic hybrid frameworks and pure organic frameworks,¹¹ which show advantages, including designable skeletons, functional groups tunability, and advanced synthesizing and processing methods. That means their properties can be specially tailored to meet different requirements according to a variety of applications. The properties of several porous framework materials are discussed in detail below and summarized in **Table 1.1**.

1.1.2.1 Porous Inorganic Frameworks

Zeolite is a porous mineral that is naturally formed from volcanic origin, composed of crystalline aluminosilicate. The pore sizes of zeolites (**Fig 1.2 a**) are rarely larger than 1 nm to maintain their structural stability. Although narrow pores contribute to good selectivity by adsorbates sizes, restricted pore sizes hinder the substance diffusion and leads to low pore volume and limited accessibility of active sites.¹² There is evidence that zeolites have excellent thermal stability¹³ but they are unstable under humid and acid/base conditions,¹⁴ which affects their durability and lifespan.

Porous carbon is a special kind of carbon material. Some examples are activated carbon, graphene and carbon nanotubes (**Fig 1.2 b**). Porous carbon is one of the most widely used commercial porous materials, with the advantages of good thermal

conductivity, high electrical conductivity, high chemical stability and mechanical strength, and adjustable pore structure.^{15, 16} Their skeletons, composed only of carbon atoms, are suitable for modification through a variety of organic chemical reactions to increase their chemical diversity.¹⁷ However, their production process has some disadvantages such as high cost, equipment corrosion, and emission of toxic gases and byproduct pollutants, therefore exploration on new production strategies is required.¹⁸

Mesoporous silicas are a type of inorganic nanoconstruct with uniform and ordered mesopores in their amorphous matrix (**Fig 1.2 c**).¹⁹ They have low thermal and hydrothermal stability, due to the high concentration of silanols on the pore walls and the shortage of crystallinity.²⁰ In addition, the distribution of potential heteroelements in modified mesoporous silica is normally very heterogeneous, due to their known amorphous structure.¹²

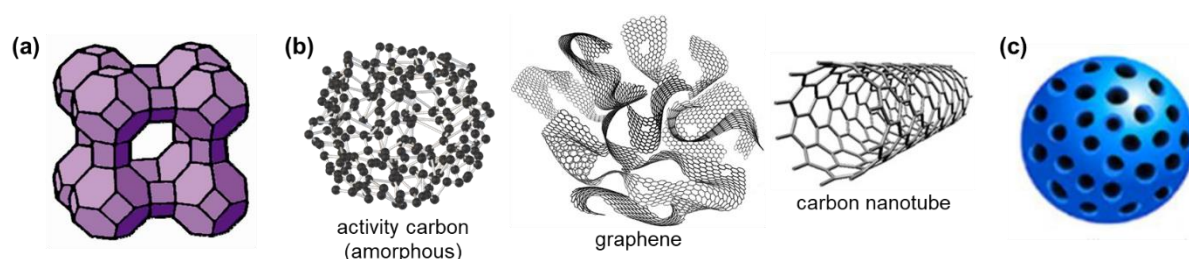


Figure 1.2 The classic structures of (a) zeolite²¹, (b) porous carbon²²⁻²⁴ and (c) mesoporous silica²⁵.

1.1.2.2 Inorganic-Organic Hybrid Frameworks

The most typically synthetic representative of inorganic-organic hybrid frameworks is the metal-organic frameworks (MOFs, **Fig 1.3**) family, which are crystalline materials with highly ordered porous structures. Like organic polymers, MOFs possess adjustable pore structures and are easy to be functionalised. Compared with other porous frameworks, MOFs often show low thermal and chemical stability because they are connected by labile coordination bonds.²⁶ Most MOFs decompose below 300 °C, and some of them may decompose quickly when in the presence of air, moisture, and solvents.¹²

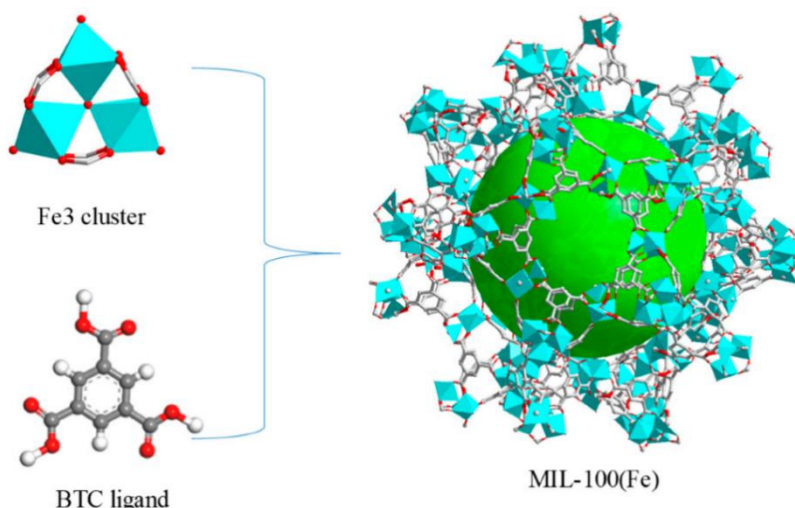


Figure 1.3 Schematic of the construction of MOF MIL-100(Fe).²⁷

Table 1.1 Properties of Zeolite, Porous Carbon, MOF and Porous Polymer.¹²

Properties	Zeolite	Porous Carbon	Mesoporous Silica	MOF	Porous Polymer
Pore size	Micropores	Micro-, meso-, and/or macropores	Mesopores	Micro- and/or mesopores	Micro-, meso-, and/or macropores
Arrangement of molecules	Crystalline	Amorphous	Amorphous	Crystalline	Amorphous or crystalline
Chemical stability	High	Excellent	Limited	Limited	Medium to excellent
Thermal stability	High	High	Medium	Low to medium	Medium to high
Chemical diversity	Low	Low to medium	Low to medium	High	Very high
Structural diversity	High	High	High	High	Very high

Note: Some properties may vary from case to case.

1.1.2.3 Porous Organic Frameworks (POFs)

The diversity of monomer candidates and synthesis methods confers POFs various physical and chemical properties. Also, functional groups can be introduced into POFs via post-synthetic modification. Therefore, porous polymer materials that meet different requirements can be made and modified through specific molecular design. The units of POFs are connected by strong covalent bonds, resulting in a satisfactory stability under humidity, high temperature and acid/base conditions.¹¹

According to their molecular structure and order of arrangement, POFs can be subdivided into covalent-organic frameworks (COFs), covalent triazine frameworks (CTFs), hypercross-linked polymers (HCPs), conjugated microporous polymers

(CMPs), porous aromatic frameworks (PAFs), polymers of intrinsic microporosity (PIMs), etc.¹¹ Among them, COFs and CTFs are typically classified as crystalline materials, while the others are amorphous.

Covalent-Organic Frameworks (COFs)

COFs are a type of microporous polymer with long-range ordered structures afforded by thermodynamically controlled reversible condensation reactions. Their skeletons are composed of light elements such as C, H, B, N and O connected by strong covalent bonds, thus they have better stability and lower density than most of the MOFs. The first COF was reported in 2005 by Yaghi,²⁸ and developed as 2D or 3D crystalline frameworks²⁹⁻³¹ displaying good thermal stability and high specific surface areas.

Compared with those 2D frameworks, 3D COFs offer larger free volume, porosity and specific surface area, making them ideal gas adsorption carriers. Experiments and theoretical calculations verified that boron atoms can effectively improve CO₂ adsorption.³² Kahveci et al. synthesized a mesoporous covalent organic network TDCOF-5 using triptycene (Trip), giving a high specific surface area of 2497 m²/g.³³ The stereo conformation of Trip allowed the boron-containing sites in the structure to be fully exposed to effectively interact with CO₂ molecules, thereby increasing the CO₂ uptake.

As mentioned above, most COFs are built by H, B, C, N, and O and thus easy to combust, inevitably causing safety issues. The design and fabrication of flame-retardant COFs require to be further explored.³⁴ A novel graphene conjugated COF nanohybrid was synthesized and used to enhance the flame retardancy and mechanical performances of epoxy resins. It was proven to reduce the release of heat, smoke and toxic gas.³⁵ Wang et al. constructed a new COF (TR-NKCOF-11, **Fig 1.4**) containing aromatic imide and ortho-positioned hydroxy groups as flame retarding units, which can release CO₂ instead of combustible gases to enhance the inherent flame retardancy of the product. It can be combined with polyethylene glycol and lithium salts to form solid polymers electrolytes with enhanced flame retardancy.³⁴ Peng et al. reported a boron-nitrogen-phosphorus-linked COFs (BNPC) through a facile self-condensation reaction of hydroxyphenylboronic acid substituted hexachlorocyclotriphosphazene, which was used as flame retardant additive for polyacrylonitrile fiber. The analyses of the flame retardant mechanism demonstrate

that the BNPC reduces the chain scission and toxic gases release and promote the formation of crosslinked P-B-N-rich char layer barrier on fiber surface.³⁶

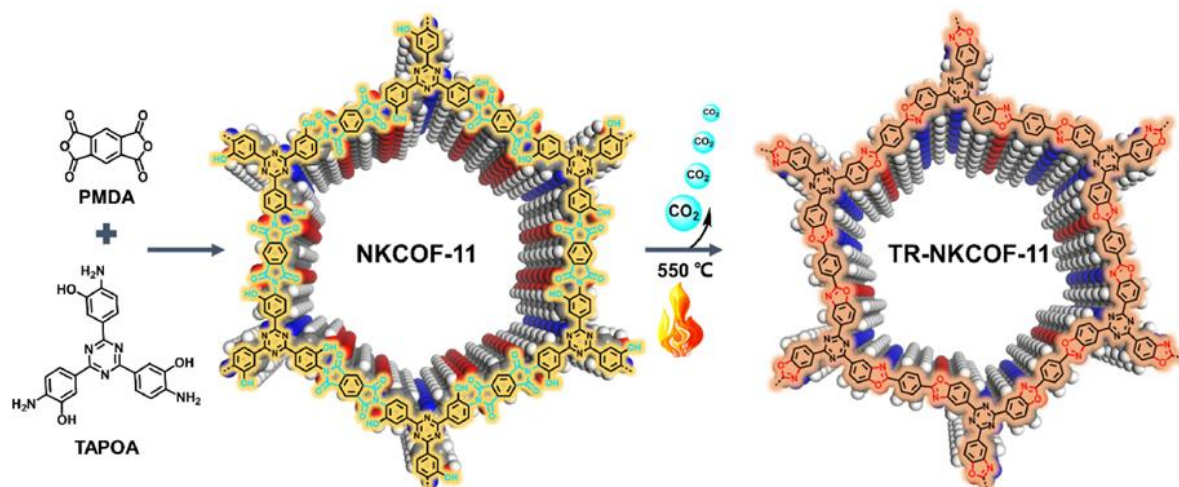


Figure 1.4 Fabrication of benzoxazole-linked TR-NKCOF-11.³⁴

Covalent Triazine Frameworks (CTFs)

CTFs represent another type of POFs with ordered structures, first reported in 2008 by Thomas et al.³⁷ CTFs are mainly composed of rigid aromatic compounds and triazine rings connected by covalent bonds and possess excellent thermal and chemical stability.

CTFs are commonly used for CO₂ capture and as flame retardant materials because of high nitrogen content (which is beneficial for flame retardancy).³⁸ Hug et al. reported two CTFs based on lutidine, pyrimidine, bipyridine, and phenyl units, and revealed that their CO₂ uptake capacities predominantly increase with the micropore volume, rather than surface areas, and the nitrogen content was found to positively contribute to the high CO₂/N₂ selectivity.³⁹ Bhunia et al. prepared adamantane CTFs, exhibiting excellent thermal stabilities (>450 °C) with BET surface areas up to 1180 m²/g, and high selectivity of CO₂ over N₂ and CH₄.⁴⁰

Qiu et al. combined CTF with black phosphorus, forming an organic-inorganic hybrid which was incorporated into epoxy resin matrices. Their thermal decomposition released reduced amounts of toxic CO, flammable volatile products and smoke.⁴¹ Gao et al. synthesized a phosphoric acid modified CTF and used it as a flame retardant (FR) and mechanical reinforcing agent of epoxy resins, which was verified to take effects in both gas and condensed phase (illustrated in 1.2.1) and could maintain flame retardant effect after soaked in 75 °C for 168 hours.⁴² Afshari et al. reported a flame-

retardant triazine-based covalent organic framework (FT-COF, **Fig 1.5**) as additive for thermoplastic polyurethane. Its thermal stability was significantly improved confirmed by the increased char residue, and decreased release of heat, smoke and CO.⁴³

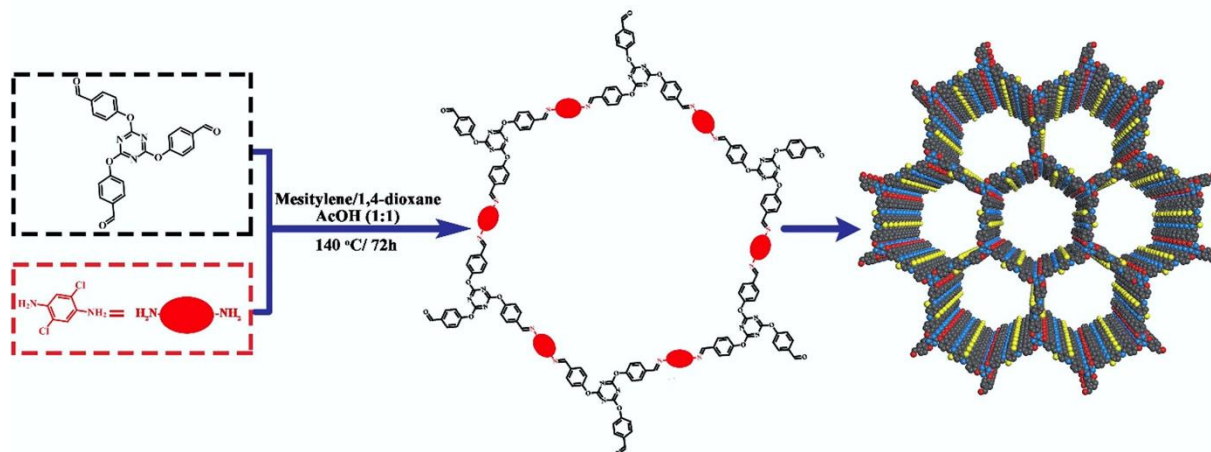


Figure 1.5 Schematic for synthetic route of FT-COF.⁴³

Hyper-Crosslinked Polymers (HCPs)

The earliest HCPs were based on polystyrene skeletons synthesized by post-crosslinking, and traced back to the late 1960s.⁴⁴ Davankov et al. proposed the concept of *hyper-crosslinked polymers* for the first time and explained the mechanism of micropore formation in hyper-crosslinked polymer materials.⁴⁵ The hyper-crosslinking mechanism prevents the collapse of the flexible polymer chains, thereby generating a large number of micropores.⁴⁶ Widespread distribution of such crosslinking sites in HCPs provides them with a characteristic high thermal stability, low density, high specific surface area and large pore volume⁴⁷.

For example, Kaliva et al. prepared a series of microporous polystyrene particles with different levels of crosslinking by emulsion polymerisation.⁴⁸ They had a high π -electron density and could interact with CO₂ molecules, which showed a better selectivity to CO₂ in a gas mixture CO₂/CH₄ = 5/95 (the composition of natural gas) than that of inorganic-organic hybrid materials MOF-5^{49, 50} and mesoporous silica materials MCM-41⁵¹, and was similar to the commercial zeolite 13X⁵². Cooper's group reported a convenient method for synthesizing hyper-crosslinked polymers using aromatic monomers containing bis(chloromethyl) groups.⁵³ They were directly obtained through self-condensation and exhibited a specific surface area of up to 1904 m²/g. Their CO₂ capture ability demonstrated to be much higher compared to commercial activated carbon and zeolite adsorbents.⁵⁴

Yu et al. prepared poly(ethylene oxide)-based composite solid polymer electrolytes (CSPE-HCPs) using hyper-cross-linked $\text{SiO}_2\text{@PMMA-co-PS}$ nanoparticles, which could maintain dimensional stability up to 260 °C and was considered to be promising electrolytes for solid-state lithium-ion batteries (**Fig 1.6**).⁵⁵

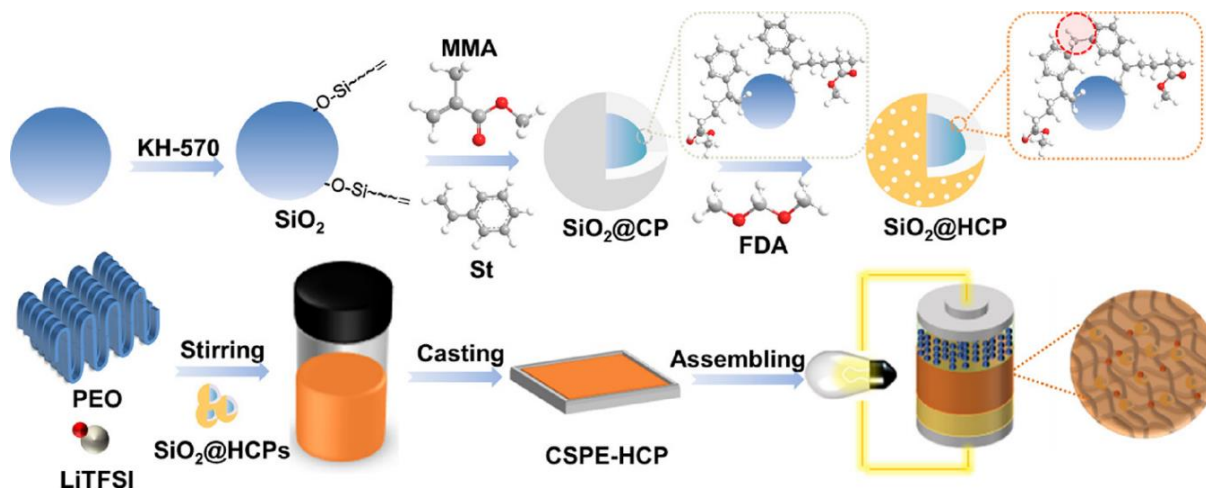


Figure 1.6 Synthesis procedure of the $\text{SiO}_2\text{@HCP}$ and CSPE-HCP.⁵⁵

Conjugated Microporous Polymers (CMPs)

CMPs are a new class of porous materials with extended π -conjugation in amorphous organic frameworks.⁵⁶ In 2007, Cooper's group first reported a series of CMPs based on poly(aryleneethynylene) networks,⁵⁷ reaching high specific surface areas over 1000 m^2/g .⁵⁷ The micropore size, micropore volume, and specific surface area of CMPs can be finely adjusted by changing the length of organic monomers⁵⁸. Prior to this work, such fine control of pore structure could only be achieved by crystalline MOFs.

Highly porous and functionalised CMPs have been reported with enhanced CO_2 adsorption ability. Cooper et al. synthesized functionalised CMPs with carboxylic acids, amines, hydroxyl groups, and methyl groups. The carboxylic acid functionalised CMPs showed the highest isosteric heat of adsorption (Q_{st}) for CO_2 and was expected to outperform amine sorbents in CO_2 capture and separation.⁵⁹ Q_{st} is an important indicator for evaluating the interaction between adsorbate and adsorbent. Researchers suggest the Q_{st} value of 50 kJ/mol as the boundary between chemical adsorption and physical adsorption.⁶⁰ The general conclusion is that a high Q_{st} guarantees a quick CO_2 capture, but more energy is required for the desorption; whereas a low Q_{st} grants an easy regeneration, but more adsorption cycles are needed to achieve an acceptable removal performance. An ideal adsorbent must balance these two factors with a

moderate Q_{st} less than 50 kJ/mol (in other words, in the range of physical adsorption).⁶¹ The cobalt/aluminium-coordinated CMPs exhibited high BET surface areas and excellent CO₂ adsorption capacities which are comparable to MOFs.⁵⁶ Eddaoudi et al. published a novel amine functionalised CMP that displayed enhanced CO₂ interactions with the framework, and a relatively higher qualitative CO₂/N₂ and CO₂/CH₄ selectivity compared with the non-functionalised polymer.⁶²

Zhu et al. synthesized two hollow-structured conjugated microporous polymer nanospheres (HCMPs) and combined them with phosphine oxide-6-oxide (DOPO, **Fig 1.7**). Both displayed excellent thermal insulating properties and effective flame retardant properties, showing a great prospect in the field of thermal insulation and flame retardancy.⁶³ Another work demonstrated by the same team illustrated a simple approach for construction of a new CMPs nanotubes nanofoam, which produced an excellent mechanical strength and thermal insulation and thus proposed as a thermal insulator and flame-retardant coating material.⁶⁴

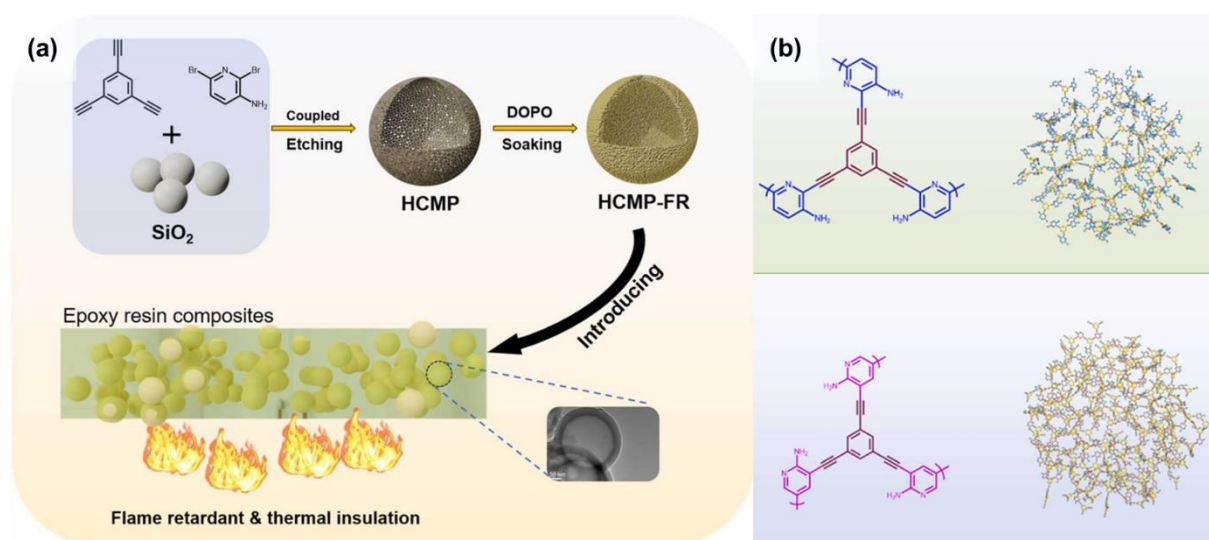


Figure 1.7 (a) Synthesis procedure of the HCMPs; (b) Structures of two CMPs.⁶³

Porous Aromatic Frameworks (PAFs)

PAFs are a type of POF prepared by C–C coupling reaction between aromatic monomers, so their frameworks are mainly composed of benzene rings connected by covalent bonds. They are suitable to be directly post-synthetically modified because of the accessible open pores and plenty of unsubstituted benzene ring sites. PAFs typically have high specific surface area and high chemical stability.

Unmodified PAFs with only aromatic motifs in their framework generally exhibit CO₂ uptakes below 100 mg/g, due to a lack of strong binding sites for this probe gas.⁶⁵ To improve that CO₂ adsorption, it proves to be necessary to functionalise PAFs with CO₂-philic functional groups. PPN-6-SO₃H, for instance, has the same skeleton structure as PAF-1 but was grafted with sulfonate groups, and its lithium salt (PPN-6-SO₃Li) was also synthesized. Both exhibited a nearly 3-fold increase in CO₂ uptake compared with nonfunctionalised PPN-6. The combination of polar groups and small pore sizes could enhance their CO₂ uptake and selective adsorption.⁶⁶ Inspired by the improved CO₂ capture obtained by the incorporation of lithium, other alkali and alkaline-earth metals were introduced by ion exchange into carboxyl-functionalised PAF, leading to an increase in Q_{st} for CO₂ and CH₄, and an improvement of Ideal Adsorbed Solution Theory (IAST) selectivity for CO₂ over N₂ and CH₄.⁶⁷ (IAST is a method to predict the multicomponent adsorption equilibrium, according to which adsorption selectivity can be calculated based on adsorption isotherms of each single component.⁶⁸) Moreover, diethylenetriamine has been grafted onto PPN-6, offering superior CO₂ capacity and selectivity over N₂ compared with sulfonated PPN-6.⁶⁹

Ma et al. synthesized quaternary pyridinium-type PAF (PAF-50) and their composites (Zn-PAF-50, **Fig 1.8**), and incorporated them into wood matrix, exhibiting a strong self-extinguishing ability, increased char residue rate and generation of large amounts of CO₂ and H₂O instead of combustible gases.⁷⁰

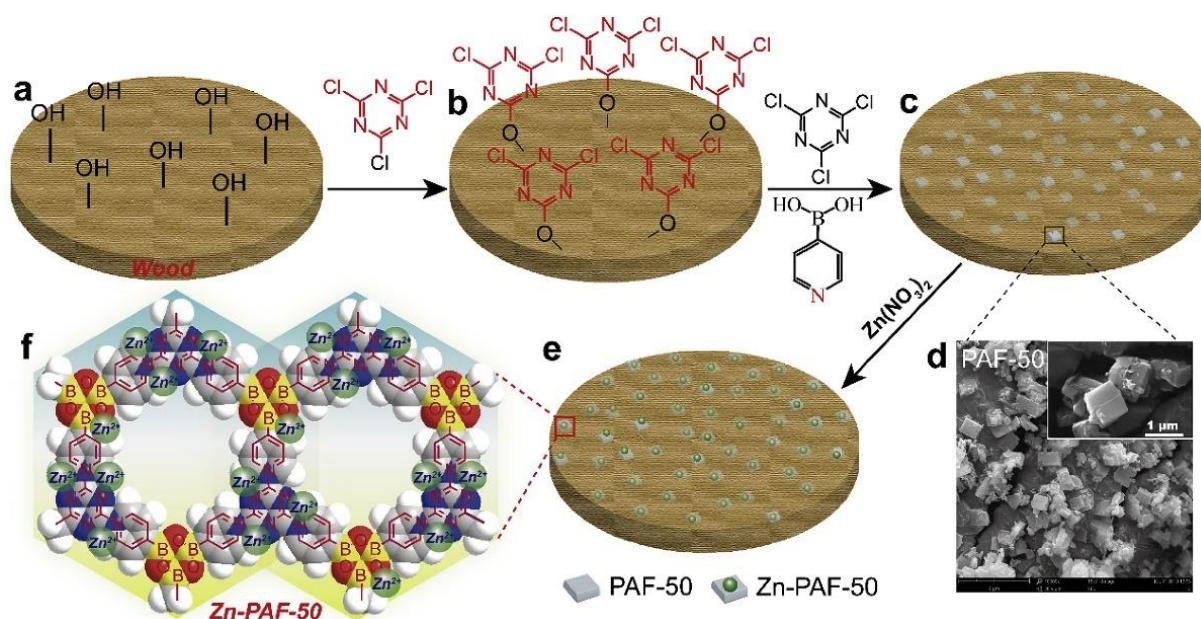


Figure 1.8 Fabrication process of the Zn-PAF-50 to wood substrate based on a situ self-assembly synthesis strategy.⁷⁰

Polymers of Intrinsic Microporosity (PIMs)

PIMs are defined as “polymers that are composed of a fully (or predominantly) fused-ring macromolecular chain that is fixed in a 2D or 3D random coil conformation due to sites of contortion, such as bridged bicyclic or spirocyclic units, so that they pack space inefficiently in the solid state”⁷¹. The first PIM was reported in a patent by McKeown et al. in 2003⁷² and was then published in an academic article in 2004⁷³. The researchers reacted bis-catechol monomer with tetrafluoroterephthalonitrile via benzodioxin formation to make a non-network polymer, named PIM-1 (**Fig 1.9**), which proved to be a soluble linear polymer. Surprisingly, despite the lack of a network structure and additional processing, the results of N₂ adsorption at 77 K of PIM-1 powder sample showed its microporosity and a high specific surface area of 850 m²/g.

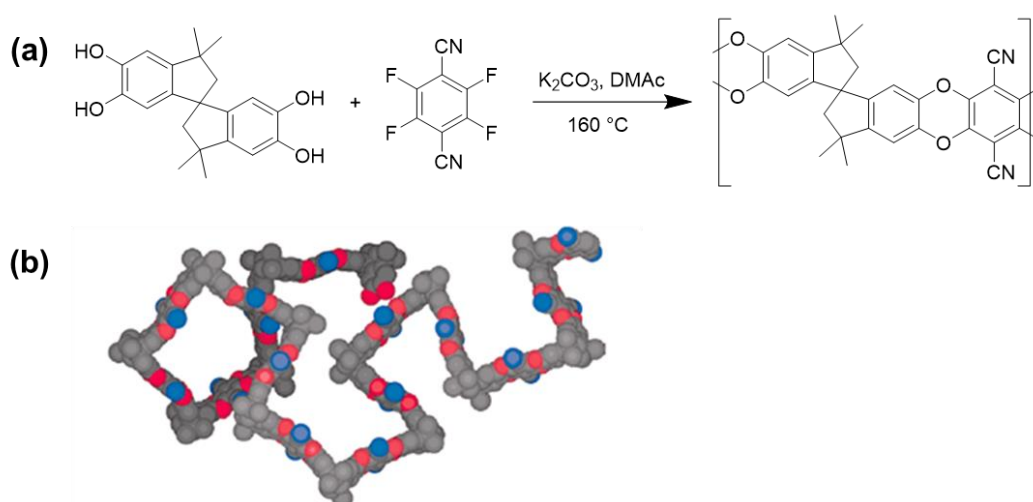


Figure 1.9 (a) Synthesis of PIM-1,⁷⁴ (b) The contorted conformation of PIM-1.⁷³

As an emerging type of organic porous material, PIMs possess desirable properties, such as high stability, a narrow pore size, adequate nanopore structure, easy synthesis and functionalisation, and good reproducibility.⁷⁵⁻⁸⁰ The microporosity of PIMs can be controlled by adjusting the rotational freedom within the polymer skeleton by changing the number of sites of contortion. Therefore, they are considered ideal adsorbents in gas capture and separation.⁸¹⁻⁸³

The intrinsic microporosity of PIMs comes from the large amount of *internal molecular free volume* formed by the inefficient packing of molecular chains. This concept was first proposed by Swager et al. referring to the three-dimensional structure of Trip.⁸⁴ In general, the molecular chains of linear polymers are flexible and thus are able to twist

sufficiently to maximize intermolecular interactions at temperatures above the glass transition temperature (T_g), effectively filling the space.⁸⁵ Nevertheless, there is always some void space among molecular chains that is not occupied for various reasons, which is called *free volume*.^{73, 86} According to the source of its formation, free volume can be divided into *excess molecular free volume*⁸⁷ (affected by external factors,⁸⁶ such as rapid cooling, removal of solvents and network formation) and *internal molecular free volume*⁸⁴ (caused by the molecular structure and conformation of the polymer chain itself)⁸⁸. The microporosity caused by excess molecular free volume may be gradually lost during time in what is called “physical aging”, where the molecular chains start packing more efficiently in the solid state. On the contrary, the internal molecular free volume would degrade only when the molecular structure changes, such as molecular rearrangement.

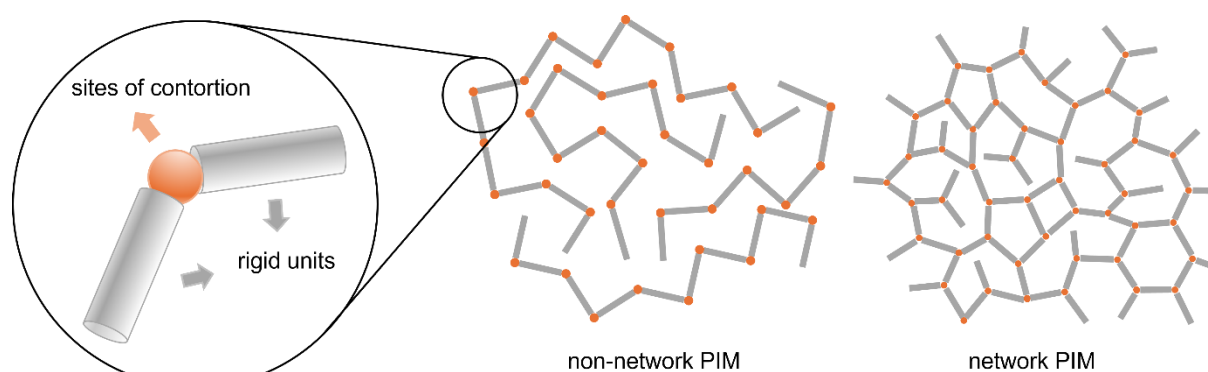


Figure 1.10 Illustration of non-network and network PIMs.^{89, 90}

According to Freeman's theory, increasing the rigidity of polymer chains and preventing chain stacking are effective ways to increase free volume.⁹¹ As the intrinsic microporosity of non-network PIMs derives mostly from the internal molecular free volume, the design of their molecular skeletons is crucial. PIMs are generally composed of two structural elements^{78, 79} (a) a rigid planar component, which is usually a fused-ring structure, and (b) a component that introduces a site of contortion (**Fig 1.10**), for example, as shown in **Fig 1.11**, a spiro centre^{92, 93}, a bridging scaffold^{75, 94, 95}, or a single bond around which the rotation of aromatic ring relative to its neighbour is hindered due to sufficient steric crowding⁹⁶⁻⁹⁸. Because of this, the polymer chains form 2D or 3D random coils,⁷¹ which cannot pack efficiently and provide enough free volume, which is much larger than that of common polymers.^{71, 99} The microporosity of network PIMs originates from both their network structure and the contorted conformation of polymer chains. A challenge for them is to accurately distinguish the contribution

respectively of intrinsic microporosity and network to the whole porosity of network PIMs. A rough way to judge is to compare the microporosity of network and non-network polymers with similar molecular structures.⁷¹

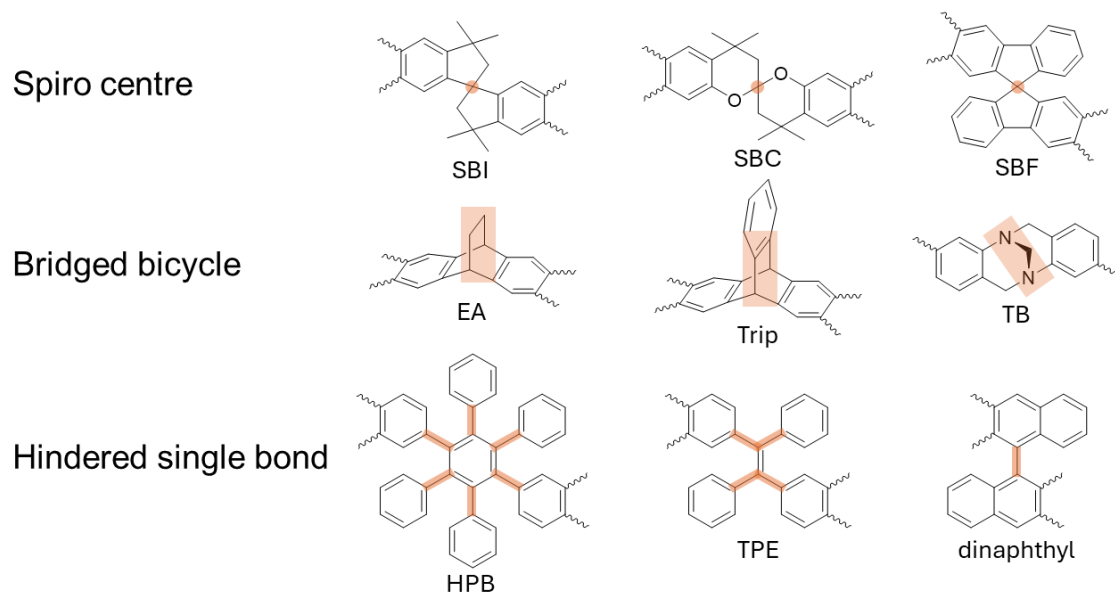


Figure 1.11 Examples of three types of contortion sites.

Properties of PIMs

PIMs are known to combine the characteristic properties of the organic glass and the porous polymer.¹⁰⁰ Non-network PIMs are usually soluble in organic solvents and have higher physical, mechanical, and thermal stabilities than organic glasses.⁹⁰ Their T_g are generally higher than their thermal decomposition temperatures (T_d) due to the rigidity of macromolecular chains.^{73, 101} Besides, PIMs exhibit characteristically “intrinsic” porosity with highly stability to external influence.

a. Porosity

PIM products generally have high BET specific surface areas (SA_{BET}).⁸⁶ The porosity of PIMs can be measured by gas adsorption-desorption. N_2 adsorption tests on different types of PIM showed that they adsorb significant amount of N_2 for $P/P_0 < 0.01$, proving the existence of micropores in PIMs.^{73, 102-104} However, researchers noted the difference between their N_2 isotherm and the typical Type I isotherm.³ Firstly, N_2 adsorption of PIMs occurred not only in the low relative pressure region but also at a relatively high relative pressure. Secondly, a significant hysteresis was observed in isotherms of PIMs. It was deduced to be the result of PIM swelling during the adsorption process due to the lack of a fixed framework (or flexibility for network-

PIMs).^{71, 85} Therefore, the calculated S_{ABET} from N_2 adsorption isotherm is not considered to be an accurate value of the real surface area of PIMs.¹⁰⁵ Smaller-sized gas probes (H_2 or CO_2) are believed to approach the free volume in PIMs better than N_2 and more accurately reflect the real values of specific surface area, pore volume, pore size, etc.⁷¹

The porosity of PIMs can be changed by adjusting the molecular structure, including the structure of the backbone units and the side groups (**Fig 1.12**). Trip-based dibenzodioxin PIMs, for instance, exhibit higher S_{ABET} than related spirobisindane (SBI) and spirobifluorene (SBF) PIMs. That was owed to the high level of inefficient packing caused by extended aromatic rings fused on Trip units.⁷⁶ Also, the S_{ABET} of the SBI-PIM using contorted Tröger's base (TB) as the linkage was slightly higher than that of similar SBI-PIM linked with straight imide and benzodioxin units.^{75, 106} The research on PIMs synthesized from spirocyclic monomers and dibenzodioxin linkages suggests that microporosity increases with the rigidity of the monomers, which is reflected by the increase in energy associated with the contortion of the dihedral angle at the spiro centre.⁹³ For the same reason, spirobichroman (SBC) or spirobis(tetrahydronaphthalene) modified PIM-1 showed lower BET surface areas than the original PIM-1, due to higher flexibility of the six-membered rings.^{107, 108}

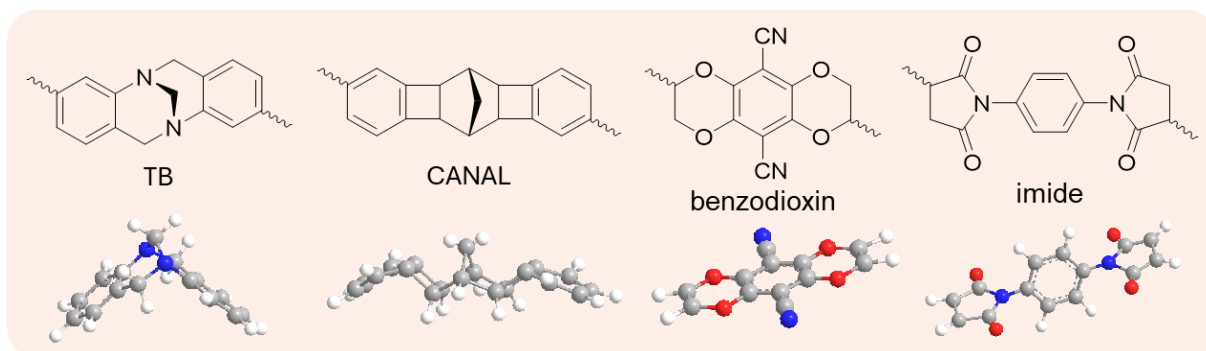


Figure 1.12 Structures of common linkages.

Side groups regulate the stacking of polymer chains by affecting the interaction between macromolecules. The reduced microporosity is usually observed in PIMs comprising polar functional groups because they enhance intra and interchain interactions. Typical examples of such groups include carboxyls,¹⁰⁹ amines,¹¹⁰ amidoximes,¹¹¹ and thioamides.¹¹² The main reason connected to this reduction of the porosity is attributed to the fact that substituents could form strong hydrogen bonding that increase the cohesive interactions, leading to densely packed polymer structures

with significant reduction of the surface areas. In addition, space occupancy of side groups likely reduces the microporosity of PIMs by “mechanically” filling the pores and reducing the free volume.¹¹³

The “intrinsic” microporosity of PIMs does not significantly change with the processing history, physical or morphological states. For example, PIM-1 displayed a good S_{ABET} in the range of 760 – 850 m²/g, which even can be maintained after being heated at 300 °C for 24 hours.¹⁰⁰ The microporosity of thin films and 3D-printed products were confirmed similar to the powdered sample.^{88, 114}

b. Solubility

Great solubility is the main advantage of non-network PIMs. It mainly originates from the rigid contortion of the macromolecular skeletons and is regulated by the pendant functionalities. Studies have proven that the introduction of pendant alkyl groups (n-propyl, i-propyl and n-butyl) improved the solubility of Trip-dibenzodioxin PIMs in $CHCl_3$.¹⁰⁰

Compared with traditional porous materials, solubility endows PIM with a wider range of characterization and processing methods.¹⁰⁰ Solution-based characterization techniques can be used for PIMs, such as liquid nuclear magnetic resonance (NMR) and gel permeation chromatography (GPC). Similarly, solution-based processing techniques are suitable for the development of PIM products for various applications, including membranes,^{85, 115, 116} coating,^{117, 118} fibers,^{119, 120} 3D printing inks,¹¹⁴ solid adsorbents allowing to be processed into different morphologies¹²¹.

c. Thermal Stability

PIMs are thermostable polymers possessing high T_d values, below which their T_g values are very difficult to locate.¹²² Thermal properties of PIMs can be characterized by differential scanning calorimetry (DSC) and thermogravimetric analysis (TGA). It can be inferred from the data listed in **Table 1.2** that: (1) Most dibenzodioxin-based PIMs and their coPIMs exhibited high T_d above 300 °C and char yields (i.e., the percentage of sample’s residual mass after complete decomposition against its initial mass) above 50%, reflecting an ideal thermal stability. (2) By comparing the T_d of PIMs containing similar spirocyclic structures, it was observed that dibenzodioxin-based PIMs containing SBF units have the highest T_d , followed by those containing SBI units, and then those containing SBC units. It is known that the rigidity of spirocyclic

structures is SBF>SBI>SBC, which concluded that enhanced rigidity of macromolecules improved the thermal properties of PIMs. (3) Hexaphenylbenzene (HPB) and Trip have a similar ability to impart thermal stability of dibenzodioxin-based PIM as SBF, which is inferred from their similar T_d values. This is probably attributed to the structural stability of aromatic HPB structure and bridged bicycle in Trip. (4) Overall, T_d values of most TB, Trip and polyimide (PI)-based PIMs and coPIMs are above 400 °C, slightly higher than that of dibenzodioxin-based PIMs. A possible reason is that the bicyclic structure of TB and Trip holds better stability. TB and PI contain N atoms, which have been confirmed to protect the organic substrates during combustion (discussed in detail in **1.2.3.4**). (5) A relatively low T_d around 260 °C is noticed to occur at PIM-EA-TB. This is owing to the loss of ethylene fragments from the ethanoanthracene (EA) units by the retro Diels-Alder reaction.⁷⁵ It infers that EA is not an ideal candidate unit for developing heat-resistant PIMs. (6) Catalytic norbornene-arene annulation (CANAL)-based PIMs have modest thermal properties, which are not significantly better than dibenzodioxin-based PIMs.

It is worth noting that the all above PIMs are not specifically designed as heat-resistant materials, but still show excellent thermal stability. This is attributed to (1) The fully fused rings in PIMs lead to their rigid polymer chains; (2) Many PIMs contain heteroatoms, such as N and O, which can improve the heat resistance of polymers and are often used in flame retardant materials; (3) Previous studies confirmed that rigid porous structure remaining in the fire can form a carbon layer preventing oxygen, mass, and heat from transferring to the substrate.¹²³ To sum up, PIMs are considered to have great potential in the field of flame retardancy.

Table 1.2 Thermal Properties of PIMs Measured by TGA at N₂ Atmosphere.

Units	Name	T _i (°C) ^a	T _{d5} (°C) ^b	RW (%) ^c	Reference
SBI, dibenzodioxin	PIM-1	493	495	62.3 (at 1000 °C)	83, 112, 124, 125
	amine–PIM-1	above 450	-	-	126
	Carboxylated PIM-1	258–309	406–472	63–70 (at 600 °C)	125
	PIM-2	450	-	65 (at 600 °C)	127
	TFMPSPIMs	352.8–370.9	437.7–486.8	59.15–64.79 (at 600 °C)	128
SBI, tetraphenylethylene (TPE), dibenzodioxin	TPE-based PIMs	475–440	-	68–79 (at 600 °C)	98
SBI, dibenzodioxin	PIM-7	410	390	-	94
SBI, EA, dibenzodioxin	PIM-8	440	385	-	
	PIM-9	400	380	-	
SBI, phenylfluorene, dibenzodioxin	Cardo-PIMs	350–420	385–480	-	
EA, dibenzodioxin	PIM-10	400	340	-	
Pentipitycene, SBI, dibenzodioxin	PPIM-ip-C				129
	PPIM-np-S	-	360–450	72–75 (at 600 °C)	
	PPIM-ip-S				
SBC, dibenzodioxin	SBC-based PIM1s	418–477	-	-	108
SBF, dibenzodioxin	SBF-PIM	565	-	-	93
HPB, dibenzodioxin	PIM-HPBs	456–552	-	58–75 (at 1000 °C)	103
Trip, dibenzodioxin	phenazine/Trip PIM	462		70 (at 1000 °C)	104
Trip, dibenzodioxin, PI	TPDA-APAF	400		60 (at 800 °C)	130
	TPDA-ATAF	420		55 (at 800 °C)	
	6FDA-APAF	440		49 (at 800 °C)	

SBC, TB	TB-MSBC	410–420		61 (at 900 °C)	131
	TB-SBC			52 (at 900 °C)	
SBI, TB	PIM-SBI-TB	435		68 (at 1000 °C)	75
EA, TB	PIM-EA-TB	260		71 (at 1000 °C)	
Trip, TB	PIM-Trip-TB	400	-	30.5 (at 1000 °C)	132
	CTTB	425		70 (at 1000 °C)	133
	MTTB	425		71 (at 1000 °C)	
	ITTB	445		76 (at 1000 °C)	
binaphthalene, TB	PIM-HNTBs	360–420		54–66 (at 800 °C)	134
TB, PI	PIM-PIs	420	510	66–68 (at 800 °C)	135
	CoPI-TBs	430–448	462–492	-	136
Dinaphthyl, TB, PI	CTB-DMNs	480–520		67–70 (at 800 °C)	137
Trip	polymer 5	420	440	80 (at 750 °C)	138
Trip, PI	6FDA-1,4-trip		518–532	above 59 (at 1000 °C)	95
SBI, PI	PIM-PIs	465–492	-	-	106
	T-PIM-PI-OH	above 400	-	-	139
CANAL, PI	CANAL-PI-MeNH ₂	-	451–488	58–60 (at 800 °C)	140
oxygencyclic pseudo-TB, bis-naphthalene PI	6FDA-OTB	421		42 (at 700 °C)	141
	6FDA-FB	436		43 (at 700 °C)	
CANAL	Poly(4a)	315		81 (at 800 °C)	142
spiro-orthocarbonate CANAL	P2	350		62 (at 800 °C)	143

^a Initial decomposition temperature ^b 5% weight loss temperature ^c Residual weight

Applications of PIMs

a. Catalysis

The first PIM was designed as a novel catalyst. McKeown et al. synthesized porous network polymers incorporating metallophthalocyanines¹⁴⁴ and metalloporphyrins¹⁴⁵, which were expected to be used as organometallic catalysts. According to their performance in oxidation reaction, phthalocyanine and porphyrin-based PIMs are more effective as heterogeneous catalysts than their low molar mass analogues.¹⁴⁶ Subsequently, various PIM catalysts have been published. A cobalt phthalocyanine PIM proved to be effective in catalytic desulfurization of salt water.¹⁴⁷ A hexazatrinaphthylene-based PIM binding of palladium showed satisfactory catalysis effect on for Suzuki carbon-carbon coupling reactions.¹⁴⁸ A (pentafluorophenyl)porphyrin manganese(III)-based dibenzodioxin-PIM demonstrated a large surface area of 1080 m²/g. It proved to be an efficient heterogeneous catalyst for cyclooctene and cyclohexane oxidation under mild conditions and showed great reusability.¹⁴⁹ TB units can be used in catalysis because of their basicity. Antonangelo et al. reported a series of TB-based PIMs, of which the TB sites catalyzed the Knoevenagel condensation of benzaldehydes and malononitrile.¹⁵⁰

b. Adsorption and Separation of Chemicals and Ions

There is a long history of the use of porous polymers including PIMs as solid-state adsorbents. Functionality and pore structure of polymer adsorbents can be fine-tuned for specific adsorption processes.⁸⁷

Maffei et al. compared the adsorption of four organic dyes by phthalocyanine network PIM adsorbent and traditional activated carbon. The results showed that the PIM provided a better selectivity than activated carbon.¹⁵¹ Satilmis et al. reported the ethanolamine modified PIM-1 adsorbent, which was investigated for dye adsorption from aqueous solution and demonstrated stronger selectivity for the anionic dye Orange II, compared to the cationic dye Safranin O.¹⁵² The pervaporation of water-ethanol mixture through the PIM-1 membranes demonstrated their great permeability.¹¹⁶ AlO_x/PIM-1 hybrid membranes with internal nanoporosity were used on reverse osmosis separation of toluene from isopropylbenzene compounds.¹⁵³ All the powder, membrane and fiber forms of PIM-1 show great performance for aniline adsorption. Among them, PIM-1 electrospun ultrafine fiber showed outstanding

performance in adsorbing aniline from the aqueous phase.¹⁵⁴ Yu et al. summarized porphyrin-based PIMs which can be used as adsorbent to adsorb iodine vapor. That process was examined to be reversible with good maintenance of surface area after reusing.¹⁵⁵ Satilmis et al. reported an amidoxime functionalised PIM-1 fibrous membrane, practically used for the extraction of U(VI) ions from aqueous systems.¹⁵⁶ Wang et al. designed a series of functional Zr-based MOF@PIM porous nanofibre membranes. Their adsorption mechanism and performance for fluoride ions in water were investigated.¹⁵⁷

c. Gas Storage and Separation

Gas storage and separation is one of the most popular applications of PIMs due to their large and stable specific surface areas and highly achievable functionalisation. Gas uptake is generally evaluated by gas adsorption-desorption using powder samples. A few works were also reported that the sample was processed into geometries to be measured.¹²¹ PIMs used for gas separation can be divided into two categories. Soluble PIMs can be processed to form membranes, across which different gases are separated due to their different permeabilities.¹⁵⁸ As functionalised solid selective adsorbents (generally in powder form), insoluble PIMs can selectively adsorb components due to the different interactions with each of them.

Gas Separation Membranes: Non-network PIMs, characteristically, can take advantage of having both high porosity and solubility. They can be dissolved in organic solvents and cast into glassy-like membranes by slow evaporation, as long as their polymer backbones own sufficiently high molecular weights.¹⁰⁰ Narrow pores provide plenty of voids, which are accessible to small gas molecules through pore diffusion, whereas larger gas molecules may get rejected. The rigidity of PIM macromolecules provides good size selectivity for gases because high activation energy is required to form enough space for large molecules to move in.¹⁰⁰

Generally, membranes that provide high selectivity give low permeabilities and vice versa, according to a trade-off mechanism that Robeson elucidated for the first time in 1991 and revised in 2008.¹⁵⁹ However, PIM-1 and PIM-7 show higher selectivity than other polymers of similar permeability.⁸⁵ PIMs containing Trip and TB units have extreme rigidity and achieved the gas permeability data that were much higher than the benchmark 2008 Robeson upper bounds for O₂/N₂, CO₂/CH₄, CO₂/N₂ and H₂/N₂.^{132,}

¹⁶⁰ A modified primary amine-PIM-1 showed higher CO₂ uptake and higher CO₂/N₂

sorption selectivity than the parent PIM-1 because of hydrogen bonds between amine groups and CO₂.¹²⁶ PIM-bpy-x shows an increased CO₂ permeability because of the high CO₂ affinity to its N-rich bipyrimidine units, which also provided better thermal stability and resistance to aging.¹⁶¹

Solid Selective Adsorbents: Network PIMs typically form amorphous powders and can be used as solid adsorbents.

For example, Ma et al. prepared a TPE-based ladder network (MP1) and its COOH-functionalised analogue (MP2) by polycondensation. They showed ideal CO₂ capture and the ability to adsorb toxic volatile organic vapours such as benzene and toluene and selective separation of xylene isomers.¹⁶² In another case, primary amines were added to PIM-1 through acid-base and hydrogen-bonding interactions. Compared with parent PIM-1, they showed higher CO₂ capacity, CO₂/N₂ selectivity, and reusability under both dry and humid conditions.¹⁶³ Similarly, Regno et al. evaluated and compared CO₂ capture properties of four TB-PIMs. It was deduced that suitable type and amount of contortion sites are crucial to generate sufficient micropore volume, and the presence of TB groups specially contribute to the interaction with the CO₂.¹⁶⁴ Satilmis et al. reported that ethanolamine modified PIM-1 offered an enhanced CO₂ affinity and a reduced affinity to N₂, thereby increasing its CO₂/N₂ selectivity.¹⁵² Zhang et al. synthesized a series of Trip-based porous PIs, which exhibited high isosteric enthalpies toward CO₂ and selectivity of CO₂/N₂, and good thermal stability.¹⁶⁵ Zhou et al. prepared a series of hyper-cross-linked PIMs through a knitting method promoted by Friedel-Crafts polymerisation. They were proven to have high CO₂ uptake and ideal selectivity of CO₂/N₂ and CO₂/CH₄.¹⁶⁶

Table 1.3 Physical Characterization of Polymers and Gas Selectivity of Some PIMs.

Polymer	S _{ABET} (m ² /g)	CO ₂ adsorption 273 K (1 bar) (mg/g) (mmol/g)	CO ₂ /N ₂ selectivity	Q _{st} (kJ/mol)	Reference
MP1	1020	- (4.24)	19.7	29.6	162
MP2	190	- (2.22)	25.2	34.2	
SPIM (PIM-1)	719	- (about 4.9)	-	-	152
ES120-24	10	- (about 3.6)	35	-	
STPI-1	4	37.3 cm ³ /g	37	-	165
STPI-2	541	74.3 cm ³ /g	107	-	
STPI-3	378	56.3 cm ³ /g	71	-	
Functionalised PIM-SBFs	669-1063	128 (2.90)–152 (3.45)	23.4-24.2	27.7-30.1	166
Functionalised PIM-HPBs	997-1390	123 (2.80)–137 (3.11)	18.7-26.5	27.9-30.4	

d. Other Applications

In addition to the above, the potential of PIMs applied in other fields starts to draw some attention. The application of PIMs in electrochemistry is rapidly developing, including but not limited to hydrogen storage and solid-electrolyte-interphase for batteries, highly selective membranes for redox flow cells, electrocatalysts for fuel cells, and microporous capacitor materials.^{167, 168} Tang et al. produced a bi-ionic PIM photocatalyst by a quaternary ammonium reaction. It performed great charge-transfer transition and charge-carrier diffusion, bringing the highly efficient photocatalysis.¹⁶⁹ Rakow et al. developed a broadly responsive indicator for organic vapours based on PIM-1 films. It could display vivid shifts in colour from green to red at relevant concentrations. The appropriate hydrophobic microporous layer prevents the sensor from interfering with water vapor.¹⁷⁰ Zhang et al. explored a 3D printing technology that is capable of handling non-network PIM solutions as printing inks. This work lays the foundation for 3D printing a wide variety of polymers into complex structures with hierarchical porosity.

In summary, the unique macromolecular structure and confirmation of PIMs endow them with a characteristic combination of properties, including good solubility, exceptional chain rigidity, and high free volume.⁷¹ As the result, it shows desirable performance and great potential in many areas. In addition to the applications listed in this part, PIMs are believed to have the potential to be applied in heat resistance and flame retardancy due to their excellent thermal stability. As far as the literature reviewed by us, there has not been relevant work published so far.

1.2 Organic Flame Retardants (FRs)

1.2.1 Flame Retardant Mechanism

Since the middle of the twentieth century, polymer materials have gradually permeated every aspect of people's daily lives because of well-developed synthesis and processing technologies.¹⁷¹⁻¹⁷³ However, polymer materials not only bring convenience but also lead to fire hazards. The limiting oxygen index (LOI) of most polymer materials is lower than 21,¹⁷⁴ which means they are flammable or combustible in air. It is well-known that large amounts of toxic and/or corrosive smoke and gases may released

during combustion, which pose a great threat to the life and property security of the public and cause serious environmental pollution at the same time.

A complete combustion process of polymers can be divided into five phases: ignition, pyrolysis, combustion, feedback and extinguishing.¹⁷⁵ A “fire triangle” of polymeric material combustion illustrates three requirements (heat, oxygen and combusting material) for a self-sustaining combustion cycle (**Fig 1.13 a**). Combustion cannot occur lacking in any one of them. In other words, flame retardation can be achieved by removing one or more of these requirements in order to inhibit or disrupt the combustion cycle.

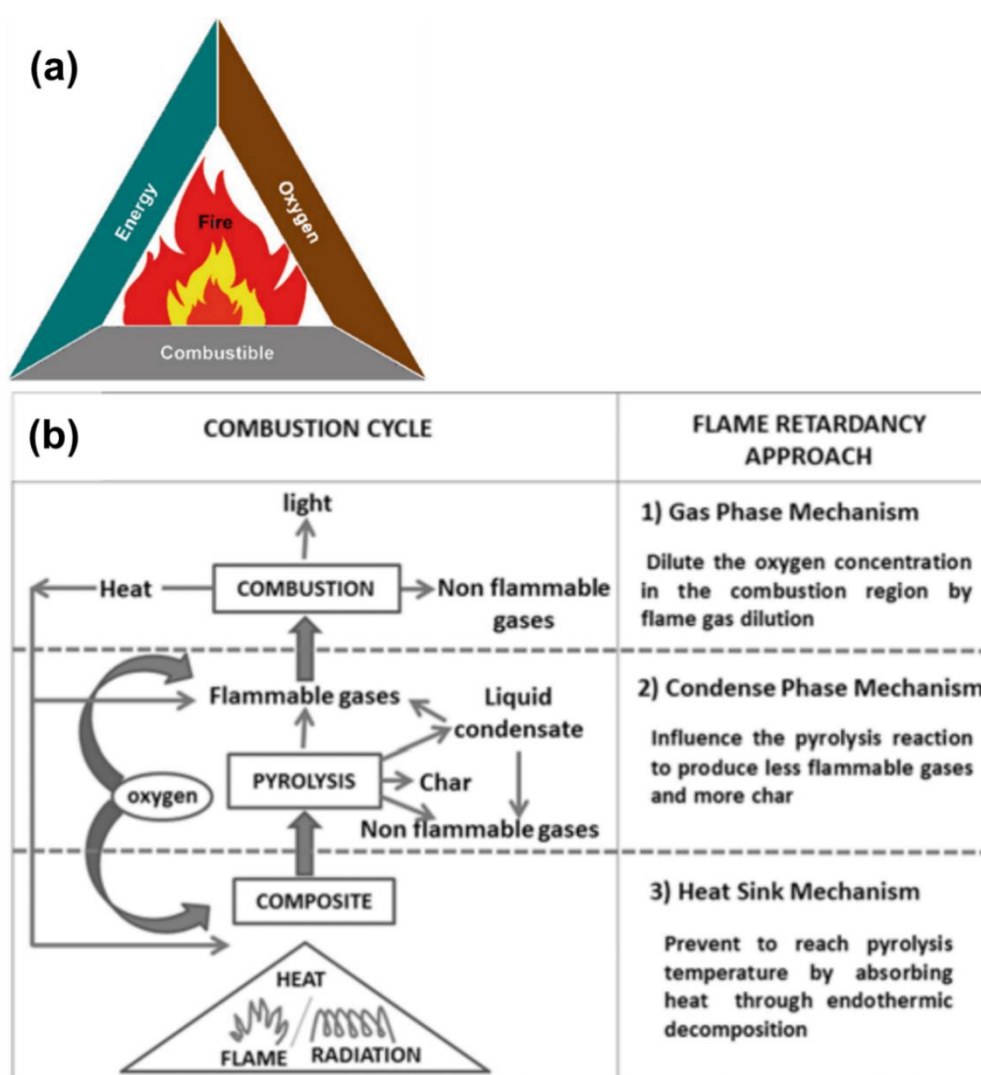


Figure 1.13 (a) A “fire triangle” of polymeric material combustion,¹⁷⁵ (b) Schematic diagram of combustion cycle and possible flame retardancy approach.¹⁷⁶

Widely recognized flame-retardant mechanisms are introduced as follows.¹⁷⁶ The first mechanism is known as *gas phase mechanism*. In combustion, FRs release non-

flammable gases that reduce the concentration of both oxygen and flammable gases. The second one is named as *condensed phase mechanism*. FRs produce non-flammable by-products and promote the formation of a char layer as a physical barrier which hinders heat and mass transfer. The third one is called *heat sink mechanism*. Polymers incorporate FRs which decompose endothermically in combustion and thus decrease the temperature of polymers under their pyrolysis temperature. Self-extinguishing then will be achieved because no more flammable gas is produced. In practice, it is difficult to attribute the flame retardant process to only one of these three mechanisms. Flame retardancy is generally determined by the combined effects of two or more of them.¹⁷⁶

1.2.2 Evaluation of Combustion Performance

Depending on the material parameters that decisively influence the combustion behaviours, the tests can be divided into the following six categories¹⁷⁷: 1. thermal stability (TGA and DSC); 2. ignitability and flammability (such as ignition temperature, ignition time and LOI); 3. flame propagation behaviour (such as tunnel test and radiation plate test); 4. heat release behaviour (cone calorimeter and calorimetry test); 5. smoke generation behaviour (such as smoke box test and dust quality test); 6. the toxicity and corrosion of combustion products (relevant chemical and biological tests). In the combustion test of commercial products, the evaluation of their flame retardancy often results from the combined effect of two or more factors. For example, ignition and burning time, flame height and flammable dripping, etc. need to be comprehensively considered in the UL94 Vertical Burn Test.

The thermal stability of polymers is closely related to their combustion behaviour,¹⁷⁷ but the two are not completely equivalent. It is commonly known that thermal stable materials generally have good flame retardancy. However, some materials with great flame retardancy are probably not good at thermal stability, such as polyvinyl chloride. TGA is a method of measuring and analysing the change of sample mass with temperature or time at the programmed temperature,¹⁷⁸ which is usually employed to evaluate the thermal stability and describe thermal decomposition behaviour of the sample and each component contained therein.¹⁷⁹ The residual weight percentage of the sample at high temperatures (relate to the flame retardancy) and T_d (reflect the thermal stability) can be obtained by analyzing its TGA curve. It is notable that T_d

includes the maximum weight loss rate temperature (T_{\max}), the initial decomposition temperature (T_i) and a series of temperatures at different degrees of weight loss (for example, T_{d5} is defined as the temperature when the sample loses 5% of its initial weight). Among them T_{d5} , T_{d10} , and T_{d20} are commonly used to evaluate their thermal properties instead of T_i in order to avoid the influence of impurities in samples. Polymers with high T_d and high residual weight percentage are considered to have excellent thermal stability because such polymers generate a tiny amount of flammable byproducts via decomposition during combustion. DSC technique can measure the T_g values of materials based on the deviation from the baseline on their DSC curves. Specifically, T_g is determined by the intersection of the tangent line of the curve and the baseline.

1.2.3 Classification of Flame Retardants (FRs)

According to ISO4880, FR is defined as a substance added to a material in order to suppress, significantly reduce or delay the propagation of flame.¹⁸⁰ Adding FRs to polymer materials gives them non-flammability, self-extinguishing performance and smoke suppression.

FRs are classified by their chemical structures, into inorganic FRs and organic FRs.¹⁸¹ Another categorization, based on interactions between polymer matrix and FRs, classifies them into reactive FRs and additive FRs.¹⁸² Considering a common low compatibility between organic and inorganic materials, the additive FRs applied in organic products is preferably organic FRs, in order to avoid the precipitation of additives and the influence on the mechanical properties of the substrate materials. According to the different elements contained, FRs can be also categorized into halogen-containing, phosphorus-containing, boron-containing, nitrogen-containing, and silicon-containing FRs and so on.

1.2.3.1 Halogen-containing Flame Retardants (FRs)

Halogen-containing FRs are mainly chloride and bromide functionalised compounds, which were developed at an early period and have been used in flame retardant industry for a long time. Nowadays, halogen-containing FRs production account for a large portion (around 21%) of global FRs market.^{183, 184}

However, halogen-based FRs may corrode metal components and release a large amount of corrosive or toxic gases and smoke in the process of combustion, which seriously affects people's health and causes environmental pollution.¹⁸⁵ Since 1990, the European Union has conducted hazard risk evaluations on some widely used halogen-based FRs. The reports identified the hazards caused by organic bromine FRs on human health. As a result, most bromine FRs have been banned in Europe since the beginning of this century. Currently, the exploration of non-halogen alternatives has become the hotspot in the area of organic FRs.^{186, 187} Therefore, the aim of this research is to develop non-halogen FRs which not only own flame retardant properties, but also minimize smoke and toxic gas emission in combustion.^{188, 189}

1.2.3.2 Boron-containing FRs

Organic boron-containing FRs have attracted much attention from researchers, because of their obvious flame retardancy, low toxicity and good smoke suppression. The first boron-containing organic FR was reported in the 1900s by Posner, who used boric acid and triethanolamine to synthesize a FR for fabrics.^{190, 191} Afterwards, a series of boron-containing FRs have been reported.

Boron-containing FRs mainly follow the condensed phase mechanism. In the combustion process, boron-containing FRs generate boric acid at first. If there were hydroxyl groups in the system, boric acid groups would react with them to form boronic esters, and then form B–C networks by removing CO₂. Such a process promotes the char formation of the polymer.¹⁹² Metaboric acids are generated via dehydration of boric acids, and then further dehydrated to afford boron trioxides. The pyrolysis products of boron trioxides will form a glassy protective coating isolating oxygen, flammable gases and smoke.^{193, 194}

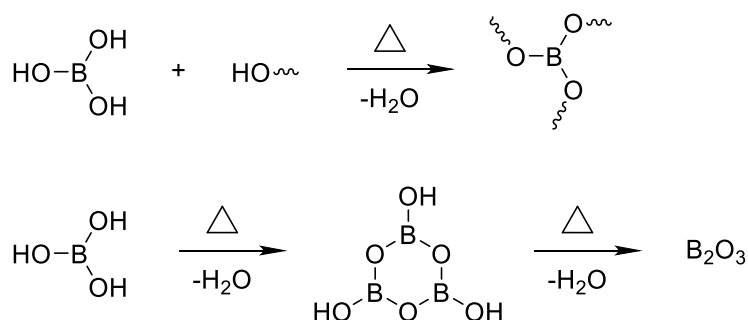


Figure 1.14 Schematic of boron-containing FRs mechanisms.

Although they showed a good flame retardant effect, the main shortcomings of boron-containing flame retardant materials are instability and poor durability caused by hydrolysis.¹⁹⁵ Therefore, boron-containing FRs are usually used in synergy with other elements. It is found that an ideal strategy is to introduce nitrogen or phosphorus into the system. The electron configuration of boron is $1s^2 2s^2 2p^1$. Boron atom possesses a vacant p orbital to accept lone pair electrons, which can be provided by nitrogen or phosphorus atoms. Coordinate bonds connecting boron to nitrogen or phosphorus greatly reduce the hydrolysis of boron-based compounds.¹⁹⁵ Morgan et al. prepared aromatic boronic acid FRs and blended them into acrylonitrile-butadiene-styrene and polycarbonate resins, showing unusual fire resistance.¹⁹⁶ Martín et al. crosslinked boron-containing novolac resins with hexamethylenetetramine, which generated boric acid at high temperatures and gave an intumescent char that slowed the degradation.¹⁹⁷ Dimethyl terephthalate-based phosphonic and boronic esters were used as FRs. They were proven to reduce heat release and contribute to char formation during combustion following the condensed phase mechanism.¹⁹⁸ Huo et al. synthesized a multifunctional B-based polyphosphonamide (PB) which was added to epoxy resins. Their high flame-retardant and smoke-suppressive efficiency was attributed to the synergy of P, B and N atoms (**Fig 1.15**).¹⁹⁹

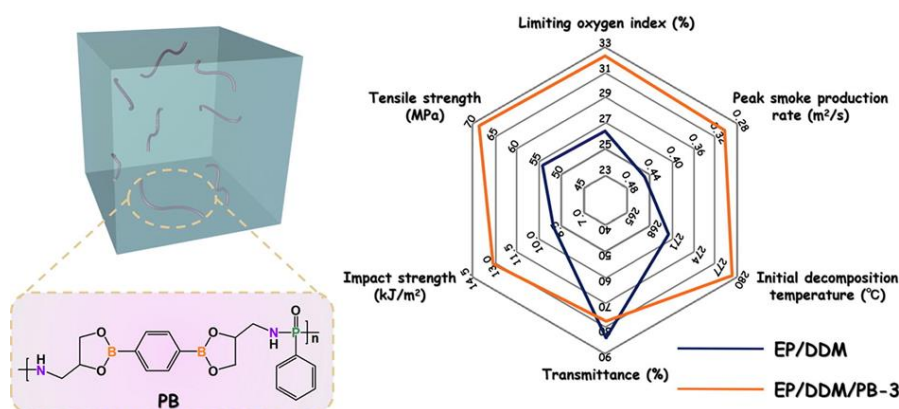


Figure 1.15 Illustration of PB structure and its flame retardancy in epoxy resin using diaminodiphenyl methane (DDM) as curing agent.¹⁹⁹

1.2.3.3 Silicon-containing Flame Retardants (FRs)

Silicon-containing polymers have excellent thermal properties, surface properties, chemical and mechanical stability,¹⁸¹ and can be used as flame-resistant coating materials or as FRs in polymer composites.²⁰⁰ Compared with traditional halogen-containing FRs, silicon-containing FRs are defined as a type of environmentally friendly

additives.¹⁸¹ Due to the complex production process and high price, research on silicon-containing FRs currently stay in the laboratory.

The flame retardant mechanism of silicone-containing FRs can be analyzed from the following aspects. (1) Silicones contain Si–O and Si–C bonds with higher bond energy than C–C bonds in carbon-based polymers. Therefore, more energy is consumed to break Si–O and Si–C bonds during the combustion.²⁰⁰ (2) Organosilicon FRs play an important role in the condensed phase.²⁰¹ Silicones burned under aerobic conditions will form silica on the surface of the matrix material as a surface barrier,²⁰² which can hinder the mass and heat transportation between condensed and gas phase.²⁰¹ Also, adding a small proportion of silicon compounds to polymer matrix was proven to significantly promote the formation of char layers.¹⁸¹ (3) The complete decomposition products of silicones are SiO₂, CO₂, and H₂O, which are neither toxic nor aggressive.²⁰⁰

Previous research has shown that synergistic systems of silicon and phosphorus or nitrogen can gain an enhanced flame retardant effect,²⁰³ manifested as excellent flame retardancy and high char yield.²⁰⁴

1.2.3.4 Nitrogen-containing Flame Retardants (FRs)

At present, nitrogen-containing FRs represent a small but fast-growing segment of FRs that meet the requirements of green chemistry and sustainable production. They have good compatibility with polymer matrices since their structure and contained elements are highly similar to most polymers.¹⁸¹ In addition, it has been reported the possibility for nitrogen-based flame retardant materials to be suitable from many recyclable plastics.²⁰⁵

According to reported studies, the flame retardancy behaviour of nitrogen-containing compounds during combustion can be mainly explained by the following three aspects. (1) Nitrogen-containing FRs decomposed in combustion will release carbon dioxide, water vapor, ammonia, nitrogen and other nitrogen oxides. These non-flammable gases can dilute flammable gases and isolate the matrix material from the air. Furthermore, the generation of water, nitrogen dioxide and nitrogen oxides will consume oxygen near the surface of the matrix material.²⁰⁶ (2) Nitrogen produced from thermal decomposition can capture free radicals in burning polymer materials. As a result, the chain reaction supporting sustained combustion will be stopped.²⁰⁷ (3) Nitrogen atoms generally exist as multi-bond atoms in polymers (i.e. connected to the

carbon chains by more than one single bond or unsaturated bond), that means a lot of energy is consumed in the process of releasing them. Endothermic decomposition of such FRs (and sublimation of certain types of nitrogen-containing compounds above 300 °C) will largely remove heat, reducing the surface temperature of polymers.^{206, 208}

The most reported organic nitrogen-containing FRs are melamine and its derivatives. Ionescu et al. synthesized aromatic triazinic polyols as additive FRs for making rigid polyurethane foams with excellent physico-mechanical properties and inherent flame retardancy.²⁰⁹ Nitrogen-containing FRs alone provide a modest performance of flame retardancy, which can be largely enhanced by suitable synergism. A typical example is phosphorus-nitrogen synergistic systems, such as phosphazene-triazine flame retardant polymers.^{176, 210} Mu et al. reported compressible melamine-based porous organic polymer as lithium battery separators, which could form an intumescent char layer between anode and cathode during burning, resulting in increasing internal resistance and preventing thermal runaway.²¹¹ Wang et al. prepared flame-retardant rigid polyurethane foams with a new phosphorous-nitrogen intumescent flame-retardant additive DPPM (**Fig 1.16**), which formed a surface charred barrier to slow down the decomposition of foams and prevented the heat and mass transfer between the gas and the condensed phases.²¹²

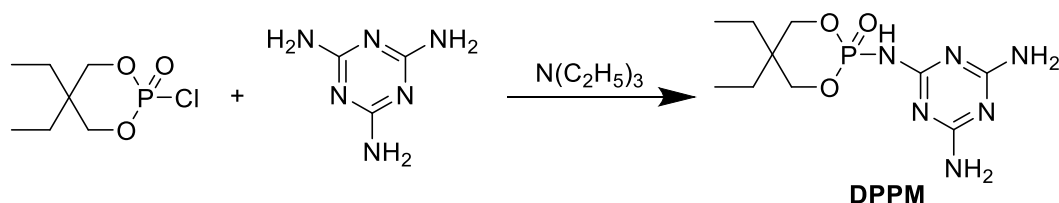


Figure 1.16 Synthesis of DPPM.

1.2.3.5 Phosphorus-containing Flame Retardants (FRs)

The importance of phosphorus-containing FRs in the current flame retardant industry is second only to halogen-containing ones. Although phosphorus-containing FRs show high efficiency in flame retardancy, they cause emissions of hazardous by-products. Phosphorus-containing compounds generally show toxicity and poor wet-heat resistance. Some of them are highly soluble in water. Once such phosphorus-containing FRs are improperly discarded into natural water, they will accumulate in bodies of aquatic species. Synergistic systems are considered to reduce the hazard of phosphorus-containing FRs. For example, the synergism of phosphorus with boron

reduces the toxicity of phosphorus compounds, and meanwhile improves the hydrolysis stability of boron-containing compounds.

Mechanisms of phosphorus-containing FRs are determined by the oxidation states of phosphorus atoms in the compounds.²¹³ When phosphorus atoms are in a high oxidation state (+3, +5), the FRs mainly follow the condensed phase mechanism. Whereas those ones with phosphorus atoms in a lower oxidation state (0, +1) primarily conform to the gas phase mechanism. For instance, phosphates effectively work in the condensed phase, producing phosphoric acid species during combustion, which can promote the carbonization of the polymer matrix by dehydration reactions.²¹⁴ Phosphine oxides are active in the gas phase by decomposing to release radicals (such as $\text{PO}\cdot$, $\text{HPO}\cdot$ and $\text{HPO}_2\cdot$), which can capture the $\text{H}\cdot$ and $\text{HO}\cdot$ generated from burned polymer matrix^{215, 216}. In practice, many phosphorus-containing FRs display both gas phase and condensed phase mechanisms.²¹⁷

The phosphorus-boron synergistic system mentioned above can not only reduce the toxicity of each single component, but also promote the formation of carbon layers. The combination of phosphorus and silicon also exhibit a similar effect.²¹⁷ Currently, P–N synergism is one of the research hotspots in the field of organic FRs, and the availability of numerous compounds has been developed and confirmed, such as phosphinamide, phosphonamide, phosphoramidates, pentaerythritol bisphosphonate, triazine, and phosphazene.²¹⁸⁻²²¹ Next, as one of the focuses of our work, the P–N synergistic system centred on phosphazene-based FRs will be further discussed.

1.2.3.6 Phosphazene-based Flame Retardants (FRs)

P–N system is one of the most promising synergisms for halogen-free FRs. Its flame retardant function is mainly manifested in the condensed phase and gas phase.²¹³ Extensive studies on P–N FRs have confirmed that the formation of cross-linked networks of polymer chains was enhanced by them during the thermal decomposition.²²² This helps to retain the polymeric matrix during the decomposition process to form a protective char layer with good thermostability²¹³ and improves the retention of P in the condensed phase²²³. Nitrogen-containing components strengthen the gas phase mechanism by diluting the concentration of both O_2 and flammable gases generated from the decomposition.²¹⁷ Two prominent types of P–N structures include phosphoramidates^{224, 225} and cyclotriphosphazenes (CTPs).^{226, 227}

Phosphazene-based FRs generally have a simple preparation process and low cost and thus have the potential to be widely used in the industry. Studies of phosphazene compounds date back to 1834, when Liebig et al. successfully synthesized halogeno-cyclo-phosphazenes (**Fig 1.17 a**).^{228, 229} Then their synthesis methods were systematically optimized by Schenck et al.²³⁰ In 1965, a rubbery elastomer of formula $(\text{NPR}_2)_n$, was prepared by ring-opening polymerisation of hexachlorocyclotriphosphazene (HCCP).²³¹ Subsequently, phosphazene has been further researched and a series of its derivatives with different properties were developed by Allcock et al.²³²⁻²³⁵

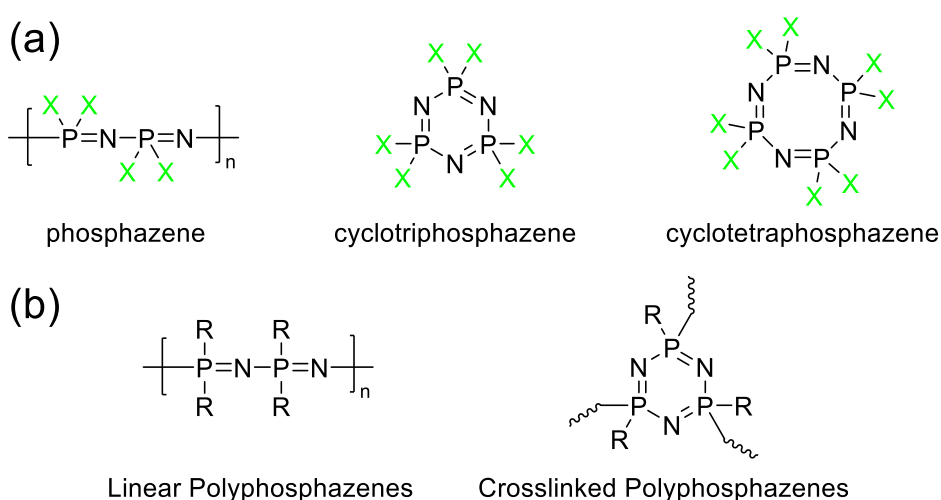


Figure 1.17 Chemical structures of (a) commonly used phosphazene precursors (X = Cl or F) and (b) two types of polyphosphazenes.

Polyphosphazenes are organic-inorganic hybrid polymers whose main chain is alternately connected by single and double bonds of phosphorus and nitrogen atoms, and the side chain is replaced by organic groups.²³⁶ Polyphosphazenes can be formed as linear chain, branched, dendritic and cross-linked architecture through the nucleophilic substitution reactions between the very active chlorine of either polydichlorophosphazene or cyclophosphazene molecules and nucleophiles.²³⁷⁻²³⁹ Polyphosphazenes are allowed to be modified by various functional groups. Thus their molecular structures can be designed by adjusting the number and type of the substituents,²⁴⁰ to meet the requirements depending on expected applications. The most studied ones are linear polyphosphazenes and crosslinked polyphosphazenes (**Fig 1.17 b**).¹⁷⁷

Linear polyphosphazenes have flexible main chains and exhibit good mechanical properties, heat resistance and flame retardancy. As a widely used FR and self-

extinguishing material,^{237, 239} high LOI and low smoke release of linear polyphosphazenes were verified by previous research.^{238, 239, 241, 242} Furthermore, the excellent compatibility between linear polyphosphazenes FRs and polymer matrix improve the comprehensive performance of them.²⁴¹ However, the development of linear polyphosphazenes suffers from the low yield, high cost, and the harsh reaction conditions of ring-opening polymerisation.²⁴³

Compared with linear polyphosphazenes, cyclocrosslinked polyphosphazenes are easier to synthesize from HCCP by nucleophilic substitution and achieve a high yield of up to 90%.¹⁷⁷ HCCP is often used as a starting material for their preparation. There are two chloride groups attached to each phosphorus atom, that are highly active and can be easily substituted with nucleophiles (like alkyl, alkoxy, phenoxy and amine),²⁴⁴ providing a satisfactory structural designability. Six N and P bonds in the cyclophosphazene ring have the same length, and the P atoms are symmetrically distributed in the ring. Therefore, a d π -p π hybrid orbital is formed in cyclophosphazene, which shows similar aromaticity to a benzene ring.²⁴⁴ That indicates cyclocrosslinked polyphosphazenes possess a stable chemical structure, which can contribute to their heat resistance. Different from flexible linear polyphosphazenes, the cyclocrosslinked polyphosphazenes own a certain rigidity caused by both the stable hexatomic ring and a high degree of crosslinking, and they can be shaped into various morphologies, such as nanotubes, microspheres and nanosheets.¹⁷⁷

According to the interaction between the substrate material and the FRs, cyclophosphazene derivatives are divided into two types: reactive FRs and additive FRs. The reactive CTP-FRs can be directly polymerised and interpenetrated into the network of substrate polymers by introducing reactive groups to the monomers (epoxy group, phenolic hydroxyl group and amino group, etc.). This can, not only, improve the flame retardancy of the substrate materials, but also enhance their mechanical stability. However, these reactive groups have a serious influence on the time and temperature of polymerisation, thus complicating the preparation process. Additive FRs have a simple operating process and great performance, but excessive addition and poor compatibility with some substrate materials weaken the mechanical properties of the final products.²⁴⁵ Therefore, the exploration of additive phosphazene FRs with better flame retardancy and lower effect on the final mechanical stability of materials is the focus of current research.

Dufek et al. presented hybrid anodes consisting of graphite and a cyclic phosphazene polymer, which could reduce flammability and enhance overcharge protection through molecular design of the polymers.²⁴⁶ Chang et al. synthesized hydroxy phenyl-substituted CTPs transformed into phosphazene-triazine cyclomatrix network polymers. Char formation of the network improved with the increase of crosslink density, which inferred that the action was operative in the condensed phase.²⁴⁷ Yao et al. investigated the polyphosphazene modified magnesium hydroxide crosslinked by boric acid (MH-PZPI-BA, **Fig 1.18**) used as a FR. It was incorporated into ethylene-vinyl acetate and undoubtedly improved the flame retardancy, toxic gas suppression and thermal stability.²⁴⁸

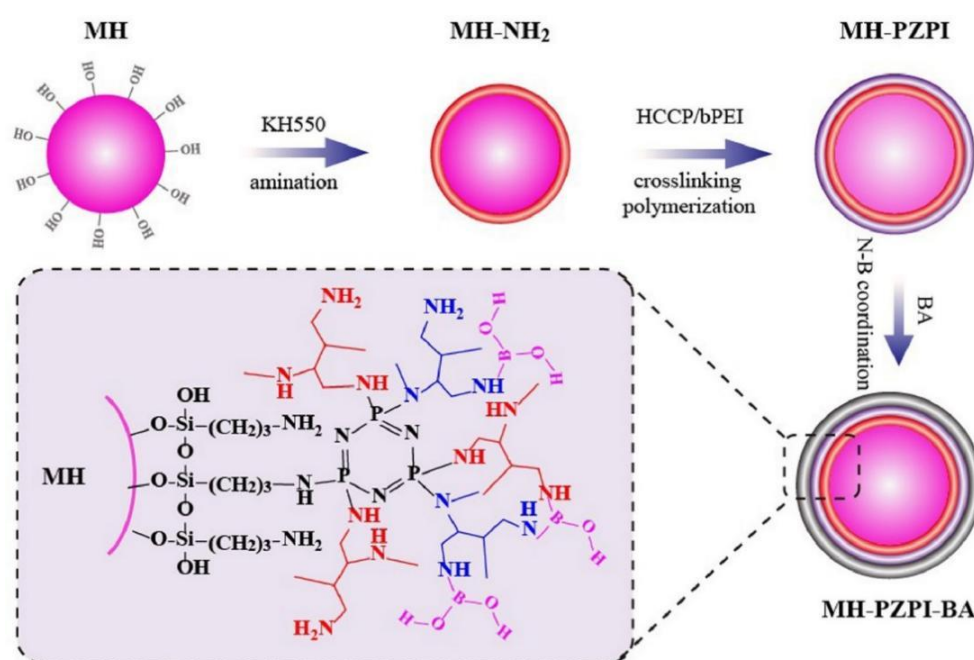


Figure 1.18 Synthesis process of MH-PZPI-BA.

Cyclocrosslinked polyphosphazenes demonstrate excellent flame retardancy, thermal stability and self-extinguishment.²⁴⁹ Their flame retardant behaviours follow the mechanism of the P–N synergistic system. Currently, cyclocrosslinked polyphosphazenes have been investigated as a meaningful branch of phosphorus FRs and are believed to be a potential substitute for halogen-containing FRs.

Aims of the Project

Plenty of research on PIMs shows their high thermal stability, especially considering their high decomposition temperatures and residual weights. This hints at their potential to be developed as FRs. Despite that, according to the literature we have retrieved, no relevant work has been reported on this topic so far, especially focusing about the systematic functionalisation of PIMs to improve their thermal stability.

Depending on the structural characteristics of PIMs and the mechanism of common flame retardant elements, PIM materials can be designed from the following aspects: (1) Selecting suitable fused ring units known for their high thermal stability (2) Introducing elements known to improve the flame retardant effects, such as boron, nitrogen and phosphorus. (3) On the basis of the first two points, tuning the porosity as much as possible, to test whether it is crucial for a good flame-retardant PIM or not.

This PhD project focuses on the synthesis of three series of PIM-based FRs. The first one contains boroxine and boronic ester-based PIMs, polymerised from aryl boronic acid monomers with different rigidity and contortion types (to introduce boron in their backbone). The second is a series of polymers composed of hexaphenylbenzenecore units and Tröger's Base linkages with different C/N ratios and porosities. The third series is based on cyclophosphazene, which could be polymerised with various catechols and amines.

Furthermore, considering the widespread application of porous polymers in gas capture and separation, CO₂ capture and CO₂/N₂ selectivity of the above polymers with sufficient specific surface areas and appropriate pore sizes will also be investigated. In addition to the excellent porosity generally possessed by PIMs, the inclusion of heteroatoms like nitrogen is expected to improve the uptake and selectivity of CO₂.

Overall, we aim to prepare novel multifunctional PIM materials possessing high porosity, great thermal stability and high heteroatom content, which are applied in the fields of flame retardation and gas adsorption and separation.

Chapter 2 – Novel Boron-containing PIMs for Flame Retardation and Gas Separation

2.1 Introduction

In this chapter, the study of boroxine and boronic ester-based polymers, as two series of organic boron-containing PIM candidates with potential application in the fields of flame retardation and gas adsorption and separation, are described.

2.1.1 Boroxine-based PIMs

Boroxine-based PIMs were selected for this study because of their excellent designability, easy preparation methods, great compatibility with substrate materials (such as polyurethane foam and resins) and their often tuneable microporosity.

1. Designability is a common advantage of most organic materials. Monomers with suitable structures can be purposely selected according to needed properties.
2. Boroxine compounds can be prepared by simple dehydration of boronic acid groups by heating them at a high temperature.²⁵⁰
3. Compared with inorganic boron-based FRs, organic boron-based materials have better compatibility with polymer matrix and avoid a decrease in flame retardancy, due to the leaching of additives.
4. Boroxine-PIMs, theoretically, could afford high porosity which is obtained not only from rigid and contorted aryl containing units but also from their highly networked structure. Abundant porosity and pore sizes distributed within an appropriate range are the keys for CO₂ uptake and selectivity.

The route used for preparing boroxine-based PIMs is illustrated in **Fig 2.1 a**. Aryl bromide precursors were firstly prepared, followed by a lithium-halogen exchange with *n*-butyllithium (*n*-BuLi) and reaction with a triisopropyl borate to synthesize aromatic boronic acid monomers.¹⁹⁶ Boroxine networks were formed via dehydration at a high

temperature heated in sand bath or microwave reactor. In this work, the feasibility of solvent-free preparation was demonstrated, which embodies the concept of green chemistry.

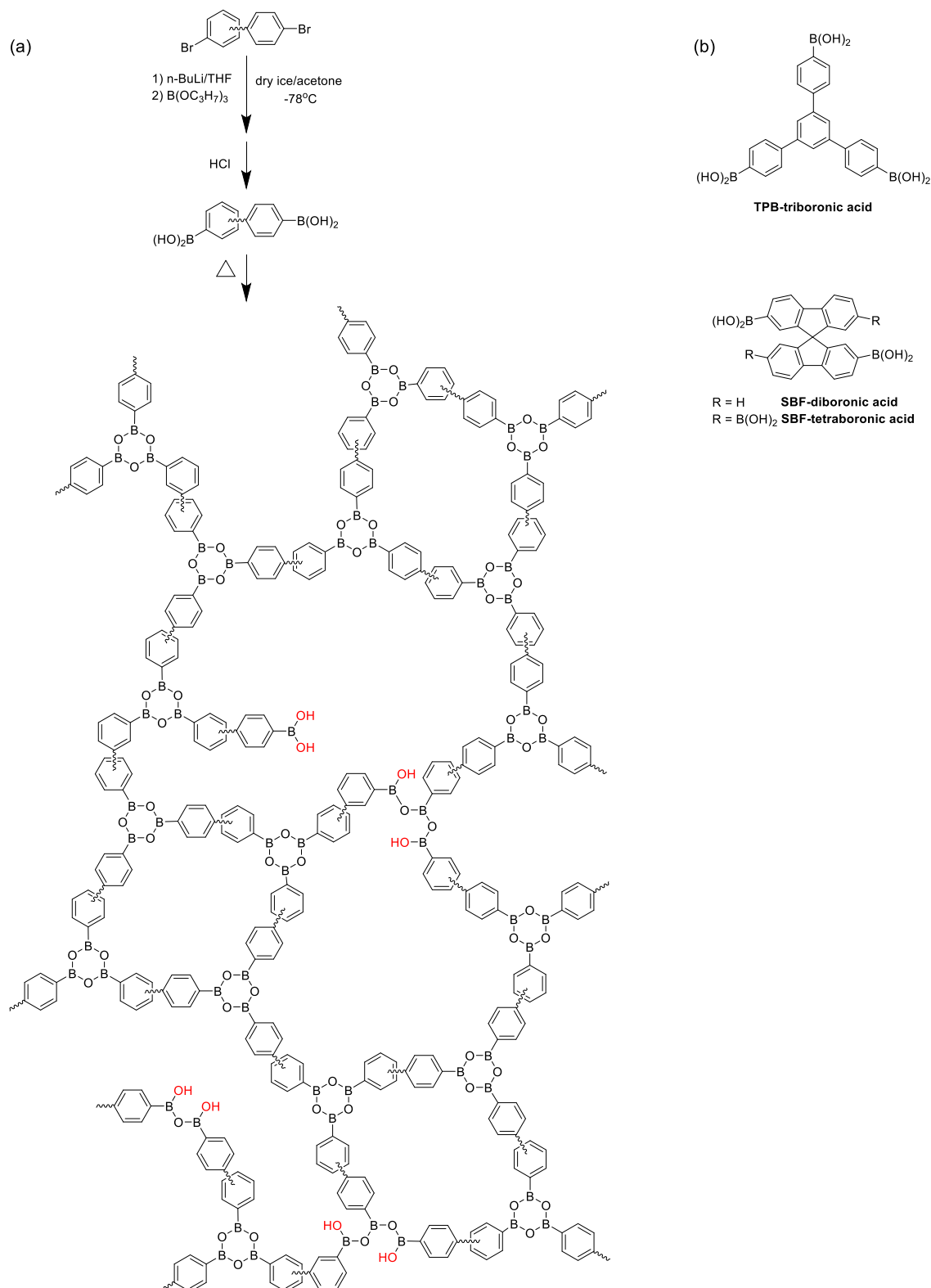


Figure 2.1 (a) Route of boroxine-based PIMs preparation; (b) Boronic acid monomers.

In practical terms, there may be a few boronic acid groups that cannot quantitatively react and remain in the final product, because it is impossible that they all, especially in the later stages of the polymerisation. This is due to the characteristic rigid conformation of PIMs, that hinders the flexible movement of the chains and hampers the reaction preventing completion. High temperatures, long reaction times, vigorous stirring and vacuum are used to maximize the level of dehydration and minimize the amount of remaining boronic acid groups and their impact on the performance of the final products. **Fig 2.1 b** shows the boronic acid monomers used in the initial section of this work, substituted triphenylbenzene (TPB) and SBF monomers.

2.1.2 Boronic Ester-based PIMs (BE-PIMs)

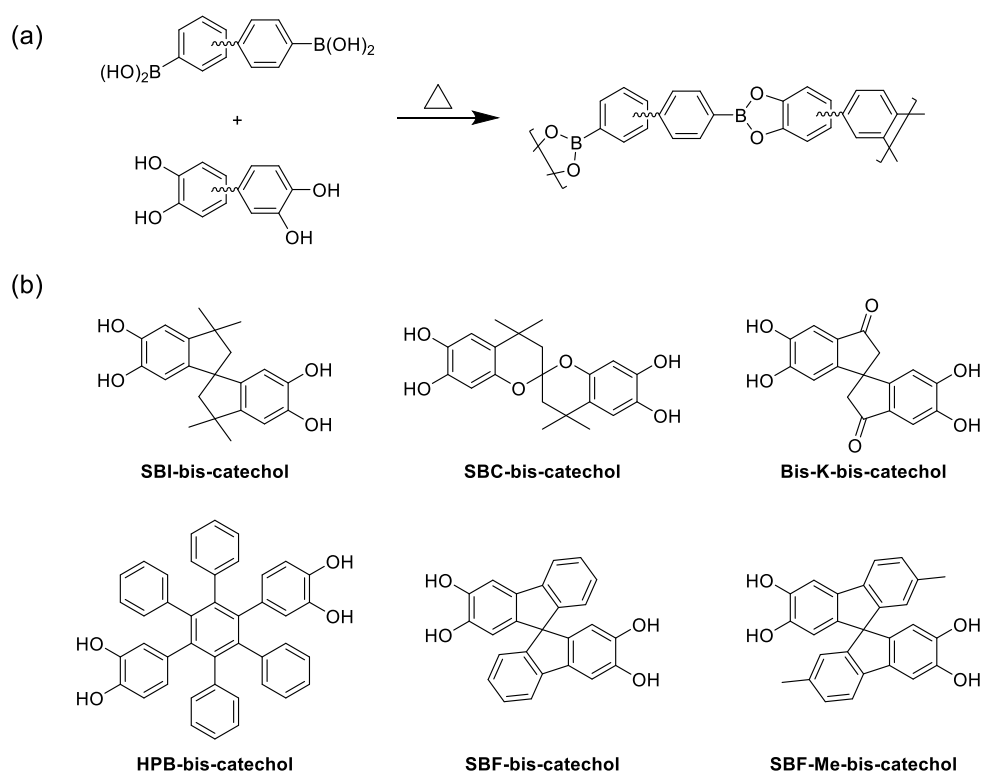


Figure 2.2 (a) Route of BE-PIMs preparation; (b) Different bis-catechol monomers.

Similar to boroxine ones, BE-PIMs also possess ideal designability, compatibility with polymer substrates, porosity, and proven environmentally friendly preparation. The difference is that these BE-PIMs are supposed to be linear copolymers instead of networks. In this case, the porosity entirely comes from rigidly contorted conformation of their macromolecular chains. Moreover, more diverse structures can be introduced through bis-catechol monomers to further enhance their designability. It is found in our

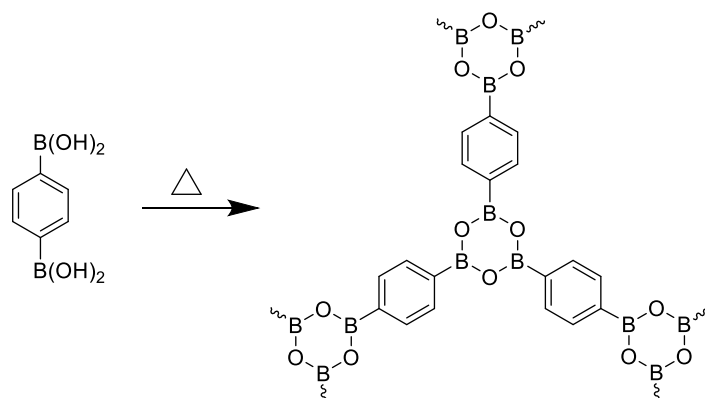
experiments that the synthesis of boronic esters showed better feasibility and repeatability than boroxines.

The same monomers used for boroxines synthesis were also prepared for the boronic esters. Six bis-catechol monomers used in this work are listed in **Fig 2.2 b**, which were either commercial compounds or synthesized referred to literature listed in **Table 2.6**. They were respectively dehydrated using microwave irradiation or Dean-Stark apparatus to prepare BE-PIMs.

2.2 Results and Discussion

2.2.1 Boroxine-based PIMs

In order to explore the best polymerisation conditions at the start, commercial benzene-1,4-diboronic acid was used to prepare the corresponding model boroxine compound. The different attempted conditions and relative results are listed in **Table 2.1**.



Scheme 2.1 Preparation of model boroxine with commercial benzene-1,4-diboronic acid.^{250, 251}

The ideal dehydration temperature of benzene-1,4-diboronic acid was found to be 207 °C, according to TGA analysis in N₂ shown in **Fig 2.4** and **Table 2.2**. Preparation of the model boroxine was attempted using different heating devices (**Table 2.1**). The reaction was placed in a hydrothermal synthesis reactor and heated in the oven. The product was characterized as almost only benzene-1,4-diboronic acid by NMR. It is speculated that the water released during the reaction cannot be easily removed from a sealed reactor and then condensed during cooling, leading to hydrolysis of the formed boroxine network. Then the monomer was refluxed in toluene/methanol (MeOH) using Dean-Stark apparatus, which was expected to be able to remove water from the

reaction but also produced unreacted monomer. It is inferred the toluene/MeOH system cannot provide a high enough temperature to dehydrate the boronic acid group.

The heating device was then adapted to place a reaction tube connected to the vacuum, which was planned to remove produced water vapour during the reaction. The bottom of the tube was submerged in a sand bath which could be heated over 200 °C. The reaction was heated at 200 °C and was sampled every 2 hours within 6 hours and every 1 hour after 6 hours. TGA in N₂ showed little difference among the weight losses of dehydration on curves of samples heated over 7 hours. Thus, it was decided the optimum condition was heating the monomer under vigorously stirring at 200 °C for 7 hours, and under vacuum.

Table 2.1 Attempted Conditions for Preparing Model Boroxine.

Monomer	Device	T/°C	Time	Products
3.6 mmol	Hydrothermal synthesis reactor / oven	220	8 hrs	Almost only monomer
3.6 mmol	Dean-Stark toluene/MeOH (v:v=4:1)	125	7 hrs	Almost only monomer
3.6 mmol	Sand bath/vacuum	200	2,4,6,7,8 hrs	Model boroxine (hydrolysed in washing with DCM, MeOH, acetone)
1.2 mmol	Microwave reactor	200	20,40,60,80,100,120 min 4,6,8 hrs	Model boroxine Yield = 100%

The microwave reaction was also conducted because it is known as a more efficient heating than traditional heating plates. The caps that seal the reaction vials are designed to allow the venting of any produced gas released reaction. The monomer was irradiated at 200 °C and was sampled every 20 minutes within 2 hours and every two hour after 2 hours. According to the results of TGA analysis in N₂, the optimal reaction time was shortened to 2 hours by using the microwave reactor.

Fourier-transform infrared spectroscopy (FT-IR) was used to evaluate the formation of the desired model boroxine by comparing the spectra of the monomer and the products.

Fig 2.3 shows the spectra of benzene-1,4-diboronic acid and two model boroxines. Characteristic peaks of boroxine compounds at 693 cm⁻¹ were found in both model boroxines, which is the low frequency out-of-plane vibration involves displacements of boron atoms syn to the displacements of aryl hydrogen atoms.²⁵² The O–H stretching peak in the range of 3411–3284 cm⁻¹ corresponding to the residual unreacted boronic

acid group is almost not detected for microwave irradiated model boroxine, and for sure much weaker than that of the product obtained employing a sand bath to heat the reaction. It can be concluded that the model boroxine can be synthesized using both methods, but microwave irradiation offered a higher degree of polymerisation and more efficiency.²⁵²

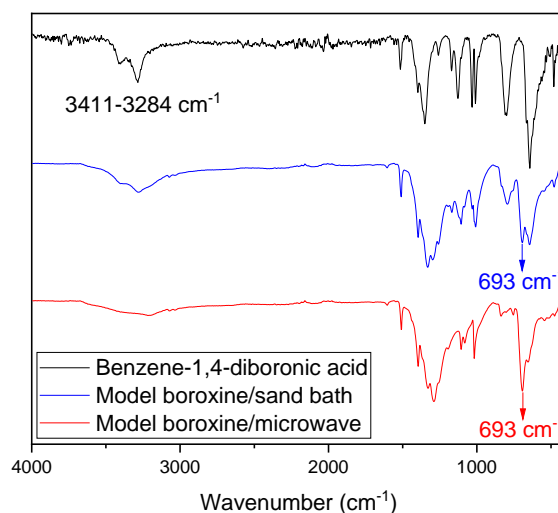


Figure 2.3 FT-IR of benzene-1,4-diboronic acid and model boroxines.

The same conclusion could be drawn from TGA in N₂ analysis of the two model boroxine (**Fig 2.4 a**). The curve of benzene-1,4-diboronic acid shows two types of weight loss. As already mentioned, the first one around 207 °C is caused by dehydration of the boronic acid group to form B₃O₃ boroxine rings. Thermal decomposition of boroxine leads to the second weight loss at 603 °C. Instead, a 3% weight loss from 111 to 207 °C could be observed for the model boroxine obtained with sand bath heating and under vacuum. By contrast, the TGA curve for microwave irradiated product does not show any obvious weight loss connected to dehydration. Also, its T_d and carbon yield are slightly higher than those for the sand bath heated product (**Table 2.2**). A possible reason is that, even connected to the vacuum, the atmosphere inside the reaction tube is relatively static, rather than gas circulating. A tiny amount of the water vapor condensed at the top of the tube during cooling and fell back into the reaction, causing a little hydrolysis of the product.

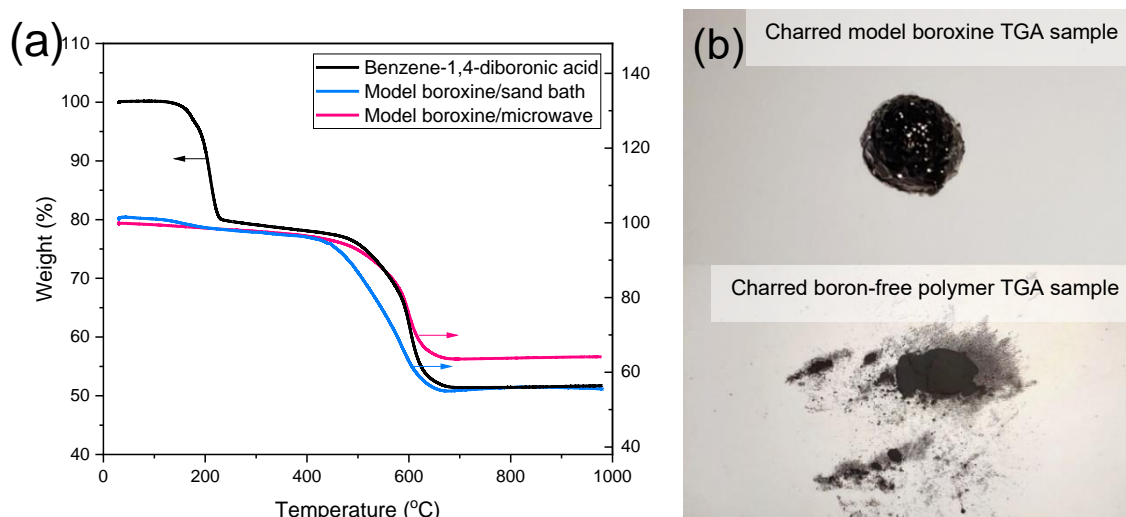


Figure 2.4 (a) TGA in N₂ of benzene-1,4-diboronic acid and model boroxines, (b) Morphology of charred model boroxine and boron-free polymer from TGA tests.

Combined with S_{ABET} values in **Table 2.2**, CO₂ adsorption and PSD in **Fig 2.5 b** and **c**, which show only the microwave irradiated model boroxine has some degree of porosity, it is speculated that the product heated by sand bath was mainly linear macromolecular chains rather than network, leading to poor porosity.

Table 2.2 Thermal Properties in N₂ and S_{ABET} of Boronic Acids and Model Boroxines.

Boronic acids and model compound		S _{ABET} ^a (m ² /g)	Decomposition Temperature (°C)				Char Yield (%)
			T _{d5}	T _{d10}	T _{d20}	T _{max}	
benzene-1,4-diboronic acid		-	190	205	233	207; 603	52
Model boroxine	Sand bath	<1	407	475	529	584	56
	Microwave	149	457	530	590	594	64
TPB-triboronic acid		-	225	402	471	141; 581	40

^a S_{ABET} were measured at CO₂/273 K.

Fig 2.4 b shows the completely decomposed samples burned at 1000 °C under N₂ atmosphere from TGA measurement. The carbon residues of boron-free polymer samples are generally in powder form. However, the residue of model boroxine appeared as a carbon shell with a smooth surface and foam-like inside. This morphology can be seen as proof of the mechanism of boron-based FRs.¹⁹⁴ Gases were released during the combustion process to form a pore structure inside, and a glassy layer was formed to cover the surface.²⁵³

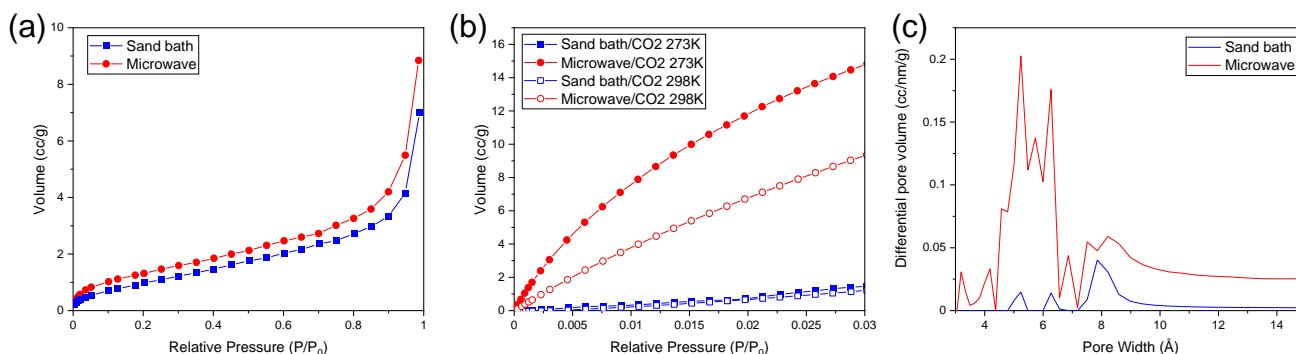
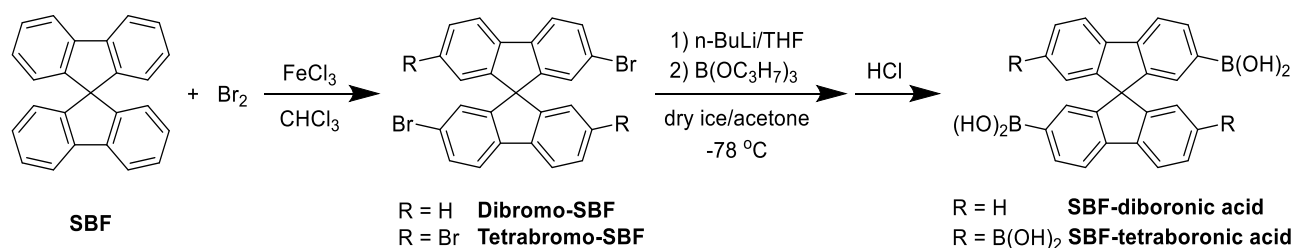


Figure 2.5 (a) N₂ adsorption at 77 K, (b) CO₂ adsorption at 273 K and 298 K, (c) PSD of model boroxines, calculated from CO₂ adsorption at 273 K by NLDFT.

Based on the results above, microwave irradiation contributed to a higher level of dehydration for preparing model boroxine, thus affording it with a complete networked structure. The product heated on the sand bath was deduced to oligomers as evidenced by the O–H peak of unreacted boronic acid groups in FT-IR spectrum, leading to a slightly lower T_d and a low porosity.



Scheme 2.2 Preparation of SBF-boronic acid with SBF.

The synthesis of dibromo SBF was attempted following reported procedures,²⁵⁴ where bromine was added to a solution of SBF in chloroform in the presence of iron chloride as the catalyst. Only a complex mixture containing mono and dibrominated compounds was obtained, according to thin layer chromatography (TLC) and NMR. The mixed compounds could not be separated by column chromatography due to their highly similar structures. Increasing the amounts of catalyst and bromine did not help in affording pure dibromo-SBF but the obtained a mixture showed obvious peaks of tetrabromo-SBF in its ¹H NMR spectrum. It seems that the ideal purity of dibromo-SBF product requires precise control of the amount of catalyst and bromine. The preparation of tetrabromo-SBF is relatively easy to control, allowing adding excess bromine to afford a high yield and purity. The extent of this reaction can be improved by appropriately increasing the amount of catalyst.²⁵⁵

Table 2.3 Attempted Conditions for Preparing Dibromo-SBF.

Solution A			Solution B		Conditions	Products
SBF	FeCl ₃	CHCl ₃	Bromine	CHCl ₃		
3.2 mmol (1 eq.)	0.01 mmol (0.004 eq.)	9 mL	6.8 mmol (2.2 eq.)	2 mL	25 °C for 23 hrs	Complex mixture
1.0 mmol (1 eq.)	0.04 mmol (0.04 eq.)	2.8 mL	3.0 mmol (3 eq.)	-	0 °C for 1 hr Warm to 25 °C over 3 hrs 25 °C for 19 hrs	Complex mixture

In this work, the amount of iron chloride was increased more than ten times the amount reported in the literature²⁵⁴ to yield a crude product, which was purified by silica gel column chromatography to obtain pure tetrabromo-SBF precursor with a low yield of 18%. In order to avoid mass loss in the purification process, the purity of crude product was further improved by adding bromine in excess. In this case, no purification was required for the raw product, of which the purity was confirmed by NMR, and the optimized yield reached 65%. Also, FT-IR spectrum shows the C–Br stretching peak at 508 cm⁻¹, inferring the successful synthesis of tetrabromo-SBF.

Table 2.4 Attempted Conditions for Preparing Tetrabromo-SBF.

Solution A			Solution B		Conditions	Products
SBF	FeCl ₃	CHCl ₃	Bromine	CHCl ₃		
3.2 mmol (1 eq.)	0.012 mmol (0.004 eq.)	6 mL	12.7 mmol (4 eq.)	5 mL	0 °C for 1 hr 25 °C for 24 hrs	Mixture
3.2 mmol (1 eq.)	0.16 mmol (0.05 eq.)	12 mL	14.2 mmol (4.5 eq.)	-	0 °C for 1 hr 25 °C for 4 hrs 0 °C for 17 hrs	Tetrabromo-SBF Y% = 18%
9.0 mmol (1 eq.)	0.45 mmol (0.05 eq.)	20 mL	40.5 mmol (4.5 eq.)	-	0 °C for 1 hr 25 °C for 4 hrs 0 °C for 17 hrs	Mixture
1.0 mmol (1 eq.)	0.05 mmol (0.05 eq.)	2.5 mL	7.8 mmol (7.8 eq.)	-	0 °C for 1 hr 25 °C for 4 hrs	Tetrabromo-SBF Y% = 65%
5.2 mmol (1 eq.)	0.25 mmol (0.05 eq.)	12 mL	39.0 mmol (7.8 eq.)	-	0 °C for 1 hr 25 °C for 4 hrs	Mixture

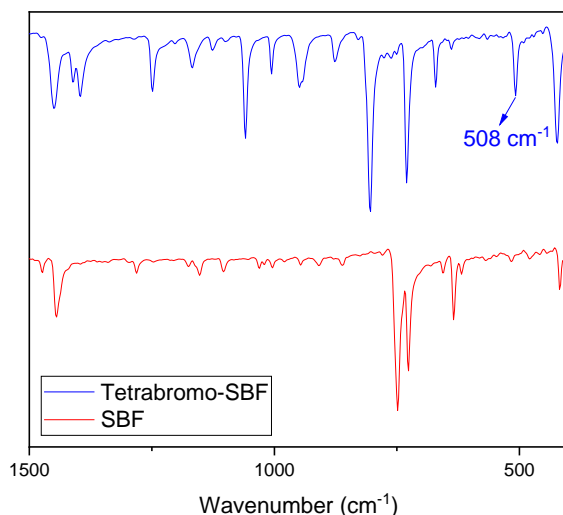
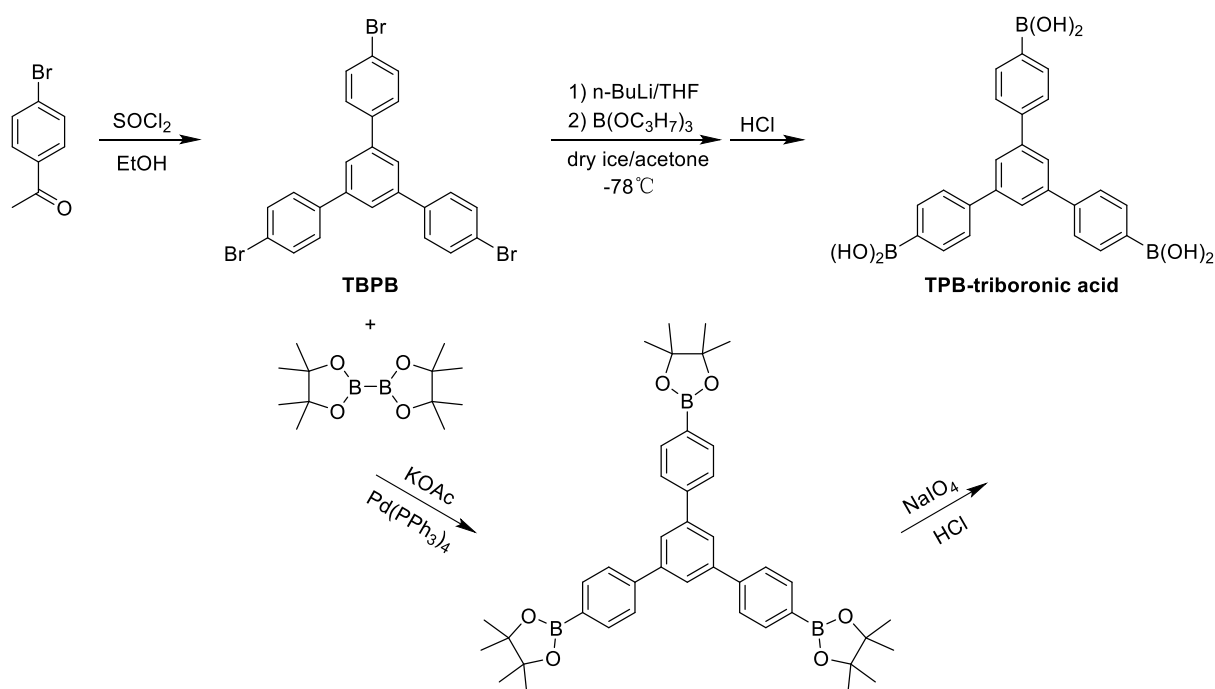


Figure 2.6 FT-IR of tetrabromo-SBF and SBF.

In our work, preparation of tetrabromo-SBF precursor still suffered from low repeatability on a larger scale (**Table 2.4**). SBF-tetraboronic acid has not been synthesized by lithium-halogen exchange after repeated attempts (**Table 2.5**) following reported procedures.²⁵⁴ Then the study focus switched to TPB-triboronic acid monomers which are easier to synthesize.



Scheme 2.3 Two routes of preparing TPB-triboronic acid.

1,3,5-Tris(4-bromophenyl) benzene (TBPB) precursor was obtained from 4'-bromoacetophenone stirred with thionyl chloride in ethanol following a reported procedure.²⁵⁶ Two routes were subsequently attempted to synthesize 1,3,5-tris(4-

phenylboronic acid)benzene (TPB-triboronic acid) as shown in **Scheme 2.3**. Route 1 is directly conducted by lithium-halogen exchange as same as mentioned above.^{257, 258} Route 2 is a two-step method by synthesizing TPB-boronic acid pinacol ester intermediate, followed by the deprotection reaction.²⁵⁹

Conditions of TPB-triboronic acid preparation on route 1 is showed in **Table 2.5**. The optimal conditions afforded the target compound with an ideal yield of 56% and relatively good purity confirmed by NMR, but it was also poorly reproducible. The structure was also convinced by FT-IR spectra that the C–Br stretching peak of TBPB at 507 cm^{-1} almost disappeared in TPB-triboronic acid sample. Meanwhile, a strong peak at 1338 cm^{-1} is found, corresponding to symmetric B–C stretching.

Table 2.5 Attempted Conditions for Preparing Boronic Acid Monomers.

Compound	Solution A		Solution B		Triisopropyl borate	Conditions	Products
	Bromo precursor	Anhydrous THF	<i>n</i> -BuLi in hexane [2.5M]				
SBF-tetraboronic acid	0.9 mmol (1 eq.)	15 mL	7.6 mmol (8 eq.)		15.0 mmol (16 eq.)	-78 °C for 2 hrs 25 °C overnight	Starting materials
TPB-triboronic acid	5.7 mmol (1 eq.)	100 mL	28.6 mmol (5 eq.)		32.1 mmol (5.5 eq.)	-78 °C for 1 hr 25 °C overnight	TPB-triboronic acid Y% = 56%
	1.8 mmol (1 eq.)	35 mL	9.2 mmol (5 eq.)		9.9 mmol (5.5 eq.)	-78 °C for 1 hr 25 °C overnight	Complex mixture

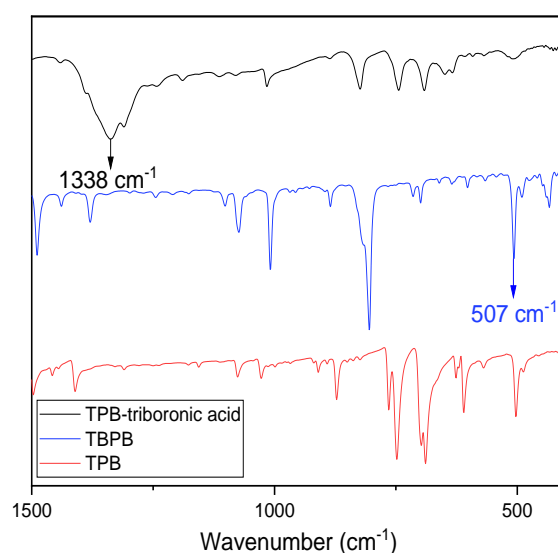


Figure 2.7 FT-IR of TPB, TBPB and TPB-triboronic acid.

Preparation of TPB-triboronic acid pinacol ester intermediate was attempted on route 2. TBPB was refluxed with potassium acetate in dioxane catalysed by palladium-

tetrakis(triphenylphosphine) overnight. However, the product showed a viscous mixture of at least eight compounds in the TLC and not possible to be purified by either recrystallization or silica gel column chromatography.

Based on the optimal conditions found for the formation of model boroxines, the TPB-triboronic acid monomer was heated in a sand bath under vacuum and microwave reactor at different temperatures (150–250 °C) and reaction times (2–7 hours). However, the monomer was found to partially melt during heating, and it is speculated that the melted part was composed of residual impurities (which is difficult to be characterised, especially based on the small amounts). Although the TPB-boroxine has not been synthesized, its thermal properties can be deduced from TGA analysis in N₂ of TPB-triboronic acid monomer. The formation of B₃O₃ rings started around 141 °C and the decomposition occurred at 581 °C, which is similar to T_d of model boroxine.

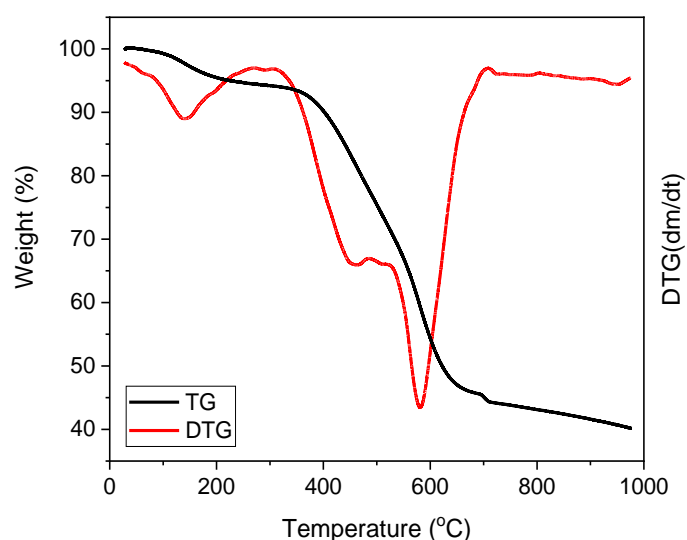
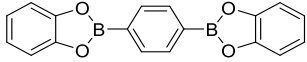
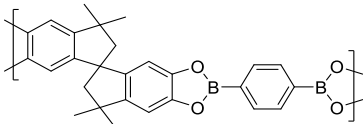
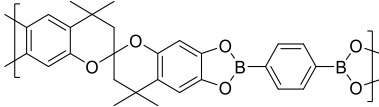
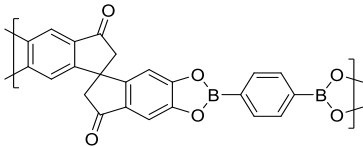
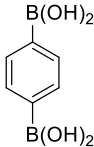
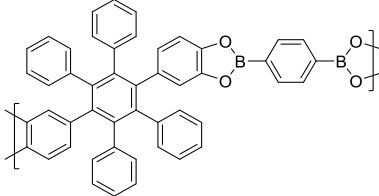
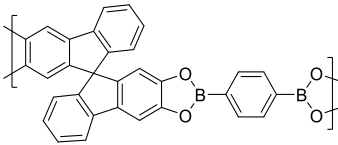
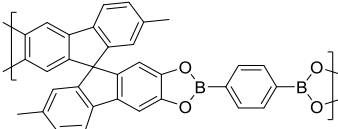


Figure 2.8 TGA in N₂ of TPB-triboronic acid.

In summary of preliminary results, microwave irradiation showed great dehydration efficiency for preparing model boroxine with a satisfactory network structure using commercial benzene-1,4-diboronic acid as the monomer. However, after many attempts, SBF-boronic acid monomers failed to be prepared, and improvements of purification and reproducibility of TPB-triboronic acid preparation have not been achieved. Therefore, the research focus on boron-containing PIMs shifted to BE-PIMs.

2.2.2 Boronic Ester-based PIMs (BE-PIMs)

Table 2.6 BE-PIMs and Their Monomers.

Model compound and Polymers	Diboronic acid	Catechol monomers
 Model boronic ester		Catechol
 BE-SBI-PIM		SBI-bis-catechol
 BE-SBC-PIM		SBC-bis-catechol
 BE-bis-K-PIM		Bis-K-bis-catechol ^a
 BE-HPB-PIM	Benzene-1,4-diboronic acid	HPB-bis-catechol ^a
 BE-SBF-PIM		SBF-bis-catechol ^a
 BE-SBF-Me-PIM		SBF-Me-bis-catechol ^a

^a The synthesis refers to a published procedure (see Experimental Section).

In addition to synthesizing boroxine, which is a homopolymer, diboronic acids can also copolymerise with bis-catechols to form boronic esters. In this work, six bis-catechols were selected to react with aryl diboronic acid to prepare ladder polymers, of which the

backbones were designed to possess rigidly contorted conformation (in **Table 2.6**). These boronic esters were dehydrated from monomers respectively in microwave reactor and Dean-Stark trap, which were confirmed capable of preparing boronic ester polymers.^{260, 261}

The model boronic ester was synthesized at first to explore the optimal reaction conditions. Following published literature,²⁶² acetonitrile (MeCN) was used as solvent, but neither reflux nor microwave irradiation achieved ideal results. Afterwards, the solvent was replaced with mesitylene aiming to increase the reaction temperature.²⁶¹ An excellent product was obtained with a high yield of 96% and great purity. It was found that the product was easily hydrolysed in the process of washing even with anhydrous solvents. This suggests that boronic esters cannot withstand general aqueous washing during work-up.

Table 2.7 Attempted Conditions for Preparing Model Boronic Ester.

Boronic acid	Catechol	Solvent	Conditions		Products
5.0 mmol (1 eq.)	10.0 mmol (2 eq.)	MeCN	Reflux N ₂	75 °C for 4 hrs	Starting materials residue
1.0 mmol (1 eq.)	2.0 mmol (2 eq.)	MeCN	Microwave N ₂	85 °C for 1 hr	Starting materials residue
1.0 mmol (1 eq.)	2.0 mmol (2 eq.)	Mesitylene	Microwave N₂	150 °C for 1 hr	Model boronic ester Y% = 96%

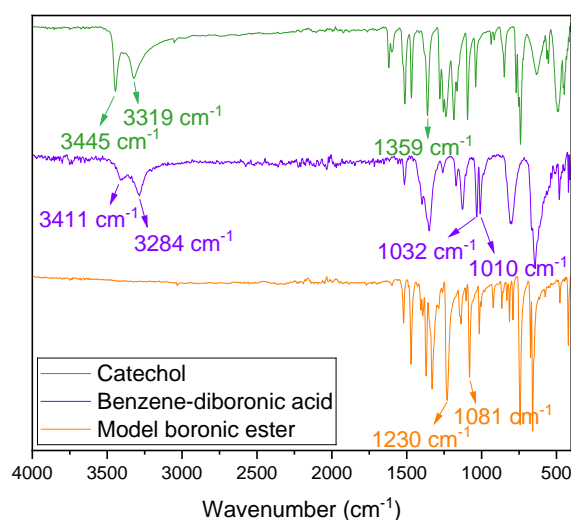


Figure 2.9 FT-IR of model boronic ester and its monomers.

In this reaction, hydroxyl groups react with boronic acid groups to form $-C_2O_2B$ rings, corresponding to the disappearance of the peaks of O–H from the monomers and the

generation of characteristic peaks from C–O stretching and B–O stretching.²⁵² The FT-IR spectra of model boronic ester and two monomers are shown in **Fig 2.9**. The peak of O–H stretching at 3445–3319 cm^{-1} for catechol and the peak of O–H stretching at 3411–3284 cm^{-1} for benzene-diboronic acid were not observed in the spectrum of model boronic ester. Two strong peaks at 1230 cm^{-1} and 1081 cm^{-1} are observed in model boronic ester, corresponding to C–O stretching and B–O stretching, which demonstrates that the correct product was successfully formed.

TGA analysis in N_2 illustrates that there is only one thermal weight loss at 318 °C in the model boronic ester, not coinciding with any weight loss of the two monomers. It indicates there are almost no unreacted boronic acid groups or hydroxyl groups remaining in the product.

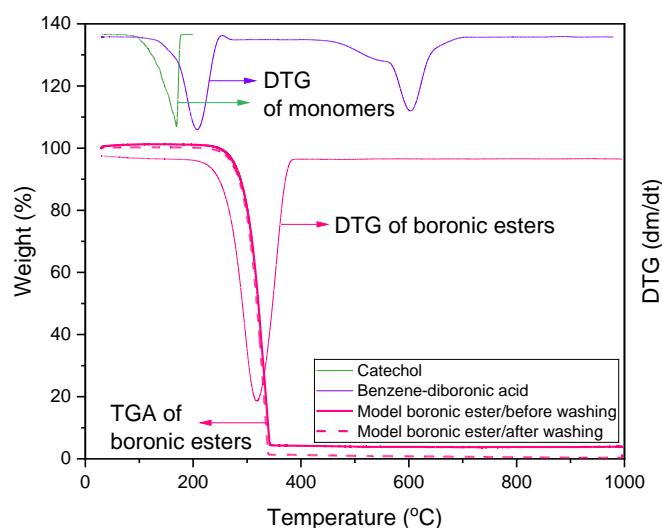


Figure 2.10 TGA and differential thermogravimetric analysis (DTG) in N_2 of model boronic ester, and DTG of its monomers.

At the beginning of this project, when preparing BE-SBI-PIM, starting reagents always remained when mesitylene was used as the solvent. It was speculated that trace amount of water in the solvent, although this solvent is not considered to be hygroscopic, could hinder the reaction, or hydrolyse boronic esters. Therefore, solvent-free conditions in the microwave reactor were attempted. Moreover, a Dean-Stark apparatus, which is widely used for dehydration reactions, also performed well on this reaction.²⁶⁰ It is noticed that the wet product must be immediately filtered off and dried under vacuum at the end of this reaction. Both devices were used to prepare these six novel BE-PIMs.

Table 2.8 Attempted Conditions for Preparing BE-SBI-PIMs.

Boronic acid	SBI-catechol	Solvent	Conditions		Products
2.0 mmol (1 eq.)	2.0 mmol (1 eq.)	Mesitylene	Microwave N ₂	150 °C for 2 hrs	Start material residue
0.2 mmol (1 eq.)	0.2 mmol (1 eq.)	-	Microwave	150 °C for 2 hrs	Mainly boronic ester Y% = 59%
1.0 mmol (1 eq.)	1.0 mmol (1 eq.)	toluene/MeOH (v:v=4:1)	Dean-Stark	120 °C for 2 hrs	Mainly boronic ester Yield = 119%

Since these boronic ester products are easily hydrolysed in solvents, solution based technique are not suitable for their characterisations. The obtained BE-PIMs were analysed by FT-IR (**Fig 2.11**) and compared with the starting materials. The peaks of B–O stretching and C–O stretching in –C₂O₂B ring would not overlap with the peaks of boronic acid and boroxine, confirming the formation of boronic ester.²⁵² Therefore, analysis of FT-IR spectra focuses on the disappearance of O–H peaks from monomers and the appearance of B–O and C–O peaks in BE-PIMs. Peaks of O–H stretching at 3416–3290 cm⁻¹ from the microwave irradiated **BE-SBI-PIM** were observed in **Fig 2.11 a**, which were consistent with the O–H stretching of benzene diboronic acid at 3411–3284 cm⁻¹ and SBI-bis-catechol at 3406–3233 cm⁻¹. The B–C stretching peak at 1361 cm⁻¹ and the C–O symmetric stretching peak at 1321 cm⁻¹ may overlap with the O–H bending at 1291 cm⁻¹ and cannot be recognized clearly. By contrast, almost no O–H stretching and strong C–O symmetric stretching at 1321 cm⁻¹ was found in the **BE-SBI-PIM** product from Dean-Stark. The peaks of C–O and B–O symmetric stretching were observed in both **BE-SBC-PIM** products, respectively located at 1140 cm⁻¹/1061 cm⁻¹ and 1135 cm⁻¹/1078 cm⁻¹. However, the microwave irradiated products still contain O–H stretching at 3443–3198 cm⁻¹ from SBC-bis-catechol. In brief, the system of Dean-Stark trap and toluene/MeOH is more suitable for preparing **BE-SBI-PIM** and **BE-SBC-PIM** than microwave irradiation.

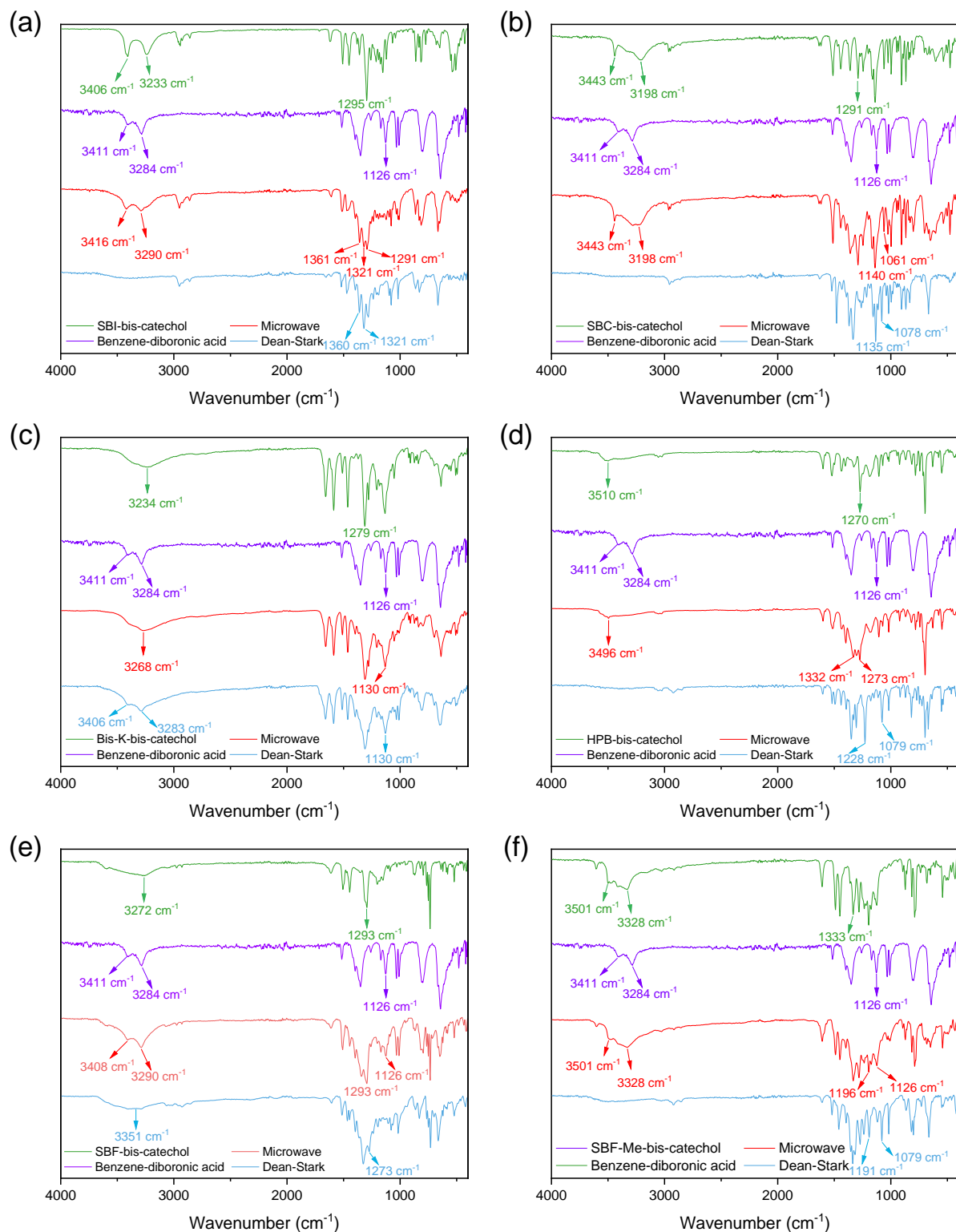


Figure 2.11 FT-IR of BE-PIMs and their monomers: (a) BE-SBI-PIM, (b) BE-SBC-PIM, (c) BE-bis-K-PIM, (d) BE-HPB-PIM, (e) BE-SBF-PIM, (f) BE-SBF-Me-PIM.

Spectra of both **BE-bis-K-PIMs** showed the presence of the O–H stretching. That of the microwave irradiated product at 3268 cm^{-1} is mainly from the bis-K-bis-catechol monomer. Whereas O–H stretching peaks at $3406\text{--}3283\text{ cm}^{-1}$ in **BE-bis-K-PIM** from Dean-Stark are considered caused by both types of monomers. Characteristic C–O symmetric stretching peaks at 1130 cm^{-1} of boronic ester are present in both products. There is a weak peak of O–H stretching at 3496 cm^{-1} in microwave irradiated **BE-HPB-PIM**. Peaks at $1332\text{--}1273\text{ cm}^{-1}$ are attributed to the overlap of O–H bending, B–C stretching and C–O symmetric stretching. By contrast, there are almost no peaks of O–H in the **BE-HPB-PIM** from Dean-Stark. Its spectrum also exhibits peaks of C–O and B–O symmetric stretching at 1228 cm^{-1} and 1079 cm^{-1} . O–H stretching peaks are observed in both **BE-SBF-PIMs**, more in microwave irradiated product than in the one obtained from Dean-Stark. The peaks of C–O symmetric stretching cannot be identified clearly due to the overlap with B–C stretching peaks in the range of $1399\text{--}1273\text{ cm}^{-1}$. No obvious B–O stretching peak was observed in both. An overlapped but clear peak of C–O symmetric stretching at 1196 cm^{-1} was found in the spectrum of microwave irradiated **BE-SBF-Me-PIM**. There are also peaks at $3501\text{--}3328\text{ cm}^{-1}$ consistent with O–H stretching of SBF-Me-bis-catechol. The product from Dean-Stark shows almost no O–H stretching, and both C–O and B–O symmetric stretching of $\text{--C}_2\text{O}_2\text{B}$ ring at 1191 cm^{-1} and 1079 cm^{-1} . In the cases of these four BE-PIMs, **BE-HPB-PIM** and **BE-SBF-Me-PIM** showed much less residual monomer from Dean-Stark than from microwave irradiation. There seems to be no significant difference between each pair of the products of **BE-bis-K-PIM** and **BE-SBF-PIM**. Further characterizations are required to evaluate their purity.

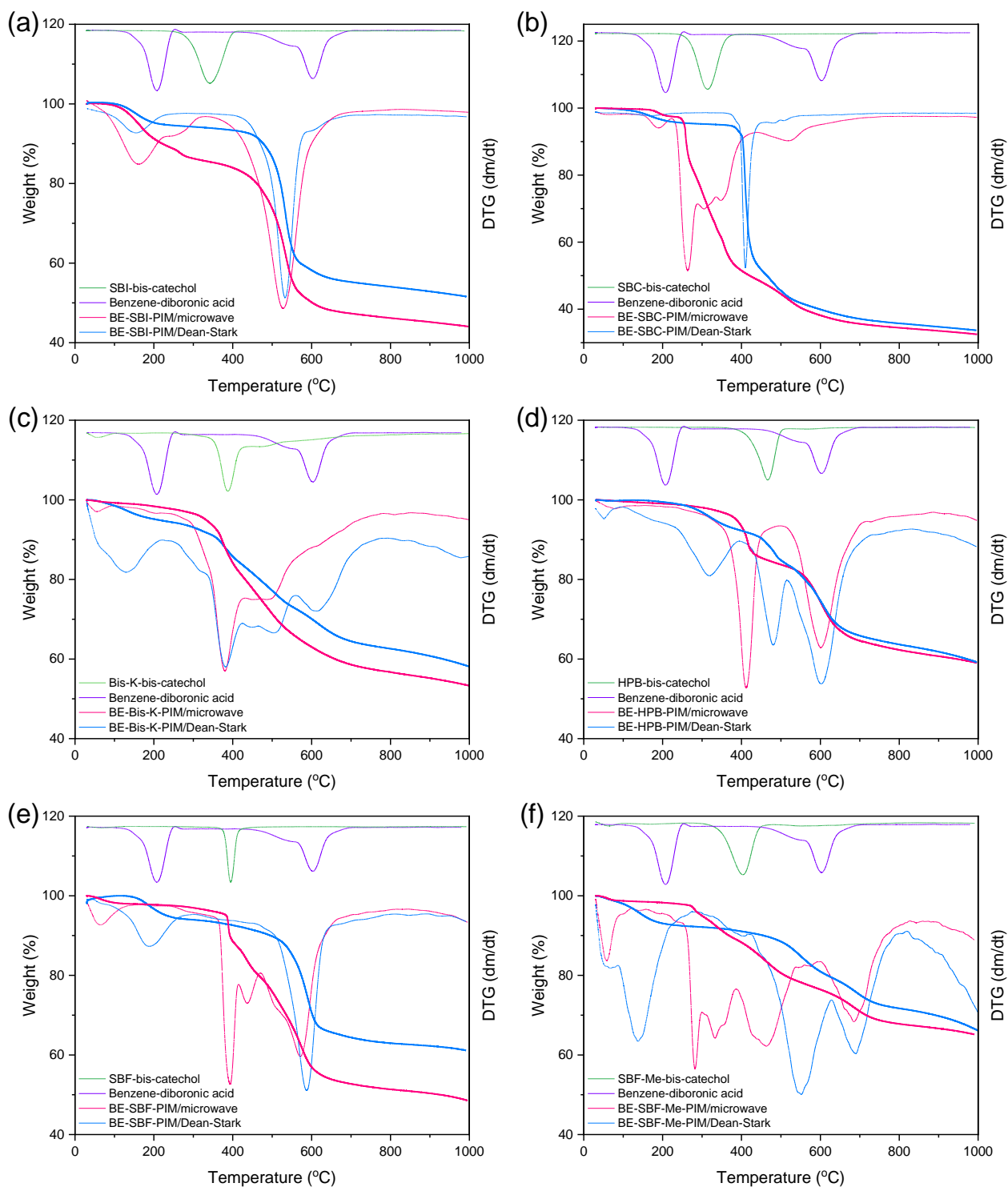


Figure 2.12 TGA and DTG in N_2 of BE-PIMs, and DTG of their monomers: (a) BE-SBI-PIM, (b) BE-SBC-PIM, (c) BE-bis-K-PIM, (d) BE-HPB-PIM, (e) BE-SBF-PIM, (f) BE-SBF-Me-PIM.

The presence of unreacted monomers can also be judged by whether the BE-PIM products show thermal weight losses at similar temperatures to monomers. The DTG

curves of two **BE-SBI-PIM** products and their monomers are shown in **Fig 2.12 a**, the first small weight loss around 160 °C came from the dehydration of a few unreacted functional groups. The largest weight loss at 530 °C was caused by the decomposition of polymer chains. There is no obvious weight loss attributed to SBI-bis-catechol or boroxine. Combining the data of T_d and carbon yields listed in **Table 2.9**, the thermal property of **BE-SBI-PIM** from Dean-Stark is slightly better than the microwave irradiated one. T_{max} of microwave irradiated **BE-SBC-PIM** is significantly lower than the product from Dean-Stark. The overlapped weight losses from 263 °C to 348 °C are inferred from a mixture of unreacted monomers and by-products, which could probably be oligomers, boronated macrocycles.²⁶³ Except for a 4% weight loss at 166 °C, **BE-SBC-PIM** from Dean-Stark showed only a sharp weight loss at 410 °C, which is believed to be thermal decomposition of the pure polymer. It also exhibits higher T_d and char yield than the microwave irradiated one. Both FT-IR and TGA support that the dehydration of **BE-SBI-PIMs** and **BE-SBC-PIMs** in Dean-Stark system gave significantly higher degrees of reaction than microwave irradiation. Therefore, the products of **BE-SBI-PIM** and **BE-SBC-PIM** prepared by Dean-Stark were selected for further characterization of gas adsorption and desorption.^{264, 265}

The T_{max} at 380 °C was observed for both **BE-bis-K-PIMs**, which is consistent with T_d of bis-K-bis-catechol. It is speculated that **BE-bis-K-PIM** chains decomposed in the range 450–500 °C. Besides, there are two weight losses that occurred at 130 °C and 614 °C in the product from Dean-Stark, corresponding to benzene-diboronic acid monomer. T_d of **BE-HPB-PIMs** is considered as the T_{max} of both products at 601 °C. Although this temperature seems like T_d of boroxine, it is believed not caused by boroxine decomposition, because no noticeable characteristic peak of boroxine at 736–762 cm^{-1} or 677–696 cm^{-1} ²⁵² was found in its FT-IR spectrum above. The weight loss at 412 °C of microwave irradiated **BE-HPB-PIM** is inferred from boronated macrocycle or interlocked cage by-products.²⁶³ The **BE-HPB-PIM** from Dean-Stark shows a weight loss at 319 °C, which could not be matched with any weight loss for the monomers but probably the boronated macrocycle by-products. Another weight loss at 481 °C is not considered as the HPB-bis-catechol but boronated cage impurities because there was no clear O–H stretching observed in its FT-IR. The T_{max} of microwave irradiated **BE-SBF-PIM** lies at 393 °C corresponding to the SBF-bis-catechol monomer. Decomposition of **BE-SBF-PIM** is believed to occur at a higher

temperature of 572 °C, which appears in both **BE-SBF-PIM**. Except for the decomposition and a 5% weight loss at 189 °C caused by a tiny amount of benzene-diboronic acid, no more weight loss was found in the **BE-SBF-PIM** from Dean-Stark. It also shows higher T_d and carbon yield, indicating better thermal properties than the microwave irradiated **BE-SBF-PIM**. On the TGA curve of microwave irradiated **BE-SBF-Me-PIM**, several weight losses in the range of 282–466 °C overlap with each other making for a tough assignment. They are inferred to be a mixture of unreacted monomers, oligomers and boronated macrocycles. The weight loss of the **BE-SBF-Me-PIM** from Dean-Stark at 140 °C was considered to be leftover solvents rather than unreacted monomer, because no clear peak of O–H was found in its FT-IR spectrum. Another weight loss at 553 °C is indicated to be a small amount of boroxine, because a clearly weak peak at 736 cm^{-1} was observed in its FT-IR spectrum, which is highly suspected to be boroxine. Both **BE-SBF-Me-PIMs** show the same weight loss at 681 °C, which was believed as the T_d .

To sum up, both **BE-bis-K-PIMs** are mixed with the boronic ester, monomers and impurities. The microwave irradiated product showed a slightly higher purity. Both **BE-HPB-PIMs** and both **BE-SBF-Me-PIMs** are made up of boronic ester and by-products. The **BE-SBF-PIM** from Dean-Stark seemed to be mainly the desired boronic ester, due to its little unreacted monomers and impurities, that can be used for gas adsorption and desorption.

To summarize all FT-IR and TGA results of **BE-bis-K-PIMs**, **BE-HPB-PIMs**, **BE-SBF-PIMs** and **BE-SBF-Me-PIMs**, only the **BE-SBF-PIM** held a significantly higher level of dehydration when prepared by Dean-Stark system rather than via microwave irradiation. Properties of the other three pairs require further judgment by SA_{BET} (details of the measurements are discussed in the part of gas adsorption-desorption below). Higher porosity indirectly indicates that molecular chains with microporous structures are more fully polymerised by monomers. On the contrary, if the product contains more oligomers, short chain or cyclic macromolecule impurities, it will show lower porosity. As shown in **Table 2.9**, **BE-SBF-Me-PIM** prepared in Dean-Stark provided significantly higher SA_{BET} than the microwave irradiated one. For **BE-HPB-PIMs**, Dean-Stark offered the slightly high SA_{BET} as well. **BE-bis-K-PIM** is the only one that was synthesized more porous in microwave reactor. Taking into account the data of FT-IR,

TGA and SA_{BET} , microwave irradiated **BE-bis-K-PIM** and all the other BE-PIMs from Dean-Stark were selected to be studied in the next step.

The thermal stability of BE-PIMs was evaluated by the T_d and char yields listed in **Table 2.9**. High decomposition temperature and high char yield are indications of good thermal stability. It was found that **BE-SBF-PIM** and **BE-SBF-Me-PIM** possess the best thermal stabilities, followed by **BE-HPB-PIM**. **BE-SBC-PIM** has the lowest heat resistance. No notable change in thermal stability with B/C ratio was found. The reason could be the B/C ratio differences among products are not large enough.

Table 2.9 Thermal Properties in N_2 and SA_{BET} of BE-PIMs.

Polymer		SA_{BET}^a (m^2/g)	Decomposition Temperature ($^{\circ}C$)				Char Yield (%)
			T_{d5}	T_{d10}	T_{d20}	T_{max}	
BE-SBI-PIM	Dean-Stark	327	213	478	521	533	52
	microwave	-	161	222	461	528	44
BE-SBC-PIM	Dean-Stark	157	360	404	408	410	34
	microwave	-	255	260	283	263	32
BE-bis-K-PIM	Dean-Stark	63	209	364	468	381	58
	microwave	92	332	372	431	380	53
BE-HPB-PIM	Dean-Stark	118	331	455	560	603	59
	microwave	88	387	414	567	601	59
BE-SBF-PIM	Dean-Stark	127	233	496	574	579	61
	microwave	-	384	393	466	393; 572	49
BE-SBF-Me-PIM	Dean-Stark	183	152	456	618	553; 681	66
	microwave	45	299	368	510	282; 682	65

^a SA_{BET} were measured at $CO_2/273$ K.

Porosity was measured by N_2 gas adsorption at 77 K. These six BE-PIMs all showed type II isotherms and low SA_{BET} values below $23 m^2/g$. That may suggest a low content of micropores, or simply that the motion of the chains does not allow the penetration of the probe gas at such a low temperature. To further address this potential issue, CO_2 adsorption of BE-PIMs samples was also conducted. The latter is important in view of the smaller molecular size of CO_2 than N_2 . The results reported in **Table 2.10** show that CO_2 can indeed penetrate better the pores, showing higher BET surface areas.

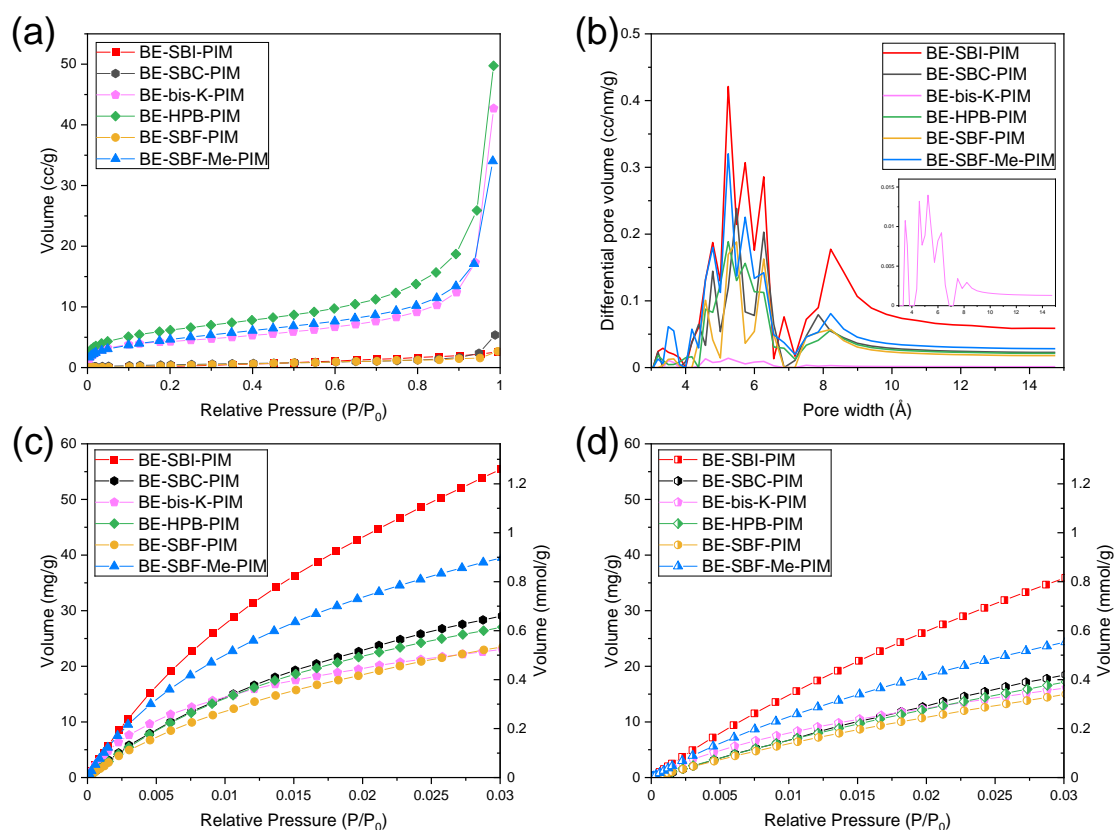


Figure 2.13 (a) N_2 adsorption at 77 K of BE-PIMs (b) PSD of BE-PIMs, calculated from CO_2 adsorption at 273 K by NLDFT, (c) CO_2 adsorption at 273 K of BE-PIMs, (d) CO_2 adsorption at 298 K of BE-PIMs.

High capacity and appropriate Q_{st} are important indicators for evaluating the affinity for CO_2 in adsorbents. We expect the values of Q_{st} are not to exceed 50 kJ/mol, to provide enough interaction between adsorbents and CO_2 to grant high and quick uptakes, but not too high to prevent an easy regeneration.^{61, 266} All these BE-PIMs show good CO_2 uptakes at 273 K and 298 K, especially **BE-SBI-PIM** and **BE-SBF-Me-PIM** (Fig 2.13 c, d and Table 2.10). The Q_{st} values of BE-PIMs listed in Table 2.10 are in the range of 30.5–45.6 kJ/mol, suggesting that the mechanism relies more on physisorption (which is only non-covalent adsorption) of CO_2 in BE-PIMs, rather than chemisorption (where the affinity for the gas is higher).⁶⁰

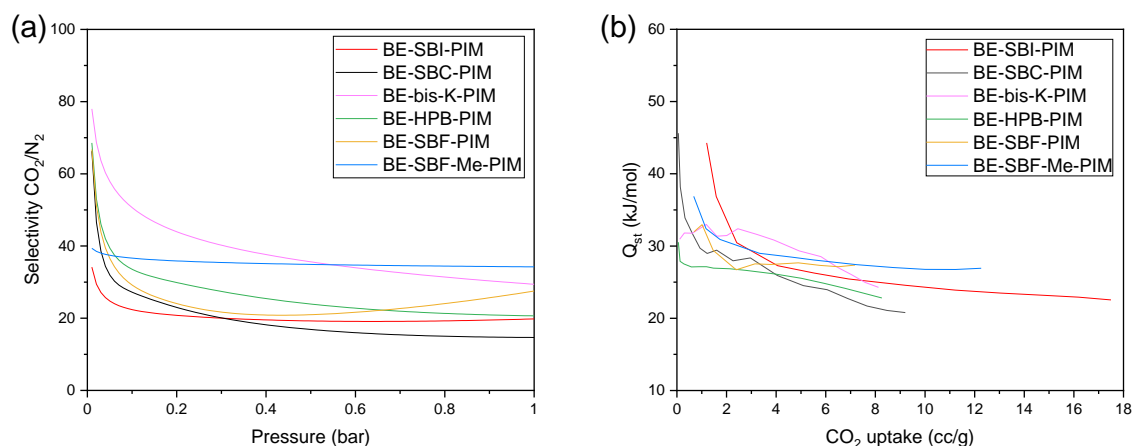


Figure 2.14 (a) IAST CO₂/N₂ selectivity (simulating a 15/85 composition), (b) Q_{st} of BE-PIMs.

To be used as ideal selective adsorption materials, BE-PIMs are expected to preferentially adsorb more CO₂ than N₂. As shown in **Fig 2.13 b**, PSD of BE-PIMs, calculated from CO₂ adsorption isotherms measured at 273 K using NLDFIT theory, shows their micropore sizes are mainly in the 3.5–8 Å region. The small pore sizes should allow the smaller CO₂ (3.3 Å) into their pores, but not the larger N₂ (3.6 Å).²⁶⁷ The CO₂/N₂ selectivity was estimated from the corresponding gas adsorption isotherms measured at 298 K by using the IAST method, and considering a mixture of CO₂ and N₂ (v/v = 15/85), as this is the typical composition of the flue gas coming from the exhausts of power plants²⁶⁸ (where the CO₂ is captured at 298 K and 1 bar, as for our experiments). The data shown in **Table 2.10** demonstrate that **BE-SBI-PIM**, which also has the highest S_{BET}, shows poor selectivity. This is not unexpected, as very porous materials allow for more CO₂ and N₂ to pass through the material, reducing the selectivity between the two gases. Despite the lowest S_{BET}, **BE-bis-K-PIM** holds the second highest value of selectivity because of the largest proportion of pores around 3.5 Å shown in **Fig 2.13 b**. The best selectivity is shown by **BE-SBF-Me-PIM**. That originates from its second largest S_{BET} and an outstanding PSD around 3.5 Å, which is suitable for CO₂ to go through but prevents the passage of N₂.

Table 2.10 Physical Characterization of Polymers and Gas Selectivity

Polymer	SA _{BET} (m ² /g)		Pore volume ^a (cc/g)	CO ₂ adsorption		IAST CO ₂ /N ₂ selectivity ^b	Q _{st} ^c (kJ/mol)
	N ₂ / 77 K	CO ₂ / 273 K		273 K (1 bar) (mg/g) (mmol/g)	298 K (1 bar) (mg/g) (mmol/g)		
BE-SBI-PIM	1	327	0.060	55 (1.25)	36 (0.82)	20	44.3
BE-SBC-PIM	2	157	0.031	29 (0.66)	18 (0.41)	15	45.6
BE-bis-K-PIM	15	92	0.025	23 (0.52)	16 (0.36)	29	30.9
BE-HPB-PIM	22	133	0.029	27 (0.61)	17 (0.39)	21	30.5
BE-SBF-PIM	13	127	0.025	24 (0.55)	15 (0.34)	28	32.0
BE-SBF-Me-PIM	17	183	0.043	40 (0.91)	24 (0.55)	34	36.9

^aAt P/P₀ ~ 0.98. ^bCalculated according to IAST at 298 K and 1 bar.^{269, 270} ^cQ_{st} (in kJ/mol) of corresponding gas at zero coverage calculated from isotherms collected at 273 K and 298 K and fitted with the Langmuir–Freundlich equation and calculated via the Clausius Clapeyron equation.

Summarizing the above results, **BE-SBF-Me-PIM** showed the best comprehensive properties in terms of thermal stability, CO₂ adsorption and CO₂/N₂ selectivity. **BE-SBF-PIM** showed excellent thermal properties and good CO₂ selectivity. **BE-bis-K-PIM** is considered to have the greatest potential because it exhibits the second highest gas selectivity and moderate thermal stability, even though, based on a low level of purity, most probably consisted only of oligomers due to inadequate dehydration. It is expected to achieve better thermal properties and porosity by optimizing the conditions of dehydration in the future.

2.3 Conclusion

The feasibility of boroxine-based PIMs was confirmed by the preparation of the model boroxine on two methods. Microwave irradiation contributed to more efficient dehydration than sand bath. The microwave irradiated model boroxine exhibited ideal microporosity and thermal decomposition behavior consistent with the mechanism of boron-based FRs. A bromo-SBF precursor and a TPB-boronic acid monomer have been synthesized. The repeatability of lithium-halogen exchange reactions and the purity of afforded products require improvement in future work.

Two different heating methods, microwave irradiation and reflux with a Dean-Stark apparatus, were used to prepare six novel BE-PIMs. Except for **BE-bis-K-PIM**, purer products for the other five were obtained with the Dean-Stark system. Characterization and analysis of their thermostability and CO₂ adsorption and selectivity were conducted respectively. It can be concluded that **BE-SBF-Me-PIM** showed the best comprehensive properties, followed by **BE-SBF-PIM**.

Compared to the reported works in **Tables 1.2** and **1.3**, our BE-PIMs show slightly lower thermal properties, porosity, and CO₂ adsorption, that probably be attributed to their unsatisfactory polymerisation degrees. Nevertheless, BE-PIMs still exhibit similar or slightly higher levels of CO₂/N₂ selectivity, which is related to their significantly higher Q_{st} values.

Chapter 3 – Novel Nitrogen-containing PIMs for Flame Retardation and Gas Separation

3.1 Introduction

Nitrogen-containing PIMs are considered as potentially good materials in the fields of flame retardancy and CO₂ adsorption and selectivity. On the one hand, the introduction of nitrogen has been proven to enhance the flame retardancy of the materials (see **1.2.3.4** in Chapter 1), and the interaction between nitrogen atoms and CO₂ molecules can also achieve high CO₂ selectivity.^{271, 272} On the other hand, abundant amounts of micropores in PIMs provide a large specific surface area for gas adsorption, and are expected to block the transfer of heat and mass in combustion. In general, PIMs are also rather well-known for their thermal stability (as shown in **Table 1.2** and relevant contents in Chapter 1).

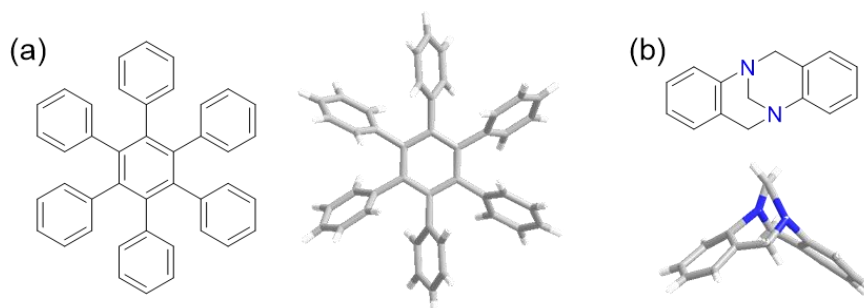


Figure 3.1 Structures and conformation of (a) HPB and (b) TB.

Hexaphenylbenzene (HPB)-based monomers were selected in this work. HPB contains six single covalent bonds around the central benzene ring, which hinders their rotation,²⁷³ and add contortion in the final polymer chains.²⁷⁴ Previous work on HPB-based PIMs also show great thermal properties even though they were not designed as heat-resistant materials (as shown in **Table 1.2** and related discussion). In this work, we decided to make HPB monomers and polymerise them via the formation of Tröger's Base (TB) units. The latter has a rigid V-shaped conformation¹¹⁵ that contributes to the rigidity and contortion of PIMs⁷⁵ and also introduce two bridged nitrogen atoms into the repeat unit.

As shown in **Fig 3.2**, it is possible to synthesize a series of TB-HPB-PIMs with different C/N ratios (hence, with different thermal properties) and porosity, simply by changing the design of the type and number of functional groups. Three “linear” TB polymers were also prepared to explore the influence of porosity on thermostability and gas capture. It is noticed that they are not completely linear due to the nonplanar conformations of TB units, but we can say that they are much more linear than TB-HPB-PIMs.

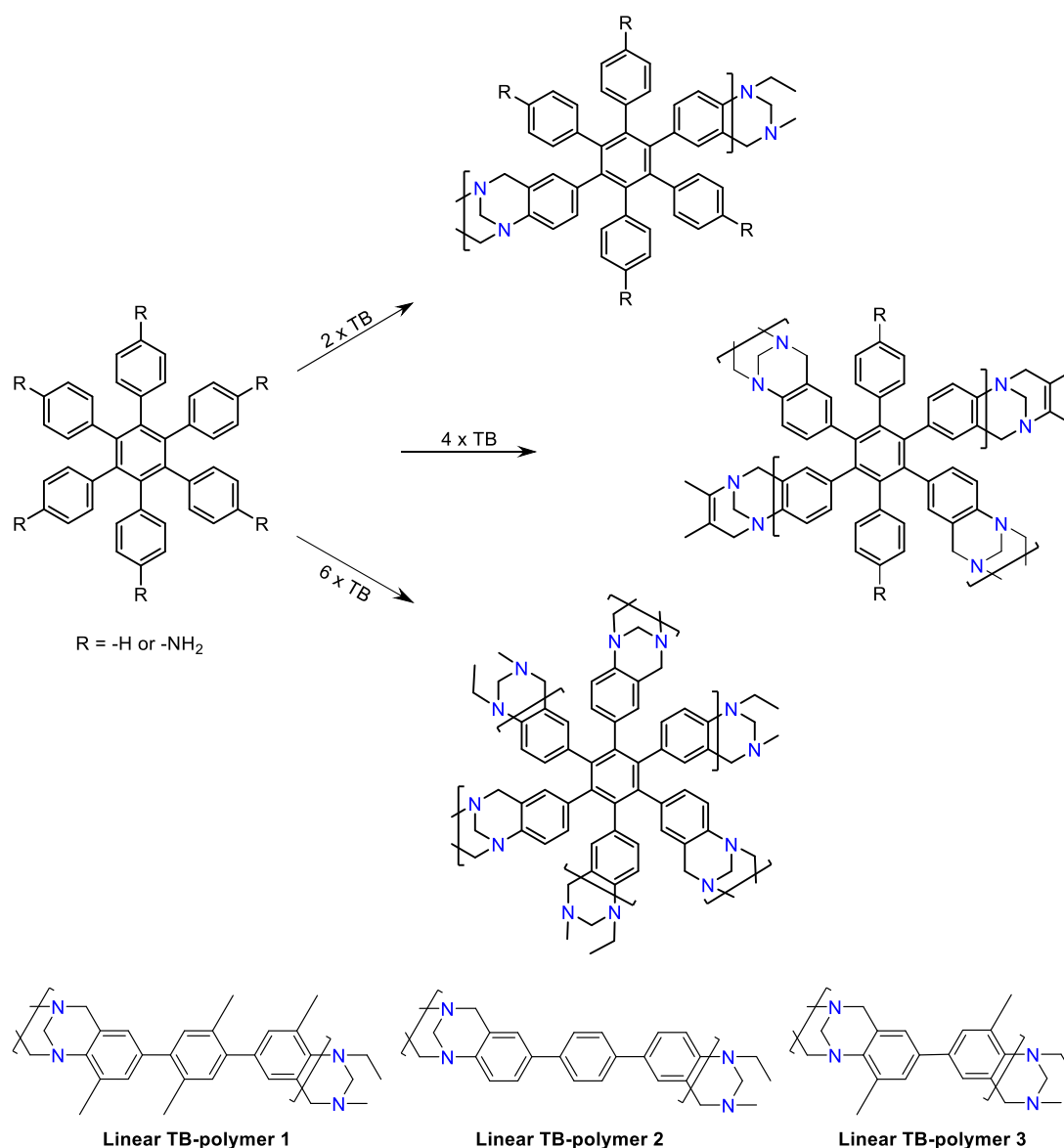
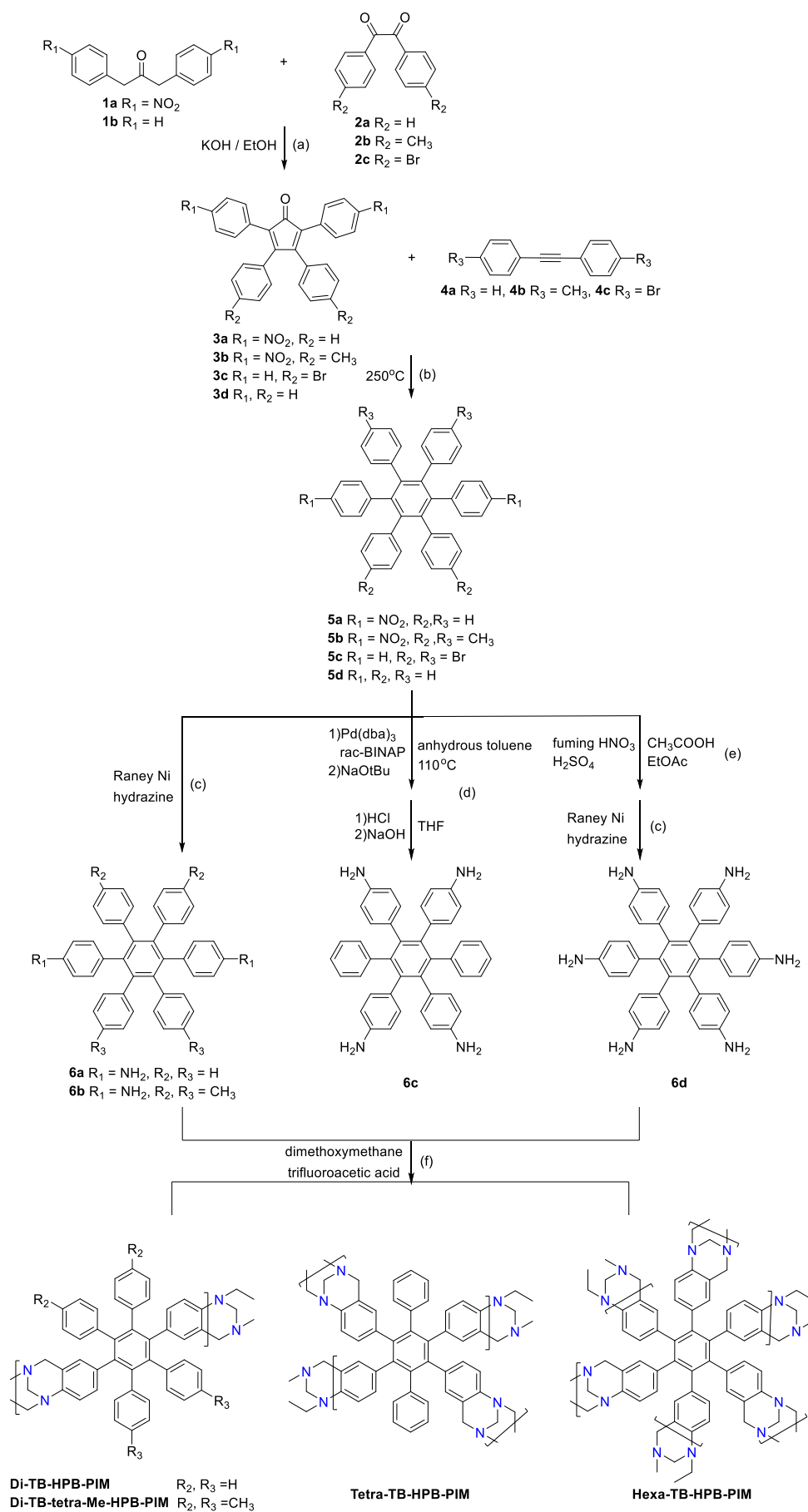


Figure 3.2 TB-HPB-PIMs and “linear” TB-polymers.

The general route for preparing TB-HPB-PIMs is shown in **Scheme 3.1**. All the HPB precursors were obtained on the similar method. Di-, tetra- and hexa-amino HPB monomers were subsequently synthesized in different ways and polymerised into the final TB-HPB-PIMs on similar conditions, which will be described later in the chapter.

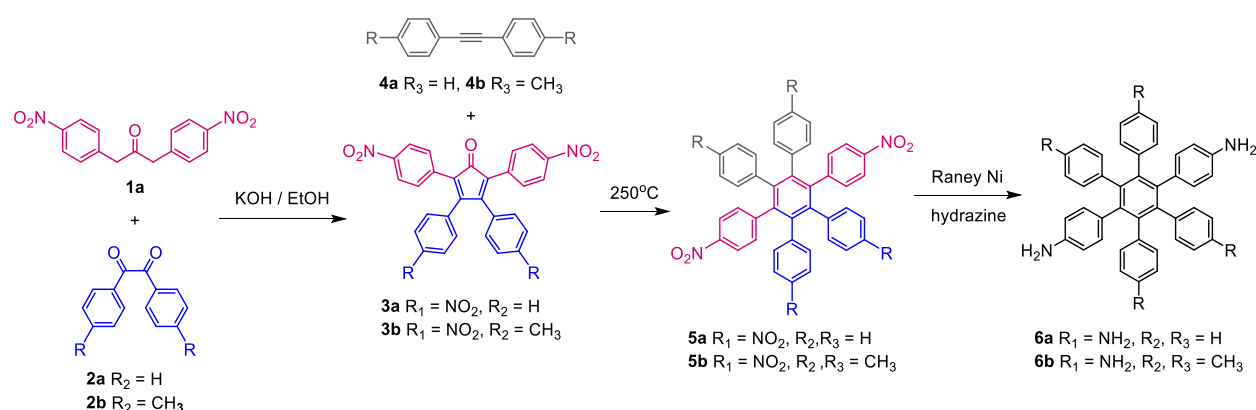


Scheme 3.1 Route for preparing TB-HPB-PIMs.

3.2 Results and Discussion

3.2.1 Diamino-HPB Monomers

According to the designed experiment, amino-HPB monomers are obtained in three steps. Firstly, the preparation of substituted nitrated cyclopentadienones (CPD) was conducted by double aldol condensation reactions with diphenylacetone and benzil (**Scheme 3.1 a**). Next, a Diels-Alder reaction between CPDs and diphenylacetylenes produced the desired nitro-HPB precursors (**Scheme 3.1 b**), which were then reduced to amino-HPB monomers (**Scheme 3.1 c**).



Scheme 3.2 Route for preparing diamino-HPB monomers.

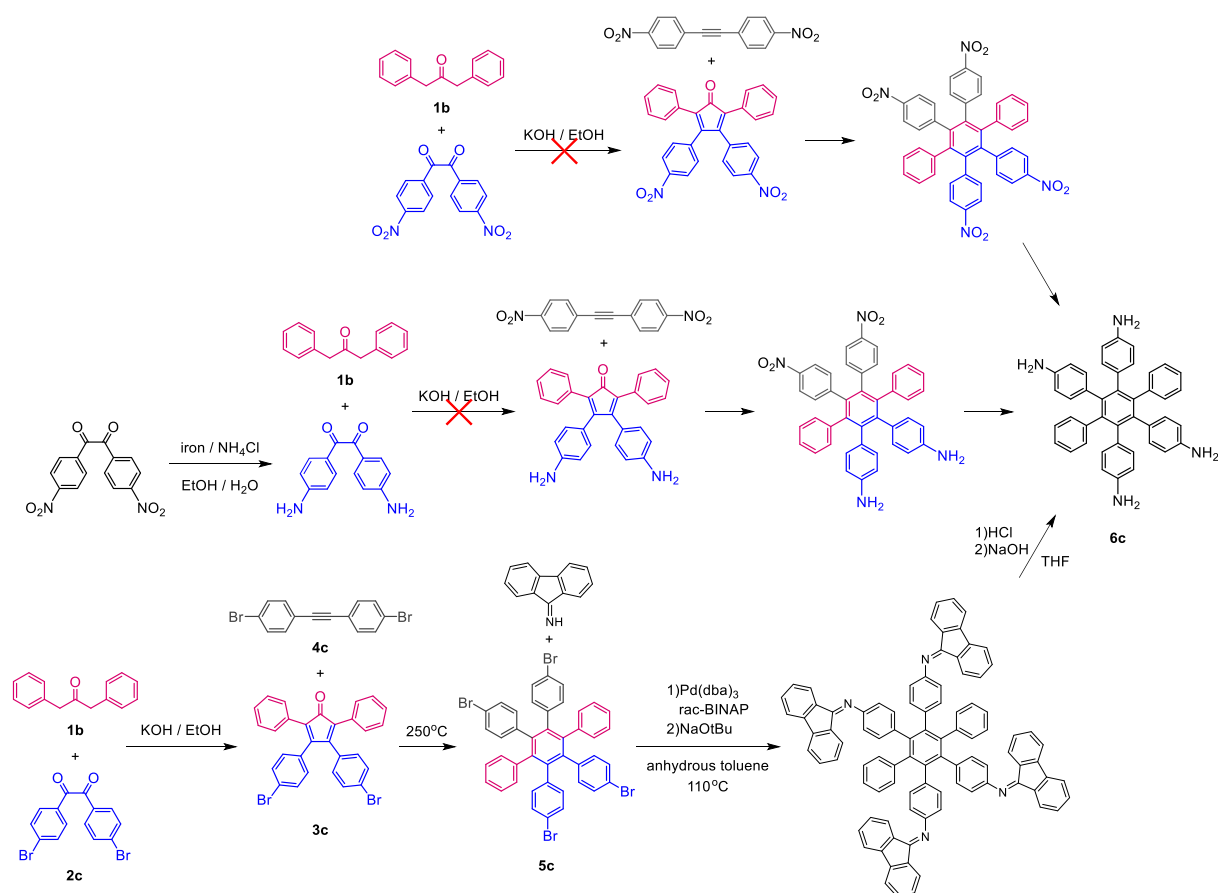
More in details, the synthesis started with HPB-based monomers with two substituents at the pseudo “*para*” position (**Scheme 3.2**). The precursor **1a**, made from 4-nitrophenyl acetic acid, is the key compound for the next steps, because it introduces substituents in the “*para*” position of HPB core. This reaction proceeded according to the published procedure¹⁰³ and gave a good yield of 70%.

Double aldol condensation reactions to synthesize CPDs were carried out as the next step. In the first attempt to prepare **3a**, precursor **1a** and benzil were refluxed in a solution of KOH in ethanol for 1 hour,¹⁰³ giving a purple-black crude product which was purified by silica gel column chromatography to afford **3a** with only a 15% yield. It is suspected that this reaction time was not left for long enough. The reaction was then repeated and was tracked with TLC every 15 minutes. The optimal reaction time was proven to be 2 hours to achieve a satisfactory yield of 67%. NMR spectroscopy confirmed the structure and the purity of the desired product, which was washed with water and ethanol ready to react in the next step. **3b** was synthesized by the same procedure as **3a** yielding 52% of pure product.

HPB structures were obtained in the third step through a Diels Alder reaction. **3a** and **4a** were homogeneously mixed in a hydrothermal synthesis reactor and heated in the oven at 250 °C. After cooling down, the crude product was washed with cold MeOH and warm hexane in turn to afford the product of **5a** with a good yield of 84%. **5b** was synthesized by the same procedure giving 68% of yield.

Diamino-HPB monomers were obtained after the reduction of the correspondent nitro-HPB precursors. **5a** was hydrogenated refluxing it with hydrazine catalysed by Raney Nickel and under N₂ atmosphere, following the published procedure,²⁷⁵ and giving 51% of **6a**. **5b** was reacted in the same way as **5a**, but silica gel column chromatography was required to purify the raw product to afford pure **6b**.

3.2.2 Tetraamino-HPB Monomer



Scheme 3.3 Routes for preparing tetraamino-HPB monomer.

It was planned to prepare tetraamino-HPB via the same route as the synthesis of diamino-HPB (route 1 in **Scheme 3.3**). However, the reaction to obtain dinitro-CPD never achieved a solid product with the expected characteristics after filtration. The mix of the two reagents provided an orange solution which immediately turned to dark

blue when adding KOH. The reaction was then heated and gradually became red within 20 minutes and then turned back to orange in 30 minutes, proving to be significantly different from the previous reactions. The progress was monitored by TLC every 20 minutes, and samples were taken every hour for ^1H NMR. The characterisation of the crude product showed that in all instances we obtained mixtures of two reagents and small amounts of unknown impurities (**Table 3.1**).

Table 3.1 Attempted Conditions for Preparing Dinitro-CPD.

1b	4,4'-Dinitrobenzil	KOH in ethanol [1% w/w]	Conditions	Work-up	Product
19.8 mmol (1 eq.)	19.8 mmol (1 eq.)	9.9 mmol (0.5 eq.)	78 °C for 3 hrs	Filtration	Starting material
0.8 mmol (1 eq.)	0.8 mmol (1 eq.)	0.6 mmol (0.75 eq.)	78 °C for 3 hrs	Filtration	Starting material
4.3 mmol (1 eq.)	4.46 mmol (1.05 eq.)	3.19 mmol (0.75 eq.)	78 °C for 4 hrs	Filtration	Starting material
1.0 mmol (1 eq.)	1.0 mmol (1 eq.)	1.0 mmol (1 eq.)	78 °C for 4 hrs molecular sieves	Filtration	Starting material
1.0 mmol (1 eq.)	1.0 mmol (1 eq.)	2.0 mmol [20% w/w] (2 eq.)	90 °C for 2 min 0 °C for 7 min	Cold filtration	Starting material
1.0 mmol (1 eq.)	1.0 mmol (1 eq.)	2.0 mmol [20% w/w] (2 eq.)	78 °C for 5 hrs	Poured into icy water, extracted by DCM	Starting material

Considering that the nitro act as electron-withdrawing group and the amino is, on the contrary, electron-donating, we thought that reactions that are not efficient for nitro groups may be effective for amino groups instead. Therefore, the synthetic route was adjusted to route 2 in **Scheme 3.3**. Diaminobenzil was first reduced from dinitrobenzil, and then synthesized with **1b** to form diamino-CPD. However, the synthesis of diamino-CPD, trailed by TLC and NMR, also failed to give any solid product. The final outcome of the reaction was verified by TLC to be a mixture of three main compounds and several trace compounds, which was evaporated and separated by silica gel column chromatography twice. One compound was proven to be diaminobenzil by NMR and consisted of around 70% of the crude product. The other two impurities could not be identified by NMR and accounted for 12% each.

Table 3.2 Attempted Conditions for Preparing Diamino-CPD.

1b	4,4'-Diaminobenzil	KOH in ethanol [1% w/w]	Conditions	Work-up	Product
0.6 mmol (1 eq.)	0.6 mmol (1 eq.)	0.6 mmol (1 eq.)	78 °C for 4 days	Cold filtration	Starting material
1.0 mmol (1 eq.)	1.0 mmol (1 eq.)	2.0 mmol (2 eq.)	78 °C for 20 hrs	Poured into icy water, extracted by ethyl acetate	Starting material

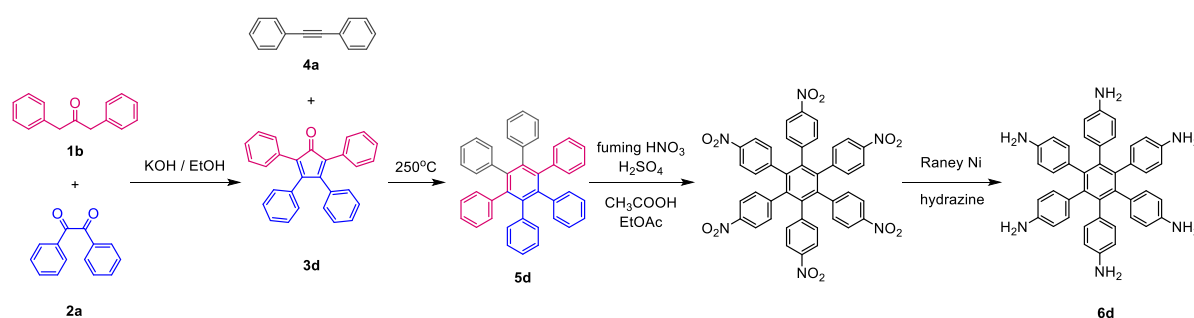
The successful synthesis of the tetra-amino HPB was achieved following the plan proposed as route 3. *N*-diphenylmethylene substituted HPB intermediate synthesized from tetrabromo-HPB was used to prepare the tetraamino-HPB monomer. Firstly, tetrabromo-HPB was successfully synthesized as shown in **Scheme 3.1 a** and **b**. Preparation of the *N*-diphenylmethylene substituted intermediate was then attempted referring to published procedures.²⁷⁶ Pd(dba)₃ and rac-BINAP were heated in anhydrous toluene under nitrogen atmosphere. A solution of tetrabromo-HPB, NaOtBu and benzophenone imine in anhydrous toluene was then added to the system and heated at 110 °C. The crude product was purified by silica gel column chromatography to obtain the target intermediate compound. We tried to improve the reaction doubling the amount of rac-BINAP and Pd(dba)₃, but the yield was only slightly increased from 39–41% to 47% (**Table 3.3**). This intermediate reacted with HCl to give the corresponding hydrochloride salt, which was neutralized with NaOH to afford the final tetraamino-HPB monomer (**Scheme 3.1 d**).

Table 3.3 Attempted Conditions for Preparing *N*-diphenylmethylene substituted HPB.

Pd(dba) ₃	rac-BINAP	Anhydrous toluene	Ph ₂ C=NH	Br ₄ -HPB	NaOtBu	Conditions	Yield
0.5 mmol (0.25 eq.)	1.0 mmol (0.5 eq.)	50 mL	10.4 mmol (5.2 eq.)	2.0 mmol (1.0 eq.)	10.4 mmol (5.2 eq.)	110 °C for 24 hrs N ₂	41%
0.5 mmol (0.25 eq.)	1.0 mmol (0.5 eq.)	50 mL	10.4 mmol (5.2 eq.)	2.0 mmol (1.0 eq.)	10.4 mmol (5.2 eq.)	110 °C for 24 hrs N ₂	39%
2.4 mmol (0.5 eq.)	4.8 mmol (1 eq.)	116 mL	25.0 mmol (5.2 eq.)	4.8 mmol (1 eq.)	25.0 mmol (5.2 eq.)	110 °C for 24 hrs N ₂	45%
3.1 mmol (0.5 eq.)	6.2 mmol (1 eq.)	150 mL	32.1 mmol (5.2 eq.)	6.2 mmol (1 eq.)	32.1 mmol (5.2 eq.)	110 °C for 24 hrs N ₂	47%

3.2.3 Hexaamino-HPB Monomer

5d was synthesized following **Scheme 3.1 a** and **b**, and then nitrated to hexanitro-HPB intermediate with fuming HNO_3 and H_2SO_4 .²⁷⁷ The hexa-substituted monomer **6d** was obtained from the nitrified intermediate by a reduction reaction as **Scheme 3.1 c**, using hydrazine catalysed by Raney Nickel. All the reactions for synthesizing the four amino-HPB monomers were repeated more than three times to ensure their good repeatability, and to obtain enough monomers for polymerisation.



Scheme 3.4 Route for preparing hexaamino-HPB monomer.

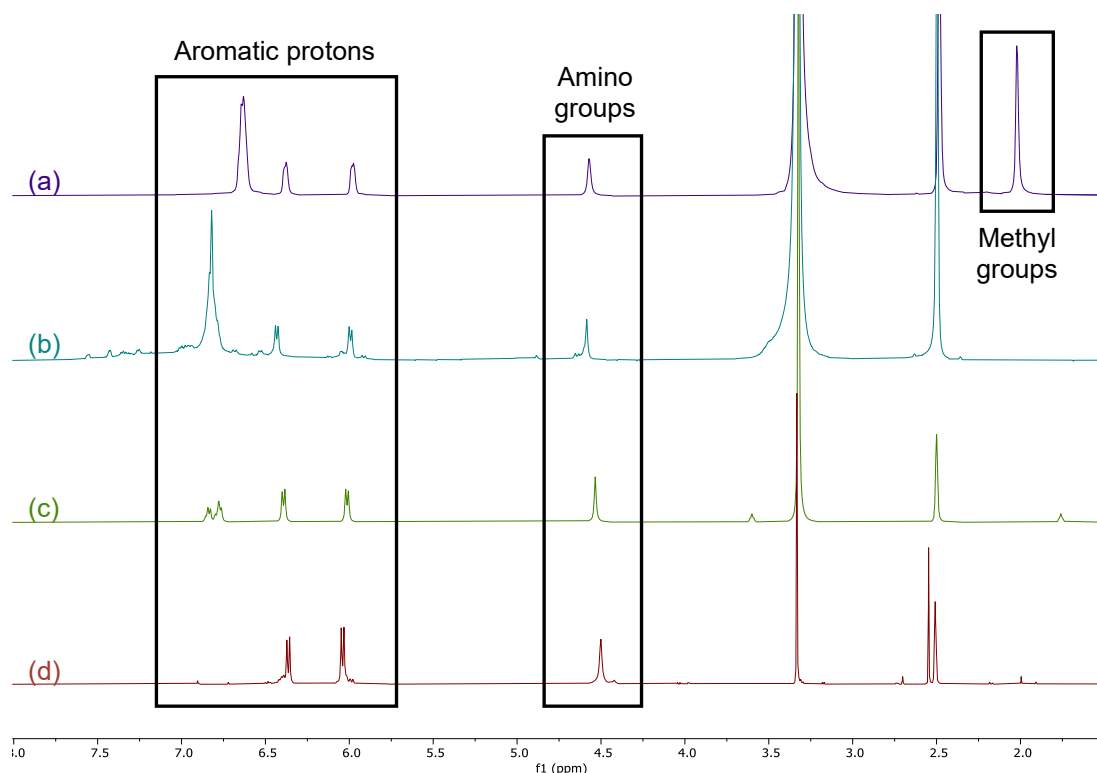


Figure 3.3 ^1H NMR of diamino-HPB monomers: (a) diamino-tetra-Me-HPB (**6a**), (b) diamino-HPB (**6b**), (c) tetraamino-HPB (**6c**), (d) hexaamino-HPB (**6d**).

The structures of all the amino-HPB monomers were confirmed by ^1H NMR (in deuterated dimethylsulfoxide (DMSO)). As shown in **Fig 3.3**, the peaks of aromatic

protons were distributed over the range of 7.0–6.0 ppm. The peaks of protons in amino groups were located around 4.5 ppm, while the peak of methyl groups in **6b** was found as a singlet centred at 2.01 ppm.

3.2.4 TB-based Polymers

The synthesis of TB-PIMs was achieved following published procedures with slight modifications (**Scheme 3.1 f**).¹⁵⁰ The solution of each amino-HPB monomer in dichloromethane (DCM) was placed in an ice bath to cool down to 0 °C. An appropriate amount of trifluoroacetic acid (acted as both acid and solvent) was added dropwise over 20 minutes. (see experimental part for more details) The reaction gradually became viscous during this process. A small amount of DCM was added to reduce the viscosity to allow sufficient stirring. Then, the reaction was warmed up to room temperature and stirred for 2–4 days. The jelly-like reaction was quenched into a mixture of ice and ammonia under vigorous stirring, and the product collected by filtration as a brown powder. In order to remove small molecule impurities and short soluble oligomers, the typical way for PIMs involves the reflux of the polymer powder in a sequence of acetone, tetrahydrofuran (THF), DCM and MeOH, until the liquid phase becomes colorless. Finally, the product was filtered off and fully dried at 80 °C under vacuum, to eliminate solvent molecules from the micropores.

Three “linear” TB-polymers were also polymerised with the same method as TB-HPB-PIMs from the relevant diamino-monomers, which were synthesized following literature procedures¹⁵⁰ or used as received from commercial compounds. All the details are shown in the experimental section.

Any solution-based technology is not suitable for characterizing these TB-HPB-PIMs, because they are insoluble in any organic solvents. Therefore, solid state ¹³C NMR (SSNMR) was used for the characterization of their molecular structures. According to the results in **Fig 3.4** and **Fig 3.5**, four TB-HPB-PIMs and three linear TB-polymers were successfully prepared. The peaks of aromatic carbons were distributed in the range of 150–100 ppm. The signature peaks of TB were found between 70–50 ppm, while the carbon peak coming from methyl groups of di-TB-tetra-Me-HPB was located at 21 ppm, and that of linear TB-polymer 1 and 3 lie at around 15 ppm.

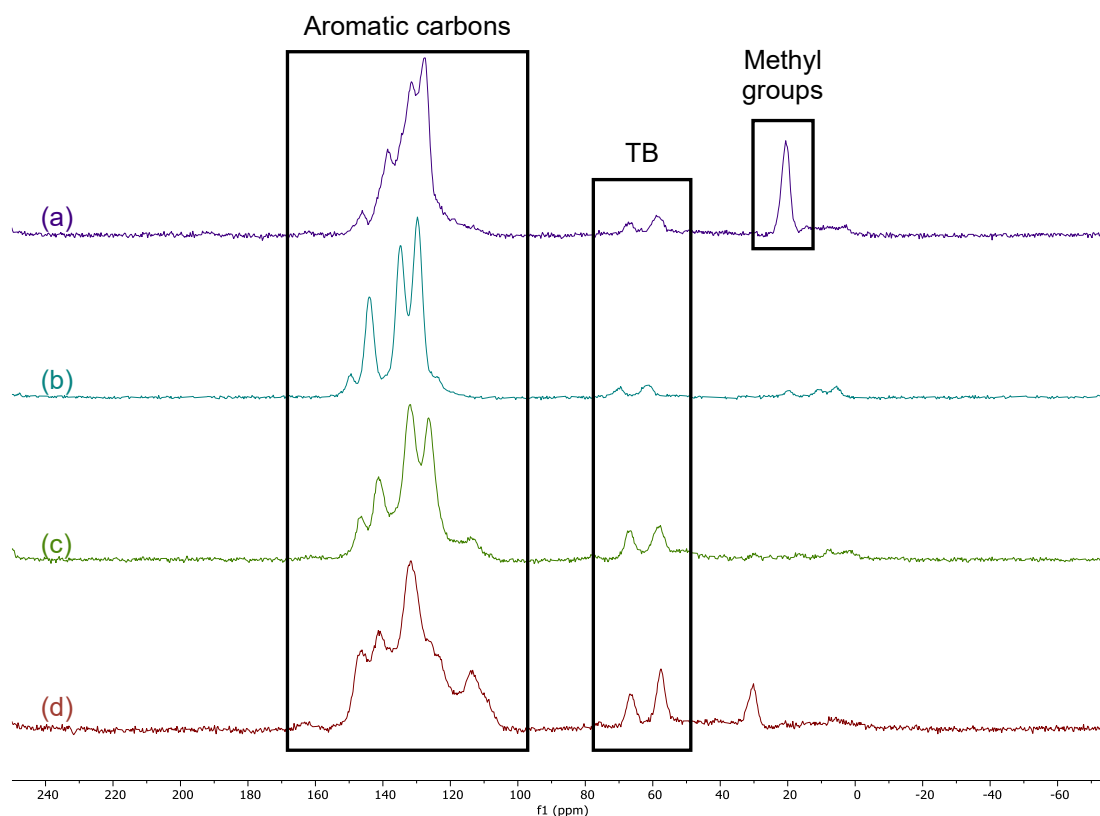


Figure 3.4 SSNMR of TB-HPB-PIMs: (a) di-TB-tetra-Me-HPB, (b) di-TB-HPB, (c) tetra-TB-HPB, (d) hexa-TB-HPB.

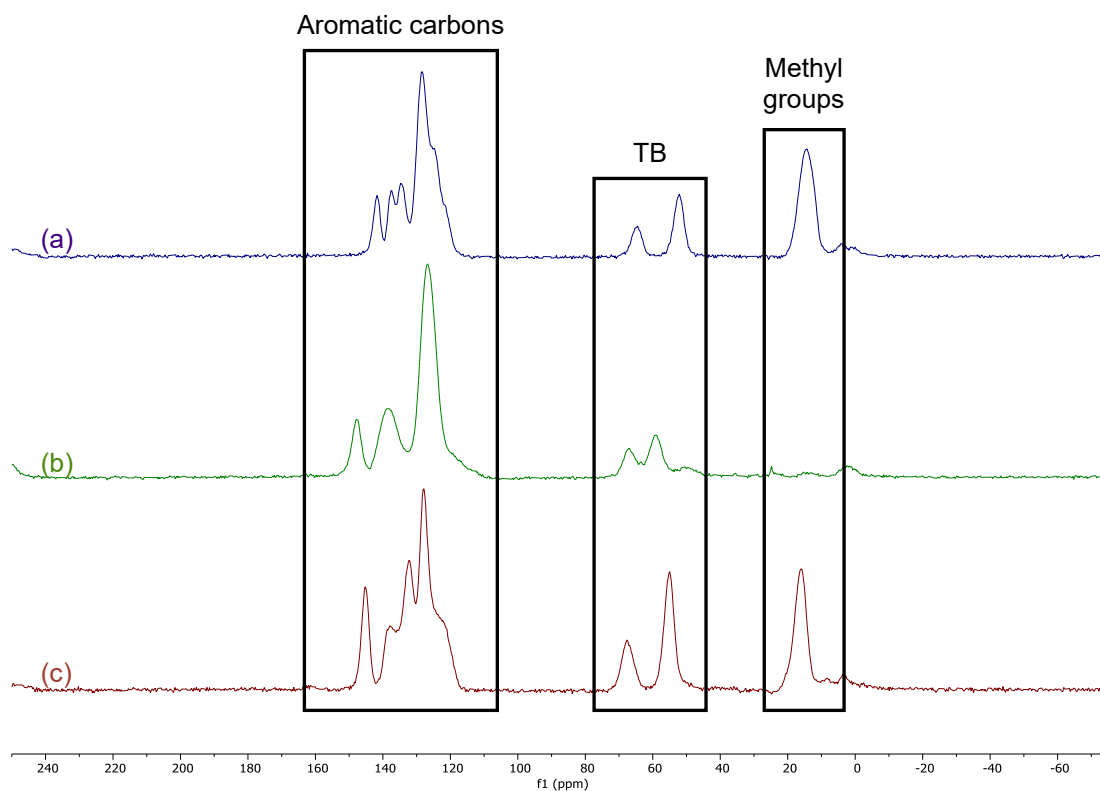


Figure 3.5 SSNMR of linear-TB-polymers: (a) linear TB-polymer 1, (b) linear TB-polymer 2, (c) linear TB-polymer 3.

Although, because of the scarce solubility of these polymers, the molecular weights of TB-HPB-PIMs cannot be measured by GPC, a satisfactory molecular weight of TB-HPB-PIMs chains could be deduced by their high yields (83–94%), and no obviously unreacted amino groups were detected by FT-IR spectra. In fact, as shown in **Fig 3.6**, the peaks of amino groups in the spectra of amino-HPB monomers were observed from 3380 to 3348 cm^{-1} , which disappeared in their relevant TB-HPB-PIMs. This suggests that amino groups have adequately been consumed to form the TB units.

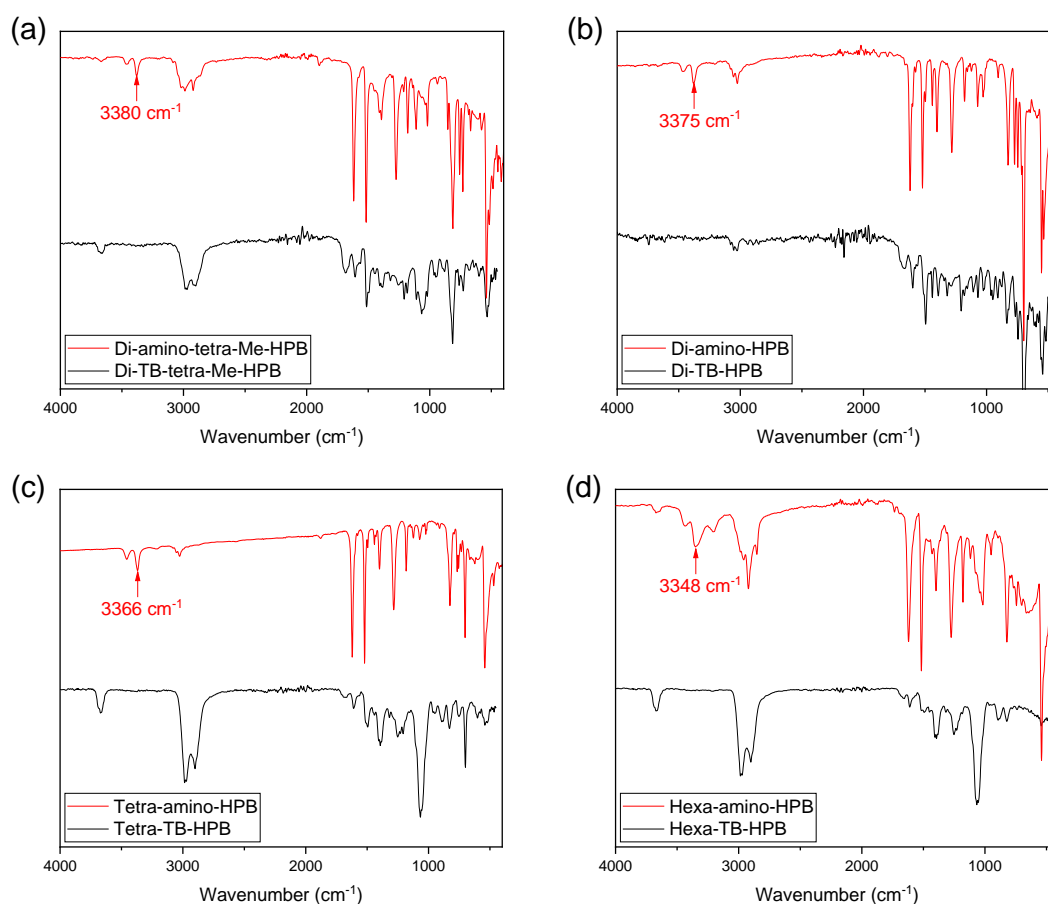


Figure 3.6 FT-IR of amino-HPB monomers and TB-HPB-PIMs.

3.2.4.1 Morphology

The difference in molecular structures can be reflected by their morphology, as characterized by scanning electron microscopy (SEM) shown in **Fig 3.7**. It is observed that di-TB-tetra-Me-HPB holds abundant pores throughout both its surface and interior. The pore sizes distribute very broadly, and the largest one can even exceed 10 μm . By contrast, the surface of di-TB-HPB is much smoother, showing only mild wrinkles and clumps. Its interior seems stacked with irregular layers. It is speculated that the

methyl groups in di-TB-tetra-Me-HPB lead to a looser packing among polymer chains. Whereas no substituent is on the di-TB-HPB chains, which are then able to be packed much better. It must be considered that the two di-TB-HPB-PIMs are supposed to be non-network despite the lack of solubility. That changes the overall morphology compared to the two networked PIMs coming from the tetra and hexa-amino HPBs. In fact, the tetra- and hexa-TB-HPB, showing similar aggregation in tiny irregular particles both on the surface and inside. Such morphology is deduced to result from an inability to neatly pack macromolecular chains due to their contorted conformation.

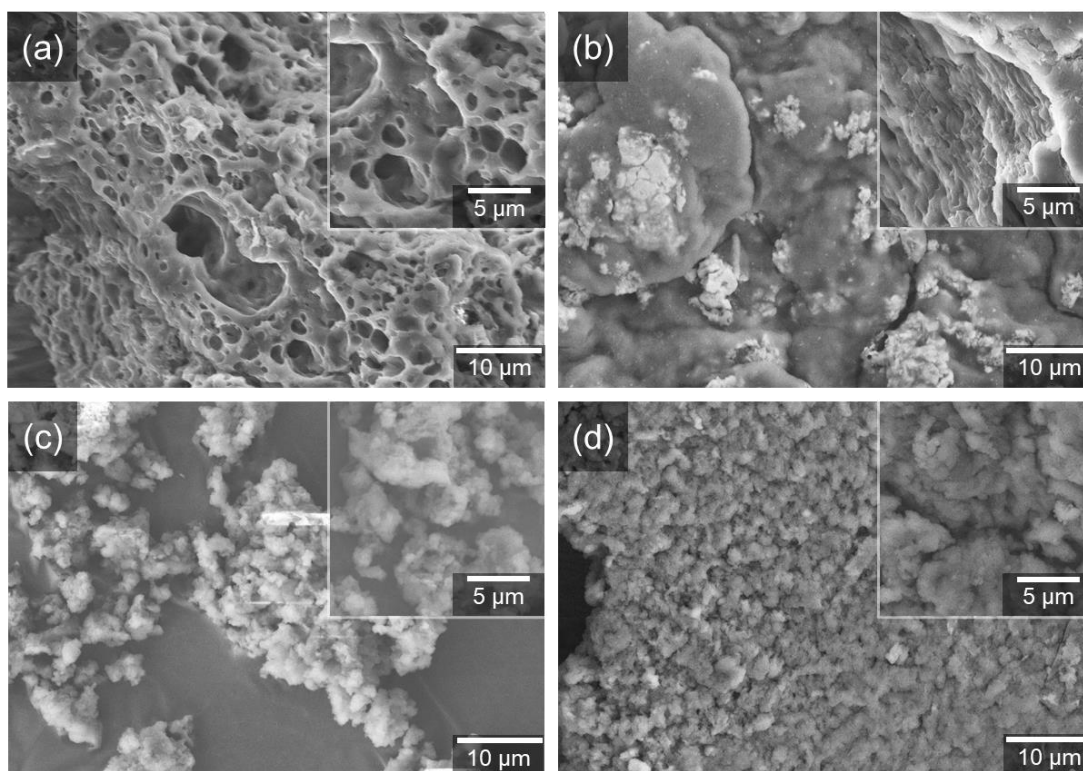


Figure 3.7 SEM of TB-HPB-PIMs: (a) di-TB-tetra-Me-HPB, (b) di-TB-HPB, (c) tetra-TB-HPB, (d) hexa-TB-HPB.

Fig 3.8 shows the SEM images of “linear” TB polymers. TB-polymer 1 exhibits a relatively flat surface with shallow holes and cracks. Its interior is filled with pores, of which the pore sizes are approximately 1–2 μm . The surface of linear TB-polymer 2 possesses the smoothest surface. Only slight wrinkles but no pores can be observed after magnification. The surface of linear TB-polymer 3 is covered with wrinkles, and the interior is rich in pores. These pore sizes are larger than that in linear TB-polymer 1, about 2–5 μm . Being ladder and soluble in common organic solvents such as chloroform and DCM, all linear TB polymers all exhibit a “smoother” morphology, and they look more similar to the correspondent ladder TB-PIM than the networked ones.

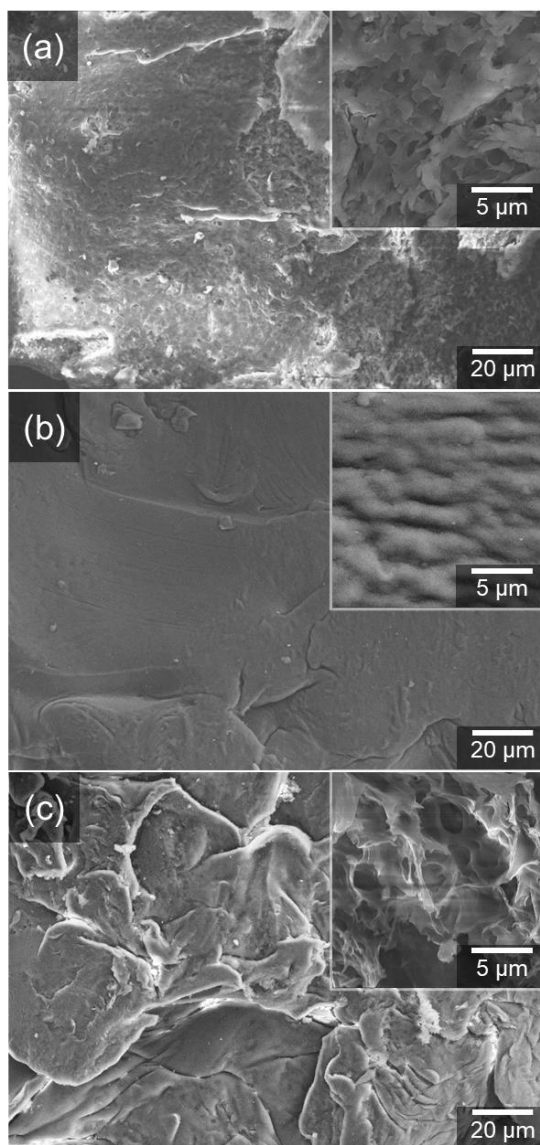


Figure 3.8 SEM of linear TB-polymers: (a) linear TB-polymer 1, (b) linear TB-polymer 2, (c) linear TB-polymer 3.

3.2.4.2 Thermal Properties

Thermal properties of TB-HPB-PIMs were evaluated by TGA analysis respectively under N_2 and air (which is 21% \pm 0.5% O_2 in N_2) atmosphere. TGA in N_2 of the four TB-HPB-PIMs show similar behaviours of mass loss (**Fig 3.9**). The weight losses below 355 $^{\circ}C$, counted as less than 5%, refer to the loss of trapped solvent. The weight losses at 400–450 $^{\circ}C$ were caused by destruction of TB units.²⁷⁸ The decomposition of main chains led to their T_{max} located in the range of 572–591 $^{\circ}C$. Similarly, three linear TB-polymers showed two weight losses respectively around 430 $^{\circ}C$ and 590 $^{\circ}C$.

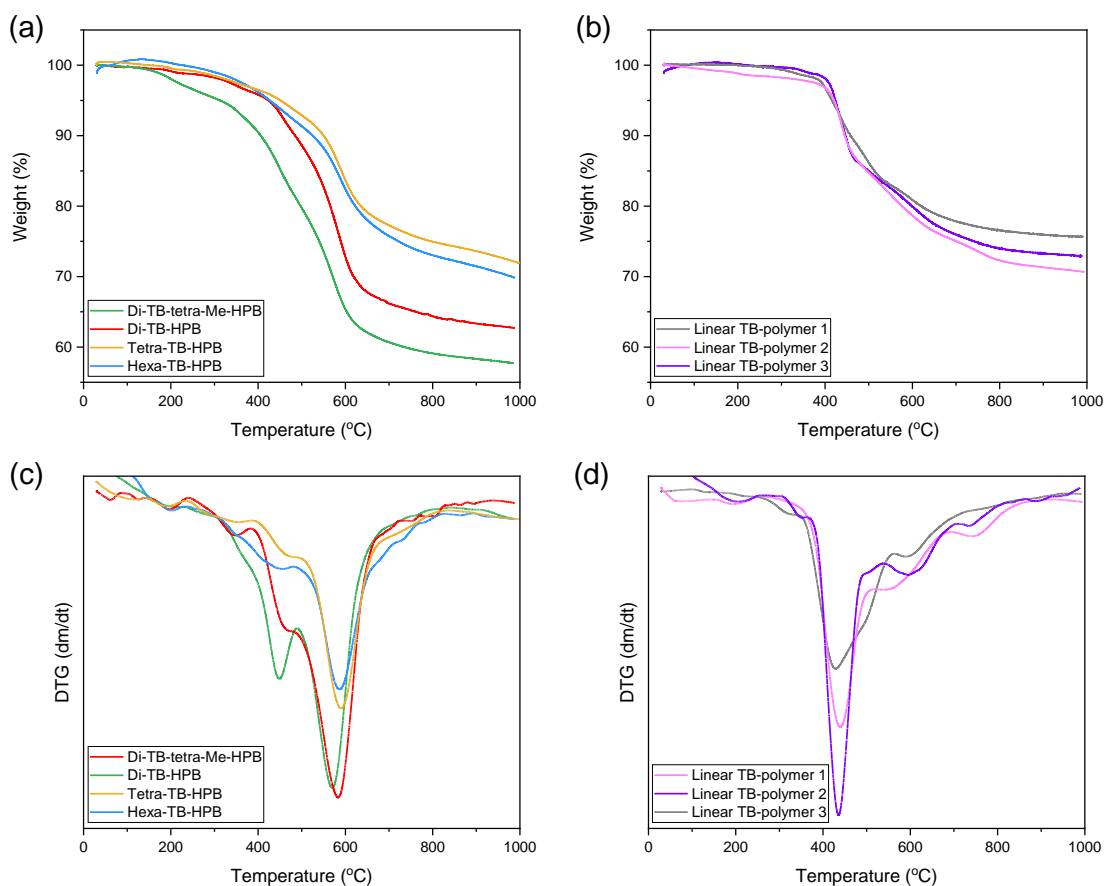


Figure 3.9 TGA analysis under N₂ atmosphere: (a) TGA of TB-HPB-PIMs, (b) TGA of linear TB-polymers, (c) DTG of TB-HPB-PIMs, (d) DTG of linear TB-polymers.

Previous research confirmed a tendency of increased char yield with decrease of C/N ratio.^{279, 280} As shown in **Table 3.4**, these polymers (either the TB-HPB-PIMs or linear TB-polymers) with C/N ratio of 8.5 to 13 gave high char yields of over 70%. With the increase of C/N ratio to 22.5–24.5, char yields dropped to approximately 60%. By comparing the results of hexa-TB-HPB and linear TB-polymer 3 having the same C/N ratio, the porosity did not obviously impact the char yield but increased values of T_d , which is an important feature for potential flame-retardant materials. A possible reason is that the porous structure is conducive to preventing mass and heat transfer. To sum up the results in **Table 3.4**. and **Fig 3.9**, tetra-TB-HPB has the best thermal stability amongst all TB-HPB-PIMs, followed by hexa-TB-HPB, because of the high T_d and char yield.

Table 3.4 Thermal Properties and SA_{BET} in N_2 atmosphere of TB-HPB-PIMs and linear TB-polymers.

Polymer	C/N ^a	SA_{BET}^b (m ² /g)	Decomposition Temperature (°C)				Char Yield (%)
			T _{d5}	T _{d10}	T _{d20}	T _{max}	
Di-TB-tetra-Me-HPB	24.5	306	394	432	526	572	58
Di-TB-HPB	22.5	330	432	487	565	582	63
Tetra-TB-HPB	13	537	440	545	630	591	72
Hexa-TB-HPB	8.5	444	408	510	616	587	70
Linear TB-polymer 1	12.5	275	416	458	620	429	76
Linear TB-polymer 2	10.5	312	420	445	576	439	71
Linear TB-polymer 3	8.5	362	425	448	604	436	73

^a C/N ratios were calculated by the quantities of C and N atoms in one repeated unit. ^b SA_{BET} were measured at $CO_2/273$ K.

In order to better explore the thermal stability of TB-HPB-PIMs in real-world situations, TGA was also measured in the air atmosphere. Opposite to the results from N_2 , highly porous tetra- and hexa-TB-HPB showed reduced thermal stability. As shown in **Fig 3.10**, each TGA curve of the four TB-HPB-PIMs showed only one obvious weight loss, concentrated in the range of 512–580 °C. The values of T_{max} arranged from high to low as that of di-TB-HPB, di-TB-tetra-Me-HPB, hexa-TB-HPB and tetra-TB-HPB. The TGA of linear TB-polymers showed two highly overlapping weight losses. Among them, linear TB-polymer 1 and 3 behaved similarly. The mass of these two samples increased by 4–5% at 294 °C, which could be caused by the adsorption of some oxygen during the analysis, leading to a partial oxidation of the backbone,²⁸¹ or by a buoyancy effect of the pan during the temperature ramping, which often happens when the densities of sample and gas change (for example, initiation of a decomposition stage).^{282, 283} The T_{max} of linear TB-polymer 2 was significantly higher than the other two linear ones, and no obvious mass gain was observed.

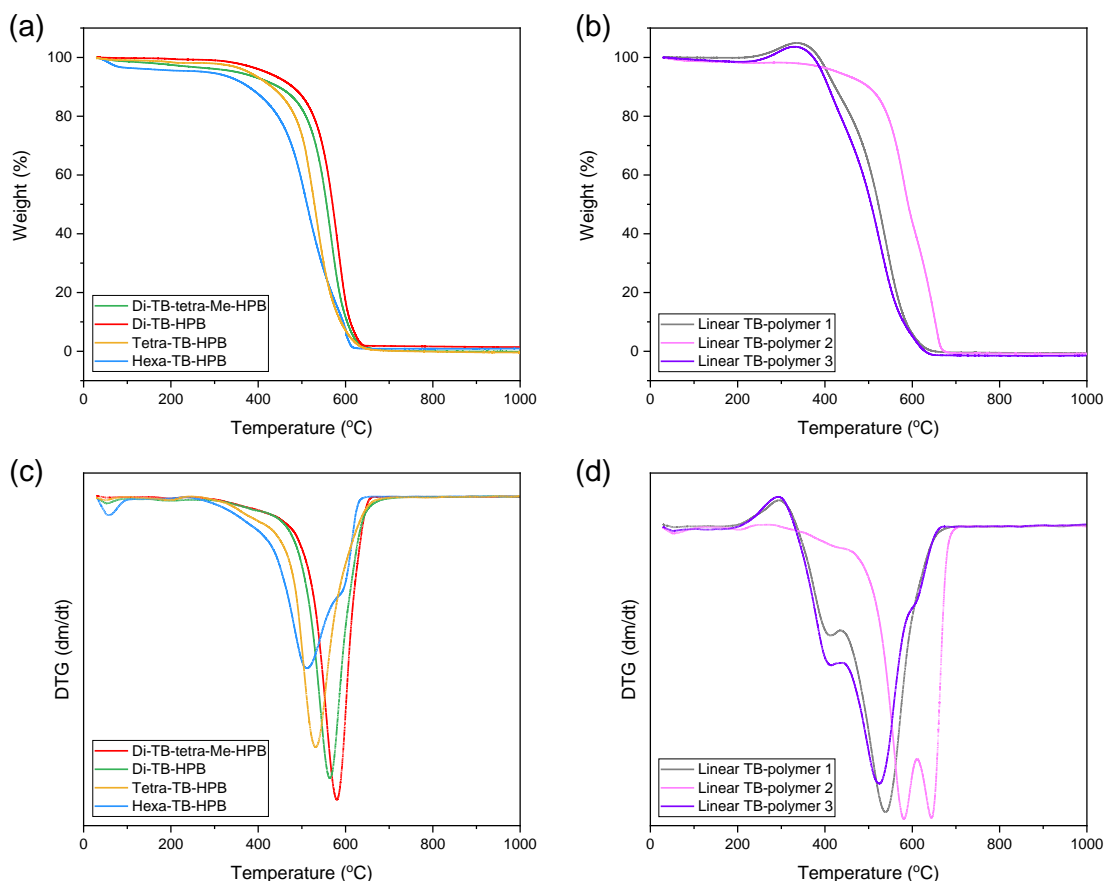


Figure 3.10 TGA analysis under air atmosphere: (a) TGA of TB-HPB-PIMs, (b) TGA of linear TB-polymers, (c) DTG of TB-HPB-PIMs, (d) DTG of linear TB-polymers.

Residual mass at 600 °C is used to evaluate thermal properties instead of char yield, since the polymers have no residual mass at 1000 °C in the air (because the completely oxidatively thermal decomposition products were gases). Based on the values of T_d and residual mass, di-TB-HPB possessed the best thermal stability. Tetra- and hexa-TB-HPB showed poor thermal properties. Comparing TGA results in nitrogen and air, the porosity could enhance the thermostability of TB-HPB-PIMs in an oxygen-free atmosphere. However, their thermal properties would be greatly impacted once the air goes into the micropores. In addition, it can be seen from **Fig 3.7** and **3.8** that di-TB-HPB and linear TB-polymer 2, which have dense and smooth surfaces, gave higher T_d and residual mass in the air, inferring better heat resistance. It is speculated that the surface blocked the diffusion of air into the sample to some extent. Although di-TB-HPB and linear TB-polymer 2 showed similar morphology and SA_{BET} , linear TB-polymer 2 held slightly higher T_d and significantly higher residual mass at 600 °C, attributed to that its C/N ratio is only half of the ratio of di-TB-HPB.

Table 3.5 Thermal Properties and S_{ABET} in air atmosphere of TB-HPB-PIMs and linear TB-polymers.

Polymer	C/N	S_{ABET}^a (m^2/g)	Decomposition Temperature ($^{\circ}C$)				Residual mass at $600^{\circ}C$ (%)
			T_{d5}	T_{d10}	T_{d20}	T_{max}	
Di-TB-tetra-Me-HPB	24.5	306	351	446	509	563	12
Di-TB-HPB	22.5	330	418	479	527	580	17
Tetra-TB-HPB	13	537	378	431	481	531	7
Hexa-TB-HPB	8.5	444	282	378	445	512	8
Linear TB-polymer 1	12.5	275	405	423	459	539	6
Linear TB-polymer 2	10.5	312	430	499	544	580-644	44
Linear TB-polymer 3	8.5	362	393	408	436	525	5

^a S_{ABET} were measured at $CO_2/273$ K.

Synergistic systems are expected to be a solution to the affected thermal properties in air resulting from open pore structures. As mentioned in Chapter 2, boron-containing materials would form a glassy coating at high temperatures, preventing the passing through of gases. In future work, the PIM molecules can be designed to contain both nitrogen and boron atoms. It is expected to not only combine the flame retardancy of nitrogen and boron, but also form a glassy layer during combustion (as mentioned in 1.2.3.2) protect our polymers from contacting air.

3.2.4.3 CO_2 Adsorption and Selectivity

Porosity was measured by N_2 adsorption at 77 K (**Fig 3.11 a**). Tetra- and hexa-TB-HPB showed Type I isotherms and high S_{ABET} to 641 and 203 m^2/g , suggesting that they are rich in micropores. The two di-TB-HPB-PIMs were considered to show Type II isotherms and S_{ABET} below 23 m^2/g . The S_{ABET} calculated from CO_2 adsorption of TB-HPB-PIMs showed a similar trend with the TB content (**Table 3.6**). This indicates microporosities of di-TB-HPB-PIMs are much lower than those of tetra- and hexa-TB-HPB. In addition, according to the PSD in **Fig 3.11 b**, tetra- and hexa-TB-HPB contain a much higher amount of narrow micropores in the range of 3-4 Å than the two di-TB-HPB-PIMs. It is concluded that TB units efficiently contributed to the microporosity of the TB-HPB-PIMs.

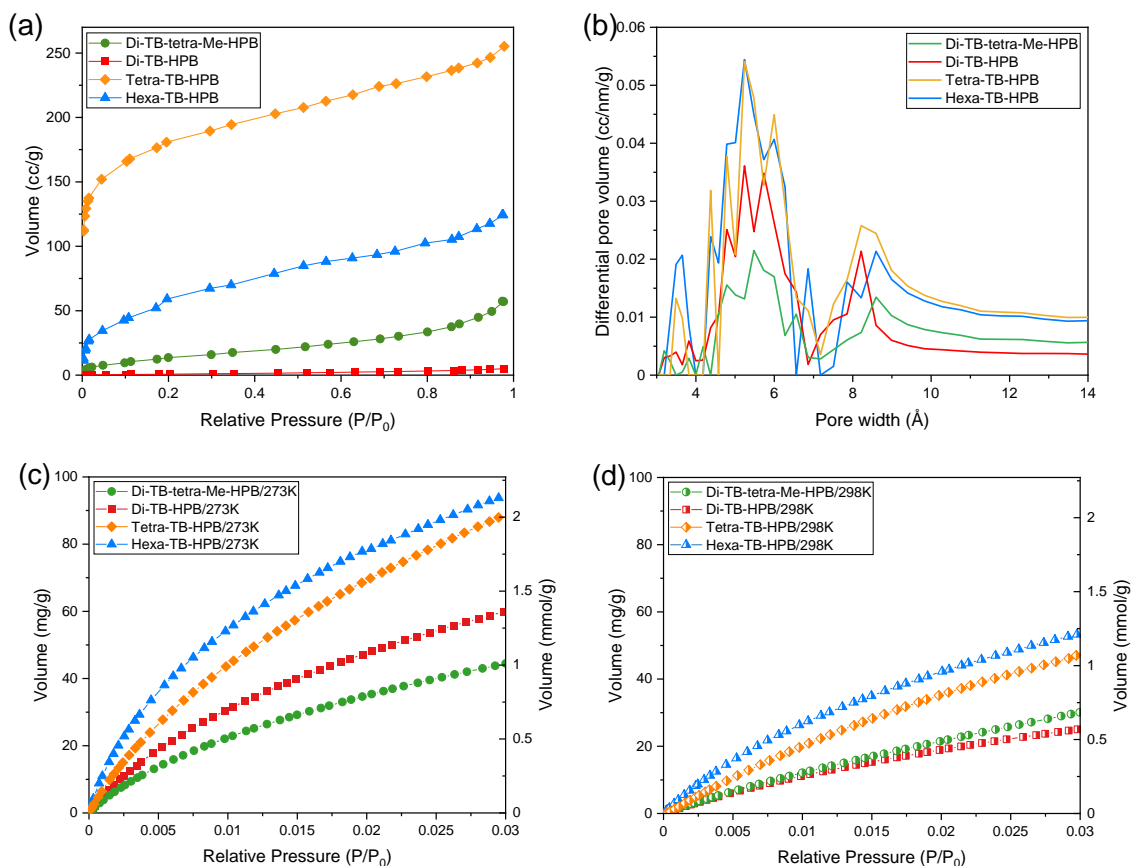


Figure 3.11 (a) N₂ adsorption at 77 K of TB-HPB-PIMs (b) PSD of TB-HPB-PIMs, calculated from CO₂ adsorption at 273 K by NLDFT (c) CO₂ adsorption at 273 K of TB-HPB-PIMs (d) CO₂ adsorption at 298 K of TB-HPB-PIMs

Linear TB-polymer 3 has the highest SA_{BET} among three linear polymers, followed by linear TB-polymer 1. Linear TB-polymer 2 shows a very low SA_{BET} . (**Table 3.6**) Due to the rigid conformation of TB units, the flexibility of linear polymers comes from the units of benzene rings connected by single bonds. Such units in linear TB-polymer 1 and 2 contain three benzene rings and thus are longer and more flexible than that of linear TB-polymer 3, which have only two benzene rings. Therefore, the packing efficiency of linear TB-polymer 3 chains is lower than the other two, causing high SA_{BET} and pore volume comparable to hexa-TB-HPB. Nevertheless, the CO₂ adsorption of linear TB-polymer 3 is much lower than that of higher functionalised hexa-TB-HPB, attributed to the network structure and high content of nitrogen atoms. Linear TB-polymer 1 chains were believed to less effective pack than linear TB-polymer 2 because of the steric occupation of methyl groups, causing a slightly higher porosity.

Table 3.6 Physical Characterization of Polymers and Gas Selectivity

Polymer	BET (m ² /g)			Pore volume ^a (cc/g)	CO ₂ adsorption			IAST CO ₂ /N ₂ selectivity ^b	Q _{st} ^c (kJ/mol)
	N ₂ /	CO ₂ /	CO ₂ /		195 K (1 bar)	273 K (1 bar)	298 K (1 bar)		
	77 K	195 K	273 K		(mg/g) (mmol/g)	(mg/g) (mmol/g)	(mg/g) (mmol/g)		
Di-TB-tetra-Me-HPB	22	364	306	0.294	139.0 (3.16)	44.6 (1.01)	30.2 (0.69)	19.7	30.9
Di-TB-HPB	7	361	330	0.309	146.1 (3.32)	60.0 (1.36)	25.1 (0.57)	25.2	31.0
Tetra-TB-HPB	641	632	537	0.349	164.9 (3.75)	88.2 (2.00)	47.2 (1.07)	45.6	45.3
Hexa-TB-HPB	203	404	444	0.255	120.6 (2.74)	94.0 (2.14)	53.4 (1.21)	44.0	38.8
Linear TB-polymer 1	54	362	275	0.304	27.7 (0.63)	53.0 (1.20)	33.3 (0.76)	18.3	29.8
Linear TB-polymer 2	4	84	312	0.184	16.6 (0.38)	61.0 (1.39)	37.5 (0.85)	28.9	27.7
Linear TB-polymer 3	205	389	362	0.278	26.0 (0.59)	56.4 (1.28)	38.2 (0.87)	27.5	25.0

^aAt P/P₀ ~ 0.98. ^bCalculated according to IAST at 298 K and 1 bar.^{269, 270} ^cQ_{st} (in kJ/mol) of corresponding gas at zero coverage calculated from isotherms collected at 273 K and 298 K and fitted with the Langmuir–Freundlich equation and calculated via the Clausius Clapeyron equation.

Q_{st} was calculated from CO_2 adsorption at 273 and 298 K. Tetra-TB-HPB showed the highest value of Q_{st} (45.3 kJ/mol), followed by hexa-TB-HPB (38.8 kJ/mol). Two di-TB-HPB-PIMs have slightly lower Q_{st} around 31 kJ/mol. As mentioned in Chapter 2, high CO_2 uptake and appropriate Q_{st} (not to exceed 50 kJ/mol) are important indicators for evaluating CO_2 adsorption materials. Among these TB-HPB-PIMs, tetra-TB-HPB had the best CO_2 adsorption and selectivity, followed by hexa-TB-HPB. The Q_{st} of all TB-HPB-PIMs are higher than that of all linear TB-polymers, especially tetra- and hexa-TB-HPB. That was inferred from a combined effect of high nitrogen content and high porosity.

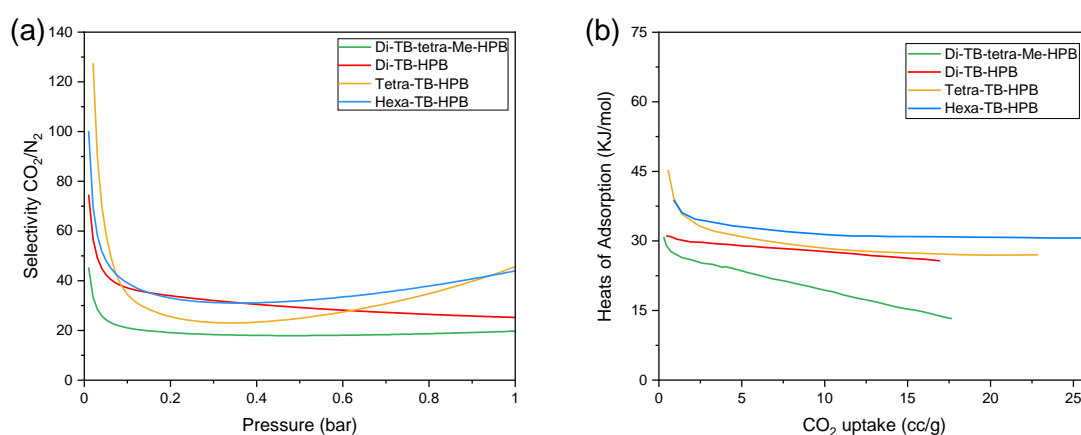


Figure 3.12 (a) IAST CO_2/N_2 selectivity (simulating a 15/85 composition), (b) Q_{st} of TB-HPB-PIMs.

Generally, gas adsorption of an adsorbent is antagonistic towards its gas selectivity. This was reflected in relevant data of three linear polymers in **Table 3.6**. Linear TB-polymer 2 exhibited the highest IAST selectivity and the lowest CO_2 adsorption. It is inferred that the three linear polymers have the same functionality, and the difference in selectivity of CO_2 over N_2 mainly comes from the sieving of the narrow pores on different gas molecules. However, it was noticed that the values of CO_2/N_2 selectivity of TB-HPB-PIMs followed the same trend of their CO_2 adsorption. The enhancement with an increased proportion of TB units in TB-HPB-PIMs on both CO_2 capacity and selectivity is speculated to result from not only its narrow microporosity but also high SA_{BET} and nitrogen content.²⁸⁴ A high SA_{BET} provides a larger adsorption surface. Nitrogen atoms in tertiary amine provide a stronger interaction with carbon atoms of CO_2 leading to high CO_2 affinity. Narrow micropores centered around 3–4 Å allow the passage of smaller CO_2 molecules but prevent the entry of larger N_2 molecules.⁷¹

3.3 Conclusion

A series of TB-HPB-PIMs were polymerised from amino-HPB monomers prepared through three different routes. Three “linear” TB-polymers were also synthesized for comparison. Their thermal properties, CO₂ adsorption and selectivity were characterized and analyzed. The results of TGA in N₂ confirmed that tetra-TB-HPB has the best thermal stability, followed by hexa-TB-HPB, contributed by the combined effect of low C/N ratio and high porosity. The thermostability of TB-HPB-PIMs in the air would be impacted by excessive contact with oxygen due to the high porosity. This issue is expected to be solved through a synergistic system of nitrogen and boron in the future. Tetra-TB-HPB also showed the best CO₂ adsorption and selectivity, followed by hexa-TB-HPB as well. This is attributed to a combined effect of the high surface area, content of nitrogen, and narrow microporosity.

Therefore, tetra- and hexa-TB-HPB exhibit excellent comprehensive properties and were expected to be applied as multifunctional materials in the fields of flame retardation and CO₂ adsorption and selectivity.

The thermal properties in N₂ of TB-HPB-PIMs are comparable to those of the reported PIMs who have similar units listed in **Table 1.2**. Compared with the functionalised HPB-PIMs listed in **Table 1.3**, although the lower porosities and CO₂ adsorption, TB-HPB-PIMs exhibited significantly higher CO₂/N₂ selectivity and Q_{st} values.

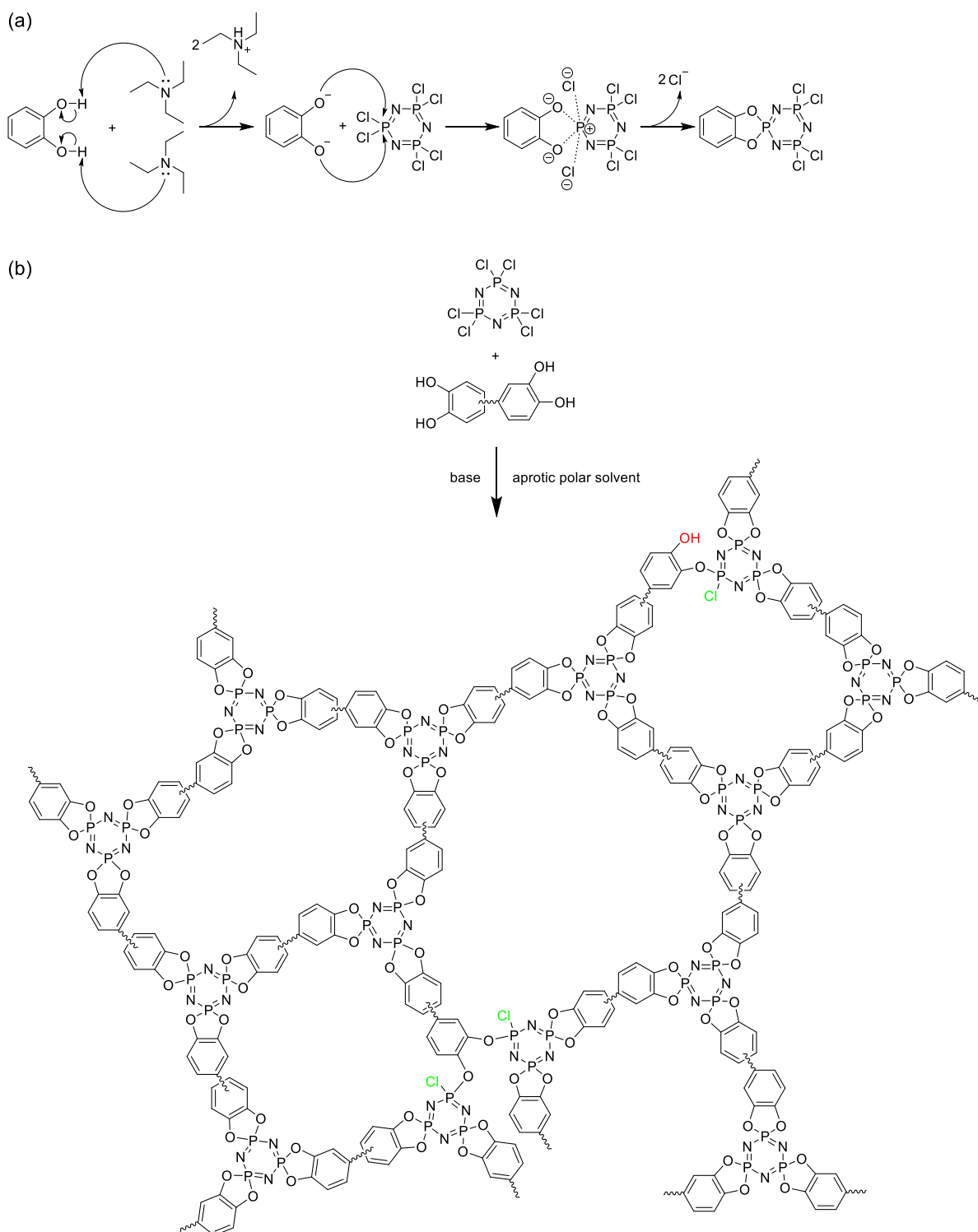
Chapter 4 – Novel Cyclophosphazene-based PIMs for Flame Retardation and Gas Separation

4.1 Introduction

The work described in Chapter 3 showed that both the enhanced microporosity and the presence of nitrogen atoms contributed significantly to increase the flame retardancy performance of TB-PIMs. As mentioned in the introduction, cyclophosphazene derivatives possess high proportions of phosphorus and nitrogen, and perform excellent P-N synergistic flame retardant effects.¹⁷⁶ Based on these two features, the work reported in this chapter aimed to investigate the feasibility of developing the novel cyclophosphazene-based PIMs, to be used as FRs.

Hexachlorocyclotriphosphazene (HCCP) is commonly used as the starting material for preparing cyclotriphosphazene (CTP) derivatives. CTP is a stable, unsaturated six-membered ring formed by alternating phosphorus nitrogen single and double bonds, which has similar aromaticity to a benzene ring.²⁴⁴ There are two highly active chloride groups attached to each phosphorus atom that can be substituted readily with different nucleophiles (like alkyl, alkoxy, phenoxy and amine).²⁴⁴ It is inferred that CTP derivatives are not only suitable for organic synthesis, but also have good compatibility with organic materials, because their molecular structures are similar to that of many carbon-based polymers. Therefore, CTPs can be deemed as potentially suitable materials to be developed as organic polymer FRs.

In this work, it was planned to react two types of compounds which possess sites of contortion typical of PIMs, bis-catechols and aromatic diamines, with HCCP to prepare CTP-PIMs as novel FRs. On the one hand, both could provide a large series of potential monomers with ideal structures to synthesize PIMs.^{285, 286} On the other hand, the latter could introduce more nitrogen atoms (a widely used element in flame retardant materials). These novel CTP-PIMs are expected to combine the advantages of both cyclophosphazene materials and PIMs.

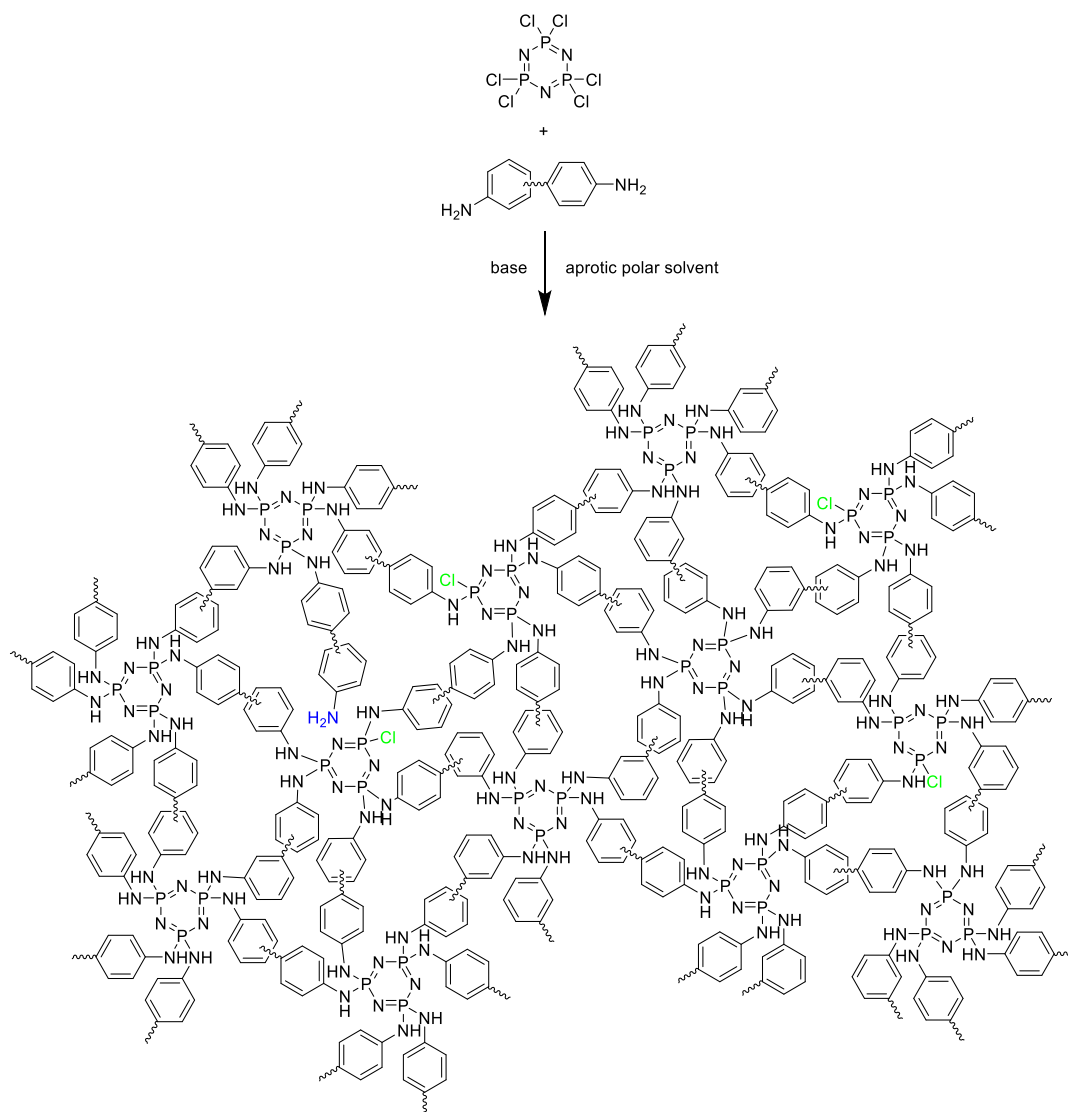


Scheme 4.1 (a) Reaction mechanism of chloride group in CTP and hydroxyl groups in catechol, (b) CTP-PIMs synthesized with bis-catechols.

The chlorides of HCCP can be substituted by bis-catechol monomers via a nucleophilic aromatic substitution-like mechanism,²⁸⁷ which is described in **Scheme 4.1 a** using the example reaction of CTP and catechol with triethylamine (Et_3N), used as a base that activates the catechol by removing the proton from the hydroxyl groups.

The more nucleophilic (negatively charged) oxygen atoms attack the phosphorus of CTP ring, replacing the chloride. The correspondent chloride salts are generated as the by-product in this process.

The theoretical stoichiometric ratio of HCCP to catechol groups is 1:3 for achieving complete substitution of chlorides. This is so as two chloride groups on each of three phosphorus atoms react with two hydroxyl groups on one catechol group. However, chloride groups may not be completely substituted in practice, especially in the later stages of the polymerisation, due to steric hindrance effects. In addition, there is a low probability that two chloride groups on the same P atom will react with hydroxyl groups from different catechols (as shown in **Scheme 4.1 b**).



Scheme 4.2 CTP-PIMs synthesized with diamines.

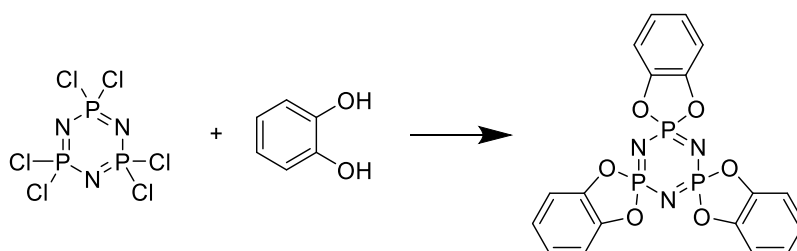
The substitution reaction between amine and HCCP follows a similar mechanism. The difference is that HCCP and amino groups react at a high stoichiometric ratio of 1:6. As shown in **Scheme 4.2**, the molecular structure of diamine-CTP products is even more crowded than that of bis-catechol-CTP. It can be anticipated that a greater percentage of unreacted amino and chloride groups will remain in the final products because of the more hindered approach compared with bis-catechol-CTP. In other words, we speculated that it would be more difficult to promote a highly efficient substitution of the amino groups with chlorides on the HCCP.

4.2 Results and Discussion

4.2.1 Catechol-based CTP-PIMs

The designed model compound, Model CTP 1, was first prepared with catechol monomer, in order to explore the feasibility of the reaction and to find the optimal conditions between HCCP and catechol groups that can be later used for polymerisation.

4.2.1.1 Model CTP 1

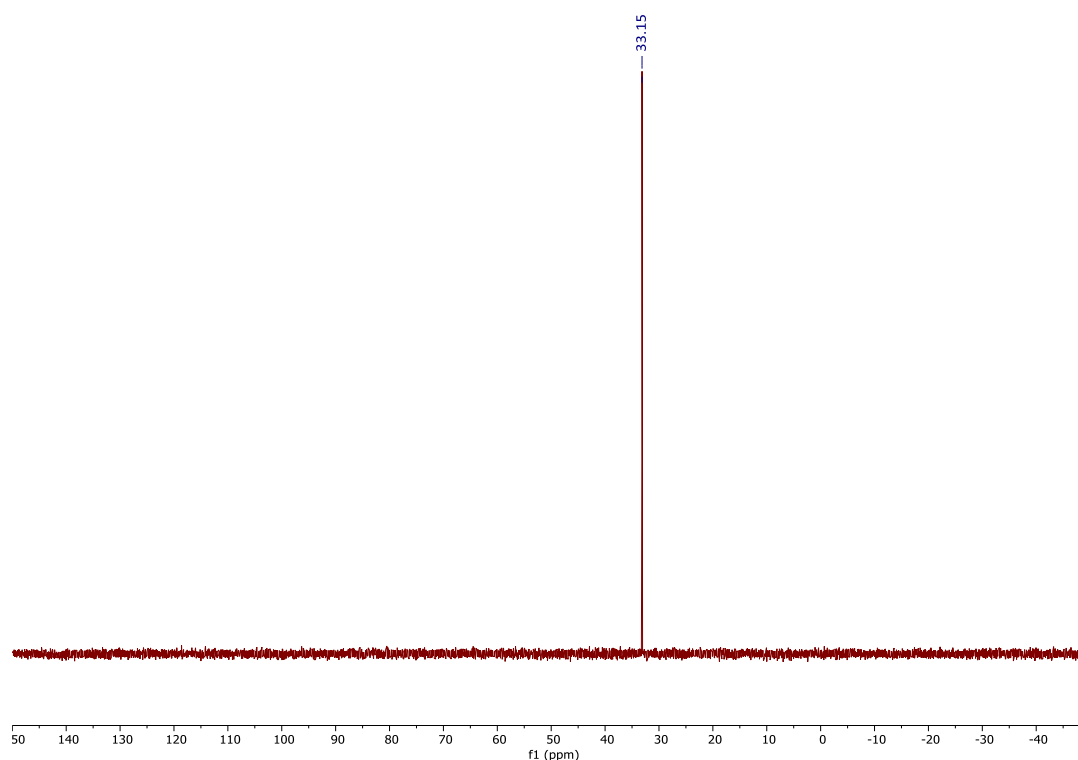


Scheme 4.3 Synthesis of Model CTP 1.

The attempted conditions and their results of Model CTP 1 preparation are listed in **Table 4.1**. HCCP and catechol were refluxed with K_2CO_3 in THF to prepare Model CTP 1 according to reported methods in the literature.²⁸⁸⁻²⁹⁰ NMR and FT-IR confirmed that the target structure of this product was obtained only with a very low yield of 3%. By changing the base to Et_3N and the solvent to anhydrous THF, and increasing the reaction time^{291, 292}, the yield was significantly increased to 53%. The obtained product was confirmed to be the correct Model CTP 1 by comparing our results with published data,²⁸⁸ and analyzing it by NMR (**Fig 4.1** and Experiment Section). It was concluded that this reaction may be facilitated by longer times and that it is rather sensitive to water.

Table 4.1. Attempted Conditions for Preparing Model CTP 1.

HCCP	Catechol	Base	Solvent	Conditions	Products and Yields
5.8 mmol (1 eq.)	17.3 mmol (3 eq.)	K ₂ CO ₃ 34.0 mmol (6 eq.)	THF 15+15 mL	Reflux N ₂	65 °C 4 hrs Model CTP 1 Y= 3%
3.3 mmol (1 eq.)	10.0 mmol (3 eq.)	Et ₃ N 20.0 mmol (6 eq.)	anhydrous THF 9+18 mL	Reflux N ₂	65 °C 40 hrs Model CTP 1 Y= 53%
2.0 mmol (1 eq.)	6.0 mmol (3 eq.)	Et ₃ N 12.0 mmol (6 eq.)	anhydrous DMF 10+7 mL	Reflux N ₂	150 °C 48 hrs Mixture of starting materials and Model CTP 1
0.6 mmol (1 eq.)	1.7 mmol (3 eq.)	NaOH 6.0 mmol (10 eq.)	MeCN 15 mL	Microwave N ₂	80 °C 1 hr Mixture of starting materials and Model CTP 1
1.0 mmol (1 eq.)	3.0 mmol (3 eq.)	Et ₃ N 6.0 mmol (6 eq.)	MeCN 1 mL	Microwave N ₂	80 °C 1 hr Model CTP 1 Y = 90%
1.0 mmol (1 eq.)	3.0 mmol (3 eq.)	Et ₃ N 6.0 mmol (6 eq.)	anhydrous THF 25 mL	Microwave N ₂	65 °C 3 hrs Model CTP 1 Y = 92%

**Figure 4.1** ³¹P NMR of Model CTP 1.

To explore the effect that higher temperatures may have on yield and purity, anhydrous dimethylformamide (DMF), with a higher boiling point of 153 °C, was selected as the

solvent in the next attempt. However, in this case, the FT-IR spectrum of the product displayed characteristic peaks of mainly the starting materials and a small amount of Model CTP 1, which is presumably a sign of lower substitution of the chloride groups by the catechol. The possibility of DMF hydrolysis under alkaline conditions was suspected, but no evidence was found from NMR of the heated mixture of anhydrous DMF and Et₃N. Thus, we simply speculated that a higher temperature was not helpful for a better outcome of the reaction.

Except for the exploration of bench reflux conditions described above, microwave irradiation was also employed to perform this reaction. The first attempt followed a reported procedure using NaOH as the base and MeCN as the solvent,²⁹³ and was left to react for 1 hour giving a mixture of unreacted monomers and Model CTP 1, as proven by FT-IR. Because of that, the base was changed back to Et₃N, as it performed well in the refluxed reactions. Along with that, the effects of concentration and solvent type on this reaction were also explored. HCCP and catechol were dissolved in as little MeCN as possible to make a reaction system with a concentration 25 times higher than before, affording a surprisingly high yield of 90%. A slightly higher yield was obtained when anhydrous THF was used as the solvent, even though the reaction was carried out at a lower temperature (in this case a longer reaction time was required).

During the characterization of the different batches of Model CTP 1, it was found that NMR (including ¹H, ¹³C and ³¹P) often did not show evident signals, even the ones where the structures of Model CTP 1 were confirmed by FT-IR and mass spectrometry. Compared with the unstable NMR measurement, FT-IR was deemed as the most reliable spectroscopy for evaluating chemical structure of Model CTP 1 products.

FT-IR analysis focused on the disappearance of O–H and P–Cl bonds signals from respectively catechol and HCCP, and the appearance of P–O bonds signals for Model CTP 1. The products prepared by reflux and microwave irradiation showed highly similar FT-IR spectra, which were consistent with the published data²⁹¹. As shown in **Fig 4.2**, the O–H stretching peak at 3445–3319 cm⁻¹, the O–H bending peak at 1360 cm⁻¹, and vibration peaks of P–Cl at 595 cm⁻¹ and 502 cm⁻¹ disappeared, concluding that there are no unreacted catechol and HCCP remaining in the new product.²⁴⁴ The P–O(–Ar) stretching is found at 826 cm⁻¹, and the peak at 1250–1247 cm⁻¹ originates from (P–)O–Ar stretching.²⁹⁴

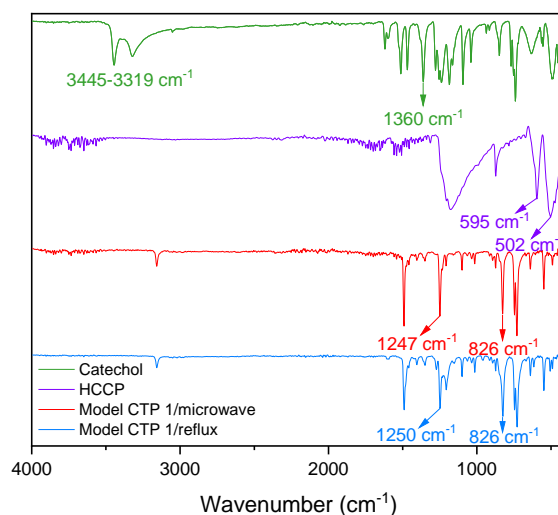
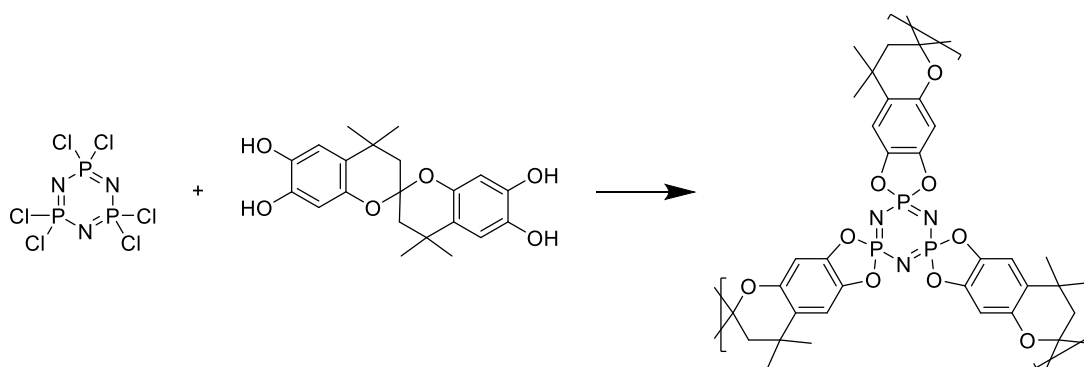


Figure 4.2 FT-IR of Model CTP 1.

To summarize the above experiments of Model CTP 1, we concluded that Et_3N is the most suitable base, and anhydrous THF is the ideal solvent. Heating at 65 °C for 3 hours in a microwave reactor afforded the Model CTP 1 with the best purity and yield. For bench reflux, the desired product could also be obtained with moderate yields by extending the reaction time to 40 hours.

4.2.1.2 CTP-SBC-PIM



Scheme 4.4 Synthesis of CTP-SBC-PIM.

The preparation of CTP-SBC-PIM was attempted, based on the optimized conditions found for Model CTP 1. The attempted conditions are summarised in **Table 4.2**. After being heated by microwave irradiation, a heterogeneous and “lumpy” solid was produced, and the anhydrous THF almost disappeared (speculated to be evaporated or absorbed into the product). To avoid solvent evaporation, THF was replaced with toluene, which has a higher boiling point of 110 °C compared to 66 °C of THF. However, this product was still a heterogeneous mixture of white and brown lumpy solids.

Table 4.2 Attempted Conditions for Preparing CTP-SBC-PIM.

HCCP	SBC-bis-catechol	Et ₃ N	Solvent	Conditions		Products
1.0 mmol (1 eq.)	1.5 mmol (1.5 eq.)	6.0 mmol (6 eq.)	anhydrous THF 15 mL	Microwave N ₂	65 °C 1 hr	Mixture of starting materials and CTP-SBI-PIM
1.0 mmol (1 eq.)	1.5 mmol (1.5 eq.)	6.0 mmol (6 eq.)	anhydrous toluene 15 mL	Microwave N ₂	65 °C 1 hr	Mixture of starting materials and CTP-SBI-PIM
3.0 mmol (1 eq.)	4.5 mmol (1.5 eq.)	18.0 mmol (6 eq.)	anhydrous THF 16+30 mL	Reflux N₂	65 °C 40 hrs	CTP-SBC-PIM Y = 94%

The brown part was separated as much as possible from the white part, then ground to fine powder, washed with anhydrous toluene and dried under vacuum (**Fig 4.3 c**). By comparing their T_{\max} reflected from DTG in N₂ in **Fig 4.3 a**, the white part is inferred to be low substituted HCCP, and the unwashed brown part is mainly SBC-bis-catechol. The brown part washed with anhydrous toluene three times was speculated to be CTP-SBC-PIM.

Such heterogeneous products reflected insufficient stirring during the polymerisation, speculated to be related to the high viscosity of the system. Different from Model CTP 1, CTP-SBC-PIM rapidly polymerises into large molecular networks under microwave irradiation. In the macroscopic view, the reaction system became more and more viscous until the stir bar was stuck, which led to insufficient stirring. Therefore, bench reflux, as a gentler heating method, was considered more suitable for preparing CTP-SBC-PIM, that needed to be further investigated. The polymerisation then was repeated according to the optimal reflux conditions for preparing Model CTP 1. The refluxed CTP-SBC-PIM product appeared as a homogeneous powder, which was lost in large quantities after washing. DTG analysis in N₂ in **Fig 4.3 b** shows the product gradually decomposed during the process, hinting at a rapid hydrolysis. The refluxed product was only quickly washed with THF for further characterisation.

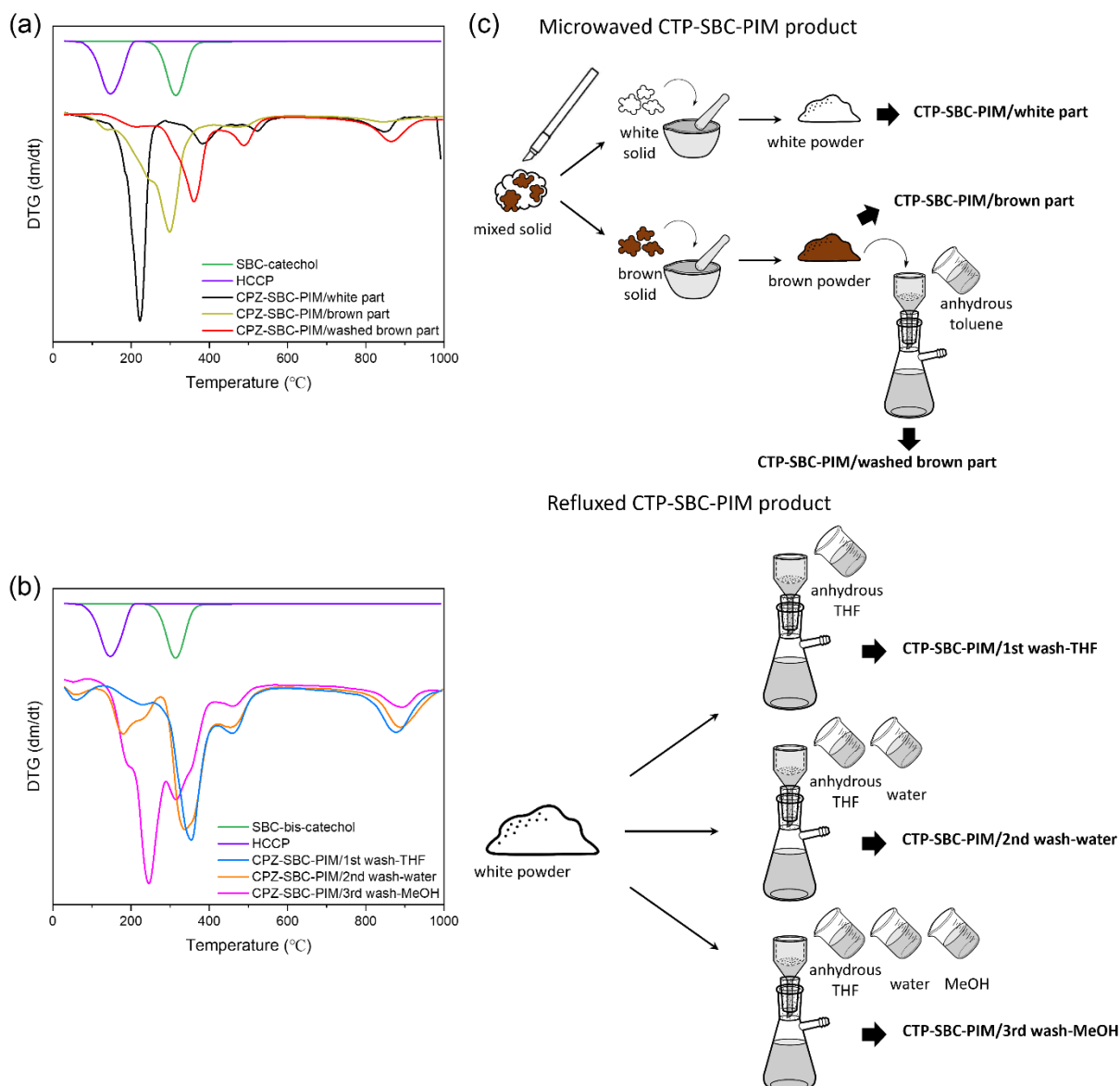


Figure 4.3 (a) DTG in N₂ of microwaved CTP-SBC-PIM and their monomers, (b) DTG in N₂ of refluxed CTP-SBC-PIM and their monomers, (c) Illustration of work-up processes of samples.

The microwaved and refluxed CTP-SBC-PIMs were tested by FT-IR (**Fig 4.4**). We found no obvious O–H stretching at 3445–3198 cm⁻¹ in the FT-IR spectra of CTP-SBC-PIM produced with both methods. The presence or not of the O–H bending peak at 1291 cm⁻¹ was not significant for this analysis, because it overlaps with other peaks making the assignment more difficult. (P–)O–Ar stretching at 1221 cm⁻¹ and P–O(–Ar) stretching at 904 cm⁻¹ were found in both but also highly overlapped with other signals. Both products, anyway, showed overlapped peaks around 502 cm⁻¹ which is suspected to be unreacted P–Cl.

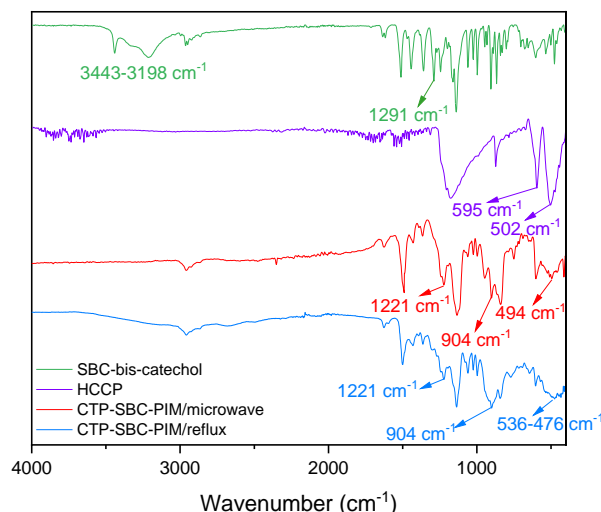


Figure 4.4 FT-IR of CTP-SBC-PIMs and their monomers.

According to the FT-IR and DTG analysis in N_2 , the washed microwaved product and the refluxed product, without excessive washing, were identified as the desired CTP-SBC-PIM product. However, both still contained a low proportion of oligomers and unsubstituted chloride groups that could not be removed by current work-up method, because the washing seems accelerating the hydrolysis of the final material.

Highly similar TGA curves of the two CTP-SBC-PIM products show less than 10% weight losses below 200 °C, likely caused by loss of small molecule impurities. Both samples exhibited three weight loss stages above 200 °C corresponding to the three DTG peaks as can be seen in **Fig 4.5**. Their T_{max} around 355–360 °C was attributed to the cleavage of P–O and C–O bonds with relevant low stability, likely to be connected to the external and more accessible bonds.^{295, 296} The two curves showed weight losses respectively at 467 °C and 489 °C. The CTP rings possibly decomposed at this stage to generate phosphate, phosphoric acid, phosphite acid, metaphosphoric acid, etc.,^{297, 298} which can promote the char formation of the matrix.²⁹⁹ Ammonia is thought to be released at the same stage. That could help to form an intumescent char layer³⁰⁰ which would cover the surface, and isolate heat and oxygen in combustion.²⁹⁷ The weight losses of about 10% at 866–877 °C were presumed to be the collapse of the carbon protective layer. Combining the T_d values and char yields in **Table 4.3**, the two CTP-SBC-PIM products own similar thermal properties.

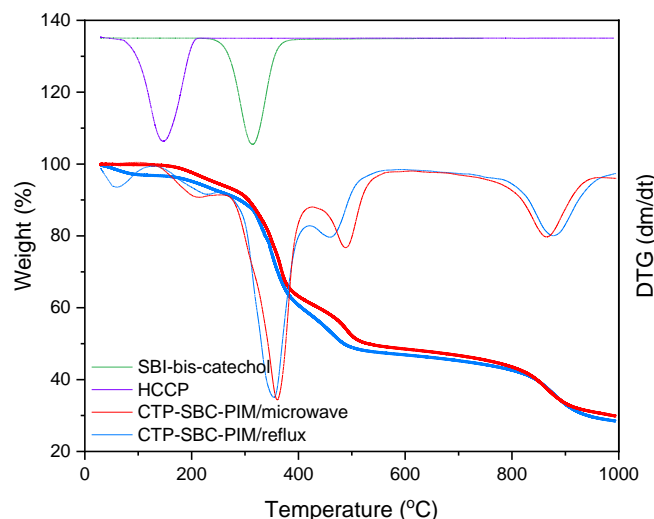
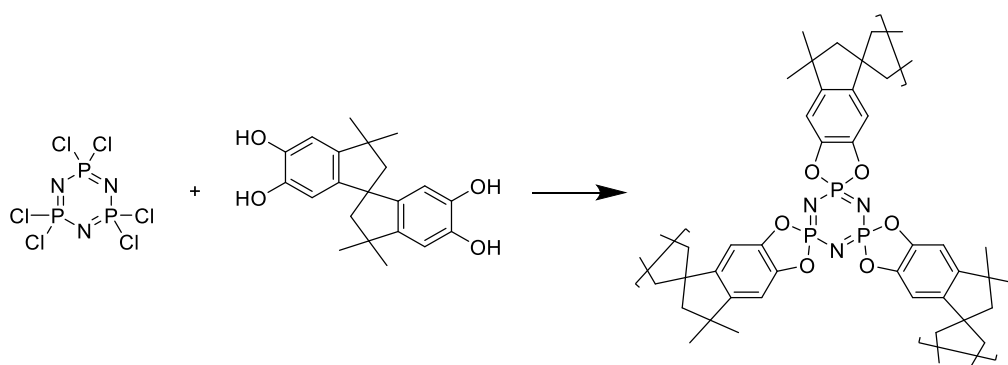


Figure 4.5 TGA and DTG in N₂ of CTP-SBC-PIMs and DTG of their monomers.

Table 4.3 Thermal Properties in N₂ of Catechol-based CTP-PIMs.

Polymer	C/P/N	Decomposition Temperature (°C)			T _{max} (°C)	Char Yield (%)
		T _{d5}	T _{d10}	T _{d20}		
CTP-SBC-PIM	reflux	204	290	338	355	28
	microwave	243	306	347	360	30
CTP-SBI-PIM	reflux	350	396	428	441	30
	microwave	169	231	336	346, 519	27

4.2.1.3 CTP-SBI-PIM



Scheme 4.5 Synthesis of CTP-SBI-PIM.

CTP-SBI-PIM was first prepared using the reflux conditions adopted for CTP-SBC-PIM and worked-up in the same manner. The product was characterized by FT-IR and found to contain unreacted functional groups, along with a yield greater than 100% that suggests impure product. Subsequently, higher reaction temperature (in higher boiling point solvents, such as toluene) and longer reaction time were attempted

expecting to promote the polymerisation. However, we still failed to obtain a pure CTP-SBI-PIM sample. As opposed as for CTP-SBC-PIM, in this case the intense heating of microwave irradiation demonstrated useful for this reaction and provided a satisfactory yield of 70%. The experimental details are shown in **Table 4.4**.

Table 4.4 Attempted Conditions for Preparing CTP-SBI-PIM.

HCCP	SBI-bis-catechol	Et ₃ N	Solvent	Conditions		Products
6.0 mmol (1 eq.)	9.0 mmol (1.5 eq.)	36.0 mmol (6 eq.)	anhydrous THF 17+30 mL	Reflux N ₂	65 °C 40 hrs	Mixture of oligomers and CTP-SBI-PIM Yield = 126%
6.0 mmol (1 eq.)	9.0 mmol (1.5 eq.)	36.0 mmol (6 eq.)	toluene 16+30 mL	Reflux N ₂	120 °C 40 hrs	Mixture of starting materials and CTP-SBI-PIM
3.0 mmol (1 eq.)	4.5 mmol (3 eq.)	18.0 mmol (6 eq.)	anhydrous THF 23+10 mL	Reflux N ₂	65 °C 112 hrs	Hydrolysed in work-up
1.0 mmol (1 eq.)	1.5 mmol (1.5 eq.)	6.0 mmol (6 eq.)	toluene 15 mL	Microwave N ₂	120 °C 1 hr	Mixture of starting materials and CTP-SBI-PIM
1.1 mmol (1 eq.)	3.2 mmol (3 eq.)	21.5 mmol (20 eq.)	anhydrous THF 20 mL	Microwave N₂	80 °C 1 hr	CTP-SBI-PIM Y% = 70%

CTP-SBI-PIMs were worked up following the optimized method of CTP-SBC-PIM described above. As shown in **Fig 4.6**, no obvious peaks of O–H stretching at 3406–3233 cm⁻¹ were observed in the spectrum of microwaved CTP-SBI-PIM. There was a flat peak covering this range in the spectrum of refluxed product, which might be attributed to unreacted hydroxyl groups. (P–)O–Ar stretching peaks cannot be found probably because they were weak and overlapped. The peaks located at 1036 cm⁻¹ are likely attributable to the P–O(–Ar) stretching, which is much stronger in the microwaved product than the refluxed one. The peak at 536 cm⁻¹ in the spectrum of refluxed product is suspected as being the P–Cl stretching (due to unreacted chloride groups). It was noticed that there are two peaks in both spectra at 2605 cm⁻¹ and 2495 cm⁻¹ coming from the by-product triethylammonium chloride,³⁰¹ which suggests that the purification method needs to be improved. It is necessary not only to avoid the decomposition of the catechol-based CTP-PIM products during washing, but also to remove from the system unreacted reagents and by-products, such as triethylammonium chloride.

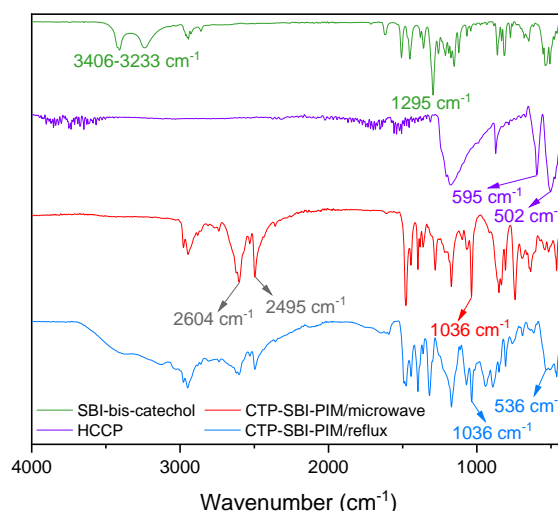


Figure 4.6 FT-IR of CTP-SBI-PIMs and their monomers.

TGA curve of the microwaved CTP-SBI-PIM formed under microwave irradiation showed a weight loss at 161 °C, which was inferred to be a small amount of unreacted HCCP (**Fig 4.7**). Although at first glance it may seem to be due the SBI-bis-catechol, the weight loss at 346 °C was not identified as a residue of SBI-bis-catechol, because of the absence of H–O peaks in its FT-IR spectrum. Thus, it was believed to be more likely belonging to the cleavage of the P–O and C–O bonds. Such weight loss was not observed in the product formed under normal reflux. According to the above FT-IR results, the refluxed sample still contained abundant amounts of chloride groups from HCCP and suspected H–O from the bis-catechol, indicating that the P–O bond may not fully form during the polymerisation. Thus, we convey that the main components found on the refluxed polymerisation were either short oligomers or unreacted monomers. Since the TGA curve did not show clear evidence related to the weight loss of the two monomers, the refluxed product was deemed to be an oligomer. The weight losses of two samples respectively at 441 °C and 519 °C were inferred to be due to the decomposition of the CTP rings. This lower T_d of the refluxed product was speculated to be caused by its lower degree of polymerisation. The mass fluctuation on both curves in the range of 819–949 °C could be attributed to the complete decomposition of the carbon layer at these high temperatures.

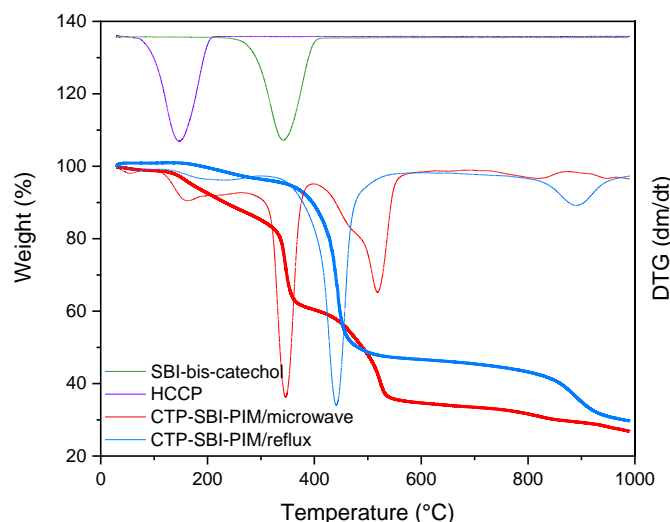


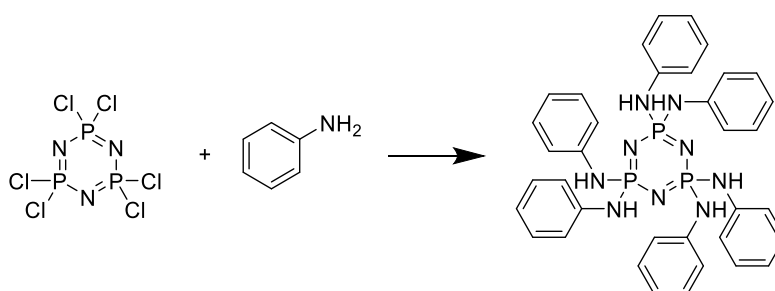
Figure 4.7 TGA and DTG in N₂ of CTP-SBI-PIMs and DTG of their monomers.

It is concluded that, although the reflux product provided higher T_d values (**Table 4.3**), microwave irradiation proved to be a better heating method for this reaction affording purer CTP-SBI-PIM with a seemingly higher polymerisation degree. This is the opposite of the better heating method shown by CTP-SBC-PIM. A possible reason is that CTP-SBI-PIM chains are more rigid than CTP-SBC-PIM, making the unreacted functional groups more difficult to approach one another. Microwave irradiation, instead, offered a higher heating efficiency, which better activated the molecules promoting a more efficient reaction.

4.2.2 Amine-based CTP-PIMs

Our research on amine-based CTP-PIMs also started with the synthesis of model compounds, in order to understand what the best polymerisation conditions are. This part was completed with the help of Kevin Almeida, an undergraduate student on our team.

4.2.2.1 Model CTP 2a



Scheme 4.6 Synthesis of Model CTP 2a.

Aniline, the simplest aromatic amine, was initially selected to react with HCCP to make Model CTP 2a, referring to similar literature work.^{302, 303} Results are summarized in **Table 4.5**. The obtained product proved to be soluble in MeCN and could not be collected by filtration at room temperature. Therefore, once completed, the reaction was evaporated under reduced-pressure to remove solvents, and then resulted in a transparent light-brown viscous liquid, which was proven as a mixture of impurities and unreacted starting materials. The reaction was significantly improved by changing the solvent from MeCN to anhydrous THF, but the yield and purity were still not satisfactory. Besides, the literature reported reactions of HCCP and diamine using the ultrasonic bath.^{304, 305} Thus, Model CTP 2a synthesis was attempted in the ultrasonic bath but we still failed to obtain the desired compound.

Table 4.5 Attempted Conditions for Preparing Model CTP 2a.

HCCP	Aniline	Et ₃ N	Solvent	Conditions	Work-up	Products
0.3 mmol (1 eq.)	4.4 mmol (15 eq.)	14.4 mmol (50 eq.)	MeCN 15 mL	Microwave 40 °C 1.5, 3, 4.5, 6 hrs	Rotary evaporation	Mixture of starting materials and impurities
0.6 mmol (1 eq.)	8.8 mmol (15 eq.)	28.8 mmol (50 eq.)	anhydrous THF 15 mL	Microwave 40 °C 1.5 hrs	Rotary evaporation	Model CTP 2a Y = 5%
0.6 mmol (1 eq.)	8.8 mmol (15 eq.)	28.8 mmol (50 eq.)	MeCN 30+4 mL	Ultrasonic bath 40 °C 1.5, 3, 4.5, 6 hrs	Rotary evaporation	Mixture of starting materials and Model CTP 2a
1.0 mmol (1 eq.)	7.8 mmol (7.8 eq.)	9.0 mmol (9 eq.)	anhydrous THF 5+8 mL	Reflux, N ₂ 60 °C 48, 96 hrs	Recrystallization PET/DCM	Starting materials
1.1 mmol (1 eq.)	6.4 mmol (6 eq.)	17.9 mmol (16 eq.)	MeCN 15+15 mL	Reflux, N₂ 40 °C 3 hrs	Crystallization ice bath	Model CTP 2a Y = 36%

The reaction of HCCP and amino compounds was also tried under bench reflux, as in previous studies.³⁰⁶⁻³⁰⁸ The reaction solvent was removed by reduced-pressure distillation first, and the crude product was recrystallized in petroleum ether/DCM, as stated in a previously published work.³⁰⁹ However, no solid precipitated during this process in our case. All the liquid obtained from the recrystallization was collected and evaporated under reduced pressure, to afford a small amount of solid that was verified by NMR to be starting materials. That means that any crude polymer we might have obtained decomposed/hydrolysed during the recrystallization step. The refluxed

reaction was then modified: more Et_3N was added, and the solvent was replaced with MeCN. When the heating was stopped, the flask was sealed well and immediately cooled in an ice bath for around 4 hours to precipitate some white crystals, which were directly collected by filtration and vacuum dried for characterization, giving a Model CTP 2a product with desired purity and yield of 36%. However, this product is hydrolysed easily in air and thus must be stored under dry conditions and characterized within three days once obtained.

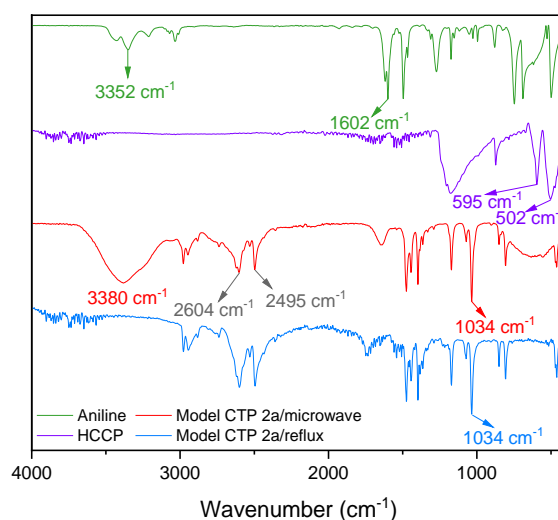
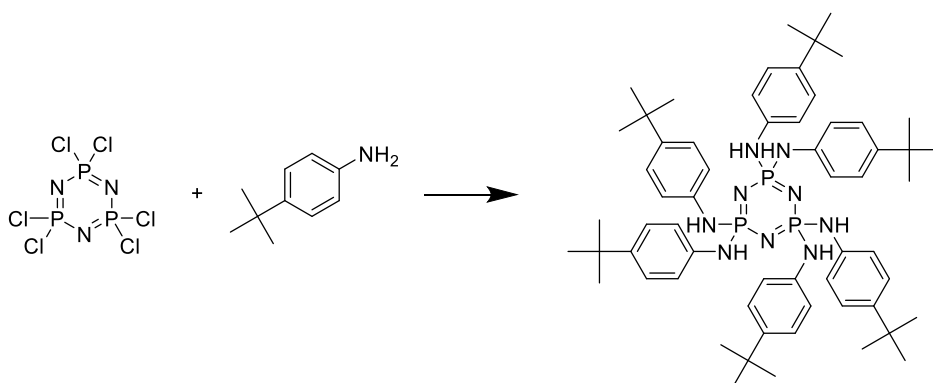


Figure 4.8 FT-IR of Model CTP 2a and their monomers.

Model CTP 2a was characterized by FT-IR. It was speculated that N–H vibration peaks in their FT-IR spectra are probably present (because amine-based CTP-PIMs contain –NH–), but weaker than that of diamines (with –NH₂). There are also peaks at 502–595 cm^{-1} from unsubstituted P–Cl, as the crowded macromolecular structure hinders amine groups from fully approaching all available chlorides. Therefore, the confirmation of a successful synthesis of amine-based CTP-PIM would focus on the formation of P–N–Ar bonds. Microwaved Model CTP 2a showed a strong peak at 3380 cm^{-1} , corresponding to N–H stretching vibration, which is inferred to be the residue of aniline monomer. Similarly, no sharp peak but a strong flat peak of P–Cl is observed in the range of 502–595 cm^{-1} , which also hints at unreacted starting material. The sharp peak at 1034 cm^{-1} is considered to belong to the P–N(Ar) stretching. Therefore, the product is believed to be Model CTP 2a mixed with residual monomers. In the spectrum of refluxed Model CTP 2a, a strong peak of P–N(Ar) stretching also appeared at 1034 cm^{-1} . Meanwhile, no obvious peaks of starting materials were observed around 3352 cm^{-1} and 502–595 cm^{-1} . In view of these features, the outcome

of the refluxed reaction can be considered purer than the microwaved one. Peaks at 2605 cm^{-1} and 2495 cm^{-1} were found in both spectra, proving the difficulty to remove the by-product triethylammonium chloride.

4.2.2.2 Model CTP 2b



Scheme 4.7 Synthesis of Model CTP 2b.

Since the complex purification process and unstable product of Model CTP 2a synthesis, the research on model compounds of amine-based CTP-PIMs turned to Model CTP 2b, which was prepared with tert-butyl-aniline and HCCP and expected to precipitate directly from the reaction system at room temperature, because of the higher molecular weight given by the t-Butyl groups. The explored reaction conditions are summarised in **Table 4.6**. The first reaction was carried out in a microwave reactor with MeCN as solvent³⁰² and became turbid after heating for 1.5 hours. The solid was filtered and fast washed with MeCN twice, giving a very low yield of ~1%. Nevertheless, this demonstrated Model CTP 2b is easier to precipitate than Model CTP 2a. Afterwards, several solvents commonly used in reported reactions of HCCP and amino compounds were tested, including anhydrous THF,³¹⁰ acetone,³¹¹ petroleum ether:DCM (v:v=7:3)³¹² and dioxane³¹³. Among them, the reactions in dioxane and anhydrous THF afforded Model CTP 2b products exhibiting highly similar peaks on FT-IR spectra. Although dioxane provided a slightly higher yield of 50%, considering its toxicity and high boiling point, anhydrous THF could offer an acceptable yield of 42% and a safer work-up operation.

Table 4.6 Attempted Conditions for Preparing Model CTP 2b.

HCCP	t-Bu-aniline	Et ₃ N	Solvent	Conditions	Work-up	Products
0.3 mmol (1 eq.)	4.4 mmol (15 eq.)	14.4 mmol (50 eq.)	MeCN 15 mL	Microwave 40 °C 1.5, 3, 4.5, 6 hrs	Rotary evaporation	Mixture of starting materials and Model CTP 2b
			anhydrous THF 15 mL		filtration	Model CTP 2b Y = 42%
0.3 mmol (1 eq.)	4.4 mmol (15 eq.)	14.4 mmol (50 eq.)	acetone 15 mL	Microwave 40 °C 1.5 hrs	filtration	Hydrolysed in work-up
			7PET:3DCM 15 mL		filtration	Hydrolysed in work-up
0.6 mmol (1 eq.)	8.8 mmol (15 eq.)	28.8 mmol (50 eq.)	dioxane 15 mL	Microwave 40 °C 1.5 hrs	filtration	Model CTP 2b Y = 50%
1.1 mmol (1 eq.)	6.9 mmol (6 eq.)	17.9 mmol (16 eq.)	anhydrous THF 18 mL	Reflux 60 °C 72 hrs	Rotary evaporation	Starting materials
1.1 mmol (1 eq.)	6.9 mmol (6 eq.)	17.9 mmol (16 eq.)	MeCN 3.4+15 mL	Reflux 80 °C 24 hrs	Rotary evaporation Crystallization ice bath	Mixture of start materials and Model CTP 2b Model CTP 2b Y = 18%

In contrast, the refluxed reaction produced no precipitate in THF and only slight turbidity in MeCN, which became clear and transparent within 5 minutes after stopping the heating. This reaction was repeated and immediately cooled in an ice bath to crystallize. The final Model CTP 2b product was obtained with a low yield of 18%, hence significantly lower than that obtained on the microwave irradiation method.

The FT-IR of Model CTP 2b (**Fig 4.9**) proved that microwave irradiation offered a better yield to the product than under reflux. A flat peak at 3394 cm⁻¹ in the spectrum of refluxed product corresponds to the N–H stretching, that was not observed in the microwaved Model CTP 2b. The rest peaks in the two spectra showed a high similarity. There were P–N stretching peaks at 1034 cm⁻¹, and no P–Cl vibration in the range of 502–595 cm⁻¹ found in both products. The peaks of triethylammonium chloride at 2605 cm⁻¹ and 2495 cm⁻¹ appeared in both as well.

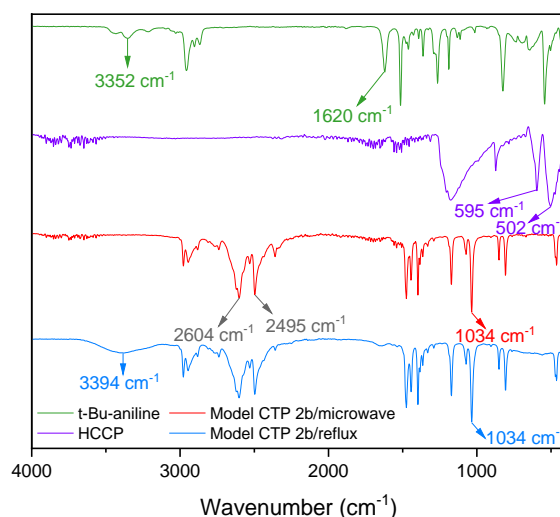
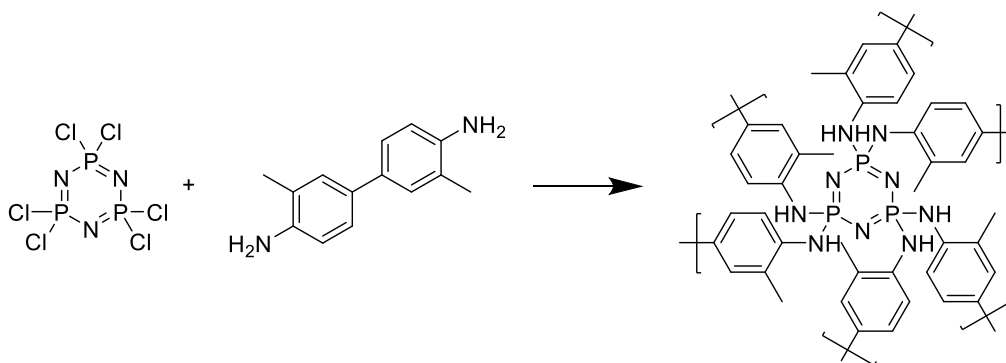


Figure 4.9 FT-IR of Model CTP 2b and their monomers.

It is concluded that, overall, microwave irradiation is a better heating method for Model CTP 2b than normal bench reflux, giving higher yields and purity. However, the purification method needs to be improved, to not only remove the by-product triethylammonium chloride, but also to prevent the hydrolysis of Model CTP 2b.

4.2.2.3 CTP-tolidine-PIM

To translate the results of the model compounds into a potential polymerisation, we started with the synthesis of CTP-tolidine-PIM, which was prepared with HCCP and o-tolidine as the diamine monomer. The product was expected to be a highly networked polymer and so, theoretically, insoluble in common organic solvents. Therefore, we anticipated that CTP-tolidine-PIM should have been easier to precipitate at room temperature than the small model compounds, and so allowed to be collected by simple vacuum filtration.



Scheme 4.8 Synthesis of CTP-tolidine-PIM.

A quick attempt was conducted using MeCN as the solvent according to results from previously published works.³⁰² In our case, similarly to the two model compounds prepared on the same conditions, no obvious solid product was observed, confirming that the published procedure was not useful to make our amine-based CTP products. After that, the polymerisation in anhydrous THF was explored using respectively microwave irradiation and reflux. Details of the conditions are listed in **Table 4.7**.

Table 4.7 Attempted Conditions for Preparing CTP-tolidine-PIM.

HCCP	Tolidine	Et ₃ N	Solvent	Conditions	Work-up	Products
0.3 mmol (1 eq.)	1.3 mmol (15 eq.)	14.4 mmol (50 eq.)	MeCN 15 mL	Microwave 40 °C 1.5, 3, 4.5, 6 hrs	Rotary evaporation	Almost starting materials
1.1 mmol (1 eq.)	3.2 mmol (3 eq.)	12.9 mmol (12 eq.)	anhydrous THF 20 mL	Microwave 80 °C 1 hr	Filtration and fully wash	Mixture of start materials and CTP-tolidine-PIM
					Crystallization ice bath	Mixture of start materials and CTP-tolidine-PIM
1.1 mmol (1 eq.)	3.2 mmol (3 eq.)	12.9 mmol (12 eq.)	anhydrous THF 10+5 mL	Reflux 80 °C 24 hrs	Filtration and fully wash	Mixture of start materials and CTP-tolidine-PIM
					Crystallization ice bath	Mixture of start materials and CTP-tolidine-PIM

The obtained solid products were first collected by filtration and washed with anhydrous THF until the filtrate became colourless and characterized after being dried under vacuum. Their FT-IR spectra (in **Fig 4.10 a**) proved to be almost identical, showing a very weak peak at 3350–3354 cm⁻¹, which may come from the N–H stretching. The P–N stretching at 1062 cm⁻¹ was also very weak, but strong P–Cl peaks around 563 cm⁻¹ were clearly observed. This indicates that a large number of chlorides were not successfully substituted by the nitrogen of the tolidine to form P–N bonds. Relevant peaks that hint at the presence of triethylammonium chloride were not found in both spectra, suggesting that washing can effectively remove this by-product. However, the continuous washing is suspected to cause hydrolysis of the final product.

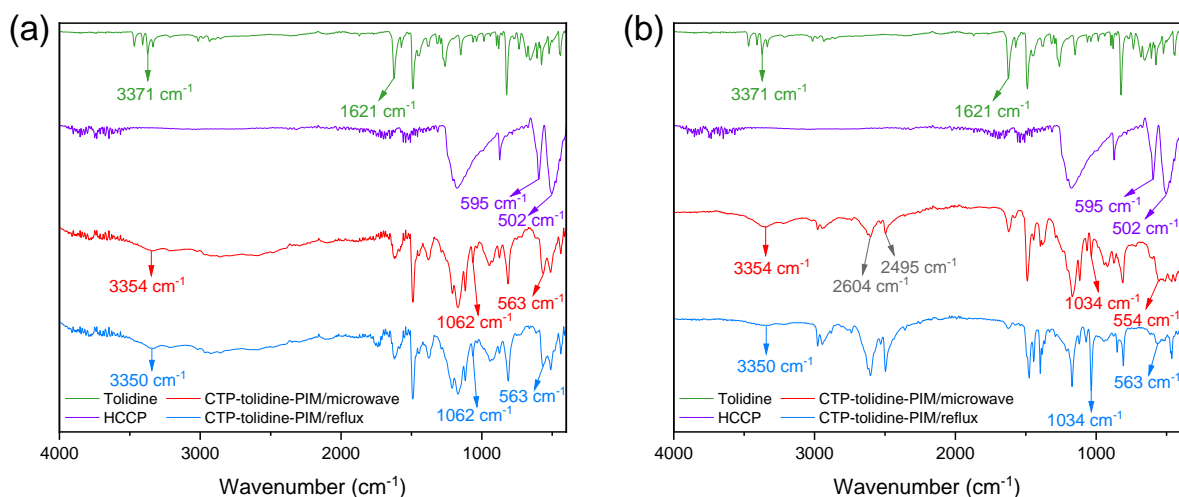


Figure 4.10 FT-IR of CTP-tolidine-PIMs and their monomers: (a) fully washed products, (b) crystallized products.

To verify it, the two polymerisations were repeated and cooled in an ice bath immediately after stopping the heating. The products were filtrated and only quickly washed two times with anhydrous THF. As shown in **Fig 4.10 b**, the purity of microwaved product was not significantly improved. While the reflux product showed a slightly stronger P–N stretching peak at 1034 cm^{-1} and a weaker P–Cl peak around 563 cm^{-1} than the one in **Fig 4.10 a**. It is deduced that the reflux conditions offer a higher degree of polymerisation than the microwave irradiation. In addition, the peaks at 2605 cm^{-1} and 2495 cm^{-1} in both products prove the remains of triethylammonium chloride due to insufficient wash.

Although the purity of the product requires further enhancement, TGA in N_2 reflects the excellent thermal properties of CTP-tolidine-PIM. As shown in **Fig 4.11** and **Table 4.8**, char yields of CTP-tolidine-PIMs were significantly higher than that of the two catechol-based CTP-PIMs previously discussed, which is believed to be due to the higher nitrogen content per repeat unit, confirming the results obtained from TB-HPB-PIMs (see **Table 3.4**, **Fig 3.10** and relevant discussion in Chapter 3). The large weight losses of the two CTP-tolidine-PIM samples in the range of $235\text{--}305\text{ }^\circ\text{C}$ originated from the unreacted monomers and oligomers. The T_{max} at $524\text{ }^\circ\text{C}$ and $528\text{ }^\circ\text{C}$ derived from the thermal decomposition of the main chains of two polymers. As mentioned above, phosphorus acids and ammonia were released at this stage promoting the

formation of the protective carbon layer, which collapses at 841 °C. Overall, thermal decomposition behaviours of the two CTP-tolidine-PIM products are almost the same.

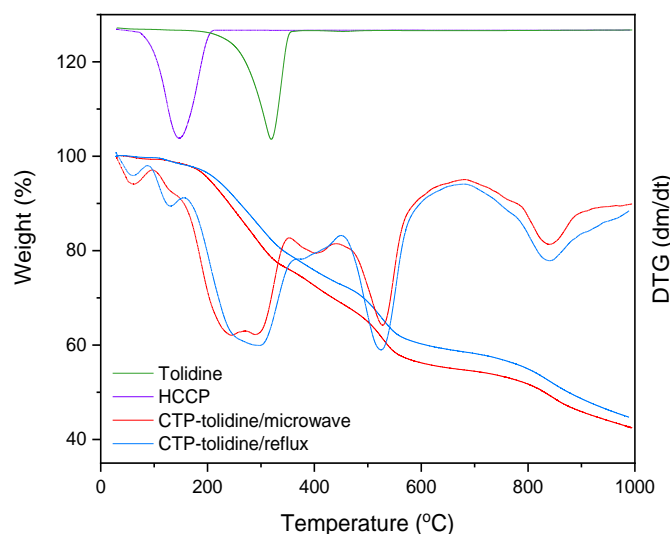


Figure 4.11 TGA and DTG in N₂ of CTP-tolidine-PIMs and DTG of their monomers.

Table 4.8 Thermal Properties of CTP-tolidine-PIMs.

CTP-tolidine-PIM	C/P/N	Decomposition Temperature (°C)			T _{max} (°C)	Char Yield (%)
		T _{d5}	T _{d10}	T _{d20}		
reflux	14/1/3	217	261	342	294, 524	45
microwave		204	241	308	246, 528	43

It is worth noting that the unsubstituted chloride groups might also cause a positive effect on their thermal stability. However, it does not mean the chlorides are worth to be retained in the product. Conversely, it is necessary to promote the substitution reaction in future work to minimize the residual chloride groups, because of the toxicity and corrosiveness of halogen elements (see **1.2.3.1** in Chapter 1).

4.3 Conclusion

In this chapter, two heating methods, namely microwave irradiation and general bench reflux, were used for the preparation of both catechol and amine-based CTP-PIMs. Through optimizing the experimental conditions, three model compounds were successfully synthesized, proving the feasibility of the preparation of catechol and amine-based CTP-PIMs. Based on the synthesis of model compounds, the conditions of polymerisations were further explored, and two catechol-based CTP-PIMs were successfully obtained. Their thermal decomposition behaviours in N₂ reflected the

great potential to be applied in the field of flame retardation. Regarding bis-catechol like PIMs, CTP-SBI-PIM performed a better thermal stability than CTP-SBC-PIM. The preparation of an amine-based CTP-PIM, instead, was only preliminarily explored as amine-based CTP compounds proved to be difficult to synthesize. Although its purity requires further improvement in future work, CTP-tolidine-PIM shows desirable thermal decomposition behaviours and significantly higher char yield than catechol-based CTP-PIMs, indicating its great potential to be developed as a FR. Compared to better-developed polymers (in **Table 1.2**), the thermal properties of CTP-PIMs are obviously lower, which are expected to be enhanced in the future by improving the synthesis conditions. Unfortunately, due to the lack of stability and easy hydrolysis, no porosity measurements of CTP-PIMs were successfully conducted. Despite our strong belief that these polymers should be porous (because the geometry of the monomers is typical of PIMs), the lack of stability prevented us from assessing the importance or not of the porosity in these new polymers.

Chapter 5 – Conclusions and Future Work

In this project, we innovatively proposed to use PIMs as FRs, which was never done before. Based on their known thermal stability, boron, nitrogen and phosphorus atoms were introduced to specifically improve the flame retardancy of PIMs, obtaining good results. Besides, CO₂ uptake and CO₂/N₂ selectivity of them were also researched, especially considering their intrinsic microporosity.

The work discussed in Chapter 2, shows the design of two types of boron-containing PIMs: boroxine-based PIMs and BE-PIMs. To test the feasibility of the reaction we prepared single molecules model compounds. The model boroxine were prepared by microwave irradiation and traditional heating respectively. The microwave irradiated product showed ideal microporosity and thermal decomposition behaviour measured in N₂, which was consistent with the mechanism of boron-containing FRs, proving the feasibility of boroxine-based PIMs preparation. Bromine-SBF precursor and bromine-TPB precursor were successfully synthesized. TPB-boronic acid monomers were prepared by lithium-halogen exchange reaction, of which reproducibility and product purity require further improvement in the future. SBF-boronic acid monomers could not be synthesized by similar conditions, though. As a future work, we believe that the lithium-halogen exchange reaction needs to be optimized to obtain pure boronic acid monomers, in order to synthesize the corresponding boroxine-based PIMs. Meanwhile, six BE-PIMs were respectively prepared by microwave irradiation and traditional heating helped by Dean-Stark, so that we could remove water formed during the polymerisation. Except from BE-bis-K-PIM, the purity of other five polymers afforded by the Dean-Stark system seems better than that corresponding obtained from microwave irradiation. Considering the comprehensive performance of their thermal stability measured in N₂ and CO₂ adsorption and selectivity, BE-SBF-Me-PIM shown the best properties, followed by BE-SBF-PIM. We expect improved performance and more precise analysis on pure BE-PIMs by further optimizing the polymerisation conditions in the future.

In Chapter 3, nitrogen was introduced via TB polymerisation into the skeleton of PIMs, in the attempt to improve/tune their flame retardant properties. Four TB-HPB-PIMs and three "linear" TB polymers were successfully synthesized, characterized, and analyzed for their thermal properties, CO₂ adsorption, and gas selectivity. TGA in N₂ confirmed that highly functionalised tetra-TB-HPB and hexa-TB-HPB exhibited superior thermal stability comparing to di-TB-HPBs, attributed to the combined effect of their low C/N ratio and high porosity. However, TGA in air suggested the opposite tendency. This infers that the high-porosity materials are excessively exposed to oxygen in the air, affecting their thermal stability. It is expected to be solved in the future by introducing boron atoms (that can form a dense glassy protective layer at high temperatures) to construct the B-N synergistic system. Tetra-TB-HPB and hexa-TB-HPB also exhibited excellent CO₂ adsorption and selectivity, due to the combined effect of high surface area, nitrogen content, and narrow microporosity.

In Chapter 4, CTPs were used as the core unit to introduce a high proportion of both nitrogen and phosphorus. Three model compounds were successfully synthesized by reacting respectively catechol and amino monomers with HCCP, demonstrating the feasibility of preparing CTP-PIMs. On this basis, the polymerisation conditions were further optimized, and two catechol-based CTP-PIMs were successfully obtained, both of which showed desirable thermal decomposition behaviours. The thermal stability measured in N₂ of CTP-SBI-PIM proved to be better than CTP-SBC-PIM. In contrast, the preparation of amine-based CTP-PIM demonstrated much more challenging, because of the crowded molecular structures. Although their purity needs to be further increased in the future, CTP-tolidine-PIM displayed a satisfactory thermal decomposition behaviour in N₂, and its char yield was significantly higher than the two catechol-based CTP-PIMs, indicating the great potential before being developed as a FR. Unfortunately, the porosity of CTP-PIMs failed to be evaluated due to lack of stability and easy hydrolysis. It is believed that they should be porous because the conformation of their monomers has the typical contortion of PIMs. We suggest that research on CTP-PIMs in next work focus on improving the purity and stability of the polymers, and then explore their thermal stability and microporosity.

Furthermore, although TGA results in N₂ have fully proven their thermal stability, all the PIMs are expected to be further characterized on flame retardancy with more

specific tests like LOI test and cone calorimeter, when enough amounts of the pure products are obtained.

Our study in this project is just the first step towards PIMs in the flame retardation field, and it has shown great potential. We expect that more research on the suitable synthesis methods and macromolecular structures will be conducted to expand the family of PIM FRs. We believe that this project pioneered the application of PIM in the field of flame retardation and lays the foundation for the research on multifunctional PIMs as flame retardant additives and gas separation materials.

This is of course a preliminary study on the use of PIMs for flame retardant applications, but considering that we were able to prepare high performing polymers even with cheap and available starting materials (for instance the "linear" TB polymers) we can say that they have a great potential for future flame retardancy applications.

Chapter 6 – Experimental Section

6.1 General Methods and Equipment

Commercially available reagents and gases were used without further purification. All reactions using air/moisture sensitive reagents were performed in oven-dried or flame-dried apparatus, under a nitrogen atmosphere.

TLC analysis refers to analytical thin layer chromatography, using aluminium-backed plates coated with Merck Kieselgel 60 GF254. Product spots were viewed either by the quenching of UV fluorescence, and in some cases by staining with permanganate stain (Preparation: potassium permanganate (3 g) + potassium carbonate (20 g) + 5% aqueous NaOH (5 mL) + water (300 mL)).

Melting points (Mp) were recorded using a Cole-Parmer Stuart™ Digital Melting Point Apparatus and are uncorrected.

FT-IR spectra were recorded using a PerkinElmer Spectrum Two FT-IR Spectrometer.

Low-resolution mass spectrometry (LRMS) were measured using The Advion Interchim Scientific expression® compact mass spectrometer.

^1H NMR spectra were recorded in deuterated solvent, as stated, using an Avance Bruker DPX 500 (500 MHz) instruments, with ^{13}C NMR spectra recorded at 126 MHz and ^{31}P NMR spectra recorded at 202 MHz.

SSNMR spectra were recorded using a Bruker Avance III spectrometer equipped with a wide-bore 9.4 T magnet (Larmor frequencies of 100.9 MHz for ^{13}C), operated by Dr. Daniel Dawson from the University of St Andrews. Samples were packed into standard zirconia rotors with 4 mm outer diameter and rotated at a magic angle spinning (MAS) rate of 12.5 kHz. Spectra were recorded with cross polarisation (CP) from ^1H using a contact pulse (ramped for ^1H) of 1.5 ms. High-power ($\nu_1 \approx 100$ kHz) TPPM-15 decoupling of ^1H was applied during acquisition to improve resolution. Signal averaging was carried out for 6144 transients with a recycle interval of 2 s. Chemical shifts are reported in ppm relative to $(\text{CH}_3)_4\text{Si}$ (TMS) using the CH_3 signal of L-alanine ($\delta = 20.5$ ppm) as a secondary solid reference.

Low-temperature N₂ (77 K and 298 K) and CO₂ (195 K, 273 K and 298 K) adsorption/desorption measurements of polymer powders were made using a Quantachrome Nova-e. Samples were degassed over 8 hrs at 80 °C under high vacuum prior to analysis. The gases were supplied by BOC and used without any further purification (N₂: purity > 99.999%; CO₂: purity > 99.995%). The specimen was measured twice in two different stations to minimize the error, providing the same results. The data were analysed with the software provided with the instrument. S_{ABET} was calculated from CO₂ adsorption isotherm at 273 K and a relative pressure P/P₀ < 0.1. NLDT and H-K analysis were performed to calculate the PSD and volume, considering a carbon equilibrium transition kernel at 273 K based on a slit-pore model; the kernel is based on a common, one centre, Lennard-Jones model. Heats of adsorption were calculated from the CO₂ curves measured at 237 K and 298 K. The data were analysed with the QuadraWin software and fitted with the Langmuir-Freundlich equation and calculated via the Clausius-Clapeyron equation.

TGA were performed using the device Simultaneous Thermal Analyzer STA Q6000 at a heating rate of 10 °C/min from 30 to 995 °C under gas flow at 20 mL/min (N₂: purity > 99.999%; air: 21% ± 0.5% oxygen, balance nitrogen).

SEM images were recorded with a Hitachi S-4800 field emission (~1 nm resolution) in secondary electron mode. SEM samples were coated with chromium / 5 nm using a Quorum Technologies Q150TE Coater.

Microwave irradiation reactions were conducted in the Discover® 2.0 microwave reactor (method: close vessel reaction, no pressure, power ≤ 300 W).

6.2 IAST Selectivity Calculation

IAST of Myers and Prausnitz²⁶⁹ is typically used to the selectivity of binary mixtures of gases from the single isotherms. The isotherms were fitted with Dual-Site Langmuir-Freundlich using the software IAST++²⁷⁰ and the selectivity (S) was calculated according to the formula:

$$S = \frac{Q_{\text{CO}_2}}{Q_{\text{N}_2}} \times \frac{P_{\text{N}_2}}{P_{\text{CO}_2}}$$

Were

P_{CO_2} is the partial pressure of CO_2 (Pa or atm)

P_{N_2} is the partial pressure of N_2 (Pa or atm)

Q_{N_2} is the N_2 uptake (mg/g or mmol/g)

Q_{CO_2} is the CO_2 uptake (mg/g or mmol/g)

6.3 Synthesis of Monomers

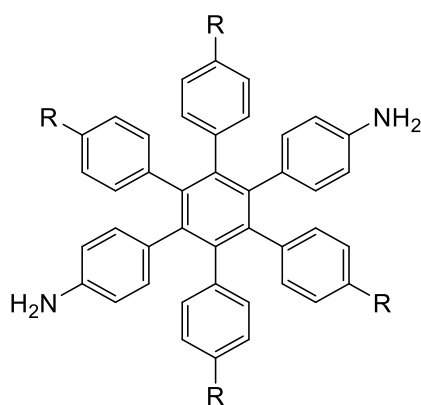
General procedure A for substituted CPDs

Substituted diphenyl acetone (1.0 eq.) and benzil (1.0 eq.) were refluxed in a solution of KOH (0.5 eq.) in ethanol (10 mL per 0.1 g KOH) for 2 hrs. The reaction was allowed to cool and filtered under vacuum. The product was washed three times with water and once with ethanol to yield a dark powder.

General procedure B for substituted HPBs

Substituted CPD (1.0 eq.) and diphenyl acetylene (1.1 eq.) were mixed in a hydrothermal synthesis reactor and heated in the oven at 250 °C for 2 hrs (ramped at 5 °C/min). The reaction was allowed to cool to room temperature. The solid was transferred to a sintered funnel with cold MeOH, filtered and washed with warm hexane three times, and dried under vacuum affording the final products.

General procedure C for di- and hexa-amino-HPBs



Nitro-substituted HPB was added to an appropriate amount of THF and stirred under N_2 atmosphere for 15 min. A spatula tip of Raney Nickel was quickly added into the solution, followed by dropwise adding hydrazine monohydrate (5.0 eq. per 1.0 eq. of nitro group). The reaction was refluxed at 60 °C overnight and then cooled to room

temperature. The Raney Nickel was isolated by filtration over celite, washed with warm THF and disposed into aqua regia. Collected filtrate was evaporated under reduced pressure. The raw product was refluxed in MeOH overnight and hot filtered to afford a brown solid.

General procedure D for BE-PIMs/Dean-Stark reaction

Benzene-1,4-diboronic (1.0 mmol) acid and bis-catechol monomers (1.0 mmol) were added 50 mL of toluene/MeOH (v:v=4:1). The reaction was stirred in a Dean-Stark trap at 120 °C for an appropriate time. After cooling to 70 °C, the reaction was immediately filtered off and thoroughly dried under vacuum overnight at 50 °C to afford the final product.

General procedure E for BE-PIMs/microwave reaction

Bis-catechol monomers and benzene-1,4-diboronic acid were irradiated in the microwave reactor under vigorously stirring at 150 °C for an appropriate time. After cooling down to room temperature, the product was filtered, quickly washed with the solvent and thoroughly dried under vacuum at 50 °C.

General procedure F for TB-PIMs³¹⁴

The aromatic amine was dissolved in dimethoxymethane (2.0–2.5 eq. per 1.0 eq. of amino group) at 0 °C. An appropriate amount of trifluoroacetic acid was added dropwise, and the mixture was stirred at room temperature for 2 to 4 days. Modest amount of DCM was allowed to add if needed (to better dissolve the aromatic amine). The reaction mixture was then slowly poured into vigorously stirred aqueous ammonium hydroxide solution (100 mL) at 0 °C and left for 4 hrs. The resulting solid was collected by filtration, washed with water and refluxed with acetone, THF, DCM and MeOH in turn. The final polymer was filtered and dried under vacuum at 80 °C overnight.

General procedure G for CTP-based Model Compounds and PIMs/reflux reaction

Catechol or amine monomers and Et₃N were fully dissolved into an appropriate solvent as Solution A. HCCP was added in the solvent to form Solution B. Solution B was added dropwise into Solution A under stirring and refluxed for an appropriate time. The

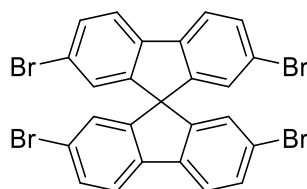
reaction was filtered and quickly washed with the solvent. The product was thoroughly dried under vacuum at 80 °C.

General procedure H for CTP-based Model Compounds and PIMs/microwave reaction

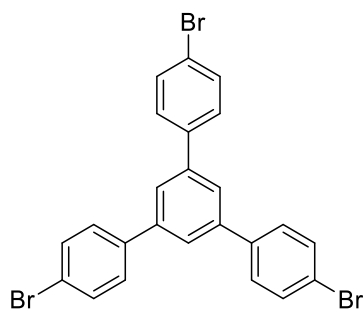
Catechol or amine monomers and Et₃N were fully dissolved in an appropriate solvent, followed by adding HCCP. The mixture was irradiated in a microwave reactor under N₂ atmosphere for an appropriate time. After cooling down to room temperature, the product was filtered, quickly washed with the solvent and thoroughly dried under vacuum at 80 °C.

5,5',6,6'-tetrahydroxy-1,1'-spirobisindane-3,3'-dione (Bis-K-bis-catechol),¹¹³ 1,4-di(3',4'-dihydroxyphenyl)-2,3,5,6-tetraphenylbenzene (HPB-bis-catechol),¹⁰³ 2,2',3,3'-tetrahydroxy-9,9'-spirobifluorene (SBF-bis-catechol)⁹³ and 2,2',3,3'-tetrahydroxy-6,6'-dimethyl-9,9'-spirobifluorene (SBF-Me-bis-catechol)¹⁰² were obtained according to the corresponding literature.

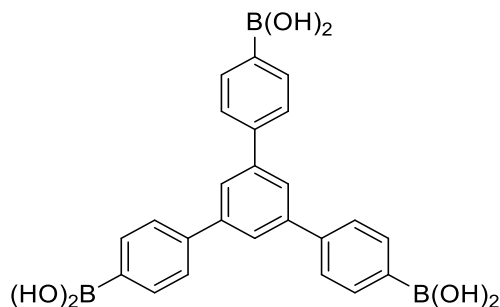
2,2',7,7'-Tetrabromo-9,9'-spirobifluorene (Tetrabromo-SBF)²⁵⁴



9,9'-Spirobifluorene (0.32 g, 1.0 mmol, 1.0 eq.) and ferric chloride (8 mg, 0.05 mmol, 0.05 eq.) were dissolved in chloroform (2.5 mL). Bromine (0.4 mL, 7.8 mmol, 7.8 eq.) was added dropwise at 0 °C. After stirring at 0 °C for 1 hr, the solution was warmed to room temperature and stirred for 4 hrs. The resulting slurry was washed with saturated sodium thiosulfate until the red colour disappeared. The aqueous phases were extracted with DCM (3x20 mL). Combined organic phases were dried over anhydrous MgSO₄, filtered, and evaporated under reduced pressure to afford white crystals (0.62 g, 65%). Mp, >300 °C (lit³¹⁵ >320 °C). ¹H NMR (500 MHz, Chloroform-*d*): δ 7.68 (d, *J* = 8.1 Hz, 4H), 7.54 (dd, *J* = 8.2, 1.8 Hz, 4H), 6.83 (d, *J* = 1.8 Hz, 4H). ¹³C NMR (126 MHz, Chloroform-*d*): δ 149.0, 139.7, 131.9, 127.5, 122.3, 121.8. LRMS (APCI+) *m/z* for [C₂₅H₁₂Br₄]⁺: calculated 629.77, found: 628.14.

1,3,5-Tris(4-bromophenyl) benzene (TBPB)²⁵⁶

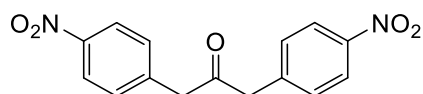
4'-Bromoacetophenone (10.00 g, 50.2 mmol, 1.0 eq.) was solubilized in 15 mL anhydrous ethanol in an ice bath. Thionyl chloride (10 mL, 138 mmol, 2.8 eq.) was added dropwise under vigorous stirring. The solution was allowed to warm up to 60 °C and stirred for 2 hrs. Afterwards, the suspension was cooled in an ice bath and water (40 mL) was added slowly under stirring. The precipitate was collected and washed with water and hot ethanol until the filtrate became colourless, then dried under vacuum afforded a yellow solid (5.34 g, 59%). Mp, 254 °C (lit³¹⁶ >200 °C). ¹H NMR (500 MHz, Chloroform- *d*): δ 7.69 (s, 3H), 7.61 (d, *J* = 8.5 Hz, 6H), 7.53 (d, *J* = 8.4 Hz, 6H). ¹³C NMR (126 MHz, Chloroform- *d*): δ 141.7, 139.8, 132.2, 129.0, 125.1, 122.3. LRMS (APCI+) *m/z* for [C₂₄H₁₅Br₃]⁺: calculated 541.87, found: 542.20.

1,3,5-Tris(4-phenylboronic acid)benzene (TPB-triboronic acid)²⁵⁷

To a vigorously stirred solution of 1,3,5-tris((4-bromophenyl))benzene (3.10 g, 5.7 mmol, 1.0 eq.) in anhydrous THF (100 mL), *n*-BuLi solution in hexanes (2.5 M, 11.4 mL, 28.6 mmol, 5.0 eq.) was added dropwise at -78 °C. After stirring for 2 hrs at room temperature, triisopropyl borate (7.4 mL, 32.1 mmol, 5.5 eq.) was added dropwise. The solution was stirred for 1 hr at -78 °C then warmed to room temperature and stirred overnight. The reaction was quenched by brine and extracted with DCM (3x200 mL). Combined organic phases were dried over anhydrous MgSO₄ and evaporated under reduced pressure to afford a brown powder. The crude product was stirred in 40 mL

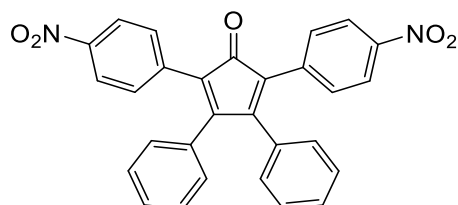
of water, and 2 M HCl (aq.) added slowly until pH = 3 was reached. After fully stirring for 1 hr, the system was neutralized with 2 M of NaOH (aq.). The product was filtered and washed with water and hot hexane three times. then dried under vacuum giving a pale brown solid (1.2 g, 56%). Mp, >300 °C (lit²⁵⁷ >300 °C). ¹H NMR (500 MHz, DMSO-*d*₆) δ 8.09 (s, 6H), 7.93 (d, *J* = 7.2 Hz, 9H), 7.85 (d, *J* = 7.9 Hz, 6H). ¹³C NMR (126 MHz, DMSO-*d*₆) δ 141.6, 134.7, 126.1. LRMS (APCI+) *m/z* for [C₂₄H₂₁B₃O₆]⁺: calculated 438.16, found: 437.71.

1,3-Bis(p-nitrophenyl) acetone (1a)



Et₃N (30.6 mL, 0.22 mmol, 2.2 eq.) was added dropwise to a stirred solution of 4-nitrophenyl acetic acid (18.10 g, 0.1 mmol, 1.0 eq.) in 90 mL of acetic anhydride. After 1.5 hrs, the reaction mixture was slowly poured into 100 mL of cold 15% HCl and a yellow-orange solid was collected and washed with water. The solid was added to a mixture of THF (50 mL) and 9M H₂SO₄ (100 mL) and refluxed overnight. After cooling down, 50 mL of water was added into the system, and extracted with DCM (3x200 mL). The organic extract was dried over anhydrous MgSO₄, filtered, and evaporated under reduced pressure. Then the crude product was refluxed with ethanol at 80 °C for 1 hr and hot filtered to afford a yellow solid (10.57 g, 70% yield). Mp, 179–181 °C (lit³¹⁷ 178–180 °C). ¹H NMR (500 MHz, Chloroform-*d*): δ 8.23 (d, *J* = 8.7 Hz, 4H), 7.37 (d, *J* = 8.7 Hz, 4H), 3.95 (s, 4H). ¹³C NMR (126 MHz, Chloroform-*d*): δ 201.9, 147.8, 141.5, 131.4, 124.0, 49.0. LRMS (APCI+) *m/z* for [C₁₅H₁₂N₂O₅]⁺: calculated 300.27, found: 300.70.

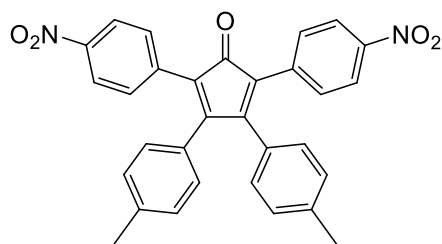
2,5-Bis(p-nitrophenyl)-3,4-diphenyl-2,4-cyclopentadien-1-one (3a)



Synthesis of **3a** followed the general procedure A. **1a** (4.81 g, 16.0 mmol) and benzil (3.40 g, 16.0 mmol) were refluxed in a solution of KOH (0.45 g, 8.0 mmol) in ethanol (45 mL) for 2 hrs to yield a red-black powder (5.09 g, 67% yield). Mp, 242–245 °C

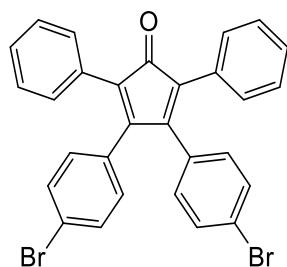
(lit³¹⁸ 245 °C). ¹H NMR (500 MHz, Chloroform-*d*): δ 8.14 (d, *J* = 8.9 Hz, 4H), 7.43 (d, *J* = 8.9 Hz, 4H), 7.37 (d, *J* = 7.5 Hz, 2H), 7.26 (d, *J* = 7.7 Hz, 4H), 6.93 (d, *J* = 8.7 Hz, 4H). ¹³C NMR (126 MHz, Chloroform-*d*): δ 197.4, 157.6, 146.9, 137.1, 131.7, 130.8, 129.7, 129.0, 128.6, 124.8, 123.4. LRMS (APCI-) *m/z* for [C₂₉H₁₈N₂O₅]⁻: calculated 474.46, found 474.43.

2,5-Bis(p-nitrophenyl)-3,4-bis(p-tolyl)-2,4-cyclopentadien-1-one (3b)



Synthesis of **3b** followed the general procedure A. **1a** (4.81 g, 16.0 mmol) and 4,4'-dimethylbenzil (3.80 g, 16.0 mmol) were refluxed in a solution of KOH (0.45 g, 8.0 mmol) in ethanol (45 mL) for 2 hrs to yield a purple-black powder (4.18 g, 52% yield). Mp, 157–159 °C. ¹H NMR (500 MHz, Chloroform-*d*): δ 8.04 (d, *J* = 8.9 Hz, 4H), 7.33 (d, *J* = 8.9 Hz, 4H), 6.97 (d, *J* = 8.0 Hz, 4H), 6.72 (d, *J* = 8.1 Hz, 4H), 2.28 (s, 6H). ¹³C NMR (126 MHz, Chloroform-*d*): δ 198.1, 157.8, 146.9, 137.6, 130.9, 129.9, 129.4, 129.3, 128.8, 124.0, 123.5, 21.6. LRMS (APCI+) *m/z* for [C₃₁H₂₂N₂O₅]⁺: calculated 502.52, found 502.41.

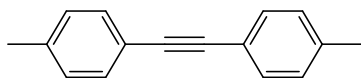
2,5-Diphenyl-3,4-bis(p-bromophenyl)-2,4-cyclopentadien-1-one (3c)



Synthesis of **3c** followed the general procedure A. 1,3-Diphenylacetone (1.05 g, 5.0 mmol) and 4,4'-dibromobenzil (1.84 g, 5.0 mmol) were refluxed in a solution of KOH (0.14 g, 2.5 mmol) in ethanol (14 mL) for 2 hrs to yield a purple-black powder (2.52 g, 83% yield). Mp, 236–238 °C (lit³¹⁹ 233 °C). ¹H NMR (500 MHz, Chloroform-*d*) δ 7.32 (d, *J* = 8.2 Hz, 4H), 7.24 (overlapping, m, 6H), 7.20–7.12 (overlapping, m, 4H), 6.76 (d, *J* = 8.2 Hz, 4H). ¹³C NMR (126 MHz, Chloroform-*d*) δ 199.7, 152.7, 131.8, 131.7,

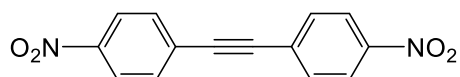
131.1, 130.4, 130.2, 128.4, 128.0, 126.1, 123.3. LRMS (APCI+) m/z for $[C_{29}H_{18}Br_2O]^+$: calculated 542.26, found 542.80.

1,2-Bis(p-tolyl)ethyne (4b)



2-Butynedioic acid (2.28 g, 20.0 mmol, 1.0 eq.), $Pd(PPh_3)_4$ (1.16 g, 1.0 mmol, 0.05 eq.), 1,4-bis(diphenylphosphino)butane (0.85 g, 2.0 mmol, 0.1 eq.) and 4-bromotoluene (6.84 g, 40.0 mmol, 2.0 eq.) were combined with DBU (6.09 g, 40.0 mmol, 2.0 eq.) in 100 mL of dimethyl sulfoxide. The resulting mixture was stirred at 110 °C for 2.5 hrs. The reaction was neutralised in 42 mL of saturated aqueous ammonium chloride and extracted with diethyl ether (4×35 mL). The organic extracts were washed with brine (100 mL), dried over $MgSO_4$ and filtered. The solvent was evaporated under reduced pressure. The crude product was recrystallised in ethanol/water. The final product was collected by filtration which afforded a yellow-brown crystal (2.05 g, 50% yield). Mp, 137–138 °C (lit³²⁰ 136.5–137.8 °C). 1H NMR (500 MHz, Chloroform- d) δ 7.34 (d, J = 8.2 Hz, 4H), 7.07 (d, J = 7.9 Hz, 4H), 2.29 (s, 6H). ^{13}C NMR (126 MHz, Chloroform- d) δ 138.2, 131.5, 129.1, 120.4, 88.9, 21.5. LRMS (APCI+) m/z for $[C_{16}H_{14}+H]^+$: calculated 207.30, found 207.14.

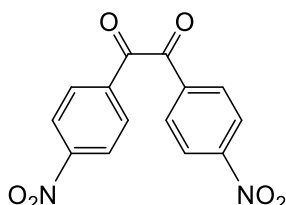
1,2-Bis(p-nitrophenyl)ethyne³²¹



1-Iodo-4-nitrobenzene (0.45 g, 1.9 mmol, 1.0 eq.) was added with $Pd(PPh_3)_4$ (42.0 mg, 0.04 mmol, 0.02 eq.) and CuI (14.0 mg, 0.08 mmol, 0.04 eq.). Then 5 mL of MeCN and 5 mL of Et_3N were added to form a heterogeneous mixture. The reaction mixture was degassed by passing through nitrogen for 30 min before adding 1-ethynyl-4-nitrobenzene (0.30 g, 2.1 mmol, 1.11 eq.). The reaction was allowed to stir at room temperature under nitrogen atmosphere overnight. The reaction was diluted with 10 mL of saturated aqueous ammonium chloride and extracted with ethyl acetate (5×30 mL). Combined organic phases were washed with brine (2×80 mL), dried over $MgSO_4$ and filtered. The solvent was evaporated under reduced pressure to give crude solid product. The crude product was recrystallised in DCM/petroleum ether. The final product was collected by filtration which left a yellow-brown crystal (0.40 g, 83% yield).

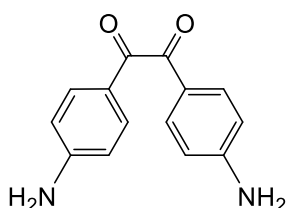
Mp, 199–202 °C (lit³²² 205–207 °C). ¹H NMR (500 MHz, Chloroform-*d*) δ 8.26 (d, *J* = 8.9 Hz, 4H), 7.72 (d, *J* = 8.8 Hz, 4H). ¹³C NMR (126 MHz, Chloroform-*d*) δ 147.7, 132.7, 128.9, 123.8, 92.0. LRMS (APCI+) *m/z* for [C₁₄H₈N₂O₄]⁺: calculated 268.05, found 267.93.

4,4'-Dinitrobenzil³²³



A mixture of 1,2-bis(4-nitrophenyl)acetylene (5.02 g, 18.7 mmol, 1.0 eq.), PdCl₂ (0.33 g, 1.9 mmol, 0.1 eq.), and 180 mL of dimethyl sulfoxide was stirred at 140 °C for 12 hrs. After being cooled, the solution was poured into water and extracted with DCM. The combined organic layer was washed with brine, dried over MgSO₄ and filtered. The crude product was purified by silica gel column chromatography (eluent: DCM) to give a yellow powder (1.34 g, 71% yield). Mp, 210–212 °C (lit³²¹ 211–213 °C). ¹H NMR (500 MHz, Chloroform-*d*) δ 8.39 (d, *J* = 8.8 Hz, 4H), 8.22 (s, 4H). ¹³C NMR (126 MHz, Chloroform-*d*) δ 190.3, 151.5, 136.7, 131.2, 124.3. LRMS (APCI+) *m/z* for [C₁₄H₈N₂O₆+H]⁺: calculated 301.04 found 301.04.

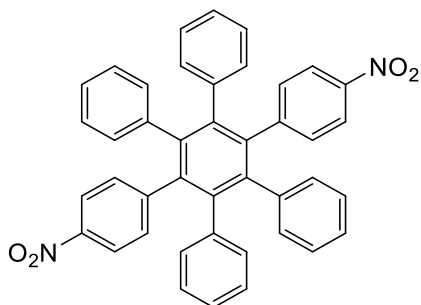
4,4'-Diaminobenzil³²⁴



4,4'-Dinitrobenzil (0.20 g, 0.7 mmol, 1.0 eq.), iron powder (0.56 g, 10.0 mmol, 15 eq.), and NH₄Cl (0.08 g, 1.5 mmol, 2.2 eq.) were added in a mixed solvent of ethanol (16 mL) and water (6 mL) and refluxed at 80 °C for 25 hrs. After being cooled, the reaction was filtered over celite. Collected filtrate was added into 15 mL of brine and extracted with ethyl acetate. The organic phase was washed with brine three times, dried with MgSO₄, filtered, and evaporated. The crude product was purified by silica gel column chromatography (eluent: ethyl acetate:DCM = 1:9) affording a brown powder (0.10 g, 63% yield). Mp, 169–171 °C (lit³²⁵ 169 °C). ¹H NMR (500 MHz, DMSO-*d*₆) δ 7.51 (d, *J*

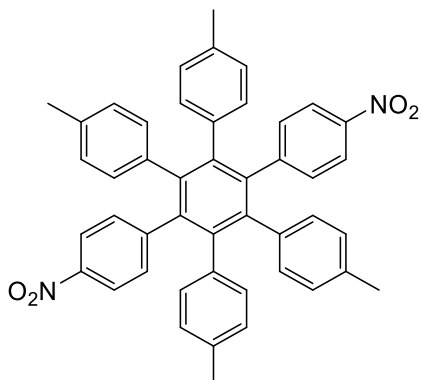
= 8.5 Hz, 4H), 6.59 (d, J = 8.8 Hz, 4H), 6.42 (d, J = 8.7 Hz, 4H). ^{13}C NMR (126 MHz, $\text{DMSO-}d_6$) δ 193.8, 155.7, 132.4, 121.1, 113.4. LRMS (APCI+) m/z for $[\text{C}_{14}\text{H}_{12}\text{N}_2\text{O}_2+\text{H}]^+$: calculated 241.09, found 241.85.

1,4-Bis(p-nitrophenyl)-2,3,5,6-tetraphenylbenzene (5a)

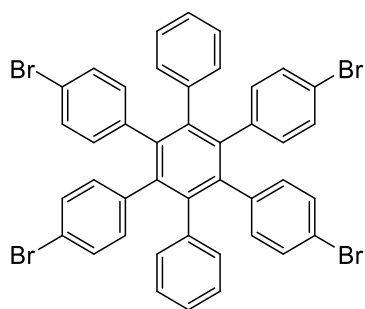


Synthesis of **5a** followed the general procedure B. **3a** (4.44 g, 9.4 mmol) and diphenyl acetylene (1.83 g, 10.3 mmol) were reacted affording a yellow-brown powder (4.88 g, 84% yield). Mp >300 °C. ^1H NMR (500 MHz, $\text{Chloroform-}d$): δ 7.77 (d, J = 8.8 Hz, 4H), 7.03 (d, J = 8.7 Hz, 4H), 6.94–6.81 (overlapping, m, 20H). ^{13}C NMR (126 MHz, $\text{Chloroform-}d$): δ 148.0, 145.7, 140.5, 139.3, 132.2, 131.2, 127.3, 126.3, 122.2. LRMS (APCI+) m/z for $[\text{C}_{42}\text{H}_{28}\text{N}_2\text{O}_4]^+$: calculated 624.68, found 624.31.

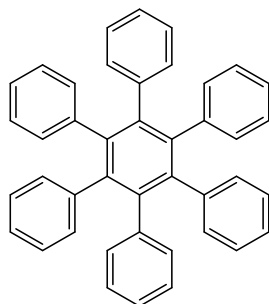
1,4-Bis(p-nitrophenyl)-2,3,5,6-tetra(p-tolyl)benzene (5b)



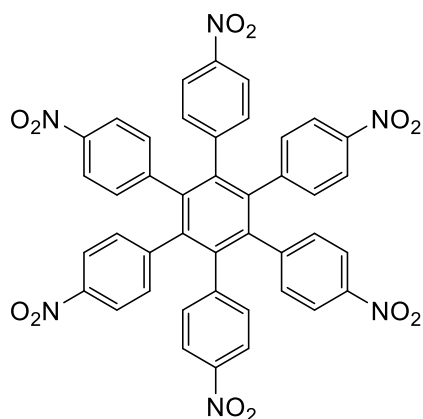
Synthesis of **5b** followed the general procedure B. **3b** (1.00 g, 2.0 mmol) and bis(p-tolyl)ethyne (0.45 g, 2.2 mmol) were reacted affording a yellow-brown powder (0.93 g, 68% yield). Mp >300 °C. ^1H NMR (500 MHz, $\text{Chloroform-}d$): δ 7.76 (d, J = 8.7 Hz, 4H), 6.99 (d, J = 8.8 Hz, 4H), 6.77–6.57 (overlapping, m, 16H), 2.13 (s, 12H). ^{13}C NMR (126 MHz, $\text{Chloroform-}d$): δ 148.6, 145.5, 140.4, 139.6, 136.5, 135.6, 132.2, 131.1, 128.0, 122.1, 21.2. LRMS (APCI+) m/z for $[\text{C}_{46}\text{H}_{36}\text{N}_2\text{O}_4]^+$: calculated 680.79, found 680.61.

1,2,4,5-Tetra(p-bromophenyl)-3,6-diphenylbenzene (5c)

Synthesis of **5c** followed the general procedure B. **3c** (2.30 g, 4.2 mmol) and bis(4-bromophenyl)acetylene (1.56 g, 4.6 mmol) were reacted affording a pale pink powder (3.44 g, 95% yield). Mp >300 °C. ^1H NMR (500 MHz, $\text{DMF-}d_7$) δ 7.70 (d, J = 8.2 Hz, 8H), 7.58 (d, J = 8.2 Hz, 8H), 7.50–7.31 (m, 4H), 7.30–7.10 (m, 4H), 6.96 (t, J = 7.9 Hz, 2H). ^{13}C NMR (126 MHz, $\text{DMF-}d_7$) δ 147.4, 134.5, 133.1, 123.7, 90.4. LRMS (APCI+) m/z for $[\text{C}_{42}\text{H}_{36}\text{Br}_4]^+$: calculated 850.29, found 850.54.

Hexaphenylbenzene (5d)

Synthesis of **5d** followed the general procedure B. Tetraphenylcyclopentadienone (3.84 g, 10.0 mmol) and diphenyl acetylene (1.96 g, 11.0 mmol) were reacted affording a pale pink powder (4.99 g, 93% yield). Mp >300 °C (lit³²⁶ >300 °C). ^1H NMR (500 MHz, $\text{DMF-}d_7$) δ 6.95 (d, J = 6.7 Hz, 12H), 6.88 (t, J = 7.4 Hz, 12H), 6.86–6.80 (m, 6H). ^{13}C NMR (126 MHz, $\text{DMF-}d_7$) δ 142.9, 141.4, 132.4, 127.7. LRMS (APCI+) m/z for $[\text{C}_{42}\text{H}_{30}]^+$: calculated 534.70, found 535.14.

Hexa(p-nitrophenyl)benzene²⁷⁷

HPB (1.60 g, 3.0 mmol) was slowly added into a mixture of 37 mL of fuming HNO₃ and 18 drops of H₂SO₄ at 0 °C. Then 7.3 mL of acetic acid and 3.7 mL of ethyl acetate was mixed and added into the reaction dropwise. The reaction was stirred for 20 hrs at room temperature and poured into 140 mL of cold water. The resulting precipitate was collected by filtration, washed twice with acetone, dried under vacuum, and then recrystallized from dimethyl sulfoxide. The crystals were isolated by filtration and washed three times with acetone to afford a yellow solid (2.34 g, 97% yield). Mp >300 °C (lit²⁷⁷ >360 °C). ¹H NMR (500 MHz, DMF-*d*₇) δ 8.08 (d, *J* = 7.8 Hz, 12H), 7.60 (d, *J* = 8.4 Hz, 12H). ¹³C NMR (126 MHz, DMF-*d*₇) δ 147.4, 146.8, 140.1, 133.7, 123.6. LRMS (APCI-) *m/z* for [C₄₂H₂₄N₆O₁₂-H]⁻: calculated 803.68, found 803.64.

1,4-Bis(p-aminophenyl)-2,3,5,6-tetraphenylbenzene (R=H) (6a)

Synthesis of **6a** followed the general procedure C. The reaction of **5a** (1.56 g, 2.5 mmol) and hydrazine monohydrate (1.2 mL, 25.0 mmol) in 35 mL of THF produced the final product (0.71 g, 51% yield). Mp >300 °C (lit³²⁷ 453 °C). ¹H NMR (500 MHz, Chloroform-*d*) δ 6.85 (m, 20H), 6.57 (s, 4H), 6.23 (s, 4H), 3.37 (s, 4H). ¹³C NMR (126 MHz, Chloroform-*d*): δ 143.4, 141.3, 140.7, 134.0, 132.5, 131.7, 131.4, 126.7, 125.1, 113.9. LRMS (APCI+) *m/z* for [C₄₂H₃₂N₂]⁺: calculated 564.71, found 564.69.

1,4-Bis(p-aminophenyl)-2,3,5,6-tetra(p-tolyl)benzene (R=CH₃) (6b)

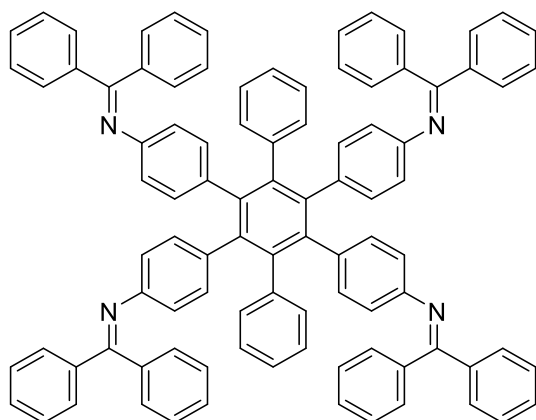
Synthesis of **6b** followed the general procedure C. The reaction of **5b** (2.72 g, 4.0 mmol) and hydrazine monohydrate (2.0 mL, 40.0 mmol) in 60 mL of THF produced the crude product which was purified by silica gel column chromatography (eluent: ethyl acetate:petroleum ether = 2:3) to yield the final product (0.20 g, 23% yield).

Mp >300 °C. ^1H NMR (500 MHz, Chloroform- d) δ 6.68 (s, 16H), 6.57 (d, J = 8.3 Hz, 4H), 6.22 (d, J = 8.4 Hz, 4H), 3.15 (s, 4H), 2.12 (s, 12H). ^{13}C NMR (126 MHz, Chloroform- d): δ 143.1, 140.6, 140.2, 138.4, 134.0, 132.4, 132.0, 131.5, 127.3, 113.9, 21.2. LRMS (APCI+) m/z for $[\text{C}_{46}\text{H}_{40}\text{N}_2]^+$: calculated 620.84, found 621.04.

Hexa(*p*-aminophenyl)benzene ($\text{R}=\text{NH}_2$) (**6d**)

Synthesis of **6d** followed the general procedure C. The reaction of **5d** (2.00 g, 2.5 mmol) and hydrazine monohydrate (3.6 mL, 75.0 mmol) in 35 mL of DMF produced the final product (2.59 g, 83% yield). Mp >300 °C (lit³²⁸ 241 °C (decomp)). ^1H NMR (500 MHz, DMSO- d_6) δ 6.36 (d, J = 8.1 Hz, 12H), 6.03 (d, J = 8.2 Hz, 12H), 4.49 (s, 12H). ^{13}C NMR (126 MHz, Chloroform- d): δ 145.0, 140.7, 132.0, 130.3, 113.2. LRMS (APCI+) m/z for $[\text{C}_{42}\text{H}_{36}\text{N}_6+\text{H}]^+$: calculated 625.80 found 626.65.

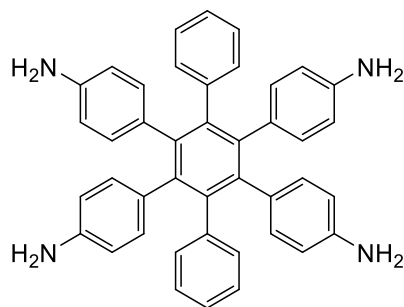
1,2,4,5-Tetra(*p*-(*N*-diphenylmethylene)phenyl)-3,6-diphenylbenzene²⁷⁶



Tris(dibenzylideneacetone)dipalladium(0) (2.19 g, 2.4 mmol, 0.5 eq.) and rac-BINAP (2.96 g, 4.8 mmol, 1.0 eq.) were charged in a 250 mL round bottom flask under N_2 atmosphere and 116 mL of anhydrous toluene was added. The solution was stirred at 110 °C for 30 min under N_2 atmosphere then cooled to room temperature. To the resultant solution was added **5c** (4.08 g, 4.8 mmol, 1.0 eq.), benzophenone imine (4.2 mL, 25.0 mmol, 5.2 eq.), sodium tert-butoxide (2.40 g, 25.0 mmol, 5.2 eq.), and the mixture was stirred at 110 °C for 24 hrs under N_2 atmosphere. The system was cooled to room temperature, diluted with DCM then filtered and evaporated under reduced pressure. The residue was subjected to column chromatography on silica gel (eluent: 2% of MeOH in DCM) and evaporated under reduced pressure to afford an orange solid (2.82 g, 47% yield). Mp >300 °C. ^1H NMR (500 MHz, Chloroform- d) δ 7.68 (d, J = 7.2 Hz, 8H), 7.42 (t, J = 7.3 Hz, 4H), 7.36 (t, J = 7.6 Hz, 8H), 7.28–7.22 (overlapping,

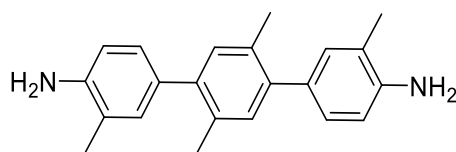
m, 12H), 6.93 (d, $J = 5.9$ Hz, 8H), 6.83 (overlapping, m, 6H), 6.66 (d, $J = 6.9$ Hz, 4H), 6.49 (d, $J = 8.1$ Hz, 8H), 6.22 (d, $J = 8.1$ Hz, 8H). ^{13}C NMR (126 MHz, Chloroform- d) δ 167.5, 148.0, 140.8, 140.5, 140.1, 139.9, 137.7, 136.0, 135.8, 132.4, 131.6, 131.4, 130.4, 130.1, 129.6, 129.2, 128.4, 128.3, 128.1, 127.9, 126.7, 125.1, 119.6, 77.3, 77.0, 76.8, 53.4. LRMS (APCI+) m/z for $[\text{C}_{94}\text{H}_{58}\text{N}_4]^+$: calculated 1243.53, found 1243.03.

1,2,4,5-Tetra(p-aminophenyl)-3,6-diphenylbenzene (**6c**)²⁷⁶

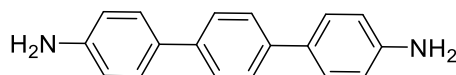


2 M aqueous HCl solution (5.7 mL, 11.4 mmol, 1.1 eq.) was added to a solution of 1,2,4,5-tetra(p-(*N*-diphenylmethylene)phenyl)-3,6-diphenylbenzene (3.28 g, 2.6 mmol, 1.0 eq.) in THF (150 mL), and the mixture was stirred at room temperature for 1 hr. The precipitate was isolated by filtration, washed with THF and petroleum ether, and dried under vacuum to afford the tetraammonium-HPB tetrachloride salt as a pale-yellow solid (0.59 g, 42% yield). Mp >300 °C. ^1H NMR (500 MHz, DMSO- d_6) δ 9.67 (s, 8H), 6.98 (d, $J = 7.8$ Hz, 8H), 6.90 (d, $J = 5.8$ Hz, 8H), 6.87–6.68 (overlapping, m, 10H). ^{13}C NMR (126 MHz, DMSO) δ 140.9, 139.8, 139.7, 132.4, 131.2, 130.1, 127.3, 126.4, 121.7. The neutralization was carried out by stirring a suspension of the salt (0.44 g, 0.6 mmol, 1.0 eq.) in 15 mL of THF with 1 M aqueous NaOH solution (2.6 mL, 2.6 mmol, 4.4 eq.). The resulting solid was filtered, washed with THF and petroleum ether, and dried under vacuum to give an off-white solid (0.21 g, 59% yield). Mp >300 °C ^1H NMR (500 MHz, DMSO- d_6) δ 6.84 (t, $J = 7.3$ Hz, 4H), 6.77 (overlapping, m, 6H), 6.39 (d, $J = 8.0$ Hz, 8H), 6.01 (d, $J = 8.0$ Hz, 8H), 4.53 (s, 8H). ^{13}C NMR (126 MHz, DMSO) δ 145.4, 142.3, 141.0, 140.4, 131.9, 131.6, 129.3, 126.7, 125.1, 113.1. LRMS (APCI+) m/z for $[\text{C}_{42}\text{H}_{34}\text{N}_4]^+$: calculated 594.76, found 595.02.

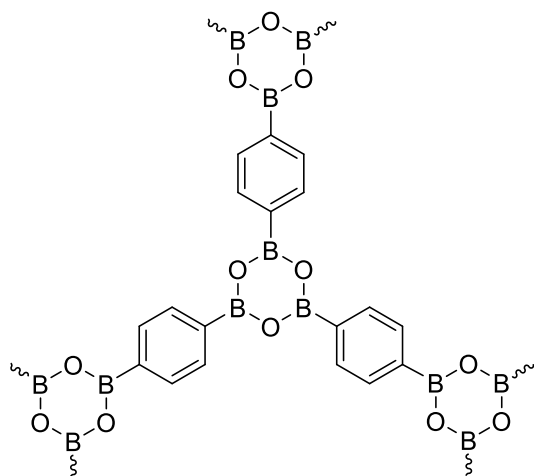
6c is air sensitive (presumably due to amine oxidation) and therefore we used its HCl-salt form in subsequent polymerisation steps.

3,2',5',3''-Tetramethyl-4,4''-diamino-p-terphenyl

Synthesis procedure refer to published literature¹⁵⁰, affording a light brown solid (68% yield). Mp, 176–177 °C (lit³²⁹ 177–179 °C). ¹H NMR (500 MHz, Chloroform-*d*) δ 7.12 (s, 2H), 7.10–7.03 (m, 4H), 6.74 (d, J = 7.9 Hz, 2H), 3.65 (s, 4H), 2.29 (s, 6H), 2.23 (s, 6H). ¹³C NMR (126 MHz, Chloroform-*d*) δ 143.4, 140.4, 132.6, 132.4, 132.0, 131.5, 128.0, 122.1, 114.7, 25.0, 20.2, 17.6. LRMS (APCI+) m/z for [C₂₂H₂₄N₂]⁺: calculated 316.45, found 317.03.

4,4''-Diamino-p-terphenyl

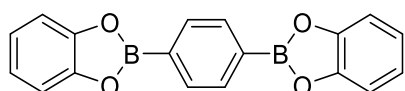
Synthesis procedure refer to published literature¹⁵⁰, affording a brown solid (67% yield). Mp, 243–244 °C (lit³³⁰ 243–245 °C). ¹H NMR (500 MHz, DMSO-*d*₆) δ 7.53 (s, 4H), 7.37 (d, J = 8.5 Hz, 4H), 6.64 (d, J = 8.5 Hz, 4H), 5.19 (s, 4H). ¹³C NMR (126 MHz, DMSO-*d*₆) δ 147.6, 137.3, 126.2, 125.0, 113.7, 38.6, 38.4. LRMS (APCI+) m/z for [C₁₈H₁₆N₂+H]⁺: calculated 261.34, found 261.14.

6.4 Synthesis of Model Compounds and Polymers**Model boroxine**

Benzene-1,4-diboronic acid (2.00 g, 1.2 mmol) was added in a 10 mL microwave vessel and then heated by microwave irradiation at 200 °C under stirring for 2 hrs. The product was dried under vacuum overnight at 50 °C affording white powder (2.00 g, yield = 100%). $S_{\text{BET}} = 149 \text{ m}^2/\text{g}$, CO_2 adsorption at 273 K/1 bar = 0.66 mmol/g, $T_{\text{max}} = 594 \text{ }^\circ\text{C}$. FTIR-ATR (cm^{-1}): 3208, 1286, 1017, 693.

SSNMR of the model boroxine failed to be measured due to its easy hydrolysis.

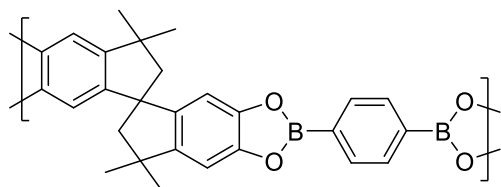
Model boronic ester



Benzene-1,4-diboronic acid (0.17 g, 1.0 mmol, 1.0 eq.) and catechol (0.22 g, 2.0 mmol, 2.0 eq.) were dissolved in 20 mL of mesitylene and reacted in the microwave reactor at 150 °C under N_2 atmosphere for 1 hr. The product was filtered and dried under vacuum overnight at 50 °C affording white powder (0.30 g, yield = 96%). Mp, $>300 \text{ }^\circ\text{C}$ (lit²⁵² $>200 \text{ }^\circ\text{C}$). FTIR-ATR (cm^{-1}): 1470, 1370, 1330, 1230, 1081, 741, 659. LRMS (APCI+) m/z for $[\text{C}_{18}\text{H}_{12}\text{B}_2\text{O}_4]^+$: calculated 314.09, found: 314.03.

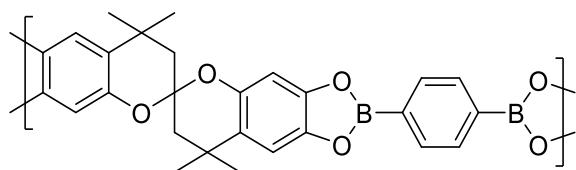
The liquid NMR of the model boronic ester failed to be measured due to its easy hydrolysis.

BE-SBI-PIM

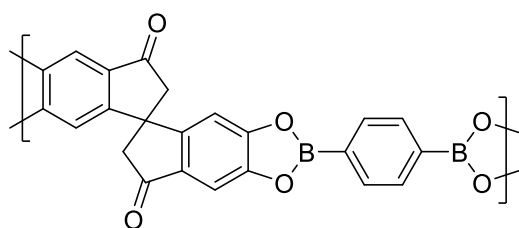


Synthesis of BE-SBI-PIM followed the general procedure D. Benzene-1,4-diboronic acid (0.17 g, 1.0 mmol, 1.0 eq.) and 5,5',6,6'-tetrahydroxy-3,3,3',3'-tetramethyl-1,1'-spirobisindane (0.34 g, 1.0 mmol, 1.0 eq.) were reacted at 120 °C for 2 hrs to yield a light-yellow solid (0.52 g, yield = 119%). $S_{\text{BET}} = 327 \text{ m}^2/\text{g}$, CO_2 adsorption at 273 K/1 bar = 1.25 mmol/g, $T_{\text{max}} = 533 \text{ }^\circ\text{C}$. FTIR-ATR (cm^{-1}): 2950, 1360, 1321, 1079, 1018, 833, 664.

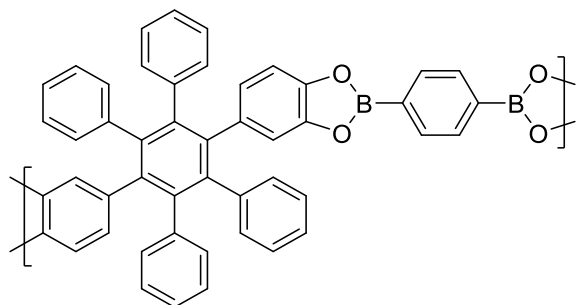
SSNMR of all BE-PIMs failed to be measured due to their unsatisfactory purity and easy hydrolysis.

BE-SBC-PIM

Synthesis of BE-SBC-PIM followed the general procedure D. Benzene-1,4-diboronic acid (0.17 g, 1.0 mmol, 1.0 eq.) and 6,6',7,7'-tetrahydroxy-4,4',4'-tetramethyl-2,2'-spirobichroman (0.37 g, 1.0 mmol, 1.0 eq.) were reacted at 120 °C for 2 hrs to yield a light-yellow solid (0.39 g, yield = 84%). SA_{BET} = 157 m²/g, CO₂ adsorption at 273 K/1 bar = 0.66 mmol/g, T_{max} = 410 °C. FTIR-ATR (cm⁻¹): 2952, 1483, 1334, 1135, 1078, 1018, 906, 670.

BE-bis-K-PIM

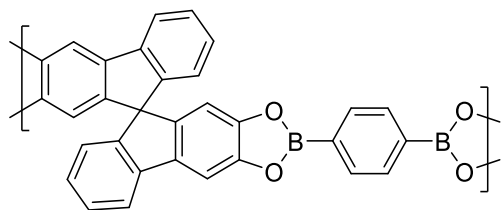
Synthesis of BE-bis-K-PIM followed the general procedure E. Benzene-1,4-diboronic acid (0.17 g, 1.0 mmol, 1.0 eq.) and 5,5',6,6'-tetrahydroxy-1,1'-spirobisindane-3,3'-dione (0.32 g, 1.0 mmol, 1.0 eq.) were reacted at 150 °C for 1.5 hrs to yield a brown solid (0.47 g, yield = 116%). SA_{BET} = 92 m²/g, CO₂ adsorption at 273 K/1 bar = 0.52 mmol/g, T_{max} = 380 °C. FTIR-ATR (cm⁻¹): 3268, 1586, 1459, 1307, 1130, 638.

BE-HPB-PIM

Synthesis of BE-HPB-PIM followed the general procedure D. Benzene-1,4-diboronic acid (0.17 g, 1.0 mmol, 1.0 eq.) and 1,4-di(3',4'-dihydroxyphenyl)-2,3,5,6-tetraphenylbenzene (0.60 g, 1.0 mmol, 1.0 eq.) were reacted at 120 °C for 3 hrs to

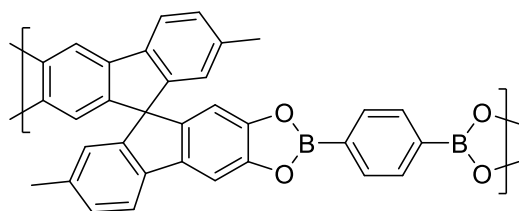
yield a brown solid (0.72 g, yield = 104%). S_{ABET} = 133 m²/g, CO₂ adsorption at 273 K/1 bar = 0.61 mmol/g, T_{max} = 603 °C. FTIR-ATR (cm⁻¹): 3051, 1350, 1228, 1079, 1022, 818, 669.

BE-SBF-PIM



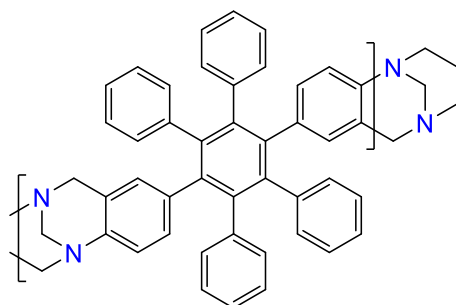
Synthesis of BE-SBF-PIM followed the general procedure D. Benzene-1,4-diboronic acid (0.17 g, 1.0 mmol, 1.0 eq.) and 2,2',3,3'-tetrahydroxy-9,9'-spirobifluorene (0.38 g, 1.0 mmol, 1.0 eq.) were reacted at 120 °C for 7 hrs to yield a brown solid (0.56 g, yield = 118%). S_{ABET} = 127 m²/g, CO₂ adsorption at 273 K/1 bar = 0.55 mmol/g, T_{max} = 579 °C. FTIR-ATR (cm⁻¹): 3351, 2927, 1325, 1273, 1018, 830, 732, 662.

BE-SBF-Me-PIM



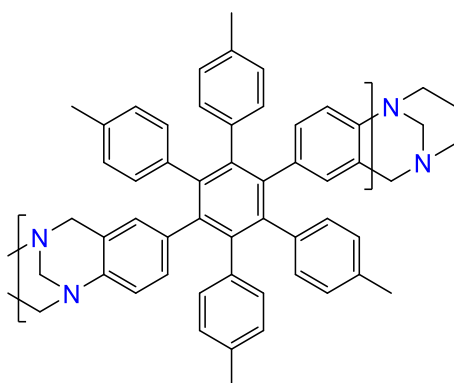
Synthesis of BE-SBF-Me-PIM followed the general procedure D. Benzene-1,4-diboronic acid (0.17 g, 1.0 mmol, 1.0 eq.) and 2,2',3,3'-tetrahydroxy-6,6'-dimethyl-9,9'-spirobifluorene (0.41 g, 1.0 mmol, 1.0 eq.) were reacted at 120 °C for 4 hrs to yield a brown solid (0.46 g, yield = 92%). S_{ABET} = 183 m²/g, CO₂ adsorption at 273 K/1 bar = 0.91 mmol/g, T_{max} = 681 °C. FTIR-ATR (cm⁻¹): 2921, 1457, 1333, 1079, 1019, 799, 664.

Di-TB-HPB-PIM



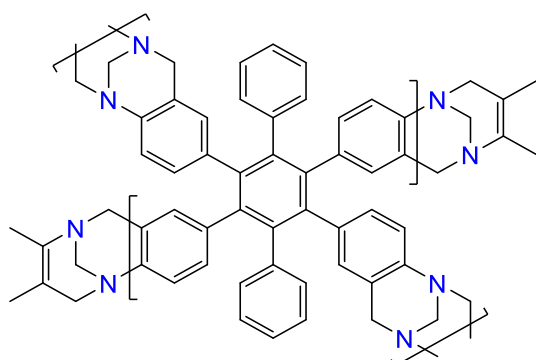
Synthesis of di-TB-HPB-PIM followed the general procedure F. The reaction of **6a** (0.71 g, 1.2 mmol, 1.0 eq.), dimethoxymethane (0.6 mL, 6.2 mmol, 5.0 eq.), trifluoroacetic acid (2.8 mL, 37.2 mmol, 30.0 eq.) and 10 mL of DCM produced di-TB-HPB-PIM (0.70 g, 94% yield). S_{BET} = 238 m²/g, CO₂ adsorption at 273 K/1 bar = 1.36 mmol/g, T_{max} = 582 °C. FTIR-ATR (cm⁻¹): 1065, 1201, 1493, 3029, 3048, 3742. ¹³C SSNMR (101 MHz) δ 146.1, 138.6, 131.6, 127.8, 66.7, 58.9, 20.6.

Di-TB-tetra-Me-HPB-PIM



Synthesis of di-TB-tetra-Me-HPB-PIM followed the general procedure F. The reaction of **6b** (1.00 g, 1.6 mmol, 1.0 eq.), dimethoxymethane (0.7 mL, 8.1 mmol, 5.0 eq.), trifluoroacetic acid (3.7 mL, 48.3 mmol, 30.0 eq.) and 25 mL of DCM produced di-TB-tetramethyl-HPB-PIM (0.84 g, 89% yield). S_{BET} = 242 m²/g, CO₂ adsorption at 273 K/1 bar = 1.01 mmol/g, T_{max} = 572 °C. FTIR-ATR (cm⁻¹): 1064, 1514, 2906, 2974, 3668. ¹³C SSNMR (101 MHz) δ 146.1, 138.6, 131.6, 127.8, 66.7, 58.9, 20.6.

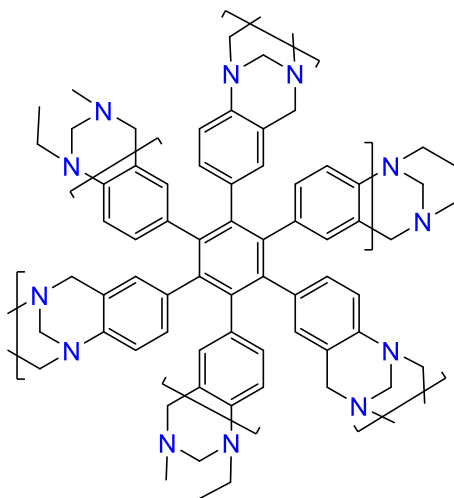
Tetra-TB-HPB-PIM



Synthesis of tetra-TB-HPB-PIM followed the general procedure F. The reaction of **6c** (0.79 g, 1.1 mmol, 1.0 eq.), dimethoxymethane (0.9 mL, 10.6 mmol, 10.0 eq.), trifluoroacetic acid (4.9 mL, 63.6 mmol, 60.0 eq.) and 11 mL of DCM produced tetra-

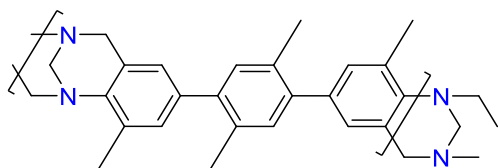
TB-HPB-PIM (0.67 g, 88% yield). S_{ABET} = 516 m^2/g , CO_2 adsorption at 273 K/1 bar = 2.00 mmol/g, T_{max} = 591 $^{\circ}\text{C}$. FTIR-ATR (cm^{-1}): 1065, 2899, 2981, 3668. ^{13}C SSNMR (101 MHz) δ 146.4, 141.3, 131.9, 126.5, 113.1, 67.4, 57.8.

Hexa-TB-HPB-PIM

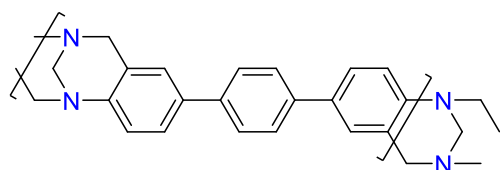


Synthesis of hexa-TB-HPB-PIM followed the general procedure F. The reaction of **6d** (0.50 g, 0.8 mmol, 1.0 eq.), dimethoxymethane (0.9 mL, 9.6 mmol, 12.0 eq.) and trifluoroacetic acid (6.5 mL, 85.0 mmol, 106.0 eq.) produced hexa-TB-HPB-PIM (0.51 g, 83% yield). S_{ABET} = 444 m^2/g , CO_2 adsorption at 273 K/1 bar = 2.14 mmol/g, T_{max} = 587 $^{\circ}\text{C}$. FTIR-ATR (cm^{-1}): 1064, 2899, 2981, 3667. ^{13}C SSNMR (101 MHz) δ 146.6, 141.4, 131.7, 113.4, 66.8, 57.5.

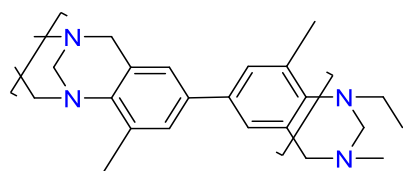
Linear TB-polymer 1



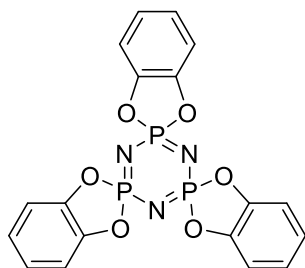
Synthesis of linear TB-polymer 1 followed the general procedure F. The reaction of 3,2',5',3"-tetramethyl-4,4"-diamino-p-terphenyl (0.80 g, 3.2 mmol, 1.0 eq.), dimethoxymethane (1.1 mL, 12.6 mmol, 4.0 eq.), trifluoroacetic acid (5.6 mL, 72.7 mmol, 23.0 eq.) and 5.5 mL of DCM produced linear TB-polymer 1 (0.60 g, 54% yield). S_{ABET} = 275 m^2/g , CO_2 adsorption at 273 K/1 bar = 1.20 mmol/g, T_{max} = 429 $^{\circ}\text{C}$. FTIR-ATR (cm^{-1}): 866, 941, 1213, 1471, 2915, 2945. ^{13}C SSNMR (101 MHz) δ 141.7, 137.4, 134.6, 128.3, 124.8, 64.5, 52.1, 14.3.

Linear TB-polymer 2

Synthesis of linear TB-polymer 2 followed the general procedure F. The reaction of 4,4''-diamino-p-terphenyl (0.40 g, 1.5 mmol, 1.0 eq.), dimethoxymethane (0.5 mL, 6.2 mmol, 4.0 eq.), trifluoroacetic acid (3.5 mL, 46.2 mmol, 30.0 eq.) and 5.5 mL of DCM produced linear TB-polymer 2 (0.19 g, 35% yield). S_{ABET} = 312 m²/g, CO₂ adsorption at 273 K/1 bar = 1.39 mmol/g, T_{max} = 439 °C. FTIR-ATR (cm⁻¹): 814, 937, 1202, 1476, 2888. ¹³C SSNMR (101 MHz) δ 147.6, 138.2, 126.7, 67.0, 59.3.

Linear TB-polymer 3

Synthesis of linear TB-polymer 3 followed the general procedure F. The reaction of 2-tolidine (0.42 g, 2.0 mmol, 1.0 eq.), dimethoxymethane (0.7 mL, 8.0 mmol, 4.0 eq.), trifluoroacetic acid (4.6 mL, 60.0 mmol, 30.0 eq.) and 10 mL of DCM produced linear TB-polymer 3 (0.46 g, 98% yield). S_{ABET} = 362 m²/g, CO₂ adsorption at 273 K/1 bar = 1.28 mmol/g, T_{max} = 436 °C. FTIR-ATR (cm⁻¹): 857, 1067, 1211, 1470, 2885, 2972. ¹³C SSNMR (101 MHz) δ 145.2, 138.1, 132.2, 127.9, 67.6, 55.1, 16.2.

Model CTP 1²⁹²

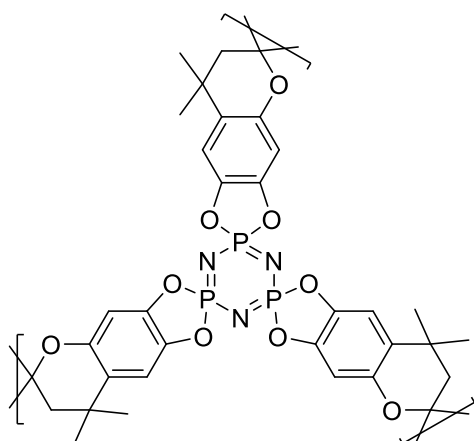
Method 1: Synthesis of Model CTP 1 followed the general procedure G. Catechol (1.10 g, 10.0 mmol, 3.0 eq.) and Et₃N (2.80 mL, 20.0 mmol, 6.0 eq.) were added to 9 mL of anhydrous THF as Solution A. HCCP (1.15 g, 3.3 mmol, 1.0 eq.) was dissolved in 18 mL of anhydrous THF to form Solution B. The reaction was refluxed under N₂

atmosphere at 65 °C for 40 hrs giving a white powder (0.81 g, 53% yield). Mp, 248–250 °C (lit²⁸⁸ 522.2 K). ¹H NMR (500 MHz, Chloroform-*d*) δ 7.10 (dd, *J* = 5.9, 3.5 Hz, 6H), 7.03 (dd, *J* = 6.0, 3.5 Hz, 6H). ¹³C NMR (126 MHz, Chloroform-*d*) δ 144.5, 123.9, 112.7. ³¹P NMR (202 MHz, Chloroform-*d*) δ 33.15. FTIR-ATR (cm⁻¹): 3155, 1489, 1250, 826. LRMS (APCI+) *m/z* for [C₁₈H₁₁O₆N₃P₃]⁺: calculated 458.20 found 457.19.

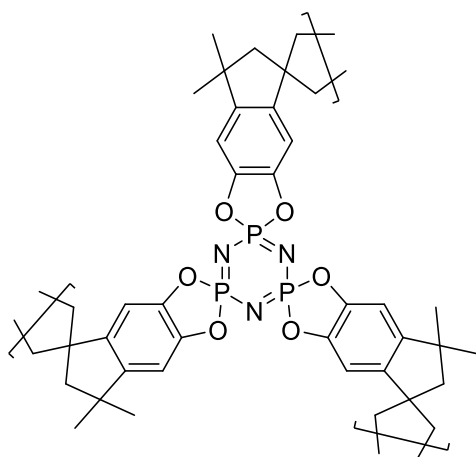
Method 2: Synthesis of Model CTP 1 followed the general procedure H. HCCP (0.35 g, 1.0 mmol, 1.0 eq.), catechol (0.33 g, 3.0 mmol, 3.0 eq.) and Et₃N (0.84 mL, 6.0 mmol, 6.0 eq.) were mixed with 25 mL of anhydrous THF. The reaction was irradiated under N₂ atmosphere at 65 °C for 3 hrs giving a light yellow powder (0.42 g, 92% yield). Mp, 249–252 °C. FTIR-ATR (cm⁻¹): 3153, 1492, 1247, 826.

NMR and Mass spec failed to be measured due to its easy hydrolysis.

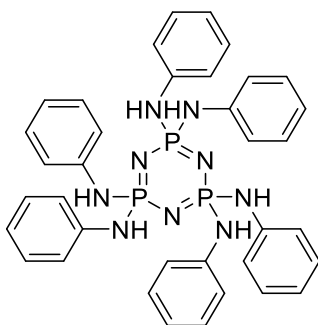
CTP-SBC-PIM



Synthesis of CTP-SBC-PIM followed the general procedure G. 6,6',7,7'-tetrahydroxy-4,4',4'-tetramethyl-2,2'-spirobichroman (1.68 g, 4.5 mmol, 1.5 eq.) and Et₃N (2.50 mL, 18.0 mmol, 6.0 eq.) were added to 16 mL of anhydrous THF to form Solution A. HCCP (1.05 g, 3.0 mmol, 1.0 eq.) was dissolved in 30 mL of anhydrous THF to form Solution B. The reaction was refluxed under N₂ atmosphere at 65 °C for 40 hrs giving a dark green powder (1.98 g, 94% yield). T_{max} = 355 °C. FTIR-ATR (cm⁻¹): 2957, 1502, 1221, 1133, 904, 536–476.

CTP-SBI-PIM

Synthesis of CTP-SBI-PIM followed the general procedure H. HCCP (0.38 g, 1.1 mmol, 1.0 eq.), 5,5',6,6'-tetrahydroxy-3,3',3',3'-tetramethyl-1,1'-spirobisindane (1.09 g, 3.2 mmol, 3.0 eq.) and Et₃N (3.00 mL, 21.5 mmol, 20.0 eq.) were mixed with 20 mL of anhydrous THF. The reaction was irradiated under N₂ atmosphere at 80 °C for 1 hr. The product was filtered before being dried to yield an off-white solid (0.57 g, 70% yield). T_{max} = 441 °C. FTIR-ATR (cm⁻¹): 2946, 1478, 1173, 1036, 849, 466.

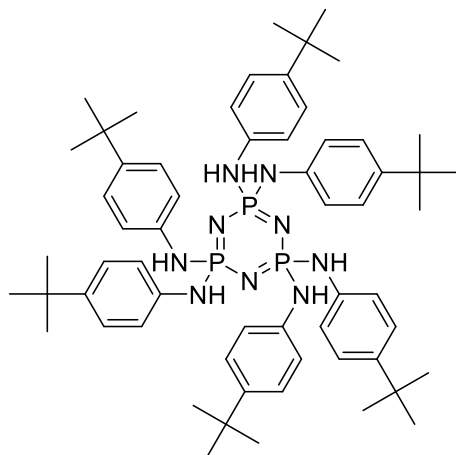
Model CTP 2a

Synthesis of Model CTP 2a followed the general procedure G. Aniline (0.60 mL, 6.4 mmol, 6.0 eq.) and Et₃N (2.50 mL, 17.9 mmol, 17.0 eq.) were stirred in 15 mL of MeCN for 1 hr at 0 °C under N₂ atmosphere as Solution A. HCCP (0.37 g, 1.1 mmol, 1.0 eq.) was dissolved in 15 mL of MeCN to make Solution B. Solution B was added into Solution A dropwise at 0 °C and stirred at 40 °C for 3 hrs before increasing the temperature to 80 °C for 80 hrs under N₂ atmosphere. The finished reaction was cooled down in an ice bath to crash out clear white crystals. The product was filtered under N₂ atmosphere and washed three times with cold MeCN to afford a white solid

(0.27 g, 36% yield). FTIR-ATR (cm^{-1}): 2978–2945, 1474, 1397, 1170, 1034. LRMS (APCI-) m/z for $[\text{C}_{36}\text{H}_{35}\text{N}_9\text{P}_3]^+$: calculated 687.23 found 687.81.

Mp failed to be measured due to its easy hydrolysis.

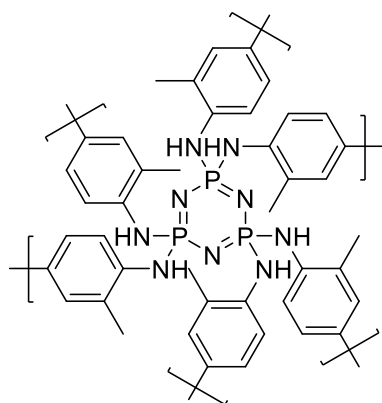
Model CTP 2b



Method 1: Synthesis of Model CTP 2b followed the general procedure G. Tert-butyl-aniline (1.10 mL, 6.9 mmol, 6.0 eq.) and Et_3N (2.50 mL, 17.9 mmol, 16.0 eq.) were stirred in 15 mL of MeCN as Solution A. HCCP (0.37 g, 1.1 mmol, 1.0 eq.) was dissolved in 3.4 mL of MeCN to make Solution B. Solution B was added into Solution A and stirred until all the reagents were fully dissolved before increasing the temperature to 80 °C and stirring for 24 hrs under N_2 atmosphere. The finished reaction was cooled down in an ice bath to crash out clear white crystals. The product was filtered under N_2 atmosphere and washed three times with cold MeCN to afford a white solid (0.24 g, 18% yield). FTIR-ATR (cm^{-1}): 3394, 2981–2946, 1473, 1398, 1173, 1034.

Mp and Mass spec failed to be measured due to its easy hydrolysis.

Method 2: Synthesis of Model CTP 2b followed the general procedure H. HCCP (0.10 g, 0.3 mmol, 1.0 eq.), tert-butyl-aniline (0.70 mL, 4.4 mmol, 15.0 eq.) and Et_3N (2.00 mL, 14.4 mmol, 50.0 eq.) were mixed with 15 mL of anhydrous THF. The reaction was irradiated at 40 °C for 1.5 hrs giving a white solid (0.13 g, 42% yield). Mp, 260–263 °C. FTIR-ATR (cm^{-1}): 2976–2944, 1475, 1398, 1172, 1034. LRMS (APCI+) m/z for $[\text{C}_{60}\text{H}_{83}\text{N}_9\text{P}_3]^+$: calculated 1023.61 found 1023.44.

CTP-tolidine-PIM

Method 1: Synthesis of CTP-tolidine-PIM followed the general procedure G. O-tolidine (0.68 g, 3.2 mmol, 3.0 eq.) and Et₃N (1.8 mL, 12.9 mmol, 12.0 eq.) were stirred in 10 mL of anhydrous THF to prepare Solution A. HCCP (0.37 g, 1.1 mmol, 1.0 eq.) and 5 mL of anhydrous THF were fully mixed as Solution B. Then Solution B was added into Solution A dropwise and refluxed at 80 °C for 24 hrs under N₂ atmosphere. After cooling down, the product was filtered and washed at least three times with anhydrous THF to afford a brown solid (0.49 g, 58%). T_{max}= 524 °C. FTIR-ATR (cm⁻¹): 3350, 2978–2944, 1475, 1393, 1169, 1034, 563.

Method 2: Synthesis of CTP-tolidine-PIM followed the general procedure H. HCCP (0.37 g, 1.1 mmol, 1.0 eq.), o-tolidine (0.68 g, 3.2 mmol, 3.0 eq.) and Et₃N (1.8 mL, 12.9 mmol, 12.0 eq.) were mixed with 20 mL of anhydrous THF. The reaction was irradiated at 80 °C for 1 hr giving a white solid (0.35 g, 42% yield). T_{max}= 528 °C. FTIR-ATR (cm⁻¹): 3354, 2979–2944, 1488, 1393–1380, 1169, 1034, 554.

Chapter 7 – References

1. Kitagawa, S., *Accounts of chemical research*, 2017, **50**(3), 514-516.
2. Davis, M.E., *Nature*, 2002, **417**(6891), 813-821.
3. Thommes, M., et al., *Pure and Applied Chemistry*, 2015, **87**(9-10), 1051-1069.
4. Králik, M., *Chemical Papers*, 2014, **68**(12), 1625-1638.
5. Vyawahare, P., et al., *AIChE Journal*, 2022, **68**(3), e17523.
6. Sing, K.S., *Colloids and Surfaces*, 1989, **38**(1), 113-124.
7. Brunauer, S., Emmett P.H., and Teller E., *Journal of the American chemical society*, 1938, **60**(2), 309-319.
8. Swenson, H. and Stadie N.P., *Langmuir*, 2019, **35**(16), 5409-5426.
9. Sinha, P., et al., *The Journal of Physical Chemistry C*, 2019, **123**(33), 20195-20209.
10. Lozano-Castelló, D., Cazorla-Amorós D., and Linares-Solano A., *Carbon*, 2004, **42**(7), 1233-1242.
11. Zhang, S., et al., *Advanced Science*, 2018, **5**(12), 1801116.
12. Liang, J., et al., *Advanced Materials*, 2017, **29**(30), 1701139.
13. Cruciani, G., *Journal of Physics and Chemistry of Solids*, 2006, **67**(9-10), 1973-1994.
14. Norouzi, O., et al., *Energies*, 2020, **13**(24), 6600-6611.
15. Liu, Z., et al., *Journal of Cleaner Production*, 2020, **247**, 119565.
16. Corujeira Gallo, S., et al., *ACS Applied Materials & Interfaces*, 2017, **9**(27), 23195-23201.
17. Ni, M., et al., *Frontiers in Chemistry*, 2023, **11**, 1205280.
18. Yin, J., et al., *Small methods*, 2020, **4**(3), 1900853.
19. Bose, S., Sarkar N., and Jo Y., *Journal of Controlled Release*, 2024, **365**, 848-875.
20. Zhao, X., Audsley F., and Lu G., *The Journal of Physical Chemistry B*, 1998,

102(21), 4143-4146.

21. Andronikashvili, T., Kordzakhia T., and Eprikashvili L., *Lap Lambert Academic Publishing*, 2015, 100-190.
22. Avantis Systems Ltd. *Amorphous carbon [Online]*, Class Connect. 2024; Available from: <https://avnfs.com/yZdpoGBURcfCF4qrVxHyEko7fLmp1Wl8M4tunuwGh1A?size=478881&type=image%2Fpng>.
23. Zhang, L., et al., *Scientific reports*, 2013, **3**(1), 1408-1416.
24. Thomas, S., et al., eds. Carbon nanotubes, in *Handbook of Carbon-Based Nanomaterials*. Elsevier, 2021, 299-319.
25. Tella, J.O., Adekoya J.A., and Ajanaku K.O., *Royal Society Open Science*, 2022, **9**(6), 220013.
26. Zhang, Z., et al., *Chemical Communications*, 2013, **49**(7), 653-661.
27. Chen, G., et al., *Molecules*, 2019, **24**(7), 1211-1224.
28. Cote, A.P., et al., *Science*, 2005, **310**(5751), 1166-1170.
29. Yuan, Y., et al., *Journal of Materials Chemistry*, 2012, **22**(47), 24558-24562.
30. Hunt, J.R., et al., *Journal of the American Chemical Society*, 2008, **130**(36), 11872-11873.
31. El-Kaderi, H.M., et al., *Science*, 2007, **316**(5822), 268-272.
32. Reich, T.E., et al., *Journal of Materials Chemistry*, 2012, **22**(27), 13524-13528.
33. Kahveci, Z., et al., *CrystEngComm*, 2013, **15**(8), 1524-1527.
34. Wang, Z., et al., *EScience*, 2022, **2**(3), 311-318.
35. Xiao, Y., et al., *Composites Part B: Engineering*, 2020, **182**, 107616.
36. Peng, H., et al., *Chemical Engineering Journal*, 2022, **430**, 133120.
37. Kuhn, P., Antonietti M., and Thomas A., *Angewandte Chemie International Edition*, 2008, **47**(18), 3450-3453.
38. Wang, W., Zhou M., and Yuan D., *Journal of Materials Chemistry A*, 2017, **5**(4), 1334-1347.
39. Hug, S., et al., *Chemistry of Materials*, 2015, **27**(23), 8001-8010.
40. Bhunia, A., et al., *Journal of Materials Chemistry A*, 2013, **1**(47), 14990-14999.

41. Qiu, S., et al., *Chemical Engineering Journal*, 2020, **401**, 126058.
42. Gao, C., et al., *Polymer Degradation and Stability*, 2021, **190**, 109613.
43. Afshari, M. and Dinari M., *Composites Part A: Applied Science and Manufacturing*, 2021, **147**, 106453.
44. Davankov, V., et al., 299 165 (1969); US Pat. 3 729 457 (1973). in *Chemical Abstracts*, 1971, **75**.
45. Tsyurupa, M. and Davankov V., *Reactive and Functional Polymers*, 2002, **53**(2-3), 193-203.
46. Davankov, V. and Tsyurupa M., *Reactive Polymers*, 1990, **13**(1-2), 27-42.
47. Xu, S., Luo Y., and Tan B., *Macromolecular rapid communications*, 2013, **34**(6), 471-484.
48. Kaliva, M., Armatas G.S., and Vamvakaki M., *Langmuir*, 2012, **28**(5), 2690-2695.
49. Babarao, R., et al., *Langmuir*, 2007, **23**(2), 659-666.
50. Yang, Q. and Zhong C., *The Journal of Physical Chemistry B*, 2006, **110**(36), 17776-17783.
51. Belmabkhout, Y. and Sayari A., *Chemical Engineering Science*, 2009, **64**(17), 3721-3728.
52. Cavenati, S., Grande C.A., and Rodrigues A.E., *Journal of Chemical & Engineering Data*, 2004, **49**(4), 1095-1101.
53. Wood, C.D., et al., *Chemistry of materials*, 2007, **19**(8), 2034-2048.
54. Martín, C.F., et al., *Journal of Materials Chemistry*, 2011, **21**(14), 5475-5483.
55. Yu, C., et al., *ACS Applied Polymer Materials*, 2023, **5**(2), 1509-1519.
56. Xie, Y., et al., *Nature communications*, 2013, **4**(1), 1960-1966.
57. Jiang, J.X., et al., *Angewandte Chemie*, 2007, **119**(45), 8728-8732.
58. Jiang, J.X., et al., *Journal of the American Chemical Society*, 2008, **130**(24), 7710-7720.
59. Dawson, R., Adams D.J., and Cooper A.I., *Chemical Science*, 2011, **2**(6), 1173-1177.
60. Bruch, L., *Surface Science*, 1983, **125**(1), 194-217.

61. Patel, H.A., Byun J., and Yavuz C.T., *ChemSusChem*, 2017, **10**(7), 1303-1317.
62. Guillermin, V., et al., *Chemical Communications*, 2014, **50**(16), 1937-1940.
63. Zhu, Z., et al., *Colloids and Surfaces A: Physicochemical and Engineering Aspects*, 2024, **681**, 132834.
64. Zhu, Z., et al., *Polymer*, 2020, **194**, 122387.
65. Tian, Y. and Zhu G., *Chemical reviews*, 2020, **120**(16), 8934-8986.
66. Lu, W., et al., *Journal of the American Chemical Society*, 2011, **133**(45), 18126-18129.
67. Ma, H., et al., *Polymer Chemistry*, 2014, **5**(1), 144-152.
68. Ismail, M., et al., *Molecules*, 2023, **28**(7), 3016-3032.
69. Lu, W., et al., *Angewandte Chemie-International Edition*, 2012, **51**(30), 7480-7484.
70. Ma, T., et al., *Composites Part B: Engineering*, 2020, **183**, 107697.
71. McKeown, N.B., *Polymer*, 2020, **202**, 122736.
72. McKeown, N.B., et al., *Microporous polymer material (WO2005012397A3)*. 2003.
73. Budd, P.M., et al., *Chemical communications*, 2004(2), 230-231.
74. Satilmis, B., *Journal of Polymers and the Environment*, 2020, **28**, 995-1009.
75. Carta, M., et al., *Science*, 2013, **339**(6117), 303-307.
76. Comesaña-Gándara, B., et al., *Energy & Environmental Science*, 2019, **12**(9), 2733-2740.
77. Wang, Y., et al., *Small Structures*, 2021, **2**(9), 2100049.
78. McKeown, N.B., *Science China-Chemistry*, 2017, **60**(8), 1023-1032.
79. McKeown, N.B., *International Scholarly Research Notices*, 2012, **2012**(1), 513986.
80. Jue, M.L. and Lively R.P., *Current Opinion in Chemical Engineering*, 2022, **35**, 100750.
81. Williams, R., et al., *Journal of Materials Chemistry A*, 2018, **6**(14), 5661-5667.
82. Zhao, S., et al., *Journal of Membrane Science*, 2018, **566**, 77-86.

83. Ahn, J., et al., *Journal of Membrane Science*, 2010, **346**(2), 280-287.
84. Long, T.M. and Swager T.M., *Advanced Materials*, 2001, **13**(8), 601-604.
85. McKeown, N.B., et al., *Chemistry*, 2005, **11**(9), 2610-2620.
86. McKeown, N.B. and Budd P.M., *Porous polymers*, 2011, 1-29.
87. McKeown, N.B. and Budd P.M., *Macromolecules*, 2010, **43**(12), 5163-5176.
88. Budd, P.M., et al., *Advanced Materials*, 2004, **16**(5), 456-459.
89. Heuchel, M., et al., *Journal of Membrane Science*, 2008, **318**(1-2), 84-99.
90. Song, W., et al., *Progress in Polymer Science*, 2023, **142**, 101691.
91. Xu, Q., et al., *Journal of Materials Chemistry A*, 2023, **11**(29), 15600-15634.
92. Bezzu, C.G., et al., *Advanced Functional Materials*, 2021, **31**(37), 2104474.
93. Bezzu, C.G., et al., *Advanced Materials*, 2012, **24**(44), 5930-5933.
94. Ghanem, B.S., et al., *Macromolecules*, 2008, **41**(5), 1640-1646.
95. Wiegand, J.R., et al., *Journal of Materials Chemistry A*, 2014, **2**(33), 13309-13320.
96. Short, R., et al., *Chemical Communications*, 2011, **47**(24), 6822-6824.
97. Du, N., et al., *Macromolecular rapid communications*, 2009, **30**(8), 584-588.
98. Ma, X. and Pinnau I., *Polymer Chemistry*, 2016, **7**(6), 1244-1248.
99. Budd, P.M., McKeown N.B., and Fritsch D., *Journal of Materials Chemistry*, 2005, **15**(20).
100. Pathak, C., et al., *Chemistry-a European Journal*, 2023, **29**(43), e202301512.
101. McKeown, N.B. and Budd P.M., *Chemical Society Reviews*, 2006, **35**(8), 675-683.
102. Bezzu, C.G., et al., *Journal of Materials Chemistry A*, 2018, **6**(22), 10507-10514.
103. Carta, M., et al., *Macromolecules*, 2014, **47**(23), 8320-8327.
104. Ghanem, B.S., *Polymer Chemistry*, 2012, **3**(1), 96-98.
105. Minelli, M., et al., *Polymer*, 2019, **170**, 157-167.
106. Ghanem, B.S., et al., *Macromolecules*, 2009, **42**(20), 7881-7888.

107. Carta, M., Msayib K.J., and McKeown N.B., *Tetrahedron Letters*, 2009, **50**(43), 5954-5957.
108. Fritsch, D., et al., *Macromolecular Chemistry and Physics*, 2011, **212**(11), 1137-1146.
109. Mason, C.R., et al., *Macromolecules*, 2011, **44**(16), 6471-6479.
110. Patel, H.A. and Yavuz C.T., *Chemical Communications*, 2012, **48**(80), 9989-9991.
111. Tan, R., et al., *Nature materials*, 2020, **19**(2), 195-202.
112. Satilmis, B. and Budd P.M., *RSC Advances*, 2014, **4**(94), 52189-52198.
113. Carta, M., et al., *Organic letters*, 2008, **10**(13), 2641-2643.
114. Zhang, F., et al., *Macromolecular rapid communications*, 2018, **39**(13), 1800274.
115. Carta, M., et al., *Polymer Chemistry*, 2014, **5**(18), 5255-5261.
116. Adymkanov, S.V., et al., *Polymer Science Series A*, 2008, **50**(4), 444-450.
117. Li, Z., et al., *RSC Advances*, 2015, **5**(126), 104451-104457.
118. Ji, C., et al., *ACS Nano*, 2022, **16**(9), 14754-14764.
119. Satılmış, B., *Current Opinion in Chemical Engineering*, 2022, **36**, 100793.
120. Wang, S., et al., *ACS Applied Polymer Materials*, 2020, **2**(6), 2434-2443.
121. Pang, S.H., et al., *ACS Macro Letters*, 2015, **4**(12), 1415-1419.
122. McKeown, N.B., *Current Opinion in Chemical Engineering*, 2022, **36**, 100785.
123. Wei, H., et al., *Journal of Materials Chemistry A*, 2018, **6**(18), 8633-8642.
124. Du, N., et al., *Macromolecules*, 2009, **42**(16), 6023-6030.
125. Du, N., et al., *Macromolecules*, 2009, **42**(16), 6038-6043.
126. Mason, C.R., et al., *Macromolecules*, 2014, **47**(3), 1021-1029.
127. Satilmis, B. and Uyar T., *European Polymer Journal*, 2019, **112**, 87-94.
128. Du, N.Y., et al., *Macromolecules*, 2008, **41**(24), 9656-9662.
129. Corrado, T.J., et al., *Proceedings of the National Academy of Sciences*, 2021, **118**(37), e2022204118.

130. Swaidan, R., et al., *Journal of Membrane Science*, 2015, **475**, 571-581.
131. Zhang, C., et al., *Industrial & Engineering Chemistry Research*, 2017, **56**(44), 12783-12788.
132. Carta, M., et al., *Advanced Materials*, 2014, **26**(21), 3526-3531.
133. Zhu, Z., et al., *Macromolecules*, 2020, **53**(5), 1573-1584.
134. Li, S.L., et al., *Polymer*, 2020, **193**, 122369.
135. Rodríguez, A., et al., *ACS Applied Polymer Materials*, 2024, **6**(6), 3342-3353.
136. Zhuang, Y., et al., *Chemical Communications*, 2016, **52**(19), 3817-3820.
137. Ma, X., Abdulhamid M.A., and Pinnau I., *Macromolecules*, 2017, **50**(15), 5850-5857.
138. Chen, Z. and Swager T.M., *Macromolecules*, 2008, **41**(19), 6880-6885.
139. Shamsipur, H., et al., *Macromolecules*, 2014, **47**(16), 5595-5606.
140. Abdulhamid, M.A., et al., *Chemistry of Materials*, 2019, **31**(5), 1767-1774.
141. Kang, S., et al., *Journal of Membrane Science*, 2021, **637**, 119604.
142. Liu, S., et al., *Journal of the American Chemical Society*, 2014, **136**(50), 17434-17437.
143. Lai, H.W.H., Liu S., and Xia Y., *Journal of Polymer Science Part a-Polymer Chemistry*, 2017, **55**(18), 3075-3081.
144. McKeown, N.B., Makhseed S., and Budd P.M., *Chemical Communications*, 2002(23), 2780-2781.
145. McKeown, N.B., et al., *Chemical Communications*, 2002(23), 2782-2783.
146. Mackintosh, H.J., Budd P.M., and McKeown N.B., *Journal of Materials Chemistry*, 2008, **18**(5), 573-578.
147. Makhseed, S., et al., *Catalysis Communications*, 2009, **10**(9), 1284-1287.
148. Budd, P.M., et al., *Journal of Materials Chemistry*, 2003, **13**(11), 2721-2726.
149. Antonangelo, A.R., et al., *Catalysis Communications*, 2017, **99**, 100-104.
150. Antonangelo, A.R., et al., *Journal of the American Chemical Society*, 2022, **144**(34), 15581-15594.
151. Maffei, A.V., Budd P.M., and McKeown N.B., *Langmuir*, 2006, **22**(9), 4225-4229.

152. Satilmis, B., Alnajrani M.N., and Budd P.M., *Macromolecules*, 2015, **48**(16), 5663-5669.
153. McGuinness, E.K., et al., *Chemistry of Materials*, 2019, **31**(15), 5509-5518.
154. Satilmis, B. and Uyar T., *Journal of Colloid and Interface Science*, 2018, **516**, 317-324.
155. Yu, Y.N., et al., *Journal of Inclusion Phenomena and Macrocyclic Chemistry*, 2022, **102**(5), 395-427.
156. Satilmis, B., et al., *Applied Surface Science*, 2019, **467**, 648-657.
157. Wang, Z., et al., *Chemical Engineering Journal*, 2023, **452**, 139198.
158. Budd, P.M. and McKeown N.B., *Polymer Chemistry*, 2010, **1**(1), 63-68.
159. Robeson, L.M., *Journal of Membrane Science*, 2008, **320**(1-2), 390-400.
160. Zhang, C., et al., *Journal of Membrane Science*, 2018, **556**, 277-284.
161. Han, X., et al., *Journal of Industrial and Engineering Chemistry*, 2020, **91**, 102-109.
162. Ma, X., et al., *ACS Omega*, 2018, **3**(11), 15966-15974.
163. Sekizkardes, A.K., et al., *ACS Applied Materials & Interfaces*, 2019, **11**(34), 30987-30991.
164. Del Regno, A., et al., *Industrial & Engineering Chemistry Research*, 2013, **52**(47), 16939-16950.
165. Zhang, C., et al., *Polymer*, 2014, **55**(16), 3642-3647.
166. Zhou, H., et al., *ACS Applied Materials & Interfaces*, 2022, **14**(18), 20997-21006.
167. Wang, L., et al., *Electrochemistry Communications*, 2020, **118**, 106798.
168. Jeon, J.W., et al., *Applied Surface Science*, 2020, **530**, 147146.
169. Tang, Q., Gong J., and Zhao Q., *Catalysis Science & Technology*, 2019, **9**(19), 5383-5393.
170. Rakow, N.A., et al., *Langmuir*, 2010, **26**(6), 3767-3770.
171. Huang, Y., et al., *Journal of Materials Chemistry A*, 2015, **3**(31), 15935-15943.
172. Jiang, S.D., et al., *Industrial & Engineering Chemistry Research*, 2014, **53**(16), 6708-6717.

173. Lei, L., et al., *Composites Science and Technology*, 2016, **128**, 161-168.
174. Mochane, M., et al., *Express Polymer Letters*, 2019 **13**(2), 159-198.
175. Xu, T., eds. Recent Developments in Different Techniques Used for the Flame Retardancy, in *Flame Retardants*. 2015, 45-77.
176. Bar, M., Alagirusamy R., and Das A., *Fibers and Polymers*, 2015, **16**(4), 705-717.
177. Zhou, X., et al., *Composites Part B-Engineering*, 2020, **202**, 108397.
178. Li, Z., et al., *Composites Part B: Engineering*, 2018, **152**, 336-346.
179. Yang, H., et al., *Composites Part B: Engineering*, 2019, **176**, 107185.
180. *International Organization for Standardization, International standard ISO4880*. 1997.
181. Lu, S.Y. and Hamerton I., *Progress in Polymer Science*, 2002, **27**(8), 1661-1712.
182. Van Krevelen, D., *Polymer*, 1975, **16**(8), 615-620.
183. Rakotomalala, M., Wagner S., and Döring M., *Materials*, 2010, **3**(8), 4300-4327.
184. de Boer, J., Harrad S., and Sharkey M., *Chemosphere*, 2023, 140638.
185. Nelson, G., *FRCA fall*, 1994, 9-12.
186. Levchik, S.V. and Weil E.D., *Polymer International*, 2005, **54**(1), 11-35.
187. Levchik, S., et al., *Polymer Degradation and Stability*, 2005, **88**(1), 57-62.
188. Waaijers, S.L., et al., *Reviews of environmental contamination and toxicology*, 2013, 1-71.
189. Drehe , M., Simulescu V., and Ilia G., *Reviews in Chemical Engineering*, 2008, **24**(6), 263-302.
190. Lin, M. and Zheng L., *Agriculture Association of Textile Chemical and Critical Reviews Journal*, 2002, **2**(2).
191. Harju, M., et al., Current state of knowledge and monitoring requirements - Emerging "new" brominated flame retardants in flame retarded products and the environment, *NILU OR*, 2009.
192. Shen, K.K., *Non-Halogenated Flame Retardant Handbook*, 2021, 309-336.
193. Chan, S.Y., et al., *Cellulose*, 2018, **25**, 843-857.

194. Dogan, M., et al., *Composites Part B-Engineering*, 2021, **222**, 109088.
195. Ling, C., Guo L., and Wang Z., *Industrial Crops and Products*, 2023, **194**, 116264.
196. Morgan, A.B., Jurs J.L., and Tour J.M., *Journal of Applied Polymer Science*, 2000, **76**(8), 1257-1268.
197. Martin, C., Ronda J., and Cadiz V., *Journal of Polymer Science Part A: Polymer Chemistry*, 2006, **44**(11), 3503-3512.
198. Benin, V., Durganala S., and Morgan A.B., *Journal of Materials Chemistry*, 2012, **22**(3), 1180-1190.
199. Huo, S., et al., *Chemical Engineering Journal*, 2022, **427**, 131578.
200. Zielecka, M., et al., *Coatings*, 2020, **10**(5), 479.
201. Han, Z., Fina A., and Camino G., *Polymer Green Flame Retardants*, 2014, 389-418.
202. Hamdani, S., et al., *Polymer Degradation and Stability*, 2009, **94**(4), 465-495.
203. Hsiue, G.H., Liu Y.L., and Tsiao J., *Journal of Applied Polymer Science*, 2000, **78**(1), 1-7.
204. Hsiue, G.H., Wang W.J., and ChangSup F.C., *Journal of Applied Polymer Science*, 1999, **73**(7), 1231-1238.
205. Lomakin, S.M. and Zaikov G.E., *Ecological Aspects of Polymer Flame Retardancy*. Vision Sports Publishing, 1999, **10**.
206. Wilén, C.E. and Pfaendner R., *Polymer Green Flame Retardants*, 2014, 267-288.
207. Wang, J., Yu S., and Xiao S., *Macromolecular Research*, 2023, **31**(4), 339-357.
208. Levchik, S.V. and Weil E.D., *Polymer International*, 2004, **53**(11), 1585-1610.
209. Ionescu, M., et al., *Cellular Polymers*, 1994, **13**(1), 57-68.
210. Mathew, D., Nair C.P.R., and Ninan K.N., *Polymer International*, 2000, **49**(1), 48-56.
211. Mu, X., et al., *Chemical Engineering Journal*, 2021, **405**, 126946.
212. Wang, C., et al., *Polymers for Advanced Technologies*, 2018, **29**(1), 668-676.
213. Velencoso, M.M., et al., *Angewandte Chemie International Edition in English*, 2018, **57**(33), 10450-10467.

214. Yang, S., et al., *Polymer Degradation and Stability*, 2016, **128**, 89-98.
215. Xue, Y., et al., *Composites Part B: Engineering*, 2020, **183**, 107695.
216. Qiu, Y., et al., *Composites Part B: Engineering*, 2019, **178**, 107481.
217. Huo, S., et al., *Progress in Polymer Science*, 2021, **114**, 101366.
218. Nazir, R. and Gaan S., *Journal of Applied Polymer Science*, 2020, **137**(1), 218-244.
219. Zhang, Q., et al., *Fire Safety Journal*, 2020, **113**, 102994.
220. Cheng, J., et al., *Journal of Applied Polymer Science*, 2020, **137**(37), 49090.
221. Huo, S., et al., *Polymer Degradation and Stability*, 2017, **146**, 250-259.
222. Mishra, N. and Vasava D., *Journal of Fire Sciences*, 2020, **38**(6), 552-573.
223. Laoutid, F., et al., *Materials Science & Engineering R-Reports*, 2009, **63**(3), 100-125.
224. Neisius, M., et al., *Industrial & Engineering Chemistry Research*, 2013, **52**(29), 9752-9762.
225. Zhao, X.M., et al., *Acs Sustainable Chemistry & Engineering*, 2016, **4**(1), 202-209.
226. Tao, K., et al., *Polymer Degradation and Stability*, 2011, **96**(7), 1248-1254.
227. Liu, H., Wang X.D., and Wu D.Z., *Polymer Degradation and Stability*, 2014, **103**, 96-112.
228. Machotova, J., et al., *Progress in Organic Coatings*, 2016, **101**, 322-330.
229. Machotova, J., et al., *Polymer-Plastics Technology and Engineering*, 2016, **56**(5), 563-571.
230. Schenk, R. and Romer G., *Chemische Berichte*, 1924.
231. Allcock, H., *Chemical Reviews*, 1972, **72**(4), 315-356.
232. Allcock, H.R. and Kugel R., *Journal of the American Chemical Society*, 1965, **87**(18), 4216-4217.
233. Allcock, H. and Kugel R., *Inorganic Chemistry*, 1966, **5**(6), 1016-1020.
234. Allcock, H.R. and Walsh E.J., *Inorganic Chemistry*, 1971, **10**(8), 1643-1647.
235. Allcock, H. and Walsh E., *Journal of the American Chemical Society*, 1972,

- 94**(13), 4538-4545.
236. Singler, R.E., Schneider N.S., and Hagnauer G.L., *Polymer Engineering and Science*, 1975, **15**(5), 321-338.
 237. Amin, A.M., et al., *Designed Monomers and Polymers*, 2009, **12**(5), 357-375.
 238. Rothmund, S. and Teasdale I., *Chemical Society Reviews*, 2016, **45**(19), 5200-5215.
 239. Allcock, H.R., *Current Opinion in Solid State & Materials Science*, 2006, **10**(5-6), 231-240.
 240. Mouritz, A.P., et al., *Composites Part a-Applied Science and Manufacturing*, 2009, **40**(12), 1800-1814.
 241. Allcock, H.R., *Dalton Transactions*, 2016, **45**(5), 1856-1862.
 242. Allen, C.W., *Journal of Fire Sciences*, 1993, **11**(4), 320-328.
 243. Yang, R., et al., *Polymer Degradation and Stability*, 2017, **144**, 62-69.
 244. Jiang, J., et al., *Polymers (Basel)*, 2019, **11**(7), 1155-1168.
 245. Teles, F., Martins G., and Antunes F., *Journal of Analytical and Applied Pyrolysis*, 2022, **163**, 105466.
 246. Dufek, E.J., et al., *Journal of Power Sources*, 2014, **267**, 347-355.
 247. Chang, Y., et al., *Macromolecules*, 2001, **34**(2), 269-274.
 248. Yao, M., et al., *Polymer Degradation and Stability*, 2021, **183**, 109417.
 249. Zhou, L., et al., *Thermochimica Acta*, 2019, **680**, 178348.
 250. Gosecki, M. and Gosecka M., *Polymers*, 2022, **14**(4).
 251. Clair, S., Abel M., and Porte L., *Chemical Communications*, 2014, **50**(68), 9627-9635.
 252. Smith, M.K. and Northrop B.H., *Chemistry of Materials*, 2014, **26**(12), 3781-3795.
 253. Jimenez, M., Duquesne S., and Bourbigot S., *Thermochimica Acta*, 2006, **449**(1-2), 16-26.
 254. Pei, J., et al., *Journal of Organic Chemistry*, 2002, **67**(14), 4924-4936.
 255. Demers, E., et al., *Crystal Growth & Design*, 2005, **5**(3), 1237-1245.

256. Das, S.K., et al., *Chemical Communications*, 2018, **54**(86), 12270-12270.
257. Huang, W.H., Jia W.L., and Wang S., *Canadian Journal of Chemistry*, 2006, **84**(4), 477-485.
258. Sheepwash, E., et al., *Angewandte Chemie-International Edition*, 2011, **50**(13), 3034-3037.
259. Jansze, S.M., et al., *Chemical Communications*, 2018, **54**(68), 9529-9532.
260. Rambo, B.M. and Lavigne J.J., *Chemistry of Materials*, 2007, **19**(15), 3732-3739.
261. Hao, D.D., et al., *Chemical Communications*, 2014, **50**(12), 1462-1464.
262. Wu, K., et al., *Angewandte Chemie-International Edition*, 2020, **59**(37), 16202-16208.
263. Zhang, G., et al., *Angewandte Chemie-International Edition*, 2014, **53**(20), 5126-5130.
264. Huang, S.L., et al., *Chemistry-an Asian Journal*, 2015, **10**(1), 24-42.
265. Martínez-Aguirre, M.A., et al., *RSC Advances*, 2015, **5**(38), 30075-30083.
266. Saleh, M., et al., *ACS Applied Materials & Interfaces*, 2014, **6**(10), 7325-7333.
267. Ra, E.J., et al., *Chemical Communications*, 2010, **46**(8), 1320-1322.
268. Huang, N., et al., *Science China-Chemistry*, 2017, **60**(8), 1007-1014.
269. Myers, A.L. and Prausnitz J.M., *AIChE Journal*, 1965, **11**(1), 121-127.
270. Lee, S., Lee J.H., and Kim J., *Korean Journal of Chemical Engineering*, 2017, **35**(1), 214-221.
271. Sekizkardes, A.K., et al., *Materials Advances*, 2022, **3**(17), 6668-6686.
272. Yang, Y.Q., Chuah C.Y., and Bae T.H., *ACS Sustainable Chemistry & Engineering*, 2021, **9**(5), 2017-2026.
273. Gagnon, E., et al., *Journal of Organic Chemistry*, 2010, **75**(2), 399-406.
274. Karunathilake, A.A.K., et al., *RSC Advances*, 2016, **6**(70), 65763-65769.
275. Khromova, N.Y., et al., *Russian Journal of Organic Chemistry*, 2016, **52**(10), 1490-1495.
276. Rabbani, M.G., et al., *Chemical Communications*, 2012, **48**(8), 1141-1143.

277. Gagnon, E., et al., *Tetrahedron*, 2007 **63**(28), 6603-6613.
278. Li, W. and Michinobu T., *Macromolecular Chemistry and Physics*, 2016, **217**(7), 863-870.
279. Darvell, L.I., et al., *Energy & Fuels*, 2012, **26**(11), 6482-6491.
280. Atabaki, F., Keshavarz M.H., and Bastam N.N., *Zeitschrift Fur Anorganische Und Allgemeine Chemie*, 2017, **643**(16), 1049-1056.
281. Díaz, C., et al., *Journal of Inorganic and Organometallic Polymers and Materials*, 2006, **16**(3), 211-218.
282. Qiu, S.L., et al., *Small*, 2019, **15**(10), 33-57.
283. Tsiptsias, C., *Measurement*, 2022, **204**, 112136.
284. Xu, C. and Hedin N., *Materials Today*, 2014, **17**(8), 397-403.
285. Usman, M., et al., *European Polymer Journal*, 2019, **120**, 109262.
286. Dong, G.X. and Lee Y.M., *Journal of Materials Chemistry A*, 2017, **5**(26), 13294-13319.
287. Iturmendi, A., et al., Chapter 2 - Polyphosphazenes: macromolecular structures, properties, and their methods of synthesis, in *Synthetic Inorganic Chemistry*. Elsevier, 2021, 47-101.
288. Tian, N.-N., Wang L.S., and Jiang R.Y., *Journal of Chemical & Engineering Data*, 2011, **56**(7), 3208-3213.
289. Saito, S., et al., *Synthesis*, 2020, **52**(21), 3253-3262.
290. Soleymani Movahed, F., et al., *The Journal of Organic Chemistry*, 2022, **87**(1), 243-257.
291. Xiong, G., et al., *Polymer*, 2022, **247**, 124787.
292. Zhou, F., et al., *Angewandte Chemie International Edition in English*, 2016, **55**(48), 15007-15011.
293. Ye, C., et al., *Organic Preparations and Procedures International*, 2009, **33**(4), 376-379.
294. Maity, D.K., et al., *Journal of Chemical Sciences*, 2016, **128**(12), 1861-1869.
295. Guo, L.J., et al., *Transition Metal Chemistry*, 2022, **47**(1), 1-9.
296. Zhao, Z.P., et al., *Journal of Applied Polymer Science*, 2013, **128**(6), 4368-4377.

297. Yu, W.H., et al., *E-Polymers*, 2022, **22**(1), 411-429.
298. Kong, J.H., et al., *Polymer Degradation and Stability*, 2023, **215**, 110465.
299. Jiang, P., et al., *Polymer*, 2015, **79**, 221-231.
300. Jiang, P., et al., *Phosphorus Sulfur and Silicon and the Related Elements*, 2014, **189**(12), 1811-1822.
301. James, M.A., et al., *Canadian Journal of Chemistry-Revue Canadienne De Chimie*, 1985, **63**(7), 1750-1758.
302. Li, Z.K., et al., *Journal of Applied Polymer Science*, 2016, **133**(17), 43336.
303. Köhler, J., et al., *Journal of Polymer Science Part a-Polymer Chemistry*, 2014, **52**(4), 527-536.
304. Kühl, S., et al., *Polymer*, 2020, **192**, 122314.
305. Wei, W., et al., *RSC Advances*, 2012, **2**(9), 3765-3771.
306. Huang, X.B., et al., *Journal of Applied Polymer Science*, 2013, **130**(1), 248-255.
307. Veldboer, K., et al., *Rapid Communications in Mass Spectrometry*, 2011, **25**(1), 147-154.
308. Ibisoglu, H. and Güzel A.M., *Polyhedron*, 2015, **100**, 139-145.
309. Çiftçi, G.Y., et al., *Polyhedron*, 2014, **77**, 1-9.
310. Türe, S., Silah H., and Tuna M., *Journal of Molecular Structure*, 2020, **1202**, 127232.
311. Onder, A. and Ozay H., *Chemical Engineering and Processing - Process Intensification*, 2021, **165**, 108427.
312. Kumar, E.S., Muralidhara M.G., and Chandrasekhar V., *Polyhedron*, 1995, **14**(12), 1571-1576.
313. Chen, Y.J., et al., *Polymer Degradation and Stability*, 2017, **140**, 166-175.
314. Carta, M., et al., *Polymer Chemistry*, 2014, **5**(18), 5267-5272.
315. Jiang, W.F., et al., *Synthetic Communications*, 2008, **38**(12), 1888-1895.
316. Simalou, O., et al., *European Journal of Organic Chemistry*, 2014, **2014**(14), 2907-2916.
317. Pal, R., et al., *The Journal of Physical Chemistry A*, 2014, **118**(19), 3479-89.

318. Potter, R.G. and Hughes T.S., *Journal of Organic Chemistry*, 2008, **73**(8), 2995-3004.
319. Chmil, K. and Scherf U., *Makromolekulare Chemie-Macromolecular Chemistry and Physics*, 1993, **194**(5), 1377-1386.
320. Shan, L., et al., *Advanced Materials*, 2015, **27**(22), 3418-3423.
321. Ruengsangtongkul, S., et al., *Organic Letters*, 2019, **21**(8), 2514-2517.
322. Akiyama, S., et al., *Bulletin of the Chemical Society of Japan*, 1995, **68**(7), 2043-2051.
323. Nakano, E., et al., *The Journal of Physical Chemistry A*, 2014, **118**(12), 2288-2297.
324. Mutoh, K., et al., *Journal of the American Chemical Society*, 2019, **141**(14), 5650-5654.
325. Kuhn, R., F. Zilliken, and Dury K., *Naturwissenschaften*, 1951, **38**, 12-13.
326. Thiemann, T., Iniesta J., and Walton D.J., *Journal of Chemical Research*, 2008(3), 173-180.
327. Sakaguchi, Y. and Harris F.W., *Polymer Journal*, 1992, **24**(10), 1147-1154.
328. Kobayashi, K., et al., *Journal of Organic Chemistry*, 2005, **70**(2), 749-752.
329. Al-Masri, M., Kricheldorf H.R., and D. Fritsch, *Macromolecules*, 1999, **32**(23), 7853-7858.
330. Wang, J.L., Freeman H.S., and Claxton L.D., *Coloration Technology*, 2007, **123**(1), 39-45.

Appendix

8.1 SSNMR

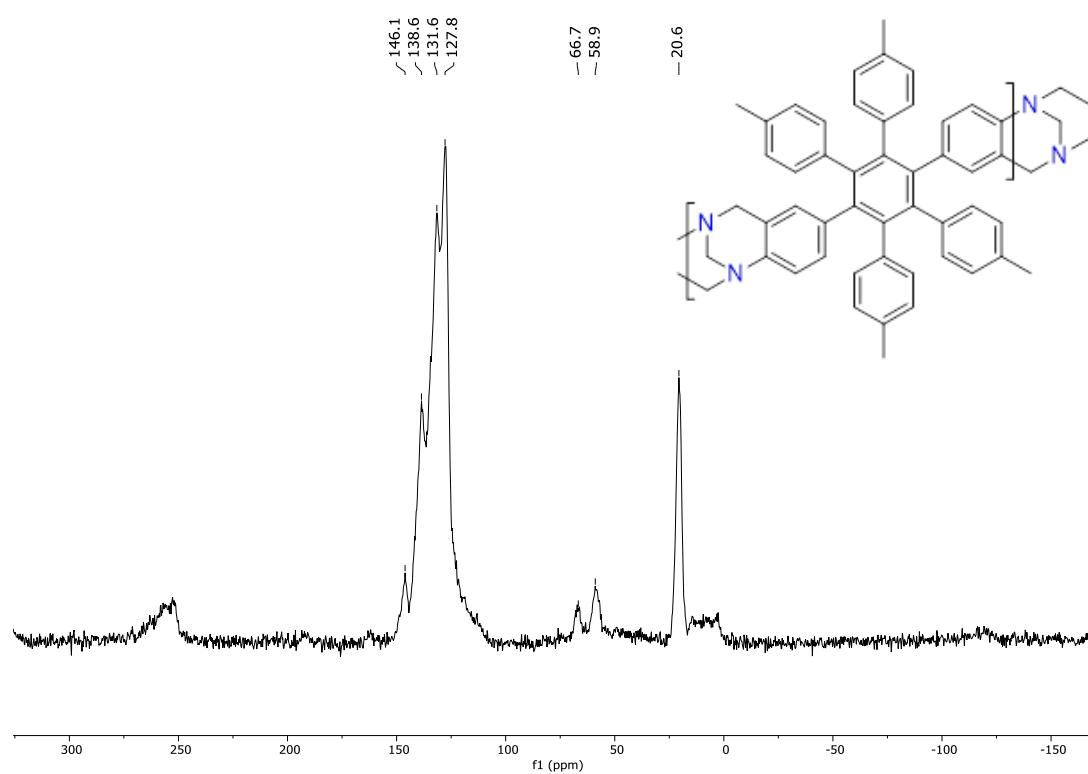


Figure SI1 SSNMR for di-TB-tetra-Me-HPB.

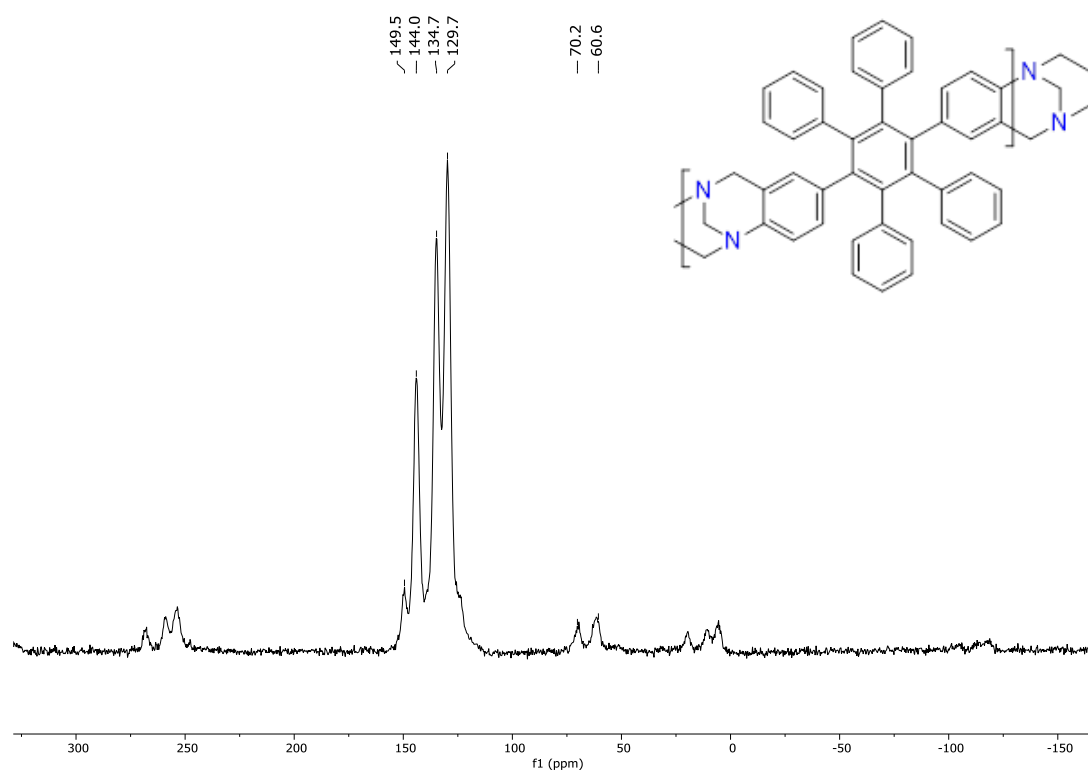


Figure SI2 SSNMR for di-TB-HPB.

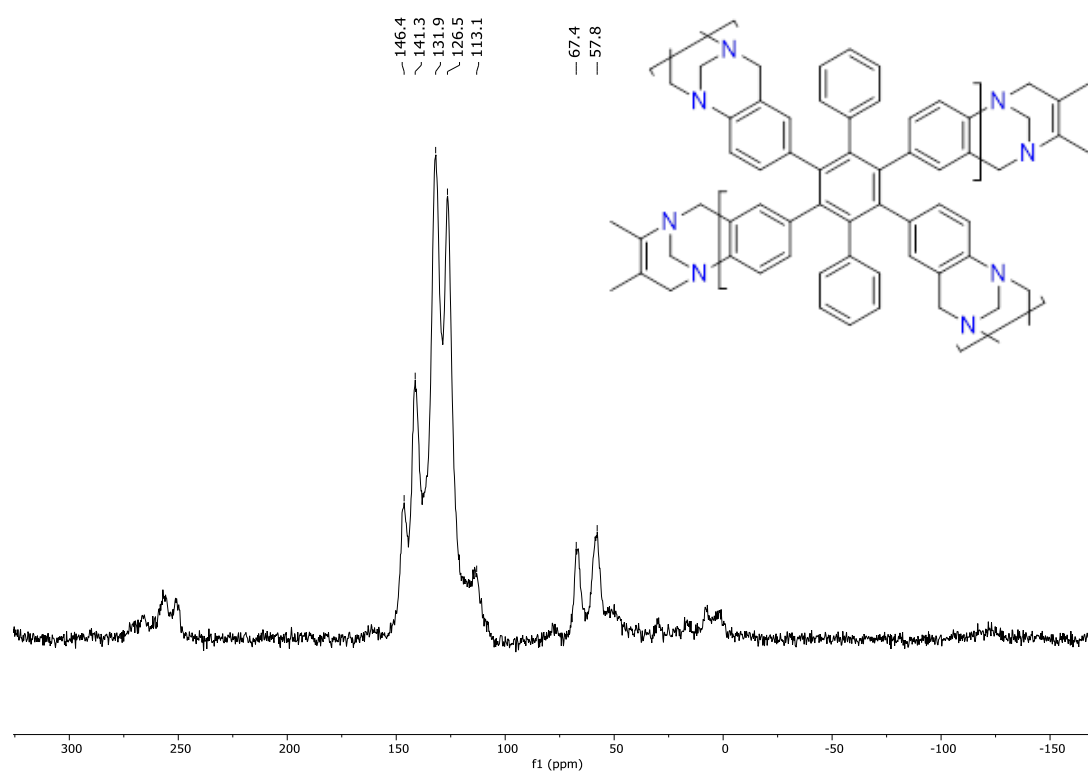


Figure SI3 SSNMR for tetra-TB-HPB.

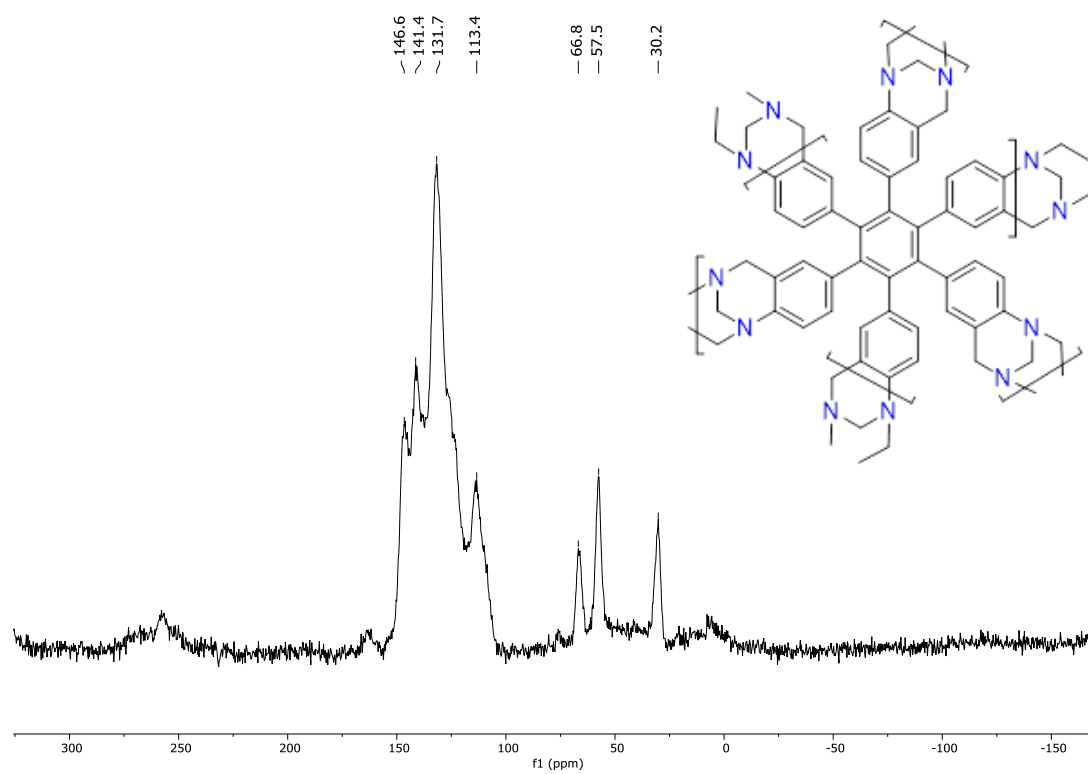


Figure S14 SSNMR for hexa-TB-HPB.

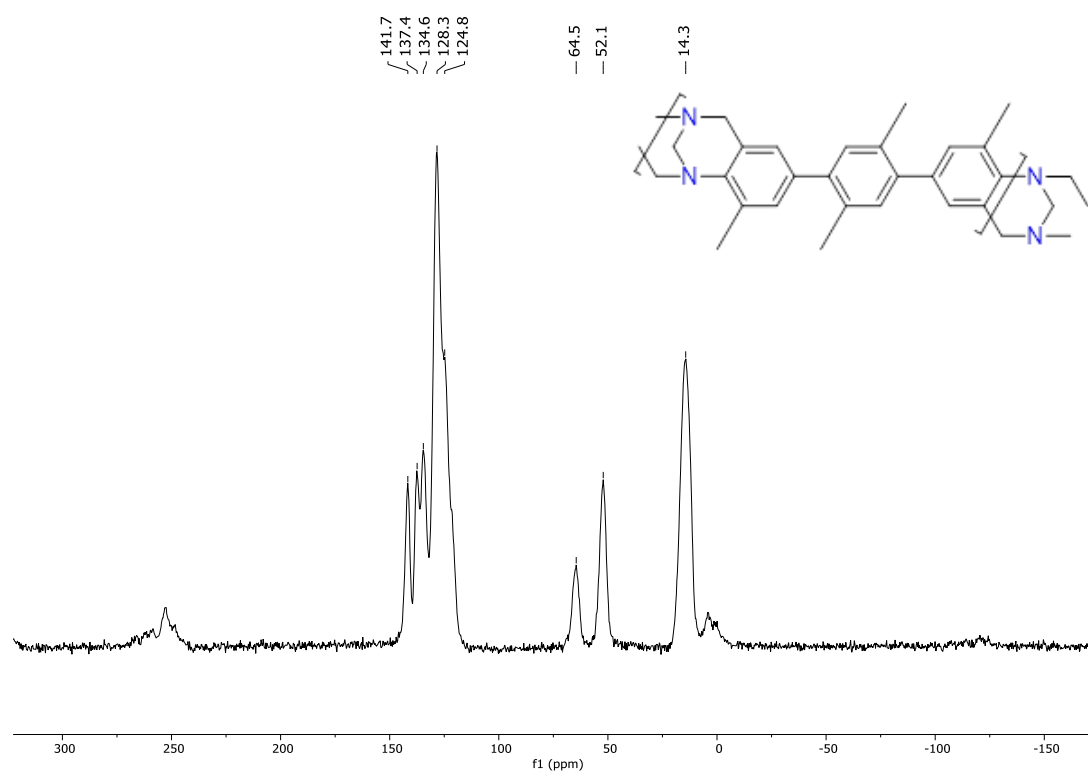


Figure S15 SSNMR for linear TB-polymer 1.

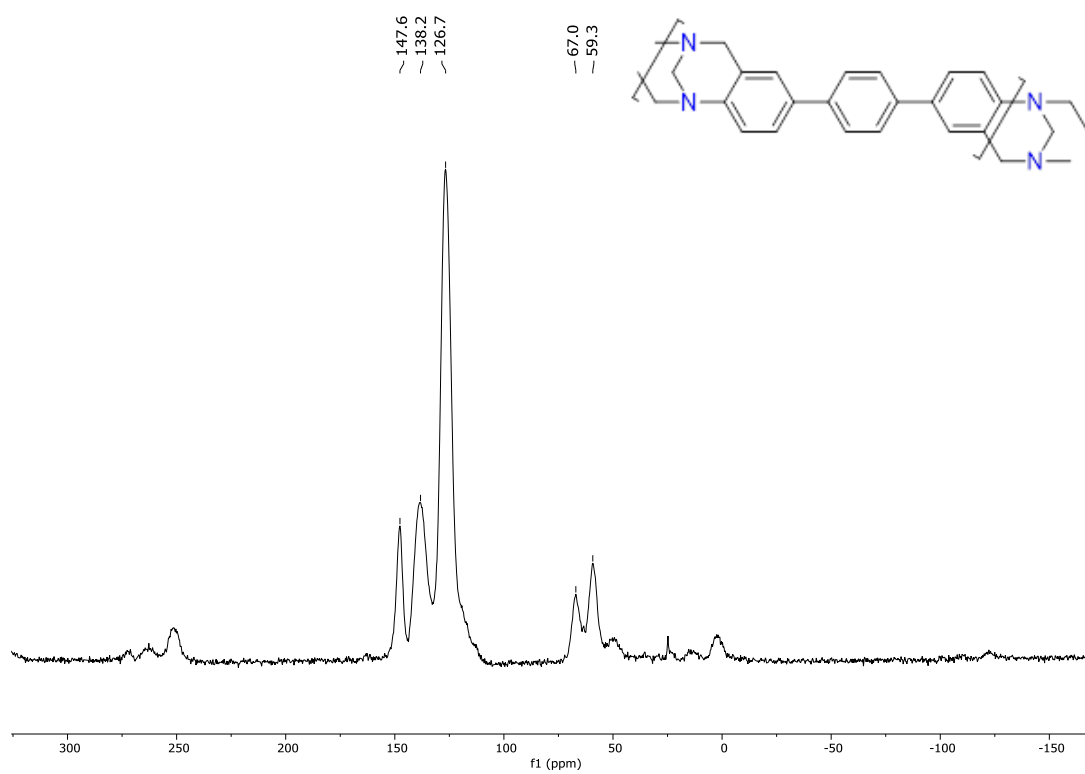


Figure SI6 SSNMR for linear TB-polymer 2.

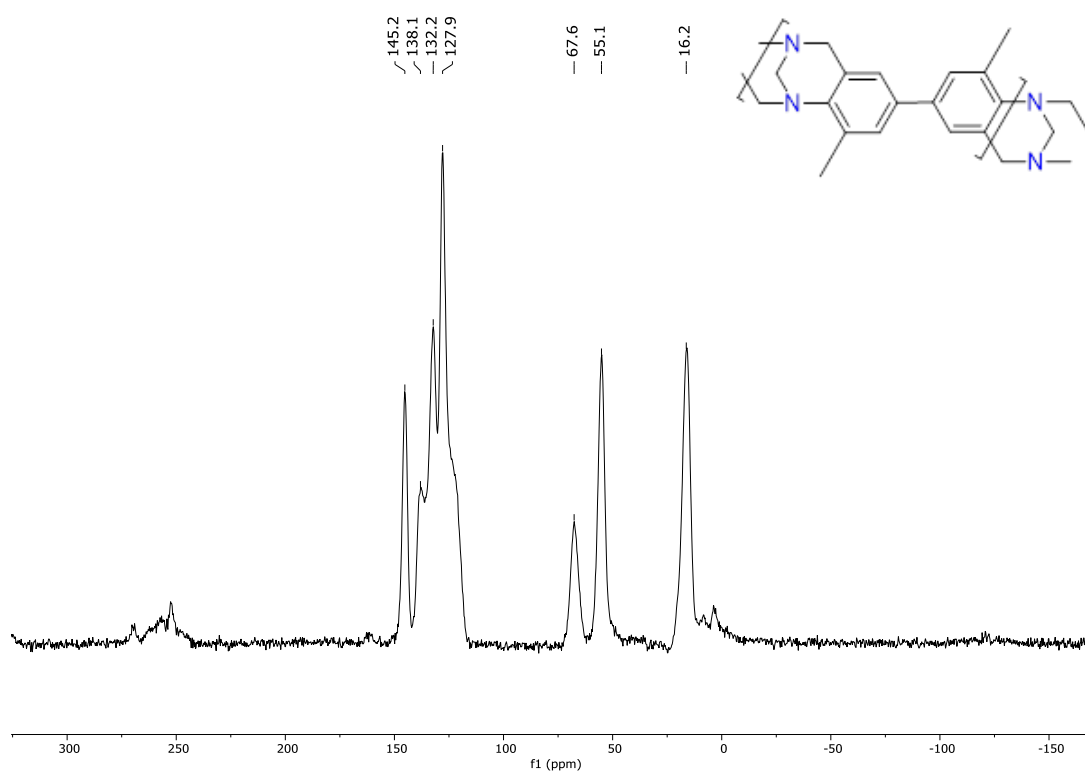


Figure SI7 SSNMR for linear TB-polymer 3.

8.2 FT-IR

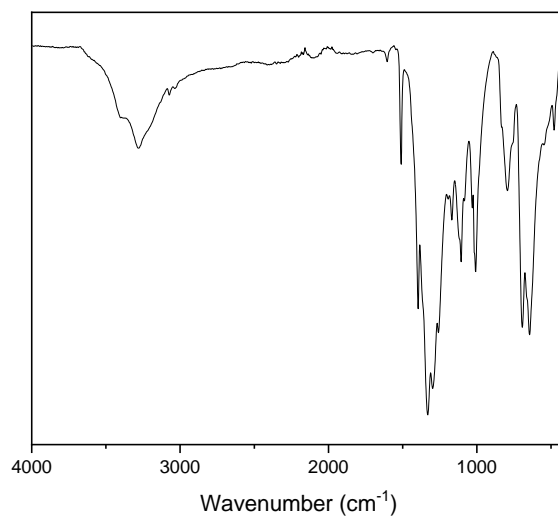


Figure SI8 FT-IR for model boroxine/sand bath.

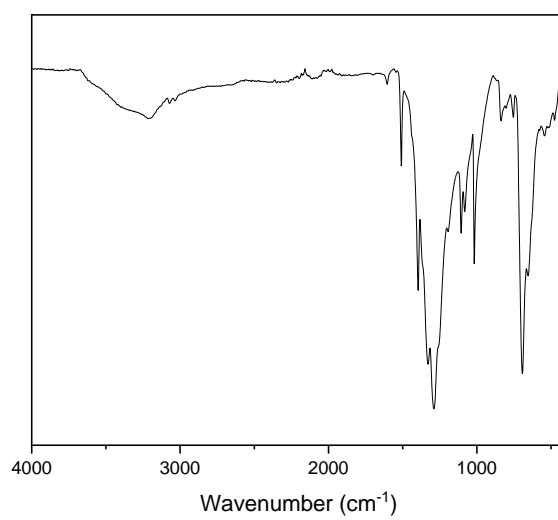


Figure SI9 FT-IR for model boroxine/microwave.

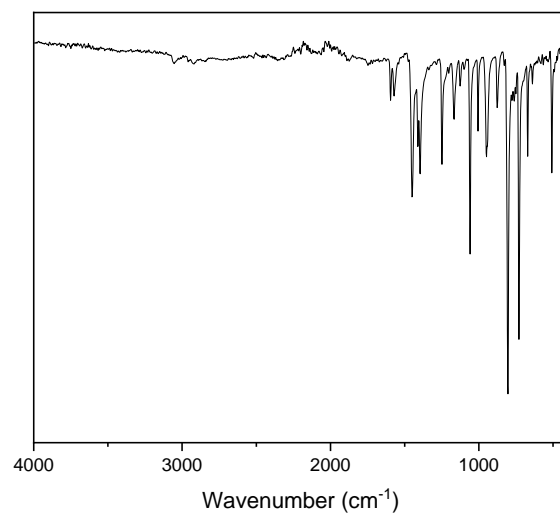


Figure SI10 FT-IR for tetrabromo-SBF.

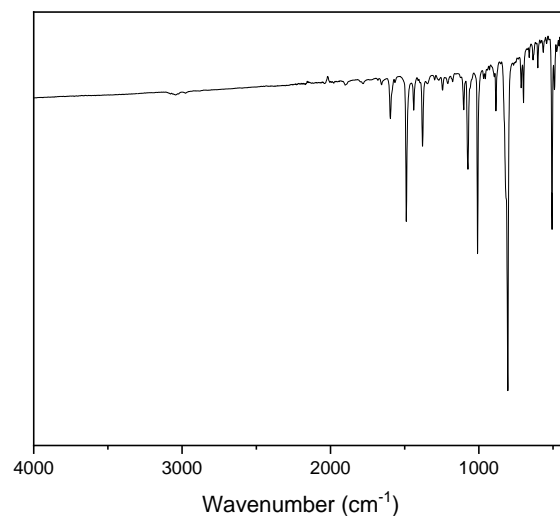


Figure SI11 FT-IR for TBPB.

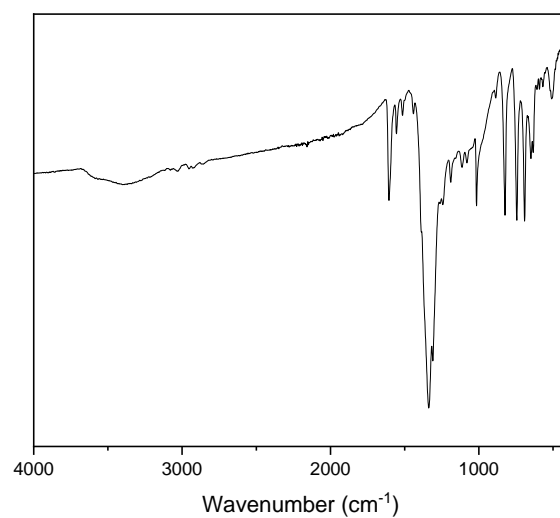


Figure SI12 FT-IR for TPB-triboronic acid.

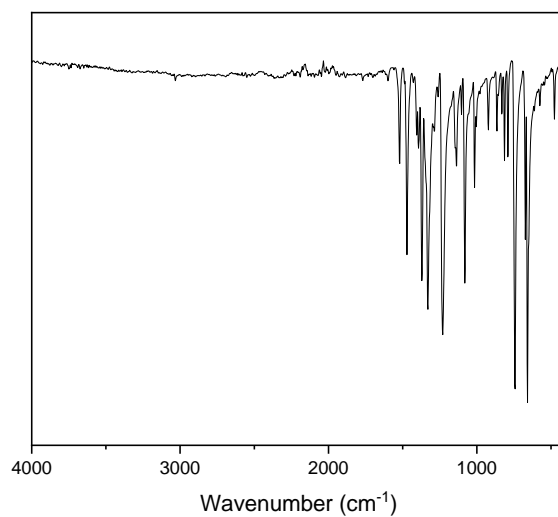


Figure SI13 FT-IR for model boronic ester.

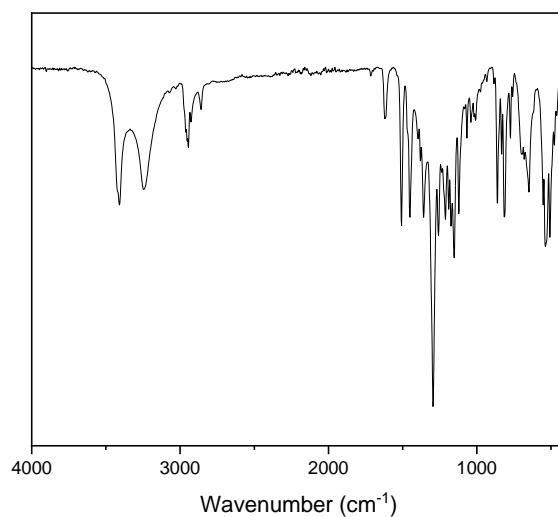


Figure SI14 FT-IR for BE-SBI-PIM/Dean-Stark.

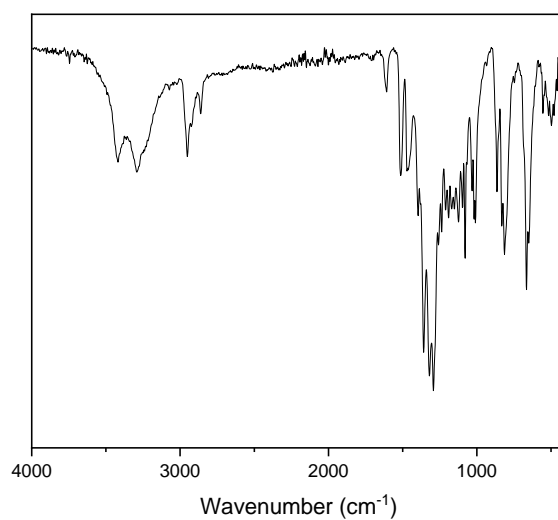


Figure SI15 FT-IR for BE-SBI-PIM/microwave.

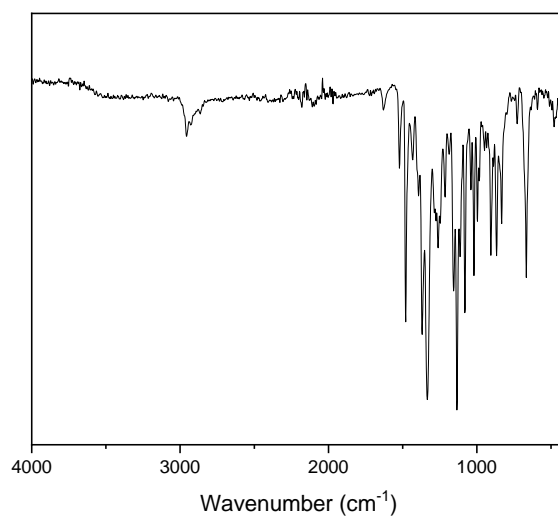


Figure SI16 FT-IR for BE-SBC-PIM/Dean-Stark.

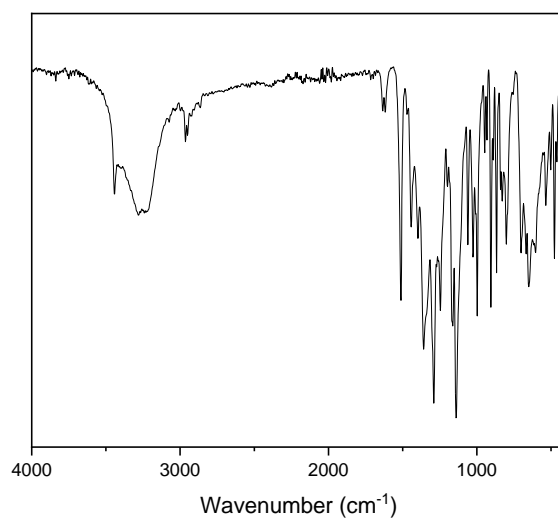


Figure SI17 FT-IR for BE-SBC-PIM/microwave.

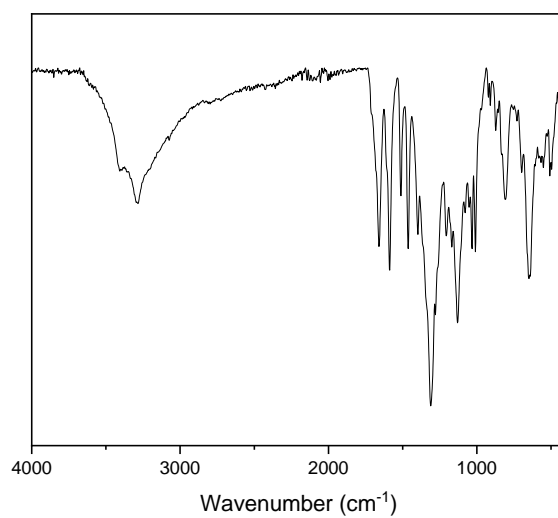


Figure SI18 FT-IR for BE-bis-K-PIM/Dean-Stark.

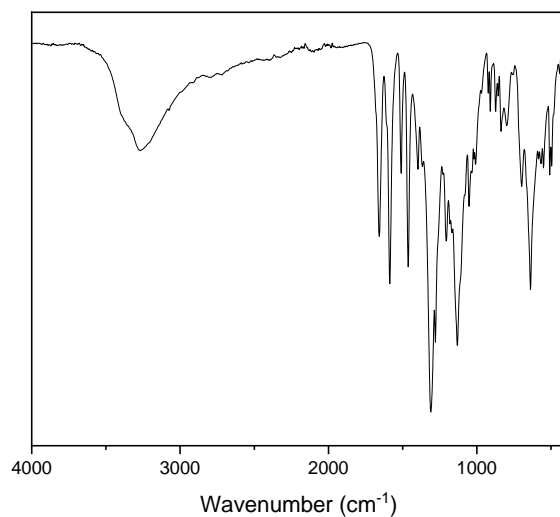


Figure SI19 FT-IR for BE-bis-K-PIM/microwave.

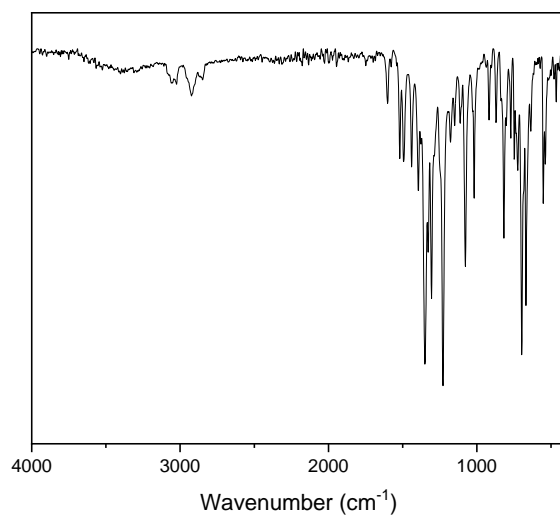


Figure SI20 FT-IR for BE-HPB-PIM/Dean-Stark.

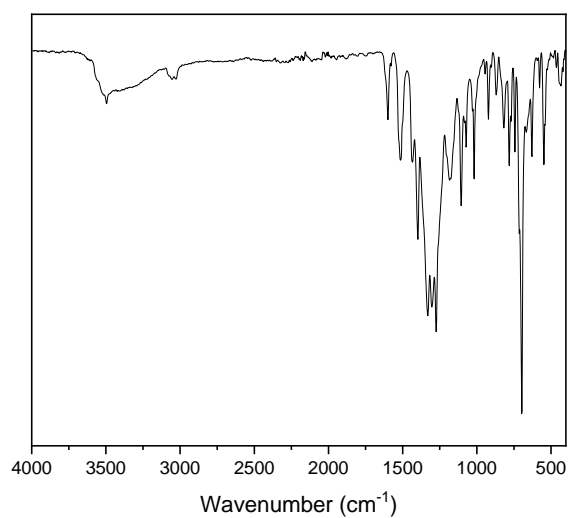


Figure SI21 FT-IR for BE-HPB-PIM/microwave.

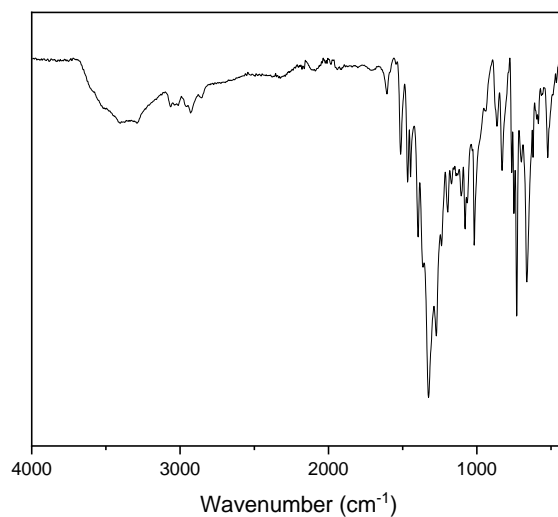


Figure SI22 FT-IR for BE-SBF-PIM/Dean-Stark.

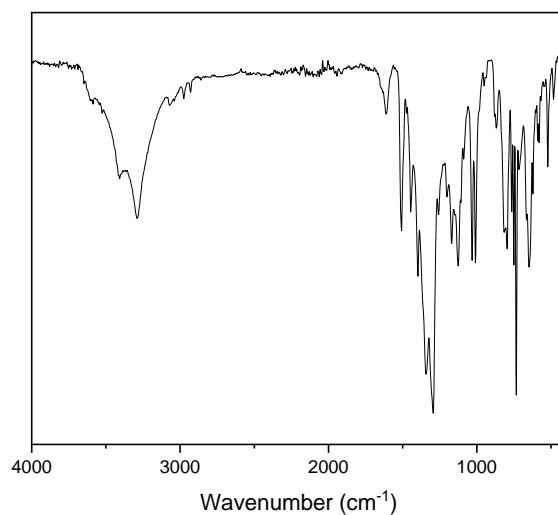


Figure SI23 FT-IR for BE-SBF-PIM/microwave.

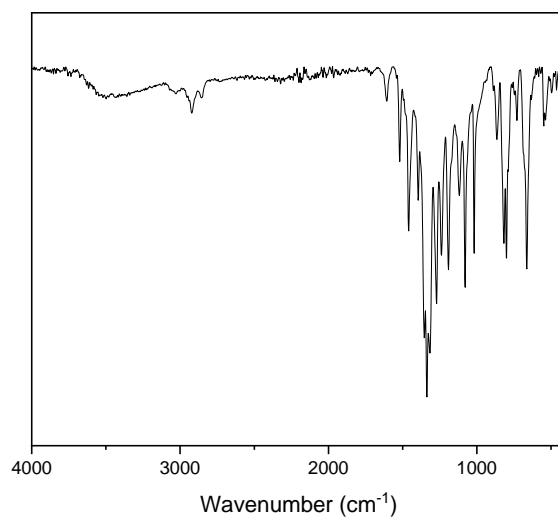


Figure SI24 FT-IR for BE-SBF-Me-PIM/Dean-Stark.

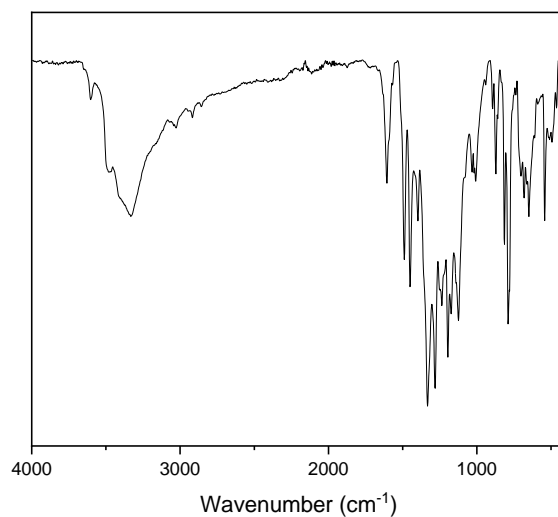


Figure SI25 FT-IR for BE-SBF-Me-PIM/microwave.

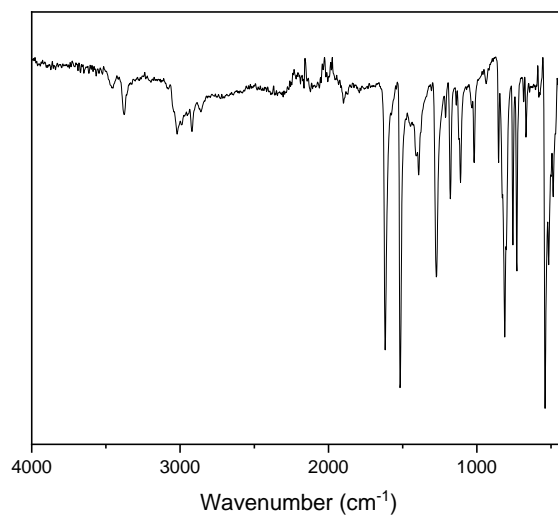


Figure SI26 FT-IR for di-amino-tetra-Me-HPB.

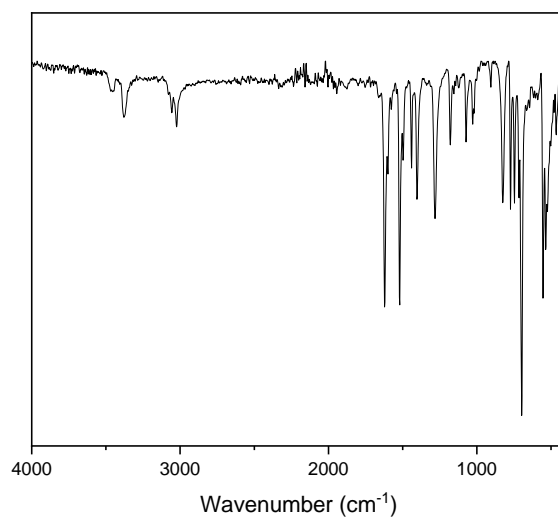


Figure SI27 FT-IR for di-amino-HPB.

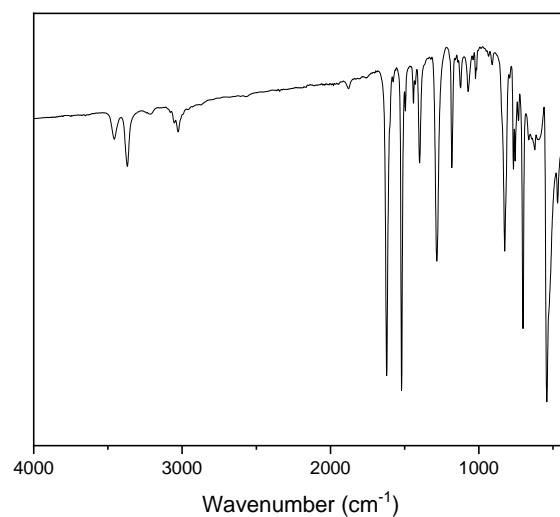


Figure SI28 FT-IR for tetra-amino-HPB.

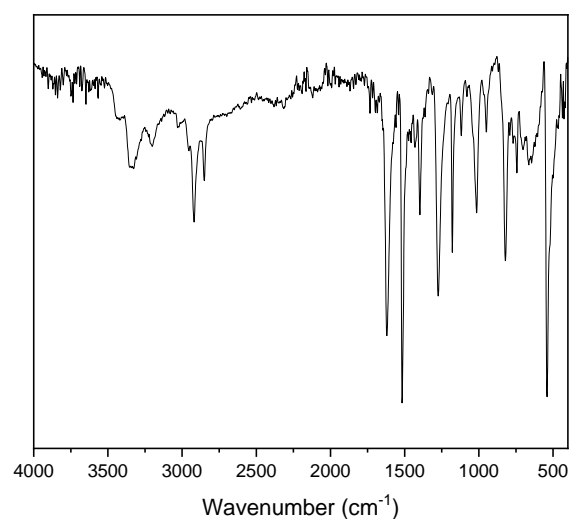


Figure SI29 FT-IR for hexa-amino-HPB.

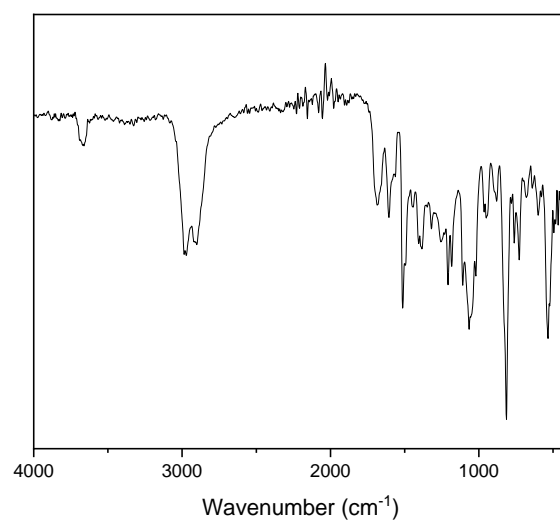


Figure SI30 FT-IR for di-TB-tetra-Me-HPB.

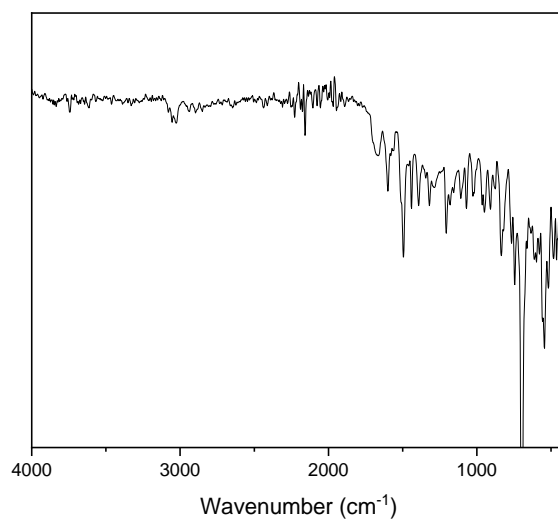


Figure SI31 FT-IR for di-TB-HPB.

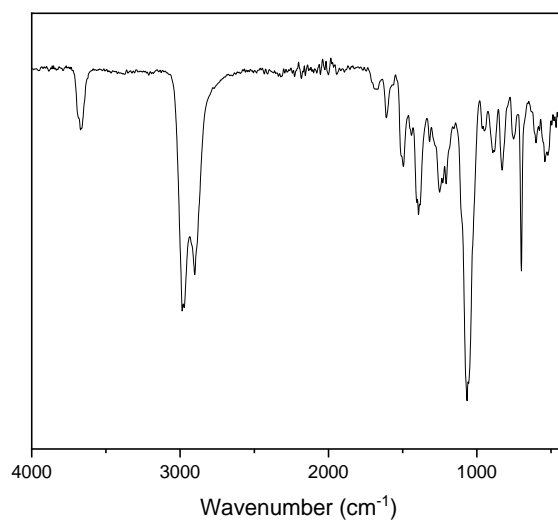


Figure SI32 FT-IR for tetra-TB-HPB.

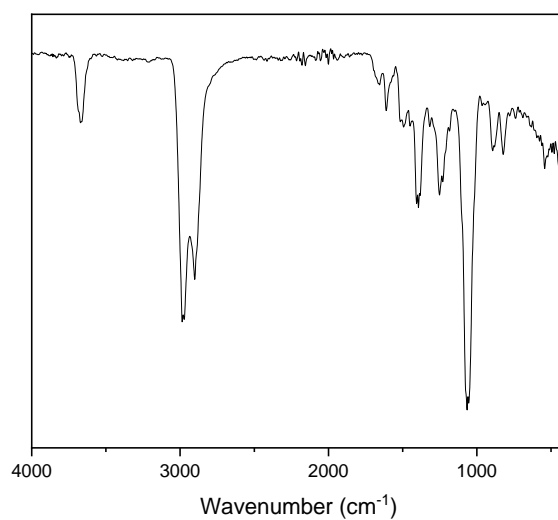


Figure SI33 FT-IR for hexa-TB-HPB.

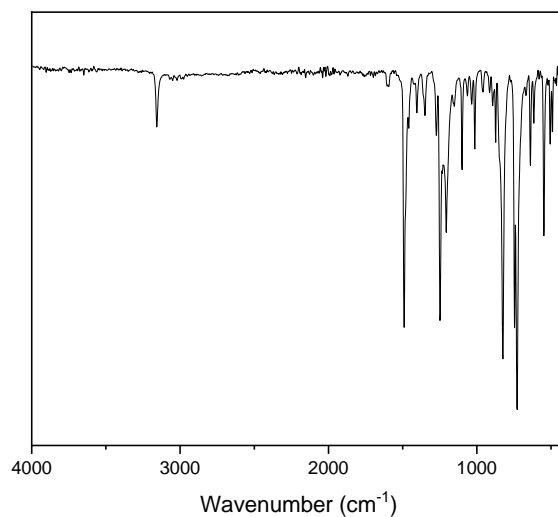


Figure SI34 FT-IR for Model CTP 1/reflux.

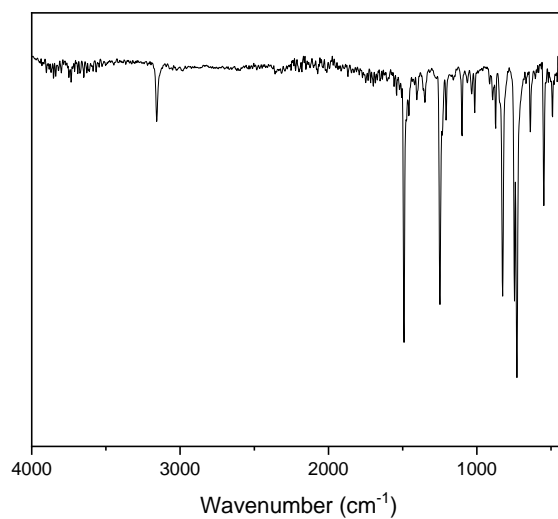


Figure SI35 FT-IR for Model CTP 1/microwave.

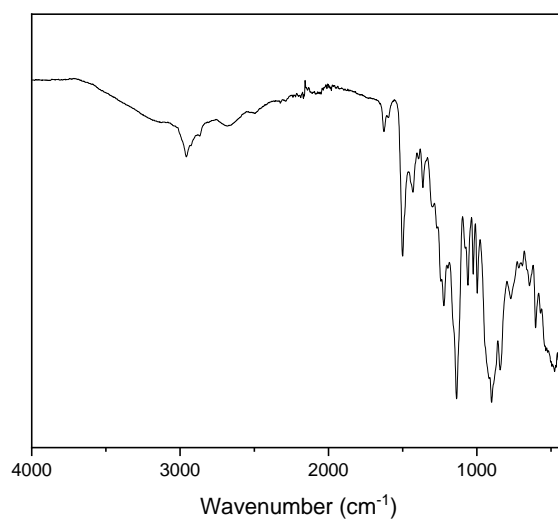


Figure SI36 FT-IR for CTP-SBC-PIMs/reflux.

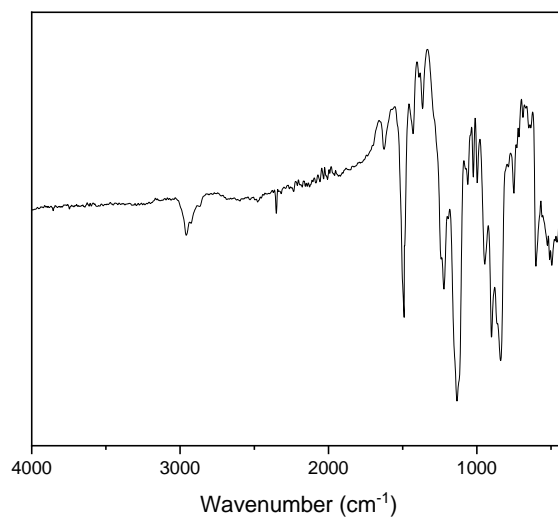


Figure SI37 FT-IR for CTP-SBC-PIMs/microwave.

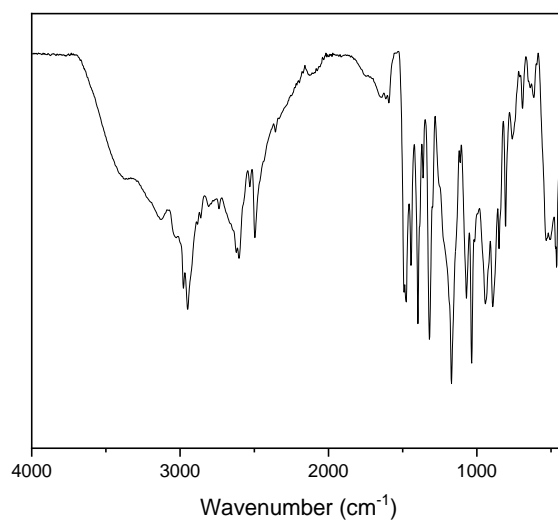


Figure SI38 FT-IR for CTP-SBI-PIMs/reflux.

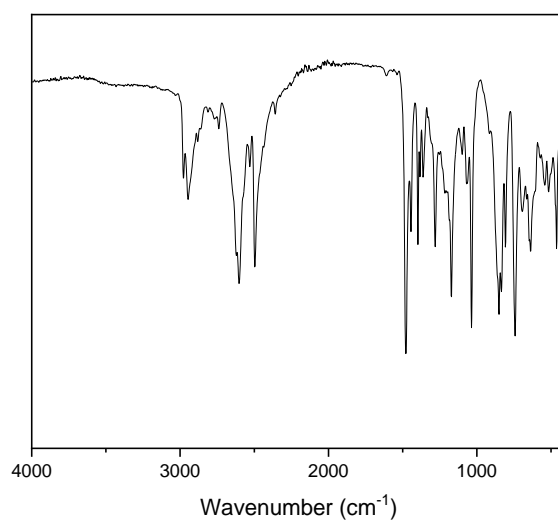


Figure SI39 FT-IR for CTP-SBI-PIMs/microwave.

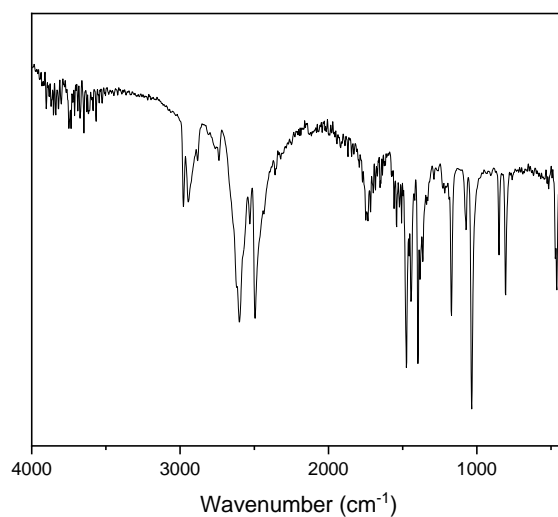


Figure SI40 FT-IR for Model CTP 2a/flux.

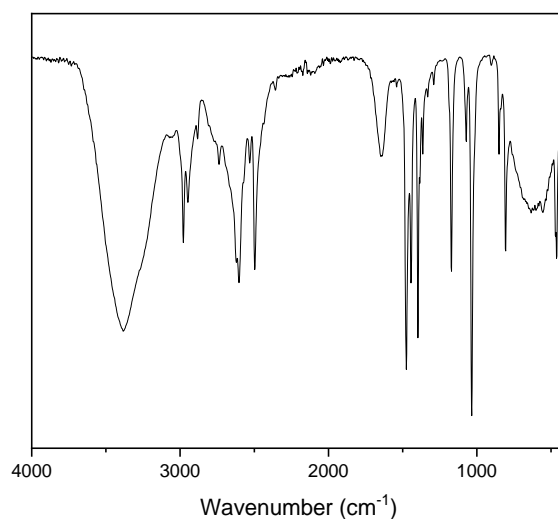


Figure SI41 FT-IR for Model CTP 2a/microwave.

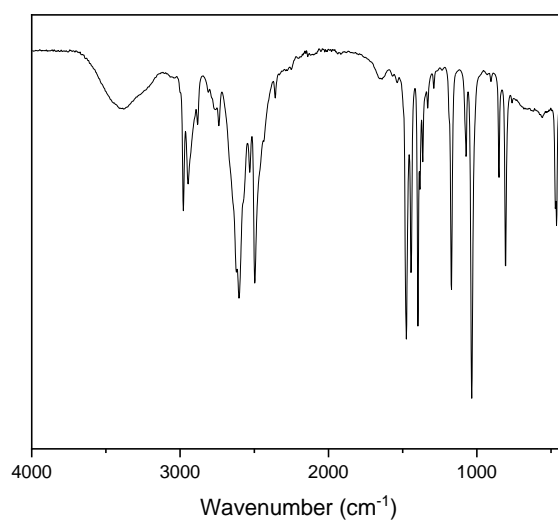


Figure SI42 FT-IR for Model CTP 2b/flux.

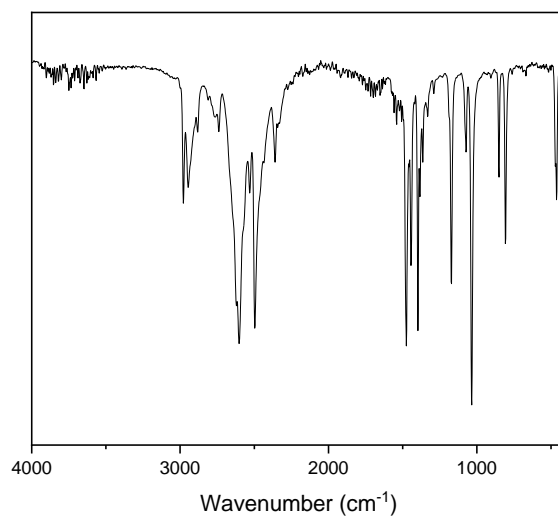


Figure SI43 FT-IR for Model CTP 2b/microwave.

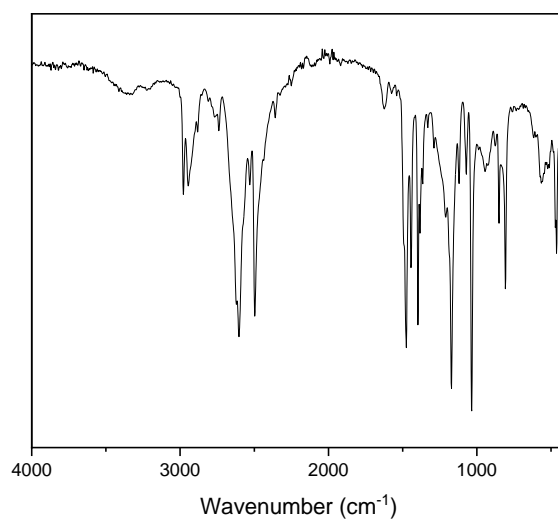


Figure SI44 FT-IR for CTP-tolidine-PIM/reflux.

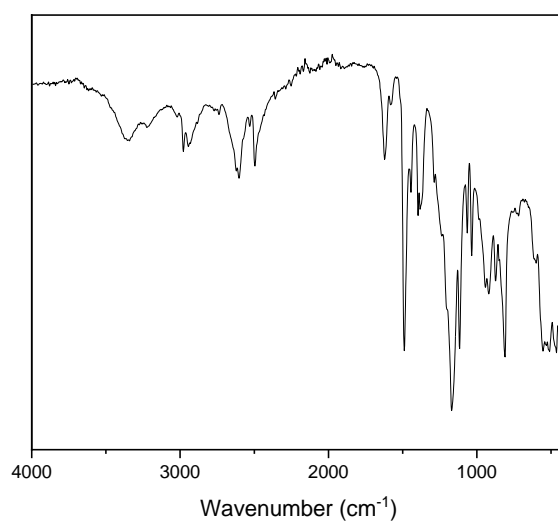


Figure SI45 FT-IR for CTP-tolidine-PIM/microwave.

8.3 TGA

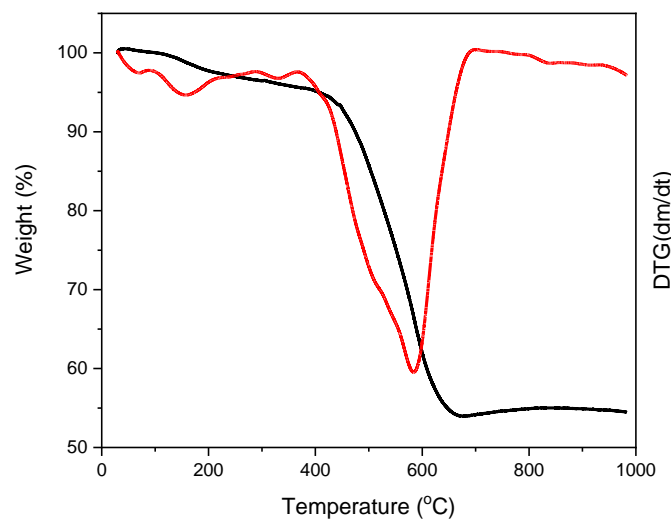


Figure SI46 TGA in N₂ for model boroxine/sand bath.

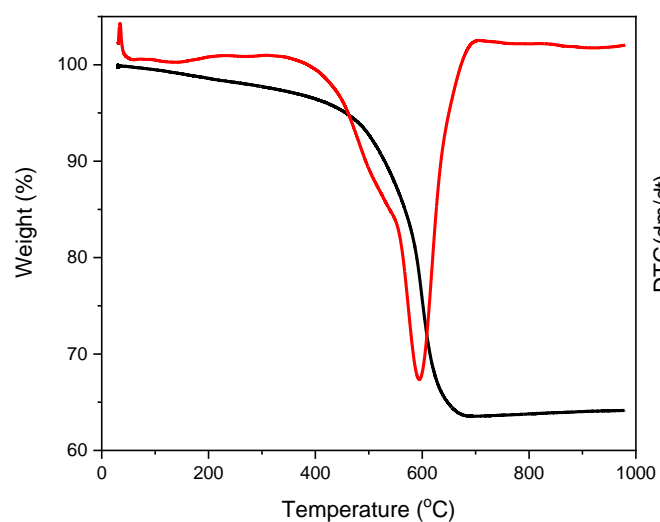


Figure SI47 TGA in N₂ for model boroxine/microwave.

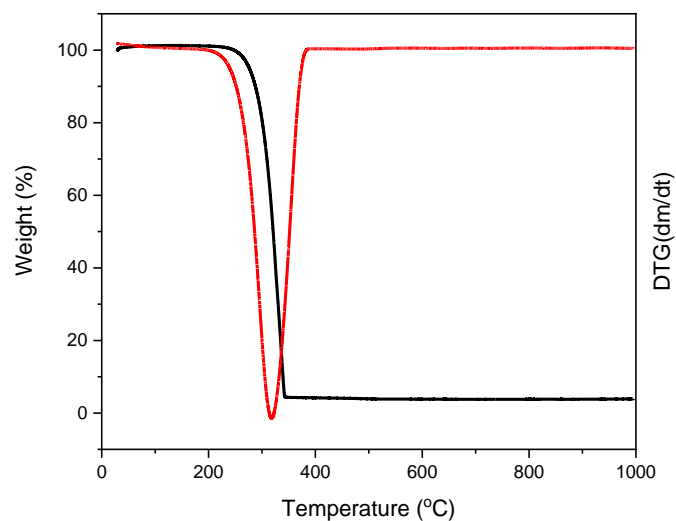


Figure SI48 TGA in N₂ for model boronic ester.

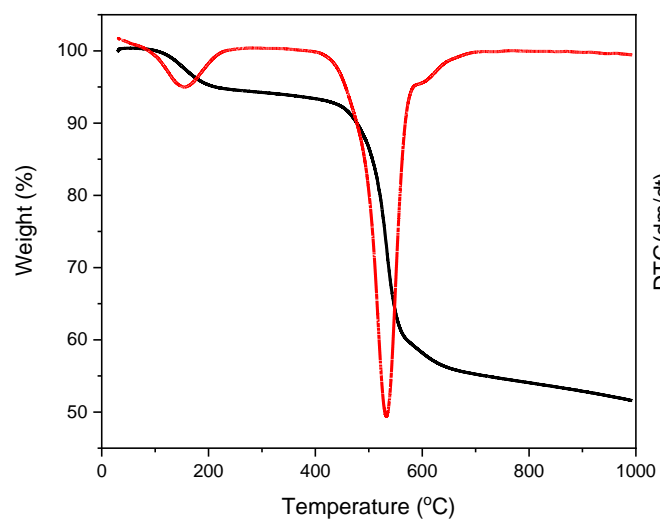


Figure SI49 TGA in N₂ for BE-SBI-PIM/Dean-Stark.

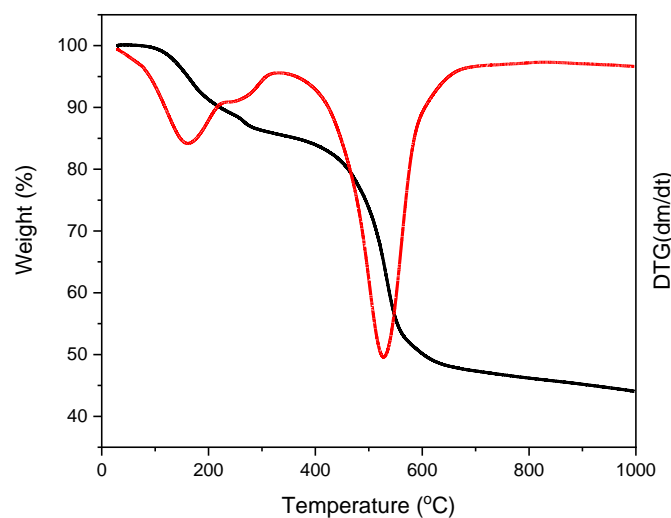


Figure SI50 TGA in N₂ for BE-SBI-PIM/microwave.

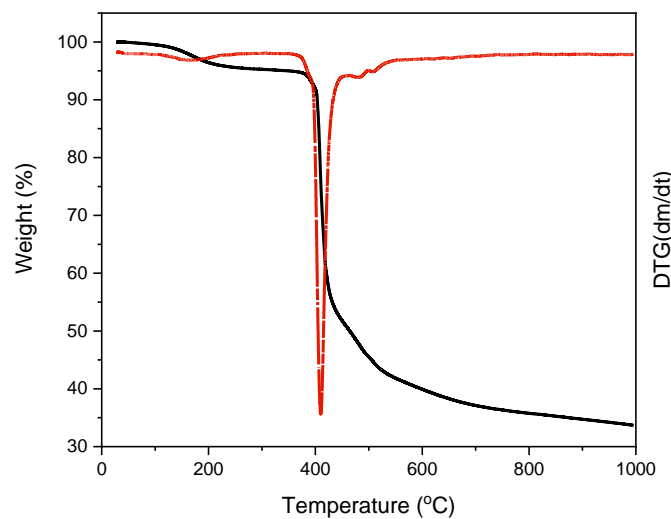


Figure SI51 TGA in N₂ for BE-SBC-PIM/Dean-Stark.

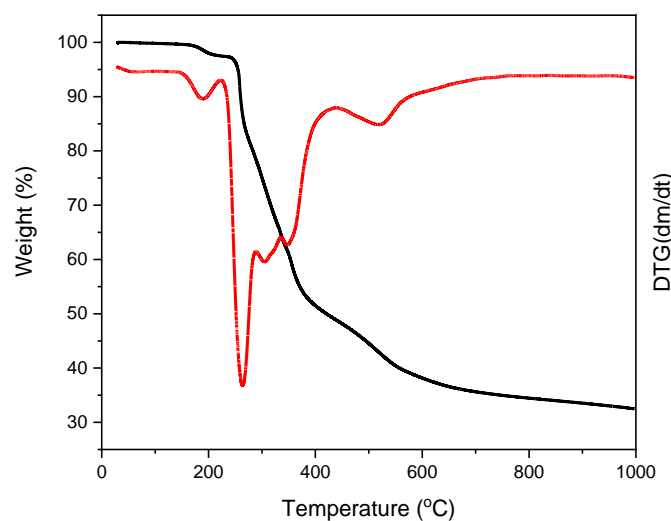


Figure SI52 TGA in N₂ for BE-SBC-PIM/microwave.

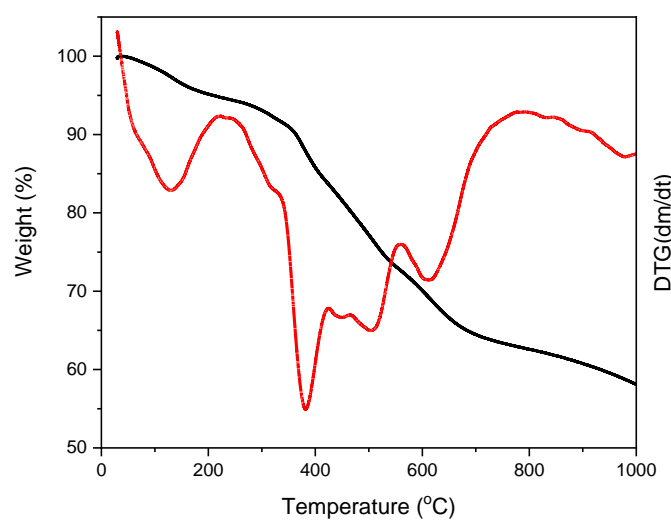


Figure SI53 TGA in N₂ for BE-bis-K-PIM/Dean-Stark.

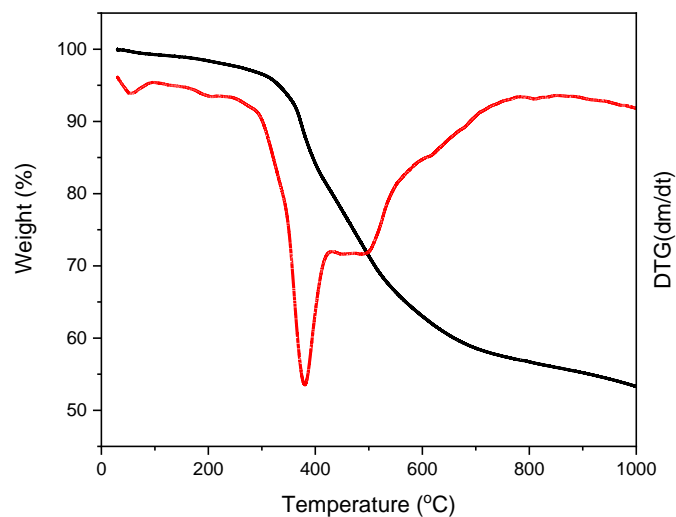


Figure SI54 TGA in N₂ for BE-bis-K-PIM/microwave.

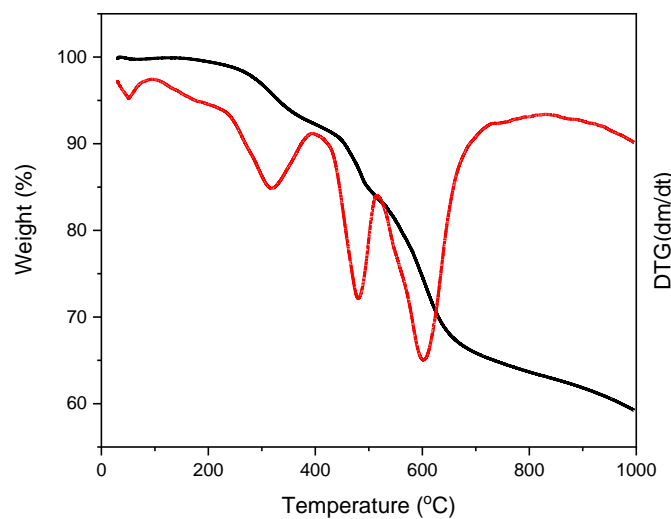


Figure SI55 TGA in N₂ for BE-HPB-PIM/Dean-Stark.

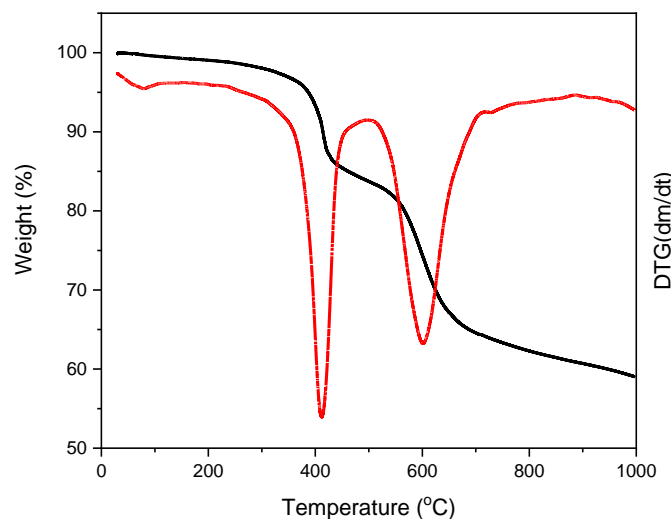


Figure SI56 TGA in N₂ for BE-HPB-PIM/microwave.

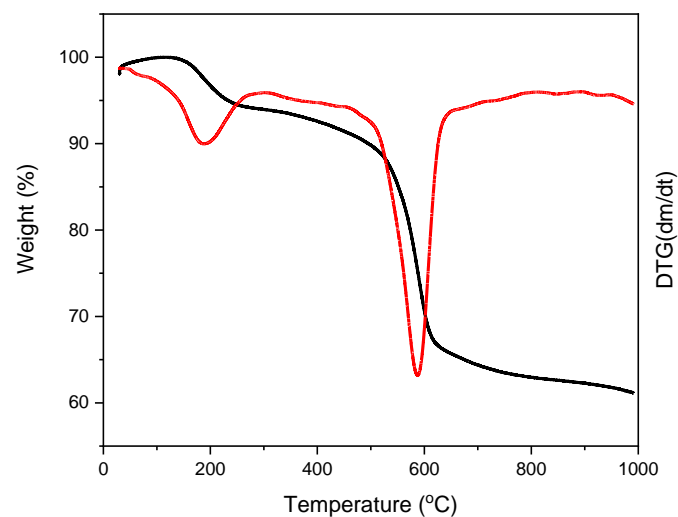


Figure SI57 TGA in N₂ for BE-SBF-PIM/Dean-Stark.

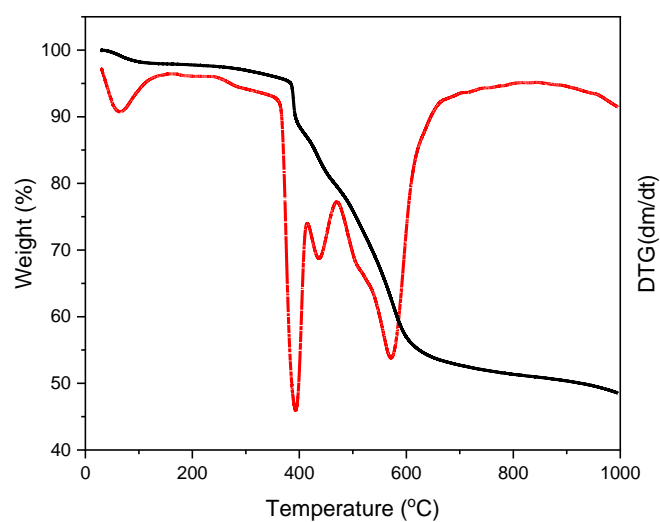


Figure SI58 TGA in N₂ for BE-SBF-PIM/microwave.

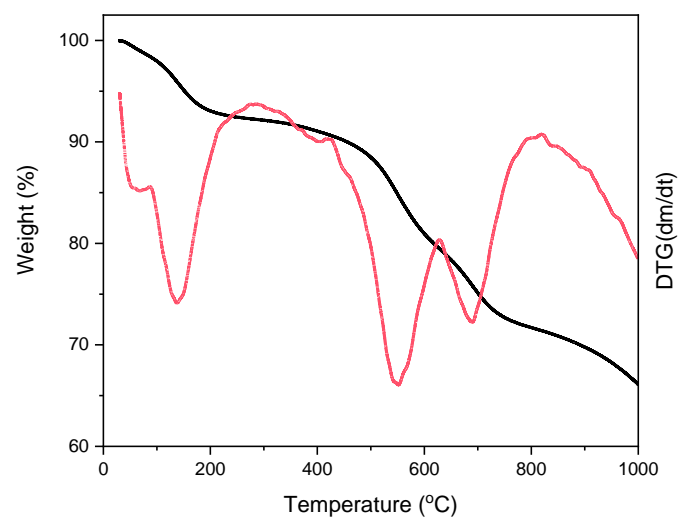


Figure SI59 TGA in N₂ for BE-SBF-Me-PIM/Dean-Stark.

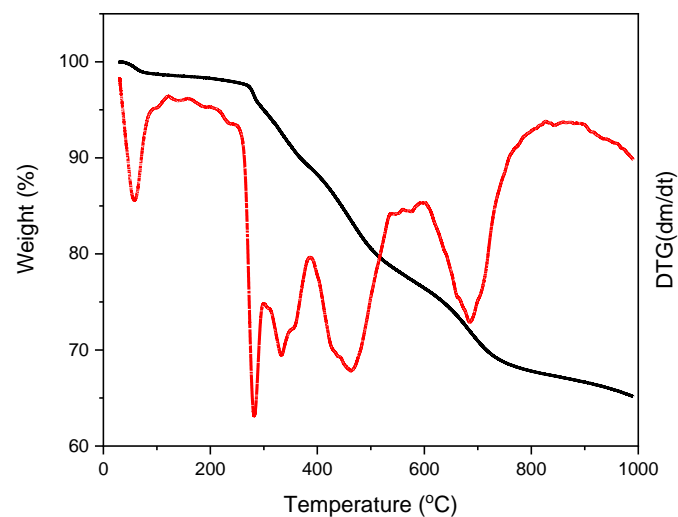


Figure SI60 TGA in N₂ for BE-SBF-Me-PIM/microwave.

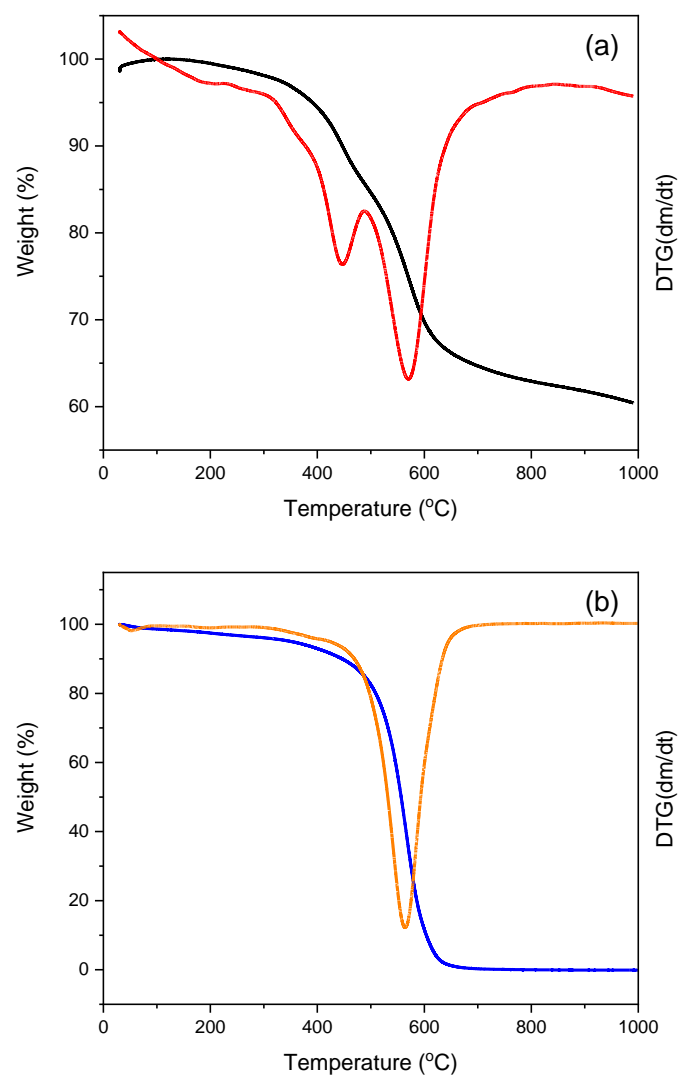


Figure SI61 TGA for di-TB-tetra-Me-HPB: (a) in N₂, (b) in air.

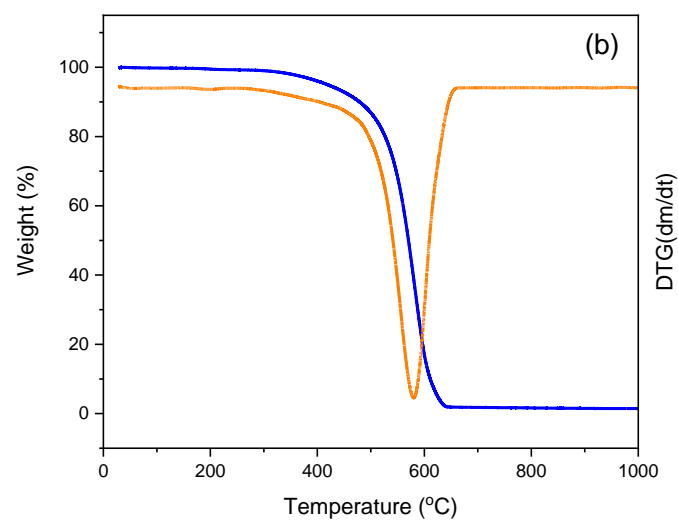
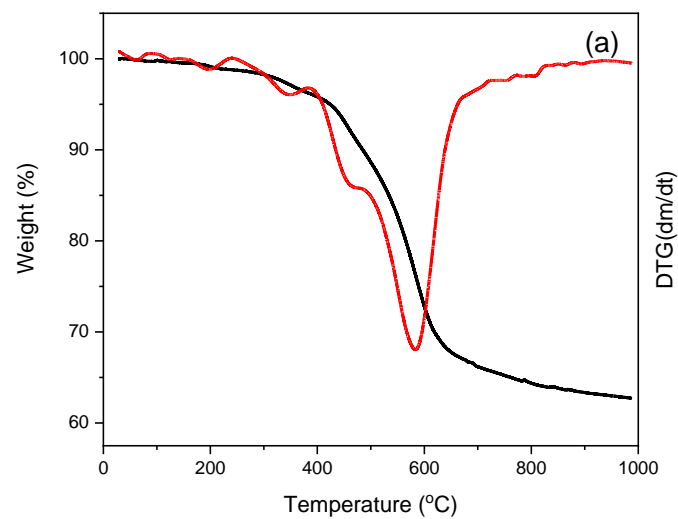
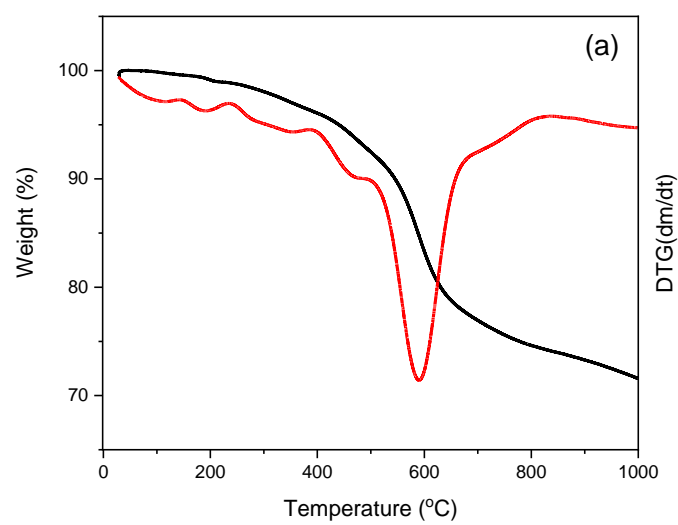


Figure SI62 TGA for di-TB-HPB: (a) in N₂, (b) in air.



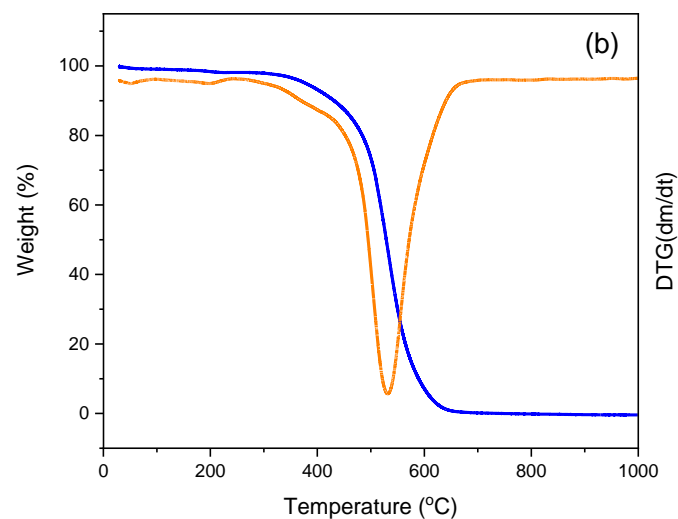


Figure S163 TGA for tetra-TB-HPB: (a) in N₂, (b) in air.

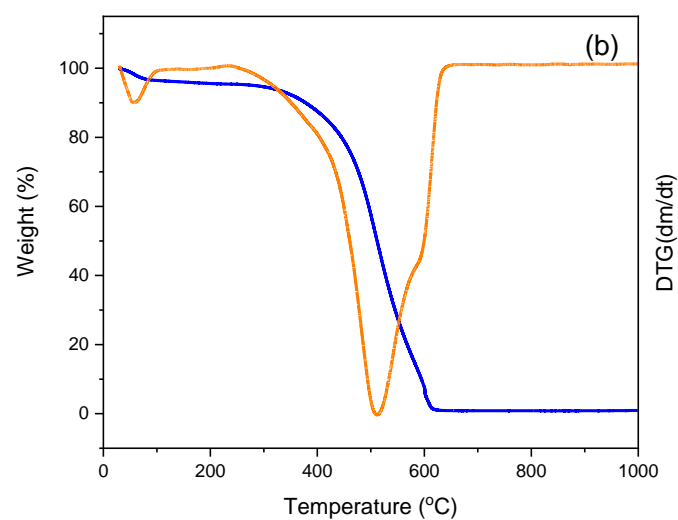
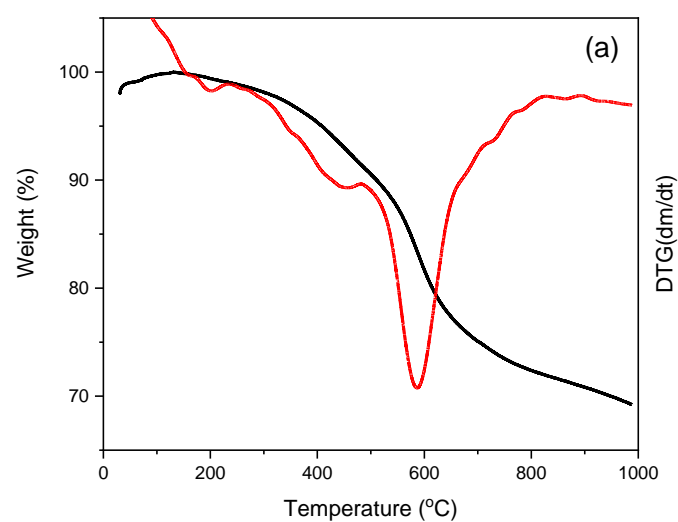


Figure S164 TGA for hexa-TB-HPB: (a) in N₂, (b) in air.

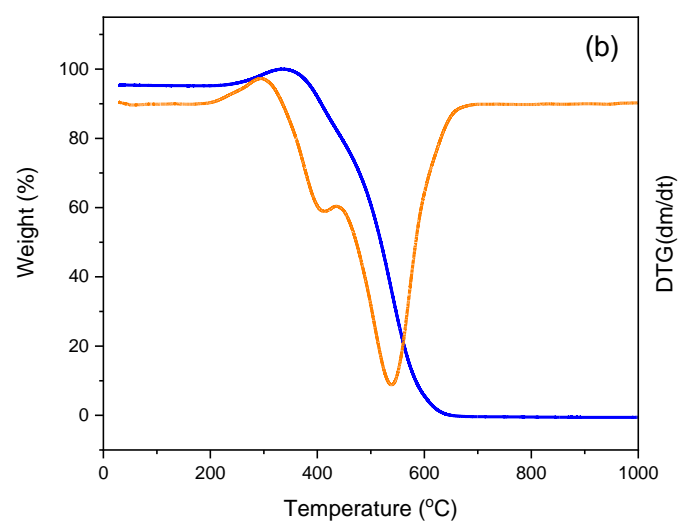
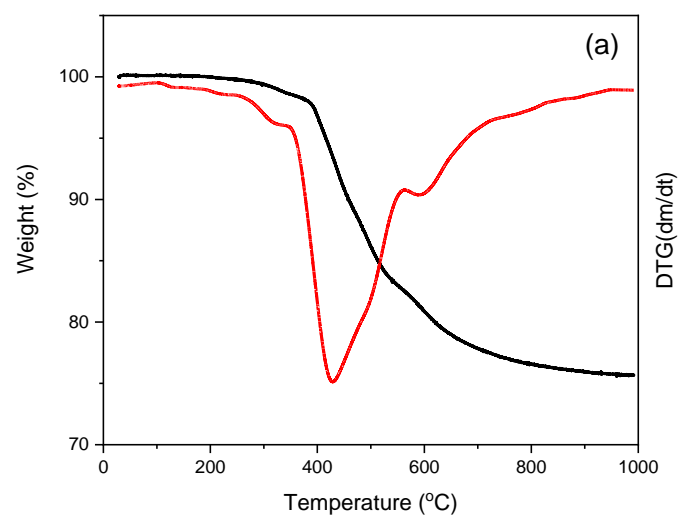
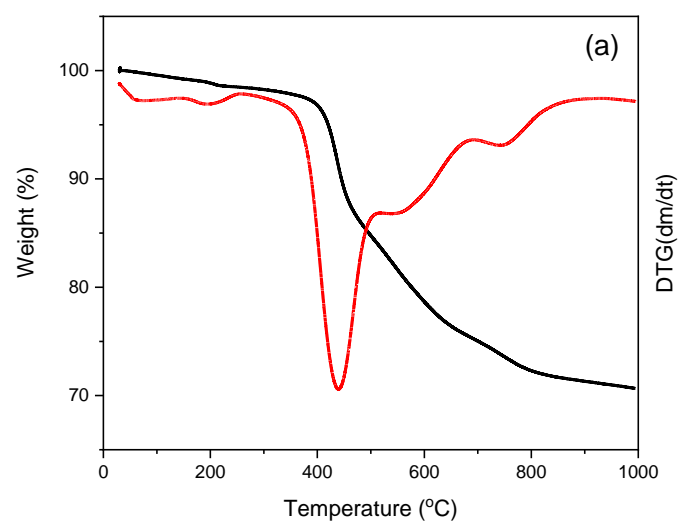


Figure SI65 TGA for linear TB-polymer 1: (a) in N₂, (b) in air.



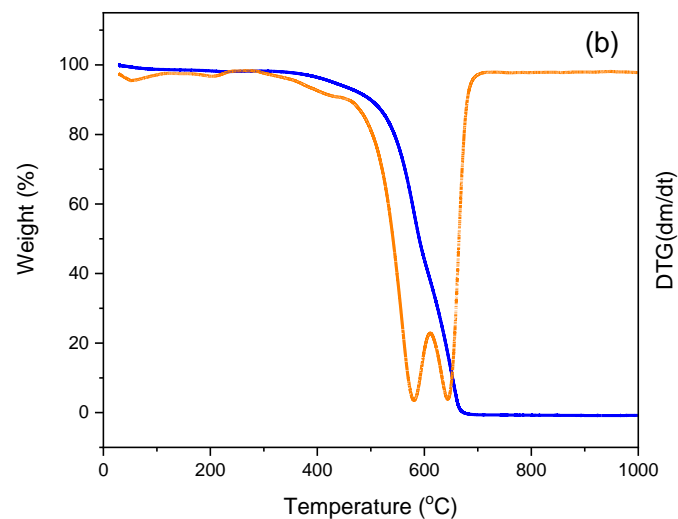


Figure SI66 TGA for linear TB-polymer 2: (a) in N₂, (b) in air.

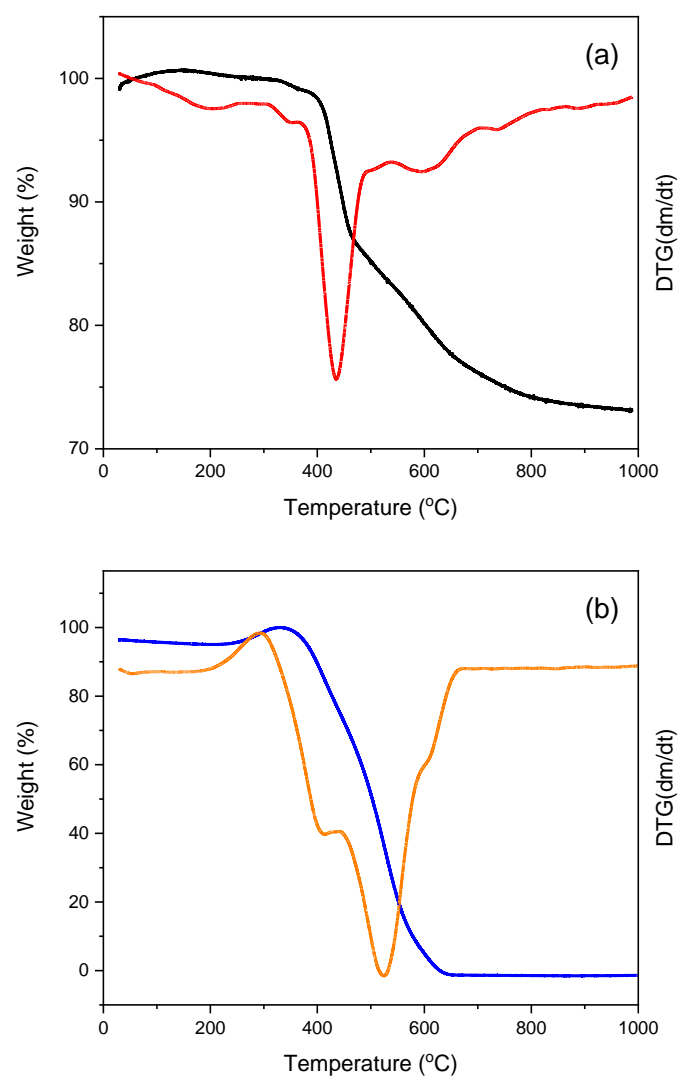


Figure SI67 TGA for linear TB-polymer3: (a) in N₂, (b) in air.

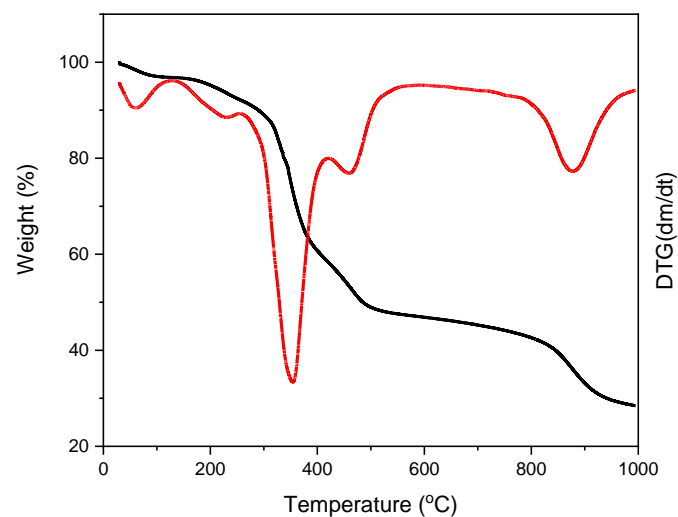


Figure SI68 TGA in N₂ for CTP-SBC-PIMs/reflux.

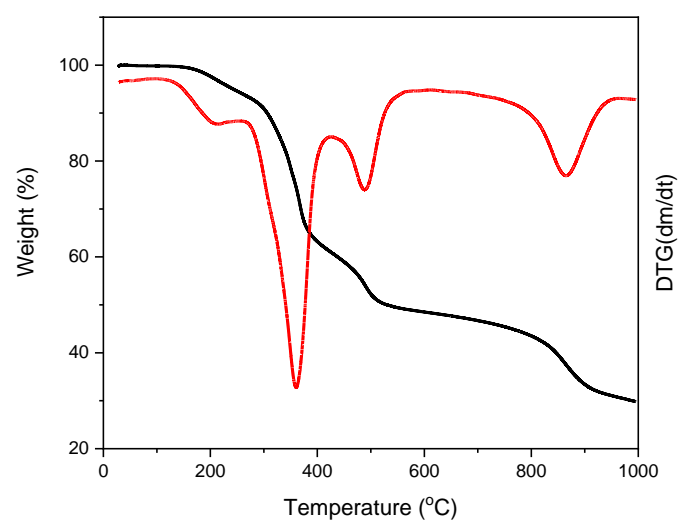


Figure SI69 TGA in N₂ for CTP-SBC-PIMs/microwave.

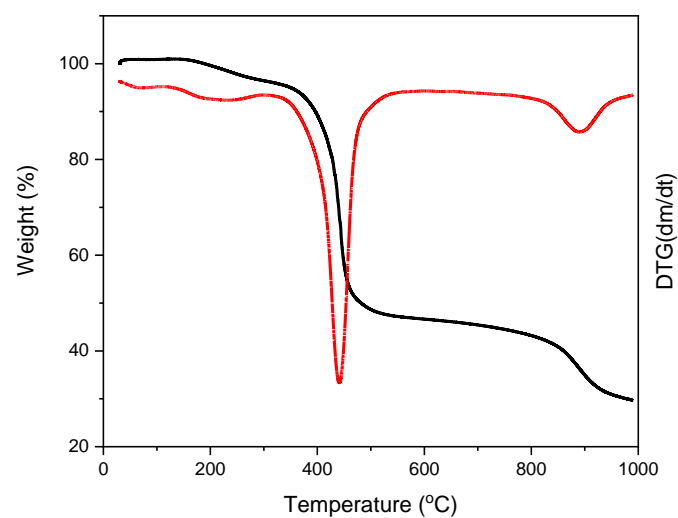


Figure SI70 TGA in N₂ for CTP-SBI-PIMs/reflux.

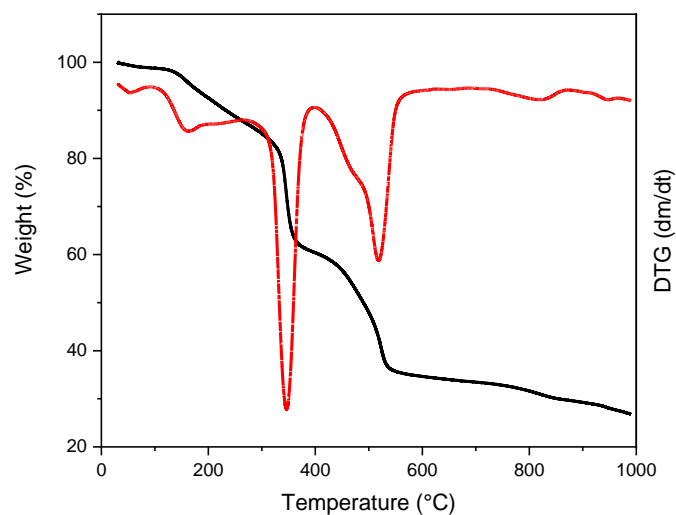


Figure SI71 TGA in N₂ for CTP-SBI-PIMs/microwave.

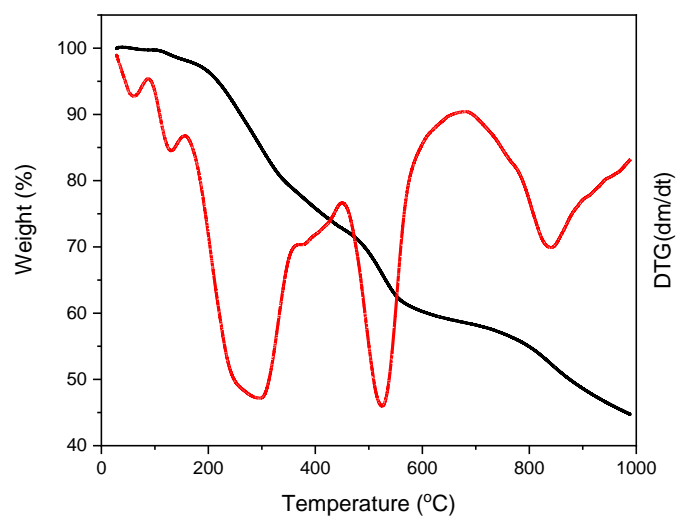


Figure SI72 TGA in N₂ for CTP-tolidine-PIM/reflux.

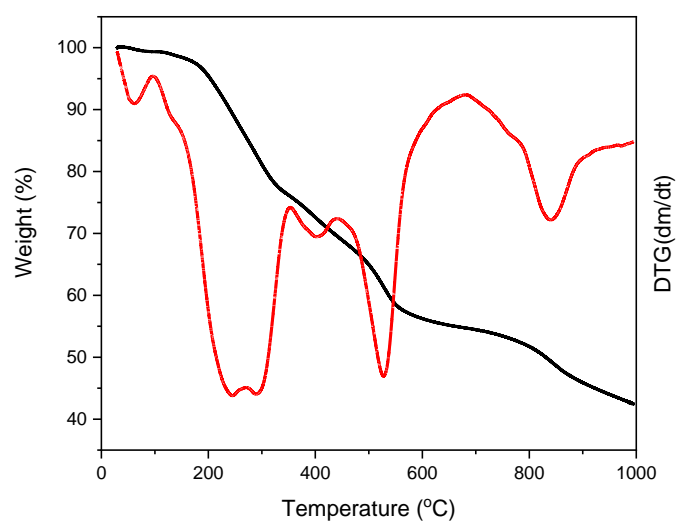


Figure SI73 TGA in N₂ for CTP-tolidine-PIM/microwave.

8.4 Isotherms

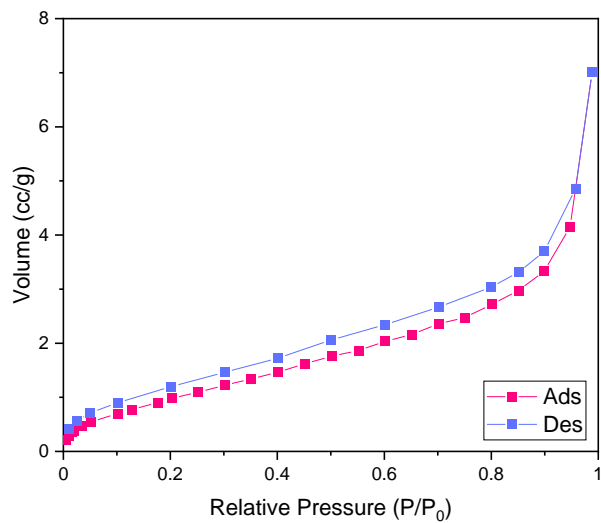


Figure SI74 N₂ adsorption-desorption at 77 K for model boroxine/sand bath

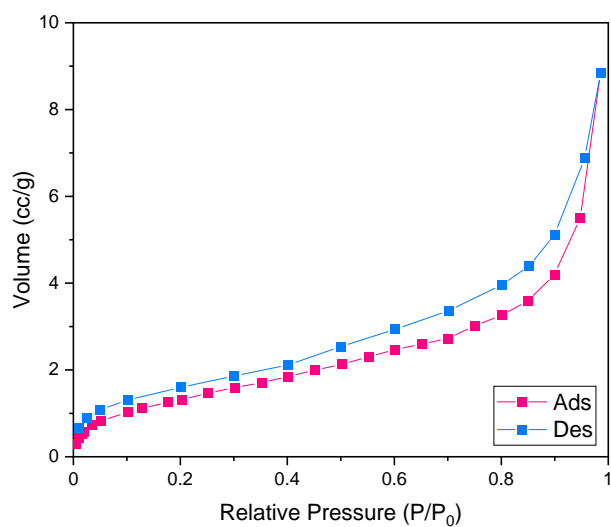


Figure SI75 N₂ adsorption-desorption at 77 K for model boroxine/microwave.

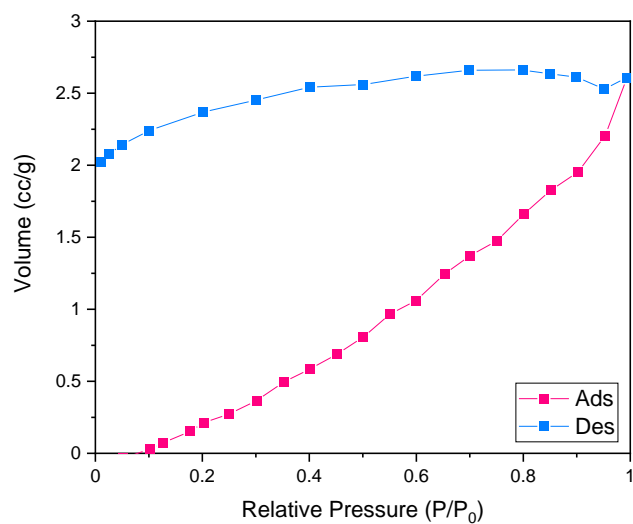


Figure SI76 N₂ adsorption-desorption at 77 K for BE-SBI-PIM.

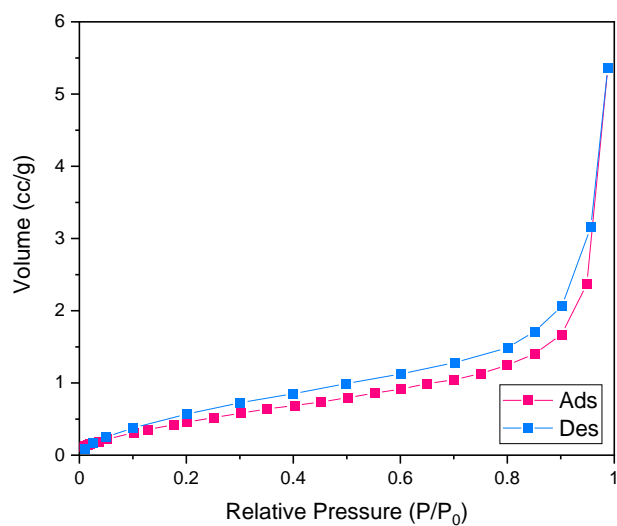


Figure SI77 N₂ adsorption-desorption at 77 K for BE-SBC-PIM.

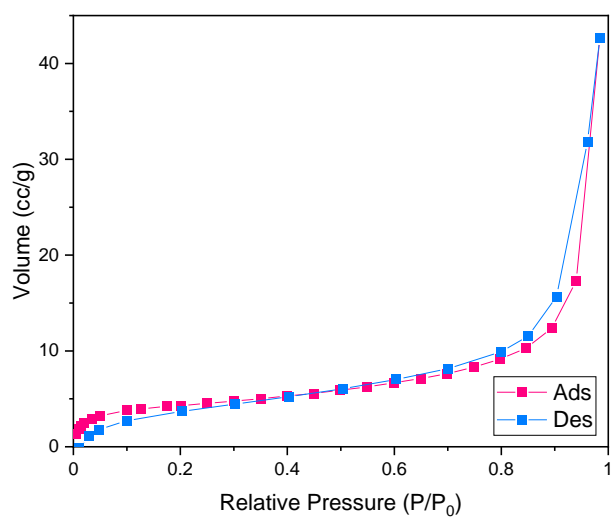


Figure SI78 N₂ adsorption-desorption at 77 K for BE-bis-K-PIM.

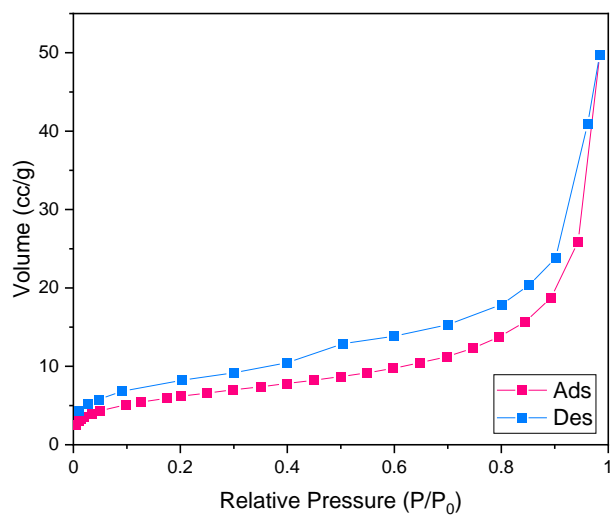


Figure SI79 N₂ adsorption-desorption at 77 K for BE-HPB-PIM.

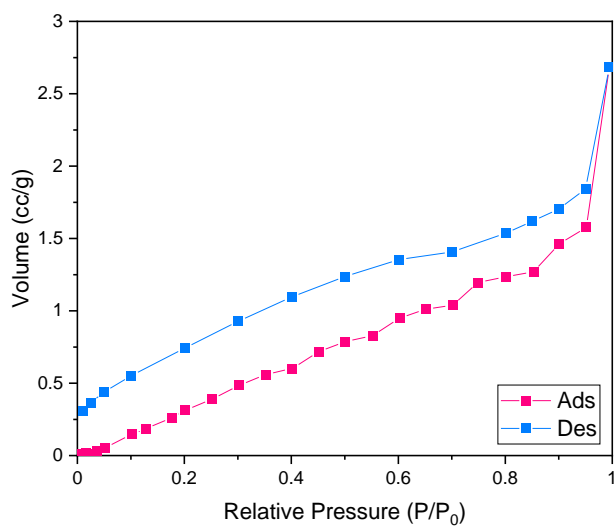


Figure SI80 N₂ adsorption-desorption at 77 K for BE-SBF-PIM.

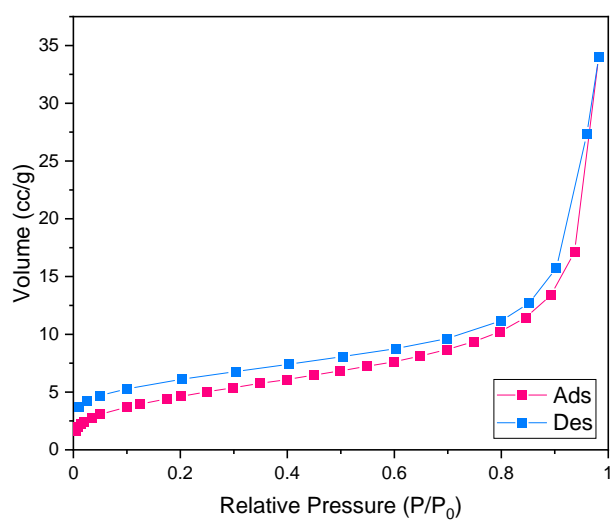


Figure SI81 N₂ adsorption-desorption at 77 K for BE-SBF-Me-PIM.

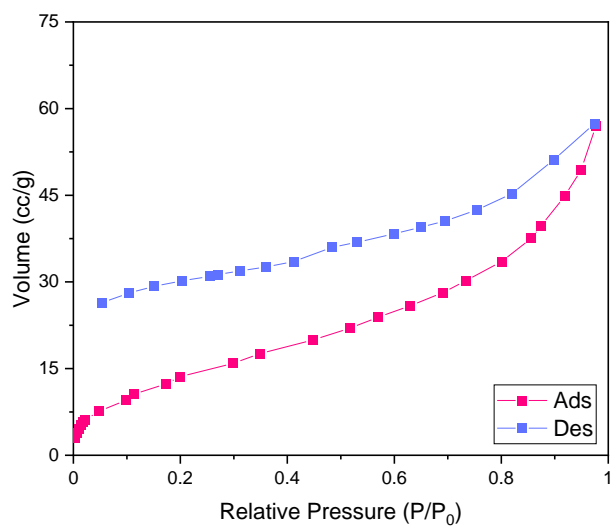


Figure SI82 N₂ adsorption-desorption at 77 K for di-TB-tetra-Me-HPB.

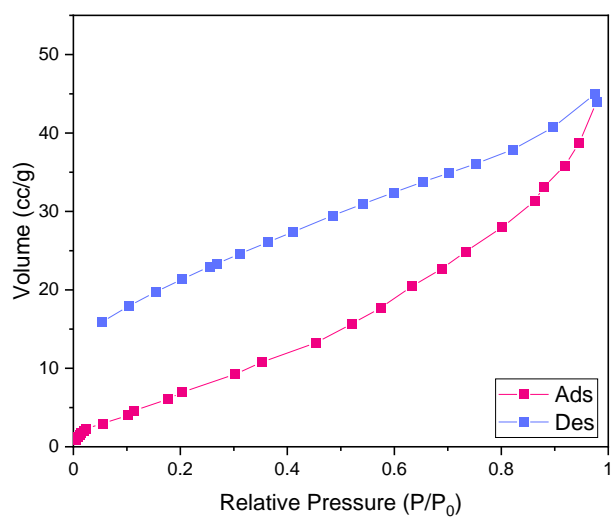


Figure SI83 N₂ adsorption-desorption at 77 K for di-TB-HPB.

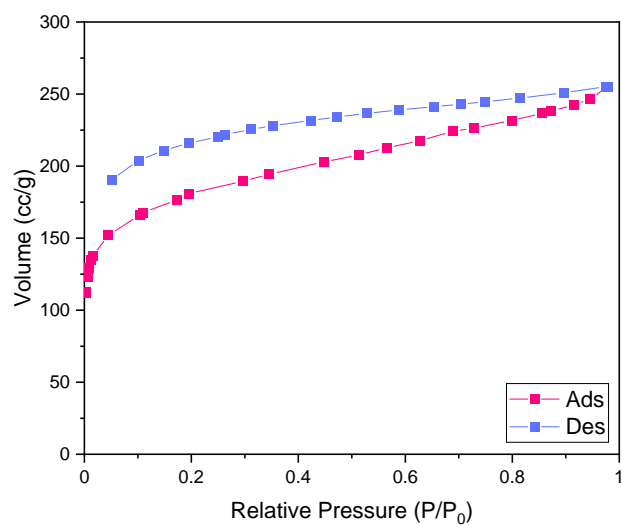


Figure SI84 N₂ adsorption-desorption at 77 K for tetra-TB-HPB.

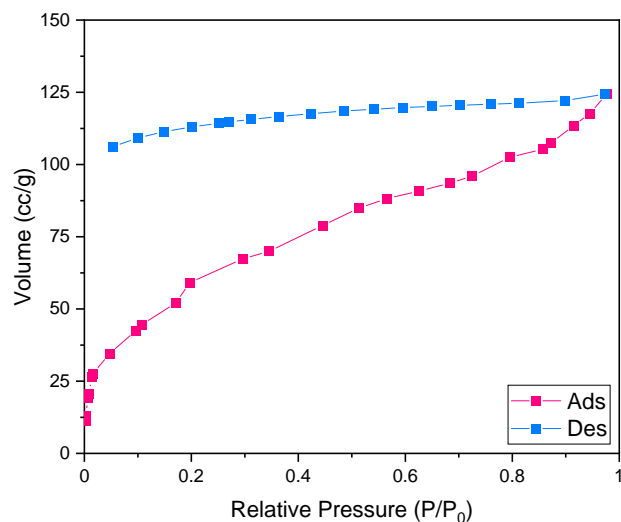


Figure SI85 N₂ adsorption-desorption at 77 K for hexa-TB-HPB.

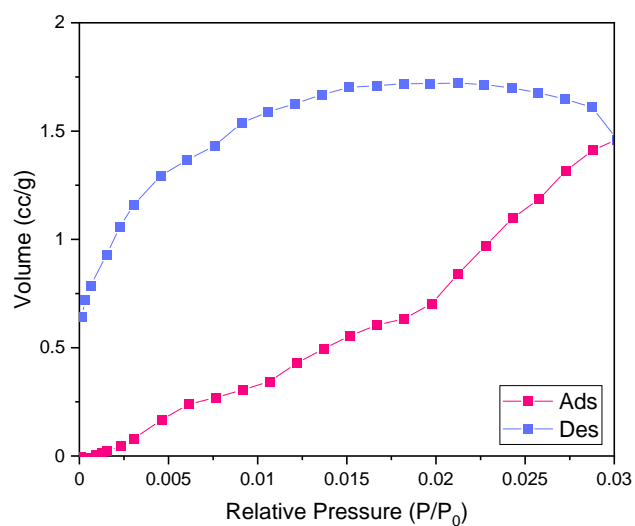


Figure SI86 CO₂ adsorption-desorption at 273 K for model boroxine/sand bath.

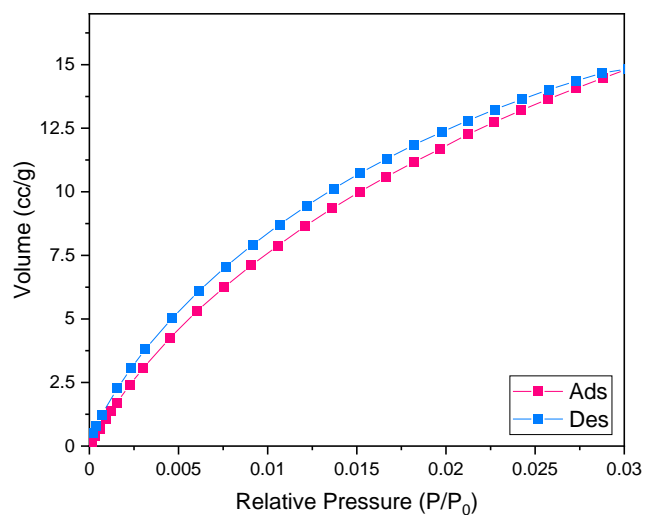


Figure SI87 CO₂ adsorption-desorption at 273 K for model boroxine/microwave.

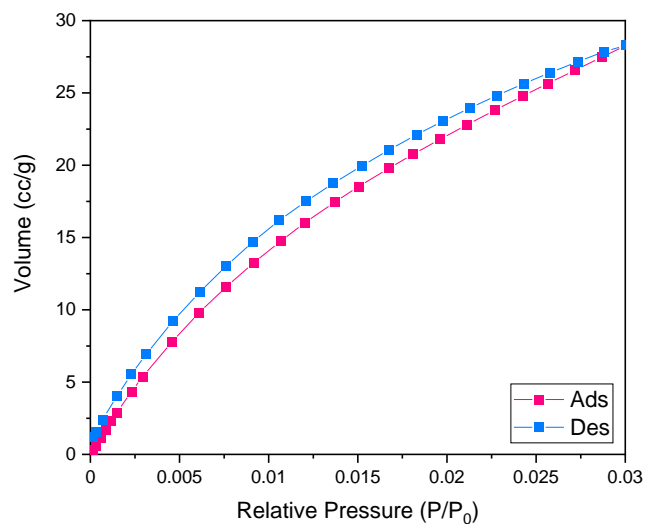


Figure SI88 CO₂ adsorption-desorption at 273 K for BE-SBI-PIM.

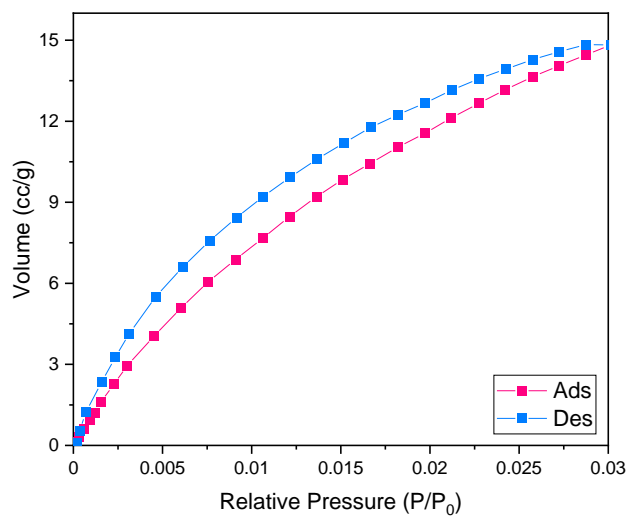


Figure SI89 CO₂ adsorption-desorption at 273 K for BE-SBC-PIM.

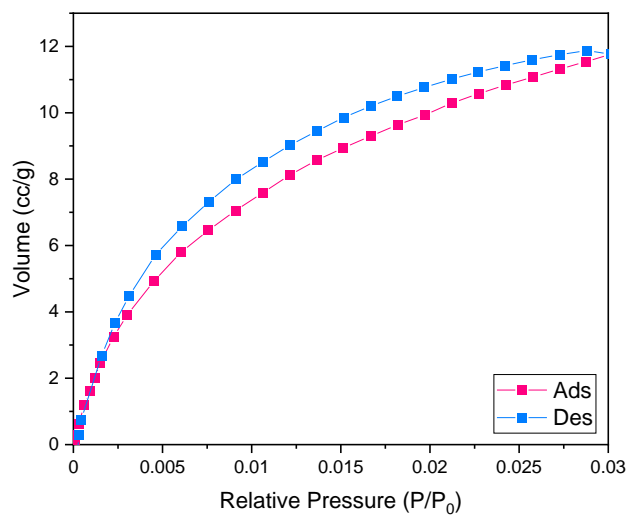


Figure SI90 CO₂ adsorption-desorption at 273 K for BE-bis-K-PIM.

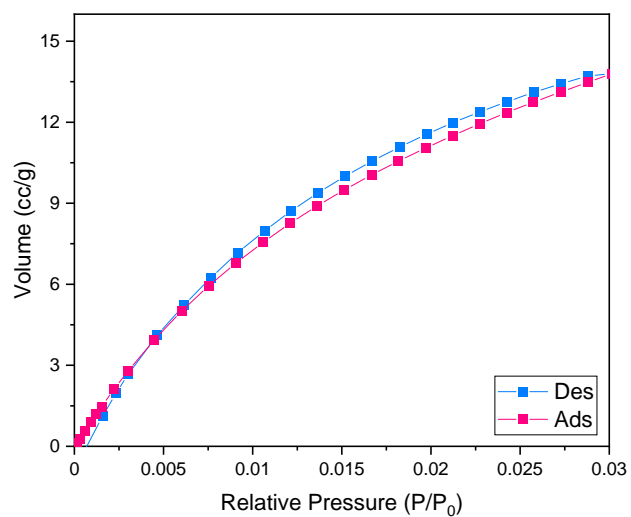


Figure SI91 CO₂ adsorption-desorption at 273 K for BE-HPB-PIM.

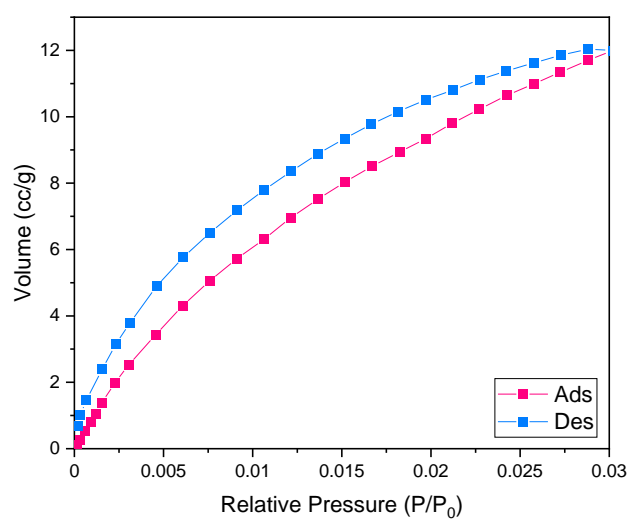


Figure SI92 CO₂ adsorption-desorption at 273 K for BE-SBF-PIM.

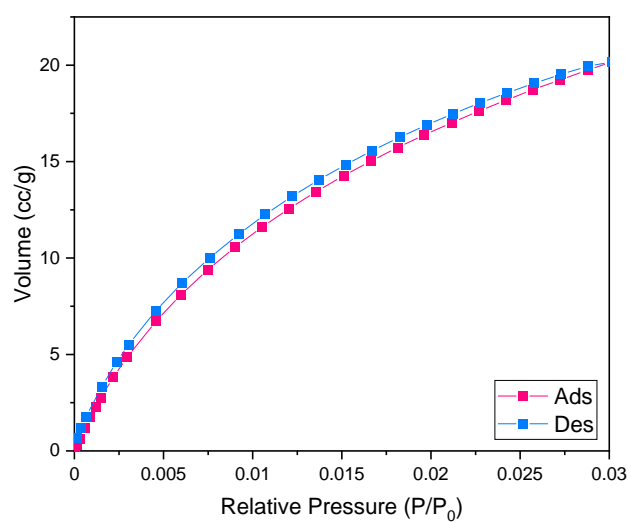


Figure SI93 CO₂ adsorption-desorption at 273 K for BE-SBF-Me-PIM.

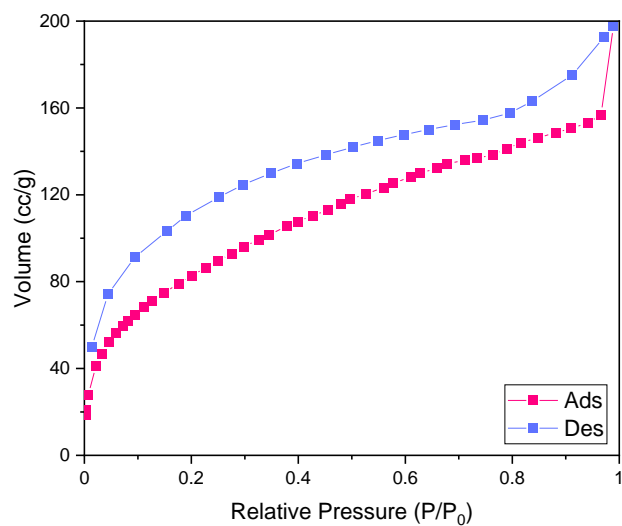


Figure SI94 CO₂ adsorption-desorption at 195 K for di-TB-tetra-Me-HPB.

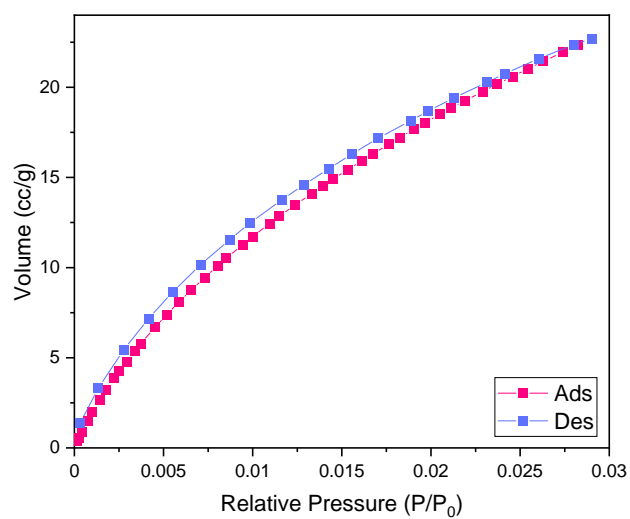


Figure SI95 CO₂ adsorption-desorption at 195 K for di-TB-tetra-Me-HPB.

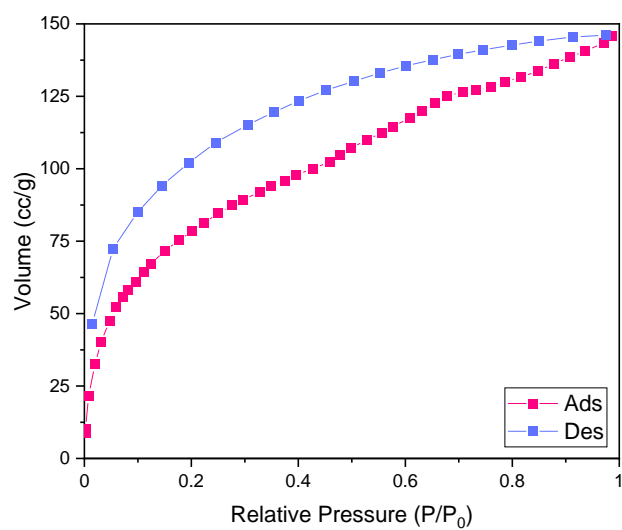


Figure SI96 CO₂ adsorption-desorption at 195 K for di-TB-HPB.

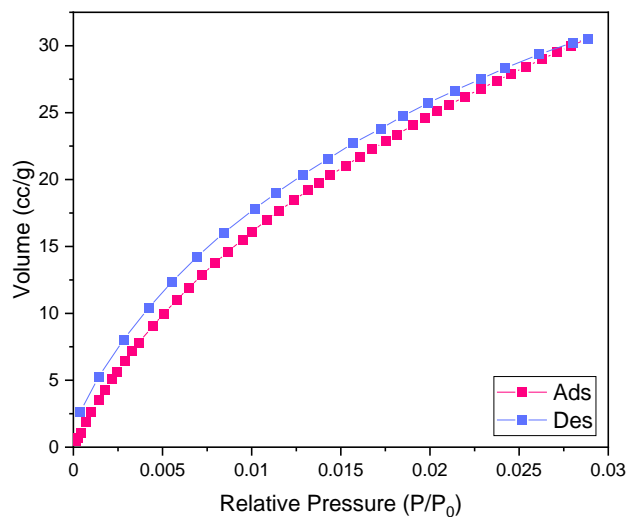


Figure SI96 CO₂ adsorption-desorption at 273 K for di-TB-HPB.

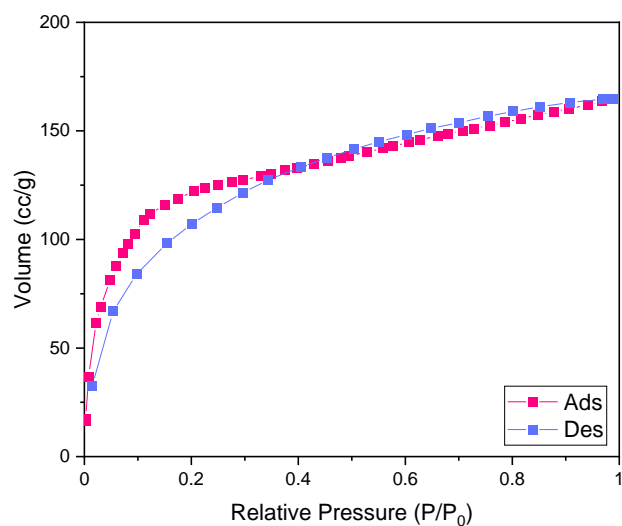


Figure SI97 CO₂ adsorption-desorption at 195 K for tetra-TB-HPB.

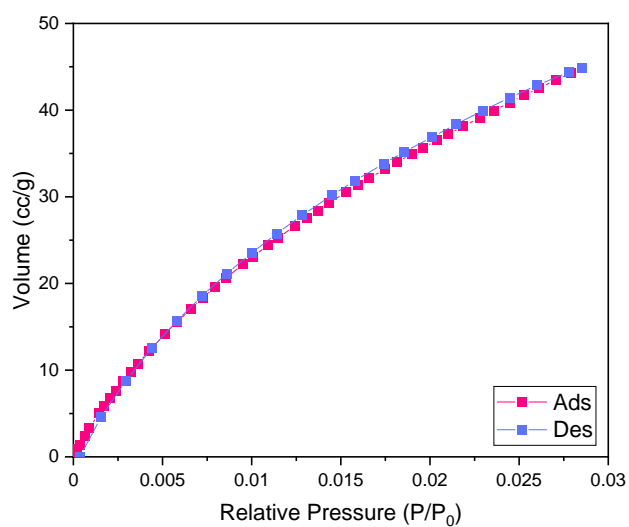


Figure SI98 CO₂ adsorption-desorption at 273 K for tetra-TB-HPB.

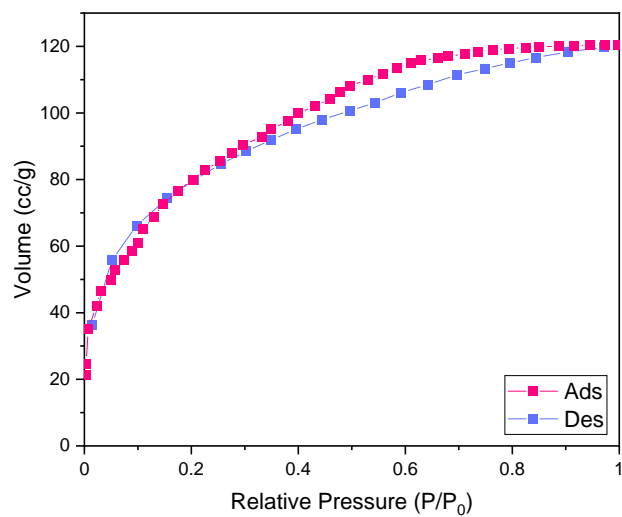


Figure SI99 CO₂ adsorption-desorption at 195 K for hexa-TB-HPB.

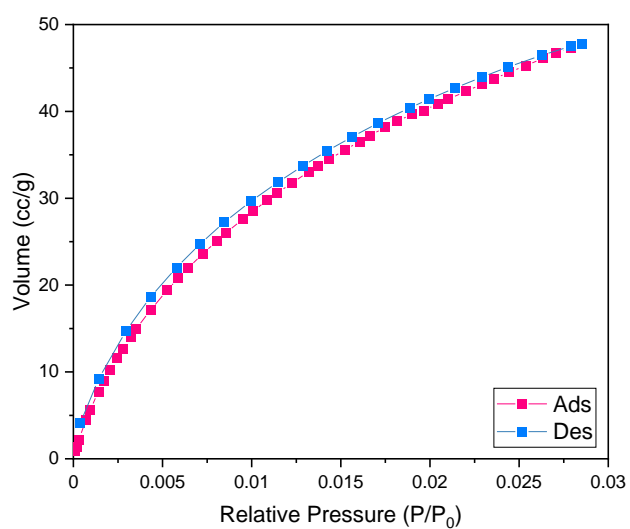


Figure SI100 CO₂ adsorption-desorption at 273 K for hexa-TB-HPB.

8.5 PSD

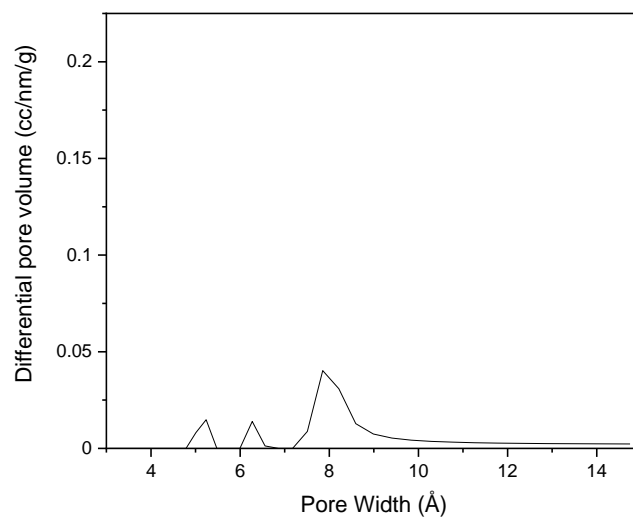


Figure SI101 PSD for model boroxine/sand bath.

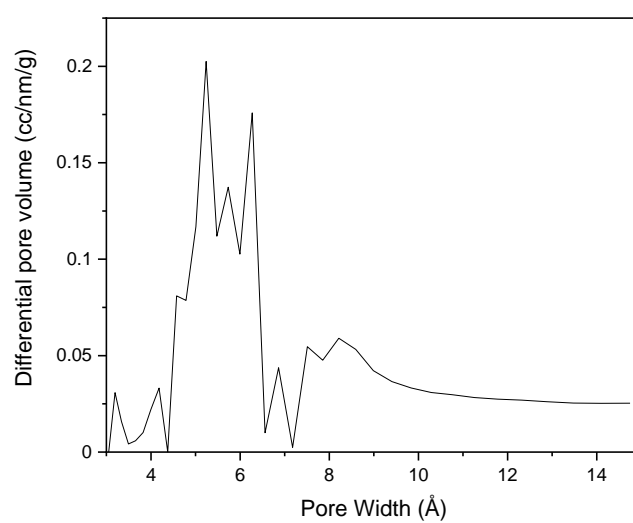


Figure SI102 PSD for model boroxine/microwave.

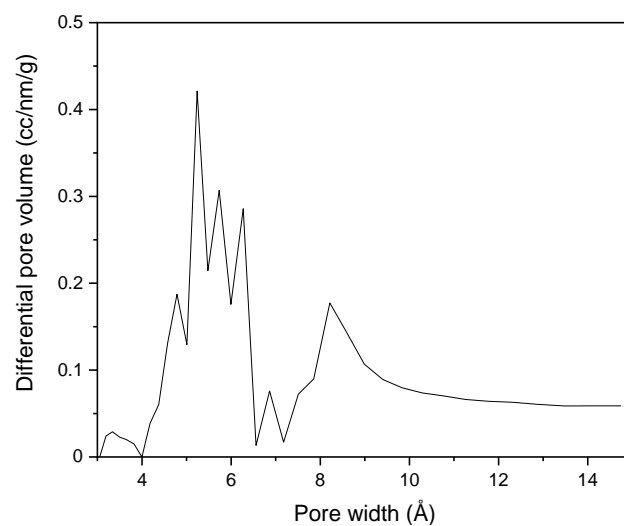


Figure SI103 PSD for BE-SBI-PIM.

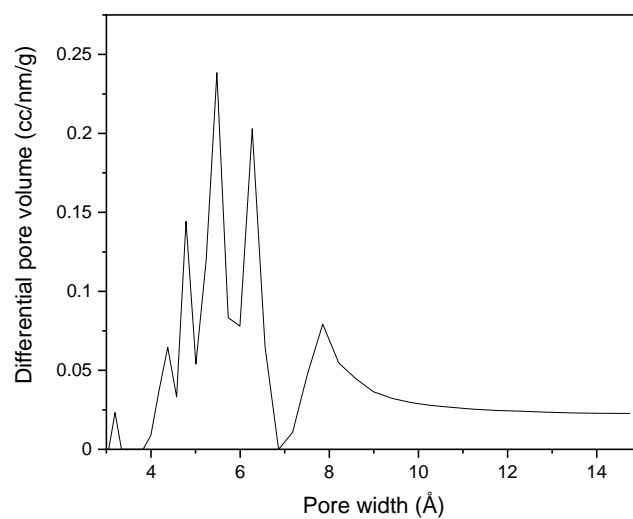


Figure SI104 PSD for BE-SBC-PIM.

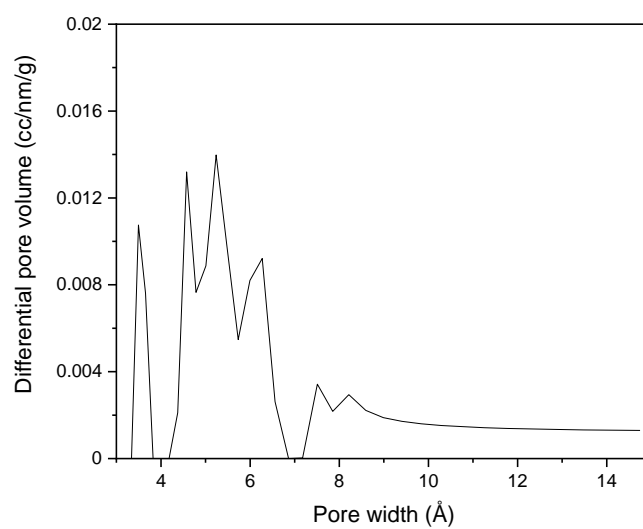


Figure SI105 PSD for BE-bis-K-PIM.

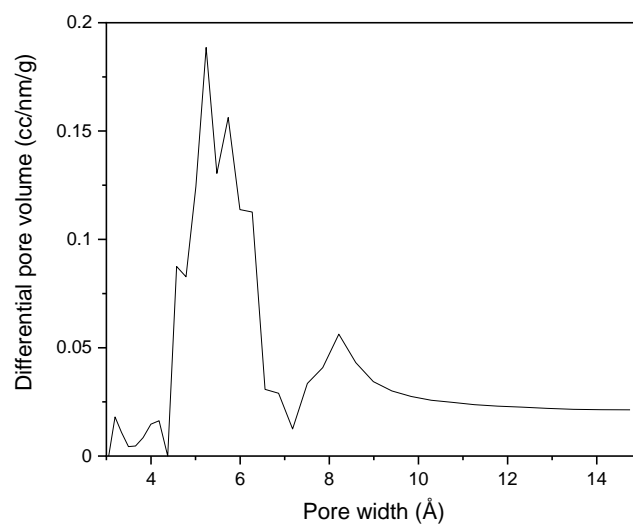


Figure SI106 PSD for BE-HPB-PIM.

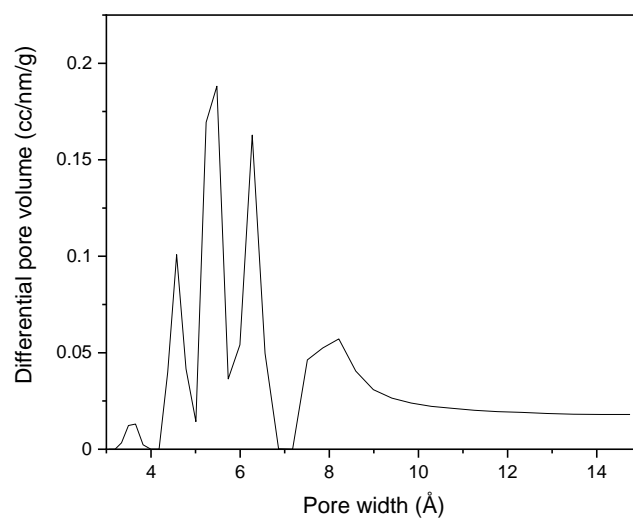


Figure SI107 PSD for BE-SBF-PIM.

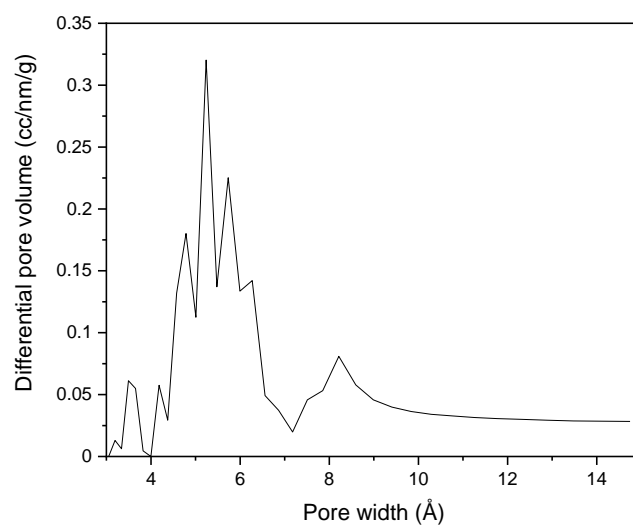


Figure SI108 PSD for BE-SBF-Me-PIM.

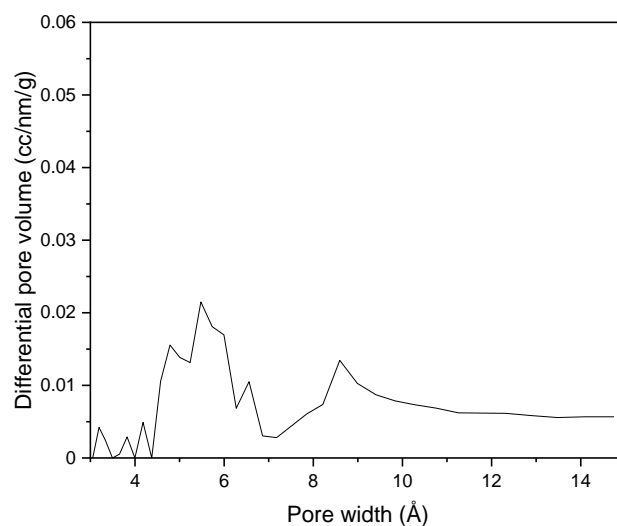


Figure SI109 PSD for di-TB-tetra-Me-HPB.

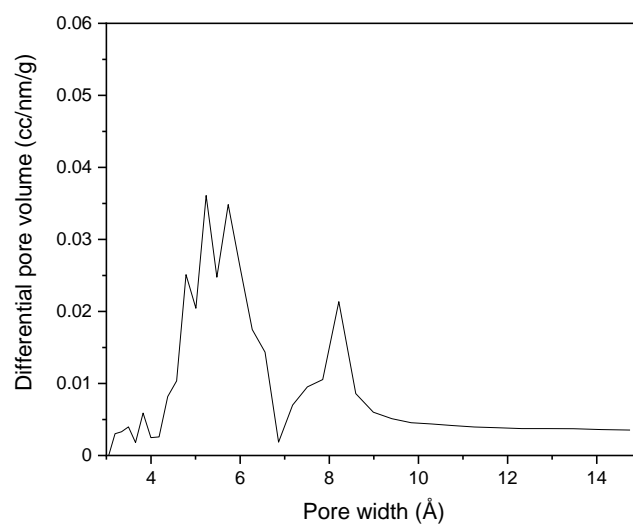


Figure SI110 PSD for di-TB-HPB.

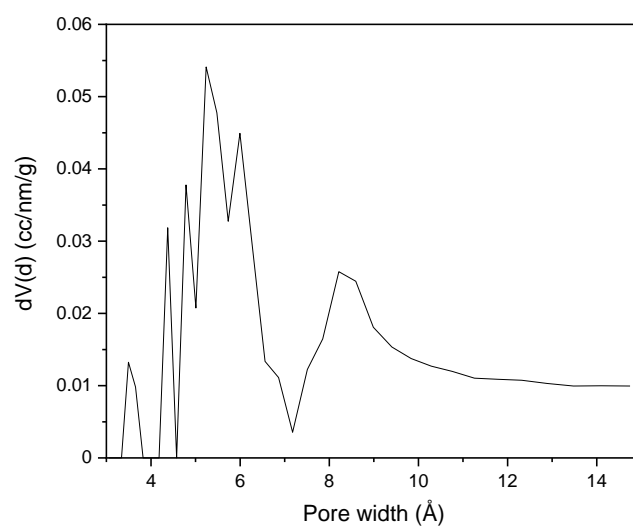


Figure SI111 PSD for tetra-TB-HPB.

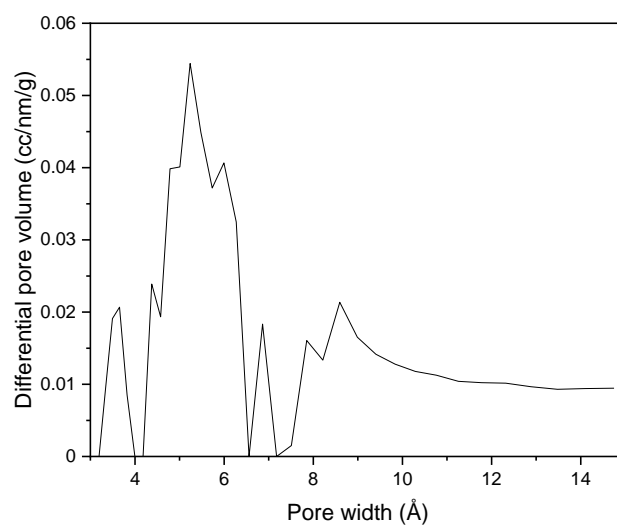


Figure SI112 PSD for hexa-TB-HPB.